Iterative tomographic X-Ray phase reconstruction

Loriane Weber

N° d'ordre NNT : 2016LYSEI085

THESE de DOCTORAT DE L'UNIVERSITE DE LYON
opérée au sein de
L'Institut National des Sciences Appliquées de Lyon

Ecole Doctorale 160
Électronique, Électrotechnique, Automatique

Spécialité de doctorat : Traitement du Signal et de l'Image

Soutenue publiquement le 30/09/2016, par :
Loriane Weber

Iterative tomographic X-Ray phase reconstruction

Devant le jury composé de :

VERDUN Francis	Professeur EPFL	Président
BLEUET Pierre	Chercheur CEA-LETI	Rapporteur
MOKSO Rajmund	Chercheur MAX IV	Rapporteur
BUFFIERE Jean-Yves	Professeur INSA-LYON	Examinateur
PEYRIN Françoise	DR INSERM	Directrice de thèse
LANGER Max	CR CNRS	Co-directeur de thèse
CLOETENS Peter	Chercheur ESRF	Invité

Département FEDORA – INSA Lyon - Ecoles Doctorales – Quinquennal 2016-2020

SIGLE	ECOLE DOCTORALE	NOM ET COORDONNEES DU RESPONSABLE
CHIMIE	**CHIMIE DE LYON** **http://www.edchimie-lyon.fr** Sec : Renée EL MELHEM Bat Blaise Pascal 3e etage secretariat@edchimie-lyon.fr Insa : R. GOURDON	M. Stéphane DANIELE Institut de Recherches sur la Catalyse et l'Environnement de Lyon IRCELYON-UMR 5256 Équipe CDFA 2 avenue Albert Einstein 69626 Villeurbanne cedex directeur@edchimie-lyon.fr
E.E.A.	**ELECTRONIQUE, ELECTROTECHNIQUE, AUTOMATIQUE** **http://edeea.ec-lyon.fr** Sec : M.C. HAVGOUDOUKIAN Ecole-Doctorale.eea@ec-lyon.fr	M. Gérard SCORLETTI Ecole Centrale de Lyon 36 avenue Guy de Collongue 69134 ECULLY Tél : 04.72.18 60.97 Fax : 04 78 43 37 17 Gerard.scorletti@ec-lyon.fr
E2M2	**EVOLUTION, ECOSYSTEME, MICROBIOLOGIE, MODELISATION** **http://e2m2.universite-lyon.fr** Sec : Safia AIT CHALAL Bat Darwin - UCB Lyon 1 04.72.43.28.91 Insa : H. CHARLES Safia.ait-chalal@univ-lyon1.fr	Mme Gudrun BORNETTE CNRS UMR 5023 LEHNA Université Claude Bernard Lyon 1 Bât Forel 43 bd du 11 novembre 1918 69622 VILLEURBANNE Cédex Tél : 06.07.53.89.13 e2m2@ univ-lyon1.fr
EDISS	**INTERDISCIPLINAIRE SCIENCES-SANTE** **http://www.ediss-lyon.fr** Sec : Safia AIT CHALAL Hôpital Louis Pradel - Bron 04 72 68 49 09 Insa : M. LAGARDE Safia.ait-chalal@univ-lyon1.fr	Mme Emmanuelle CANET-SOULAS INSERM U1060, CarMeN lab, Univ. Lyon 1 Bâtiment IMBL 11 avenue Jean Capelle INSA de Lyon 696621 Villeurbanne Tél : 04.72.68.49.09 Fax :04 72 68 49 16 Emmanuelle.canet@univ-lyon1.fr
INFOMATHS	**INFORMATIQUE ET MATHEMATIQUES** **http://infomaths.univ-lyon1.fr** Sec :Renée EL MELHEM Bat Blaise Pascal 3e etage infomaths@univ-lyon1.fr	Mme Sylvie CALABRETTO LIRIS – INSA de Lyon Bat Blaise Pascal 7 avenue Jean Capelle 69622 VILLEURBANNE Cedex Tél : 04.72. 43. 80. 46 Fax 04 72 43 16 87 Sylvie.calabretto@insa-lyon.fr
Matériaux	**MATERIAUX DE LYON** **http://ed34.universite-lyon.fr** Sec : M. LABOUNE PM : 71.70 –Fax : 87.12 Bat. Saint Exupéry Ed.materiaux@insa-lyon.fr	M. Jean-Yves BUFFIERE INSA de Lyon MATEIS Bâtiment Saint Exupéry 7 avenue Jean Capelle 69621 VILLEURBANNE Cedex Tél : 04.72.43 71.70 Fax 04 72 43 85 28 Ed.materiaux@insa-lyon.fr
MEGA	**MECANIQUE, ENERGETIQUE, GENIE CIVIL, ACOUSTIQUE** **http://mega.universite-lyon.fr** Sec : M. LABOUNE PM : 71.70 –Fax : 87.12 Bat. Saint Exupéry mega@insa-lyon.fr	M. Philippe BOISSE INSA de Lyon Laboratoire LAMCOS Bâtiment Jacquard 25 bis avenue Jean Capelle 69621 VILLEURBANNE Cedex Tél : 04.72 .43.71.70 Fax : 04 72 43 72 37 Philippe.boisse@insa-lyon.fr
ScSo	**ScSo*** **http://recherche.univ-lyon2.fr/scso/** Sec : Viviane POLSINELLI Brigitte DUBOIS Insa : J.Y. TOUSSAINT viviane.polsinelli@univ-lyon2.fr	Mme Isabelle VON BUELTZINGLOEWEN Université Lyon 2 86 rue Pasteur 69365 LYON Cedex 07 Tél : 04.78.77.23.86 Fax : 04.37.28.04.48

*ScSo : Histoire, Géographie, Aménagement, Urbanisme, Archéologie, Science politique, Sociologie, Anthropologie

Remerciements

« En essayant continuellement, on finit par réussir; donc:
plus ça rate, plus on a de chances que ça marche. »

Table of contents

Résumé

L'imagerie par contraste de phase suscite un intérêt croissant dans le domaine biomédical, puisqu'il offre un contraste amélioré par rapport à l'imagerie d'atténuation conventionnelle. En effet, le décalage en phase induit par les tissus mous, dans la gamme d'énergie utilisée en imagerie, est environ mille fois plus important que leur atténuation. Le contraste de phase peut être obtenu, entre autres, en laissant un faisceau de rayons X cohérent se propager librement après avoir traversé un échantillon. Dans ce cas, les signaux obtenus peuvent être modélisés par la diffraction de Fresnel. Le défi de l'imagerie de phase quantitative est de retrouver l'atténuation et l'information de phase de l'objet observé, à partir des motifs diffractés enregistrés à une ou plusieurs distances. Ces deux quantités d'atténuation et de phase, sont entremêlées de manière non-linéaire dans le signal acquis.

Dans ces travaux, nous considérons les développements et les applications de la micro- et nanotomographie de phase.

D'abord, nous nous sommes intéressés à la reconstruction quantitative de biomatériaux à partir d'une acquisition multi-distance. L'estimation de la phase a été effectuée via une approche mixte, basée sur la linéarisation du modèle de contraste. Elle a été suivie d'une étape de reconstruction tomographique. Nous avons automatisé le processus de reconstruction de phase, permettant ainsi l'analyse d'un grand nombre d'échantillons. Cette méthode a été utilisée pour étudier l'influence de différentes cellules osseuses sur la croissance de l'os. Ensuite, des échantillons d'os humains ont été observés en nanotomographie de phase. Nous avons montré le potentiel d'une telle technique sur l'observation et l'analyse du réseau lacuno-canaliculaire de l'os. Nous avons appliqué des outils existants pour caractériser de manière plus approfondie la minéralisation et les l'orientation des fibres de collagènes de certains échantillons.

L'estimation de phase, est, néanmoins, un problème inverse mal posé. Il n'existe pas de méthode de reconstruction générale. Les méthodes existantes sont soit sensibles au bruit basse fréquence, soit exigent des conditions strictes sur l'objet observé. Ainsi, nous considérons le problème inverse joint, qui combine l'estimation de phase et la reconstruction tomographique en une seule étape. Nous avons proposé des algorithmes itératifs innovants qui couplent ces deux étapes dans une seule boucle régularisée. Nous avons considéré un modèle de contraste linéarisé, couplé à un algorithme algébrique de reconstruction tomographique. Ces algorithmes sont testés sur des données simulées.

Résumé étendu

Dans cette thèse, nous nous intéressons à la micro et nano-tomographie par rayons X, en contraste de phase, ainsi qu'à ses applications et ses développements.

La technique du contraste de phase par rayons X s'avère particulièrement intéressante pour observer des tissus mous (tissus biologiques), dans la gamme d'énergie utilisée en imagerie (10 à 100keV), car elle offre un contraste environ mille fois plus important que l'imagerie d'atténuation conventionnelle. Une telle technique a été rendue possible par l'essor des synchrotrons, dont le rayonnement produit est très intense (flux de photons élevé) et très cohérent spatialement et temporellement (monochromaticité). Le flux intense du rayonnement synchrotron produit à l'Installation Européenne de Rayonnement Synchrotron (ESRF, Grenoble, France) permet de traverser des matériaux denses, comme par exemple l'os, tout en obtenant un bon rapport signal-sur-bruit. Sa cohérence spatiale permet d'exploiter la réfraction des rayons X induite par les structures observées; le décalage en phase du rayonnement incident nous donne accès à son indice de réfraction complexe. Sa monochromaticité fait de cette technique une technique d'imagerie quantitative. Couplée aux détecteurs développés au sein de l'ESRF (de taille 2048x2048 pixels, et prochainement 4096x4096) (Labiche et al., 2007), elle offre une haute résolution sur un champ de vue relativement large. En outre, elle est non destructive et ne nécessite pas de marquage particulier pour observer les échantillons. Les domaines d'application des techniques utilisant le rayonnement synchrotron sont vastes : médecine, que ce soit dans le domaine de l'imagerie (Horng et al., 2014) ou de la radiothérapie (Dilmanian et al., 2002), science des matériaux, pouvant aller des biomatériaux (Komlev et al., 2010) aux métaux (Maire, Buffière, Mokso, Cloetens, & Ludwig, 2006), environnement (Rivard, Lanson, & Cotte, 2015) ou encore patrimoine culturel (Pouyet, Fayard, & Salomé, 2015).

Une imagerie quantitative nécessite néanmoins l'utilisation d'algorithmes d'estimation de phase sur les images acquises; la plupart de ces algorithmes sont conçus pour des objets homogènes. D'autres algorithmes ont été imaginés pour l'observation d'objets hétérogènes, mais nécessitent plusieurs acquisitions. L'acquisition multiple de données se fait au détriment de la dose délivrée et du temps de scanographie. Ainsi, l'emploi d'algorithmes itératifs régularisés pourrait permettre l'utilisation de moins de données, réduisant alors la dose délivrée et le temps d'acquisition. Les objectifs de ces travaux étaient donc de développer et d'implémenter de tels algorithmes pour la reconstruction tridimensionnelle de la phase. Jusqu'alors, l'introduction d'information a priori et de régularisation était faite dans le domaine des projections, ce qui n'est pas forcément idéal ; par exemple, l'emploi de régularisation TV, qui favorise une image homogène par morceaux, a plus de sens dans le domaine objet que dans celui des projections. Ainsi, le fait d'itérer entre les domaines des projections et de l'objet favorise la régularisation dans le domaine objet, plutôt que dans celui des projections. D'autre part, cette thèse avait pour but l'implémentation d'un outil de simulation d'image en contraste de phase sur la plateforme d'imagerie virtuelle VIP (Creatis, Villeurbanne), jusqu'alors inexistant.

Le Chapitre I s'intéresse à la physique des rayons X et à la tomographie assistée par ordinateur (CT). Nous y présentons en détails le rayonnement synchrotron, ainsi que les interactions pouvant avoir lieu entre un faisceau de rayons X et la matière qu'il traverse (interactions photoélectriques, interactions par effet Compton, créations de paires, diffusion Rayleigh). Ces principes physiques nous permettent d'aborder l'imagerie par contraste de phase, qui s'intéresse au décalage en phase induit par un objet sur un faisceau incident cohérent.

Dans toute cette section, les coordonnées utilisées sont représentées sur la Figure 1. Le plan (x, y), noté $\boldsymbol{x}$, est le plan de projection. L'axe z suit la direction de propagation du faisceau de rayons X.

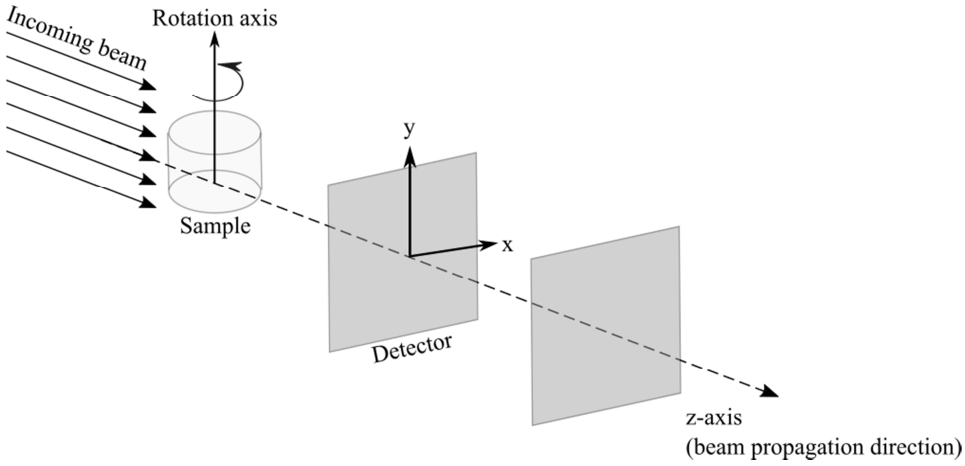

Figure 1: Schéma des coordonnées utilisées dans ce manuscrit.

La matière peut être caractérisée, entre autres, par son indice de réfraction complexe n:

$$n(\boldsymbol{x}, z) = 1 - \delta_n(\boldsymbol{x}, z) + i\beta(\boldsymbol{x}, z). \tag{0.0.1}$$

La partie réelle de l'indice de réfraction n, $(1 - \delta_n)$, est liée au décalage de phase φ_θ induit par l'objet, via la relation:

$$\varphi_\theta(\boldsymbol{x}) = -\frac{2\pi}{\lambda}\int \delta_n(\boldsymbol{x}, z)\, dz \tag{0.0.2}$$

La partie imaginaire de n, β, est liée à l'atténuation B_θ de l'objet :

$$B_\theta(\boldsymbol{x}) = \frac{2\pi}{\lambda}\int \beta(\boldsymbol{x}, z)\, dz \tag{0.0.3}$$

En d'autres termes, le décalage en phase φ_θ et l'atténuation B_θ peuvent être vus comme les projections de δ_n et β à l'angle θ, à un facteur multiplicatif près, qui dépend de la longueur d'onde λ du faisceau. Ces indices δ_n et β, respectivement appelés *décrément de l'indice de réfraction* et *indice d'absorption*, dépendent de la composition du matériau, et de l'énergie du faisceau de rayons X. Or, pour les tissus mous, et dans la gamme des rayons X durs (10 à 100keV), on observe que le décrément de l'indice de réfraction est environ mille fois supérieur à l'indice d'absorption, comme l'indique la Figure 2.

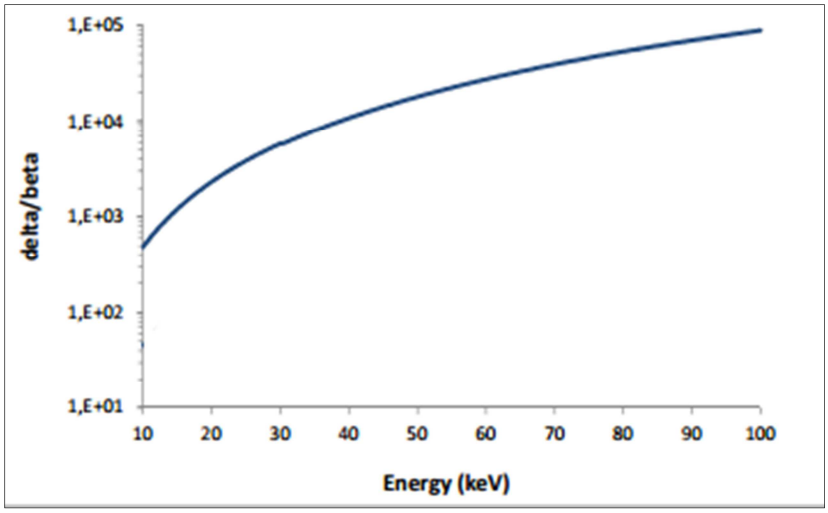

Figure 2: Ratio $\boldsymbol{\delta_n/\beta}$ pour les tissus mous en fonction de l'énergie du faisceau (domaine des rayons X durs).

À titre de comparaison, la Figure 3 montre une image acquise en absorption (imagerie conventionnelle d'atténuation), et son équivalent acquis en contraste de phase (par la méthode du cristal analyseur, décrite plus loin). Ces images ont été acquises sur la ligne ID17 de l'ESRF (Grenoble). On remarque bien que le bord des structures est mis en évidence dans l'image en contraste de phase (*edge-enhancement effect*).

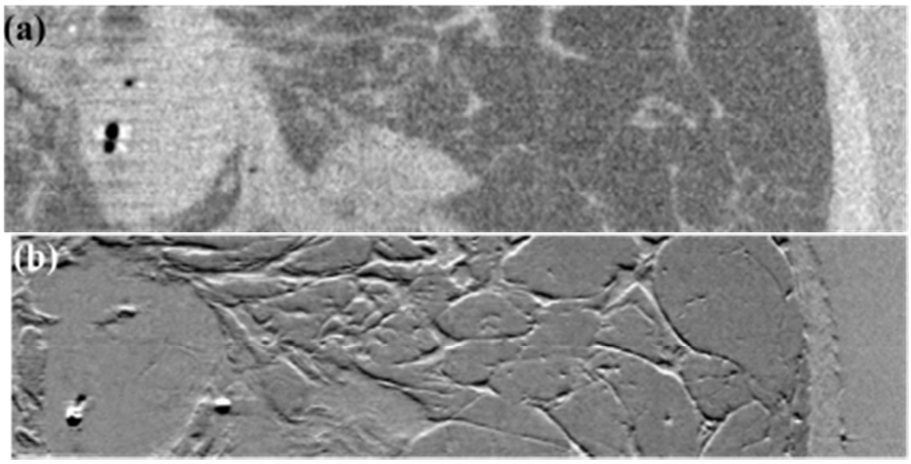

Figure 3: Coupe sagittale d'un sein porteur d'une tumeur (a) en imagerie d'absorption et (b) en imagerie par contraste de phase par analyseur, à 60keV. La taille effective du pixel est de 92µm, et l'image représente une zone de 6,4 cm en longueur par 1,6 cm en hauteur.

Expérimentalement, il existe plusieurs techniques d'imagerie par contraste de phase :

- La plus ancienne est la technique des cristaux interféromètres, qui utilise trois cristaux en géométrie Laue (*i.e.* en transmission), parfaitement alignés (Bonse & Hart, 1965). Le premier cristal sépare le faisceau incident en deux faisceaux cohérents, le second les fait interférer sur un troisième (appelé cristal analyseur). L'échantillon est placé entre le deuxième et le troisième cristal, les franges d'interférences induites par l'échantillon sont enregistrées par le détecteur. Son application à l'imagerie 3D des tissus mous a été démontrée plus tard (Momose, Takeda, Itai, & Hirano, 1996; Momose, 2003).

- La technique par cristal analyseur utilise deux cristaux en géométrie de Bragg (*i.e.* réfraction). Le premier cristal sert à rendre le faisceau incident monochromatique ; le second (cristal analyseur) est placé entre l'échantillon et le détecteur, et agit comme un filtre angulaire en sélectionnant seulement certains angles de réfraction du faisceau (Chapman et al., 1997). Cette technique nécessite une installation très stable, et elle est réputée longue, du fait que les cristaux réduisent considérablement le flux de photons. Elle trouve des applications dans le domaine biomédical, et particulièrement en mammographie (Fiedler et al., 2004; Keyriläinen et al., 2005) et en imagerie du cartilage et de l'os (Izadifar, Chapman, & Chen, 2014; Majumdar et al., 2004; Mollenhauer et al., 2002). Des efforts ont été fait pour rendre cette technique compatible avec les doses délivrées en routine clinique (Keyriläinen et al., 2008; Mittone, Gasilov, Brun, Bravin, & Coan, 2015).

- La technique d'interférométrie à grilles ne nécessite pas forcément un faisceau cohérent en entrée, mais le rend cohérent au moyen d'une première grille. Ceci rend possible l'utilisation de sources conventionnelles (Pfeiffer, Weitkamp, Bunk, & David, 2006). L'utilisation de grilles est fondée sur le principe du *self-imaging* (répétition du motif de grille) ; en effet, lorsqu'un faisceau cohérent traverse une grille induisant un décalage en phase conséquent, le motif de la grille est répété à distance régulière (appelée distance de Talbot fractionnaire).

- La technique de propagation libre (Figure 4) vise à enregistrer les interférences créées par l'échantillon sur le faisceau incident cohérent. Cette technique repose sur le principe de la diffraction de Fresnel. Elle nécessite un faisceau cohérent, et possiblement monochromatique (qui rend l'imagerie quantitative). La technique dite de propagation libre consiste à laisser le faisceau se propager librement après avoir traversé l'échantillon. Des franges d'interférences se créent à mesure que l'on s'éloigne de l'échantillon. Le détecteur, placé à une certaine distance de l'échantillon (appelée *distance de propagation*), enregistre ces franges d'interférences. L'intensité recueillie est une combinaison de la déviation de phase et de l'atténuation du faisceau induites par l'échantillon.

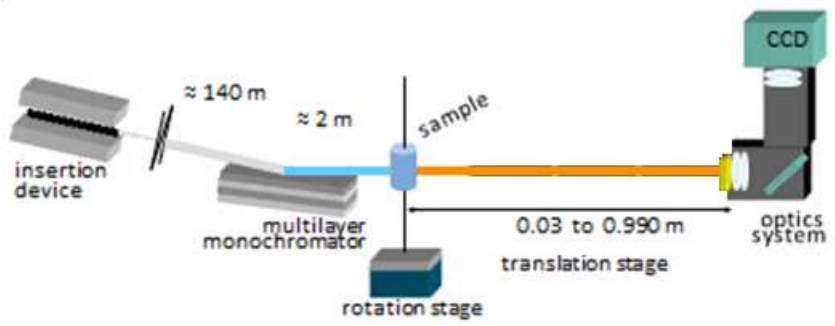

Figure 4: Système d'acquisition en propagation libre, comme existant sur la ligne ID19 de l'ESRF (Grenoble).

Dans ces travaux, nous nous intéressons particulièrement à l'*holotomographie*, qui résulte en une acquisition en propagation libre à plusieurs distances de propagation. Les deux lignes de lumières ID19 et ID16A de l'ESRF permettent, entre autres, une acquisition holotomographique. La différence notable entre ces deux lignes est qu'ID19 utilise un faisceau parallèle, donnant accès à des résolutions micrométriques, alors qu'ID16A opte pour un faisceau divergent, donnant accès à des résolutions pouvant aller jusqu'à quelques dizaines de nanomètres, pour la même technique. Ces deux techniques sont présentées dans ce manuscrit.

Le contraste de phase nous permet donc de mettre en évidence des structures que l'on n'aurait pas pu discerner en imagerie d'atténuation classique. Bien que les projections acquises puissent être directement utilisées dans un algorithme de tomographie classique (type Rétroprojection filtrée), il convient souvent d'appliquer, au préalable, un algorithme d'estimation de la phase. Dans ce cas, on récupère des projections de l'information de phase, que l'on peut de la même manière utilisée dans une rétroprojection filtrée. Par exemple, la Figure 5 montre une coupe transversale reconstruite d'une biopsie de sein, acquise en interférométrie à grilles (sans estimation de phase), et à droite son équivalent après estimation de phase. Le contraste est nettement amélioré.

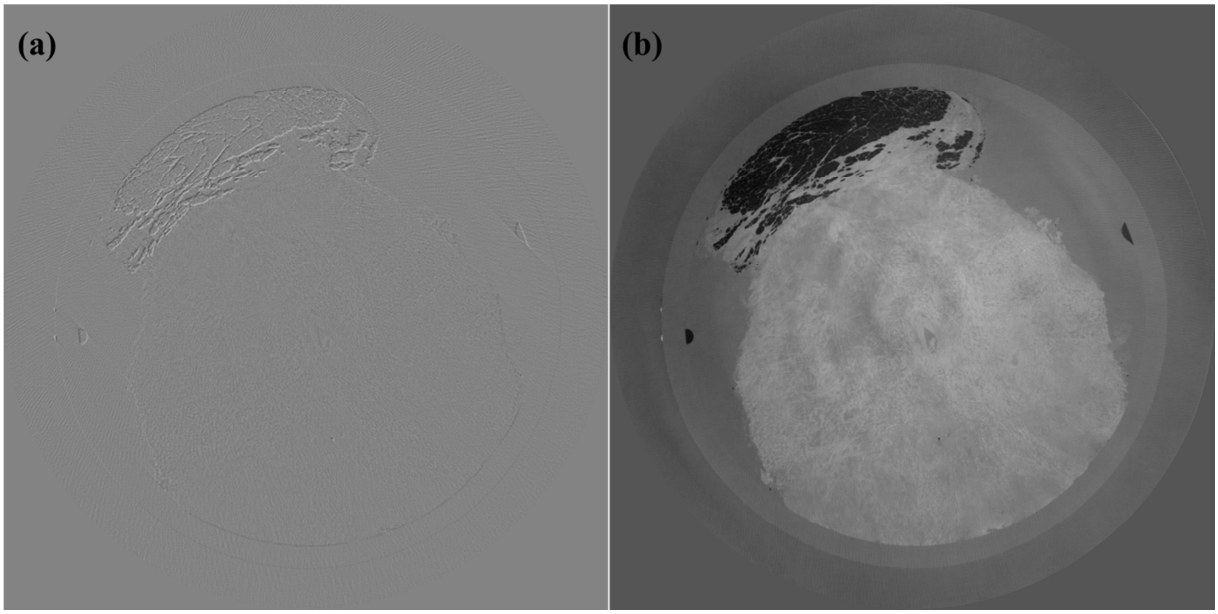

Figure 5: Coupe transversale d'une biopsie de sein. La figure (a) montre le signal acquis avec la technique d'interférométrie à grilles, sur la ligne ID17 de l'ESRF (Grenoble). La figure (b) montre le signal après estimation de phase. L'image représente une zone de 1,5 cm sur 1,5 cm.

Puisque l'intensité acquise combine, de manière non-linéaire, l'atténuation et la déviation de phase, cette étape d'estimation de phase peut être vue comme un problème inverse mal posé. Les algorithmes d'estimation de phase se fondent sur différents modèles de contraste, souvent linéarisés, et reposent eux-mêmes sur différentes hypothèses quant à l'objet imagé.

Le chapitre II s'intéresse aux différents modèles de contraste utilisés en propagation libre, ainsi qu'aux méthodes d'estimation de phase existantes. Les algorithmes de reconstruction tomographique analytiques et algébriques sont également mentionnés, avant de faire l'état de l'art des algorithmes combinant estimation de phase et reconstruction tomographique.

Il existe plusieurs modèles de contraste, reposant sur différentes hypothèses quant à la nature de l'objet. Les plus connues, et que nous étudions dans ces travaux, sont l'Équation du Transport de l'Intensité (TIE), la Fonction de Transfert du Contraste (CTF) et le modèle mixte. Chacun de ces modèles exprime l'intensité acquise à une distance de propagation D, $I_D(\boldsymbol{x})$, en fonction d'autres paramètres, tels que le décalage de phase $\varphi_\theta(\boldsymbol{x})$ ou la longueur d'onde λ du faisceau.

L'équation du transport d'intensité (TIE) est valable pour des mesures non-interférométriques, comme c'est le cas en propagation libre, pour un faisceau parallèle et des distances de propagations relativement courtes (Teague, 1982). Elle s'exprime comme suit :

$$I_{D,\theta}(\boldsymbol{x}) = I_{0,\theta}(\boldsymbol{x}) - \frac{\lambda D}{2\pi}\nabla_{\boldsymbol{x}}\left(I_{0,\theta}(\boldsymbol{x})\nabla_{\boldsymbol{x}}\varphi_{\theta}(\boldsymbol{x})\right) \tag{0.0.4}$$

où θ désigne l'angle de rotation de l'objet, $I_{0,\theta}(\boldsymbol{x})$ est l'intensité dans le plan de contact, $I_{D,\theta}(\boldsymbol{x})$ l'intensité mesurée à la distance de propagation D, λ la longueur d'onde du faisceau incident et $\nabla_{\boldsymbol{x}}$ est le gradient dans le plan (x, y).

Ce modèle a donné lieu à une méthode d'estimation de phase très utilisée, la méthode dite de Paganin (Paganin, Mayo, Gureyev, Miller, & Wilkins, 2002). Elle permet de retrouver le décalage en phase d'un objet homogène, connaissant son rapport δ_n/β (tabulé), à partir d'une mesure à une seule distance de propagation:

$$\varphi_{\theta}(\boldsymbol{x}) = \frac{\delta_n}{2\beta}\ln\left(\mathcal{F}^{-1}\left\{\frac{\mathcal{F}(I_{D,\theta}(\boldsymbol{x})/I_{0,\theta}(\boldsymbol{x}))}{1 + \lambda D\pi\frac{\delta_n}{\beta}||\boldsymbol{f}||^2}\right\}\right) \tag{0.0.5}$$

où $\boldsymbol{f} = (f_x, f_y)$ désigne les coordonnées fréquentielles, et $\mathcal{F}$ la transformée de Fourier.

Le modèle CTF (Fonction de Transfert du contraste) est valide si la phase varie lentement et si l'objet est peu atténuant (Cloetens et al., 1999). Il s'exprime comme suit :

$$\tilde{I}_{D,\theta}(\boldsymbol{f}) = \delta_{Dirac}(\boldsymbol{f}) - 2\cos(\pi\lambda D|\boldsymbol{f}|^2)\,\tilde{B}_{\theta}(\boldsymbol{f}) + 2\sin(\pi\lambda D|\boldsymbol{f}|^2)\tilde{\varphi}_{\theta}(\boldsymbol{f}) \tag{0.0.6}$$

où ~ désigne la transformée de Fourier et δ_{Dirac} la distribution de Dirac.

Le modèle mixte, développé plus tard par Guigay *et al.* (Guigay, Langer, Boistel, & Cloetens, 2007), est en fait une combinaison des deux modèles précédents, et est valable pour une phase variant lentement (quel que soit l'atténuation de l'objet). Il s'exprime par :

$$\begin{aligned}\tilde{I}_{D,\theta}(\boldsymbol{f}) \approx \tilde{I}_{D,\theta}^{\varphi=0}(\boldsymbol{f}) &+ 2\sin(\pi\lambda D|\boldsymbol{f}|^2)\,.\,\mathcal{F}\{I_{0,\theta}\varphi_{\theta}\}(\boldsymbol{f}) \\ &+ \cos(\pi\lambda D|\boldsymbol{f}|^2)\frac{\lambda D}{2\pi}\mathcal{F}\{\nabla_{\boldsymbol{x}}\cdot(\varphi_{\theta}\nabla_{\boldsymbol{x}}I_{0,\theta})\}(\boldsymbol{f})\end{aligned} \tag{0.0.7}$$

où $\tilde{I}_{D,\theta}^{\varphi=0}$ est la transformée de Fourier de l'intensité acquise à la distance D, quand l'objet est à la position angulaire θ, en supposant que le décalage de phase soit nul.

Parmi les différents algorithmes d'estimation de phase, ceux que nous avons utilisés en holotomographie avec faisceau parallèle reposent sur l'approche mixte.

En notant ψ_{θ}, A_D et $\Delta_{D,\theta}$ les quantités suivantes:

$$\psi_{\theta}(\boldsymbol{x}) = I_{0,\theta}(\boldsymbol{x}).\varphi_{\theta}(\boldsymbol{x}) \tag{0.0.8}$$

$$A_D(\boldsymbol{f}) = 2\sin(\pi\lambda D|\boldsymbol{f}|^2) \tag{0.0.9}$$

$$\Delta_{D,\theta}(\boldsymbol{f}) = \cos(\pi\lambda D|\boldsymbol{f}|^2)\frac{\lambda D}{2\pi}\mathcal{F}\{\nabla_{\boldsymbol{x}}\cdot[\psi_{\theta}(\boldsymbol{x}).\nabla_{\boldsymbol{x}}\ln(I_{0,\theta}(\boldsymbol{x}))]\}(\boldsymbol{f}), \tag{0.0.10}$$

le modèle mixte se réécrit sous la forme:

$$\tilde{I}_{D,\theta}(\boldsymbol{f}) = \tilde{I}_{D,\theta}^{\varphi=0}(\boldsymbol{f}) + A_D(\boldsymbol{f})\tilde{\psi}_\theta(\boldsymbol{f}) + \Delta_{D,\theta}(\boldsymbol{f}) \tag{0.0.11}$$

La quantité $\tilde{\psi}_\theta(\boldsymbol{x})$, liée à la phase, peut être exprimée comme le minimum d'une fonctionnelle (méthode des moindres carrés), où un terme de régularisation est habituellement ajouté:

$$\begin{aligned}&\tilde{\psi}_\theta(\boldsymbol{f})\\&= \arg\min_{\tilde{\psi}_\theta} \sum_D \left|A_D(\boldsymbol{f})\tilde{\psi}_\theta(\boldsymbol{f}) - [\tilde{I}_{D,\theta}(\boldsymbol{f}) - \tilde{I}_{D,\theta}^{\varphi=0}(\boldsymbol{f}) - \Delta_{D,\theta}(\boldsymbol{f})]\right|^2 + \alpha\left|\tilde{\psi}_\theta(\boldsymbol{f})\right.\\&\left. - \tilde{\psi}_{0,\theta}(\boldsymbol{f})\right|^2\end{aligned} \tag{0.0.12}$$

Elle est estimée itérativement (typiquement en 3 à 5 itérations), en prenant en compte l'a priori $\tilde{\psi}_{0,\theta}$:

$$\begin{aligned}&{\psi_\theta}^{(i+1)}(\boldsymbol{x})\\&= \mathcal{F}^{-1}\left\{\frac{\sum_D A_D(\boldsymbol{f}).\left[\tilde{I}_{D,\theta}(\boldsymbol{f}) - \tilde{I}_{D,\theta}^{\varphi=0}(\boldsymbol{f}) - {\Delta_{D,\theta}}^{(i)}(\boldsymbol{f}) + \alpha\tilde{\psi}_{0,\theta}(\boldsymbol{f})\right]}{\sum_D A_D(\boldsymbol{f})^2 + \alpha}\right\}(\boldsymbol{x})\end{aligned} \tag{0.0.13}$$

Plusieurs méthodes ont été mises en place pour créer l'a priori $\psi_{0,\theta}$.

Tout d'abord si l'on suppose un objet homogène, les projections d'atténuation sont simplement converties en projections de phase via la relation :

$$\tilde{\psi}_{0,\theta}(\boldsymbol{f}) = \ell(\boldsymbol{f}).\mathcal{F}\left\{\frac{\delta_n}{2\beta} I_{0,\theta} \ln\left(I_{0,\theta}\right)\right\}(\boldsymbol{f}) \tag{0.0.14}$$

où ℓ désigne un filtre passe-bas. Tout comme pour la méthode de Paganin, celle-ci suppose de connaître le matériau, afin d'avoir accès à ses coefficients δ_n et β.

Enfin on peut considérer l'objet comme hétérogène, mais composé d'un nombre fini de matériaux homogènes. Dans ce cas, il convient de reconstruire le volume d'atténuation, le seuiller, et convertir chaque partie en phase en leur appliquant un coefficient δ_n/β spécifique. On obtient ainsi un volume en phase, que l'on projette (transformée de Radon) pour avoir les projections en phase. Mathématiquement, dans le cas où l'on considère deux matériaux « a » et « b », on peut exprimer le volume a priori ainsi :

$$\delta_{n,0}(\boldsymbol{x}, z) = m(\boldsymbol{x}, z).\beta(\boldsymbol{x}, z) \tag{0.0.15}$$

avec :

$$m(\boldsymbol{x}, z) = \begin{cases}\delta_a/\beta_a\,, & \beta(\boldsymbol{x}, z) < t\\ \delta_b/\beta_b\,, & \beta(\boldsymbol{x}, z) \geq t\end{cases} \tag{0.0.16}$$

où t désigne le seuil, habituellement celui détermine par la méthode d'Otsu (Otsu, 1979).

Si on considère que l'objet est constitué d'une multitude de matériaux, ce qui est souvent le cas dans les objets hétérogènes, on peut appliquer, au lieu d'un seuillage, une fonction qui lie μ à δ_n/β (Langer, Cloetens, Pacureanu, & Peyrin, 2012).

Une fois la phase de chaque projection estimée via la méthode choisie, nous obtenons des projections de phase, qui peuvent être utilisées dans un algorithme de reconstruction tomographique (comme la rétroprojection filtrée (FBP), par exemple). Par la suite, d'autres méthodes telles que les méthodes algébriques ou itératives ont été utilisées pour la reconstruction tomographique. Nous détaillons ici les plus connues : ART (Gordon, Bender, & Herman, 1970), SIRT (Dines & Lytle, 1979), SART (Andersen & Kak, 1984), EST (Miao, Förster, & Levi, 2005). Plus récemment, ce type de méthodes a été combiné avec l'estimation de phase, dans une seule et même étape. Nous parlons alors d'*algorithmes combinés*, puisqu'ils combinent estimation de phase et reconstruction tomographique, habituellement réalisées en deux étapes indépendantes. Ces méthodes combinées font également appel à la régularisation, souvent nécessaires pour résoudre un problème mal posé. Nous introduisons les méthodes de régularisation les plus connues à la fin de ce chapitre.

La première étude (Chapitre III) porte sur l'étude de différents algorithmes d'estimation de phase pour une application à des données biologiques en ingénierie tissulaire osseuse. Ces données ont été acquises en micro-tomographie par contraste de phase, à plusieurs distances de propagation, sur la ligne ID19 de l'ESRF. Il s'agit ici de biomatériaux ensemencés avec différentes cellules osseuses (des ostéoblastes, qui induisent la formation de l'os et des pré-ostéoclastes, responsables de la résorption de l'os). Ce type d'échantillons, particulièrement étudié en médecine régénérative, permet d'observer l'influence des cellules sur la croissance de l'os. Nous utilisons ici l'imagerie par contraste de phase, qui nous donne accès à un volume quantitatif de tissus minéralisés, nouvellement minéralisés et mous, contraste que nous n'aurions pu obtenir en imagerie d'atténuation classique. Une précédente étude (Langer, Cloetens, Guigay, & Peyrin, 2008) faisant l'hypothèse d'objets homogènes, n'avait pas permis la visualisation des cellules ensemencées. Nous montrons ici que l'emploi de régularisation plus avancée (hypothèse d'objets hétérogènes) nous permet d'améliorer la qualité d'image et la quantification de nos échantillons. Nous sommes ainsi capable de différencier trois types de matériaux, et calculer leur densité: les cellules osseuses, les tissus mous, le tissu osseux synthétique.

Nous disposons de trois échantillons par type de cellules ensemencées : ostéoblastes (OBs), ostéoclastes (OCs) et combinaison des deux (OBs + OCs). Ces échantillons ont été imagés sur la ligne ID19, en micro-tomographie par contraste de phase, à plusieurs distances de propagation (holotomographie). L'énergie du faisceau était de 30keV. Une acquisition se constituait de 2000 projections, avec un temps d'exposition de 0.4 s par projection, à quatre distances de propagation (0,01 ; 0,33 ; 0,45 et 0,99 m). La taille effective de pixel était de 5 µm, donnant un champ de vue d'environ 10mm par 7mm.

Les indices de réfraction en 3D de ces échantillons ont été reconstruits via un algorithme d'estimation de phase suivi d'une reconstruction tomographique (FBP). Pour l'estimation de la phase, nous avons comparé quatre méthodes différentes, présentées précédemment: la méthode de Paganin (objet homogène), qui est une méthode *directe* d'estimation de la phase, contrairement aux méthodes *régularisées*, telles que la méthode mixte homogène, la méthode mixte hétérogène avec seuillage (objet bi-matériaux), la méthode mixte hétérogène avec fonction (objet multi-matériaux).

La Figure 6 montre un exemple d'une coupe reconstruite avec la méthode mixte homogène, pour un échantillon ensemencé d'ostéoblastes. On y voit le capillaire en verre entourant l'échantillon, le biomatériau, les tissus mous et les cellules présents dans ses pores. Nous avons choisi une région d'intérêt dans cette coupe, pour comparer les 4 méthodes d'estimation de phase. Ces résultats sont présentés à la Figure 7. Qualitativement, on remarque des franges de contraste de phase autour des pores pour certaines méthodes (sous-images A et C). La méthode de Paganin (sous-image P) nous

donne une reconstruction plus floue que celle des méthodes régularisées. Visuellement, la sous-image B (méthode mixte hétérogène avec seuillage) semble présenter une image nette, dépourvue de franges de contraste indésirables.

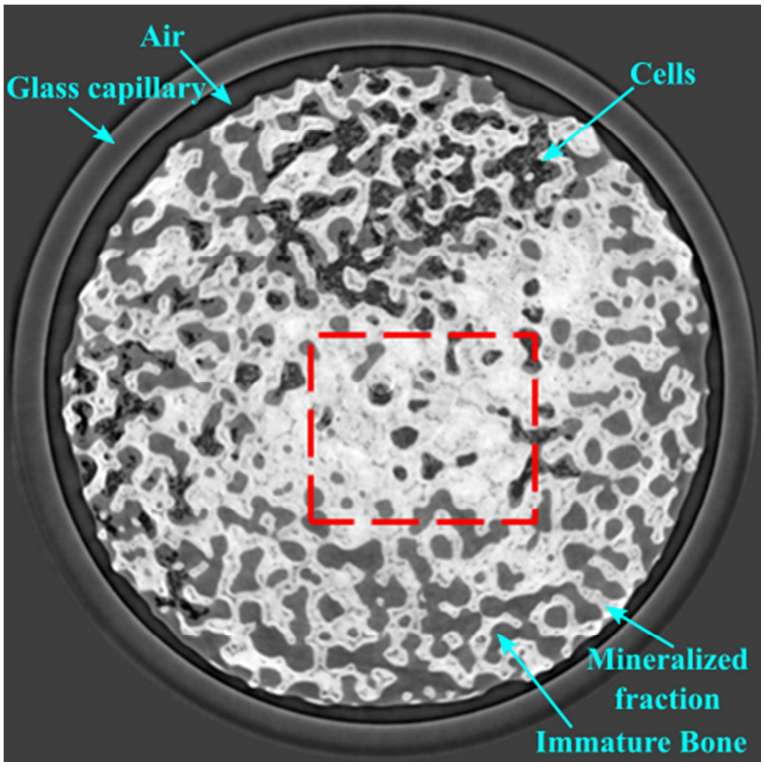

Figure 6: Coupe tomographique d'un biomatériau ensemencé avec des ostéoblastes, reconstruite avec la méthode mixte homogène. La sélection en pointillés rouges correspond à la zone présentée en Figure 7.

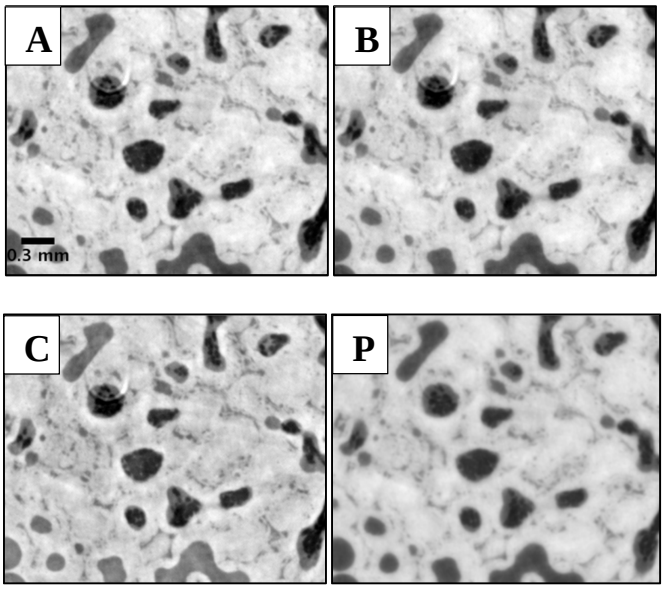

Figure 7: Sélection d'une coupe reconstruite avec [A] l'approche homogène mixte, [B] l'approche hétérogène mixte mettant en œuvre un seuillage, [C] l'approche hétérogène mixte mettant en œuvre une fonction et [P] la méthode de Paganin. La barre d'échelle correspond à 0,3mm. La zone présentée mesure 2,90mm par 2,42mm.

En holotomographie, nous reconstruisons des images dont les niveaux de gris correspondent à la quantité $-\frac{2\pi}{\lambda}\boldsymbol{\delta_n}$. La fenêtre de visualisation est tout d'abord ajustée, de manière à ce que le niveau de gris correspondant à l'air se trouve à zéro. Ensuite, les images obtenues sont converties en masse volumique en appliquant la formule de (Guinier, 1994):

$$\delta_n \approx 1.35 \times 10^{-6} \rho \times \lambda^2 \qquad (0.0.17)$$

où la masse volumique ρ est exprimée en g/cm^3, et la longueur d'onde λ en Å.

La Figure 8 présente les histogrammes, en masse volumique, des reconstructions (via les 4 méthodes citées) de la coupe présentée ci-dessus. Dans cette coupe, on distingue à l'œil quatre matériaux principaux : le biomatériau, les tissus mous, les cellules osseuses et l'air. Or, les méthodes Paganin et mixte homogène ne permettent de distinguer que 3 classes dans l'histogramme, alors que les méthodes régularisées avec un a priori hétérogène en distinguent quatre, comme attendu. D'autre part, la masse volumique théorique des tissus mous avoisine les 1,06 g/cm^3 [ICRU-44] contre 1,80 g/cm^3 pour le biomatériau étudié. La méthode B se révèle ainsi plus quantitative, car plus proche des valeurs théoriques.

En conclusion, les études qualitative et quantitative ont montré que cette méthode mixte hétérogène avec seuillage apparaît comme le meilleur compromis parmi les méthodes étudiées, pour ces échantillons.

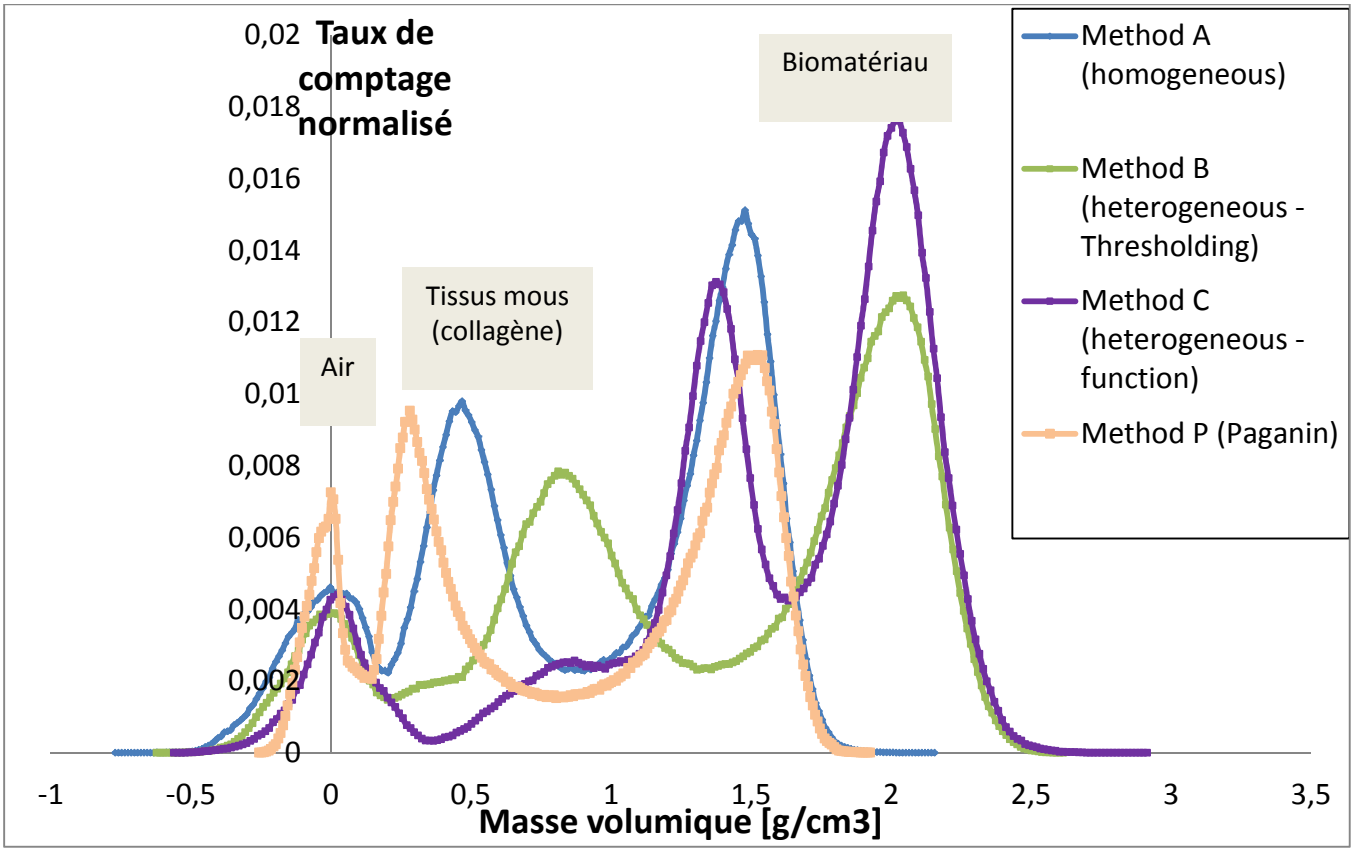

Figure 8: Histogrammes de masse volumique, pour la même coupe reconstruite, par le biais des quatre méthodes décrites (homogène, hétérogène avec seuil, hétérogène avec fonction, Paganin). Les

histogrammes de niveaux de gris ont été convertis en masse volumique et réajustés de manière à ce que l'air soit à zéro. La coupe étudiée correspond à un sous-volume de 0,33 mm^3.

Une étude statistique a été réalisée pour déterminer l'influence des différentes cellules osseuses sur la formation, ou la résorption, de tissus osseux. Ce travail a été publié dans le journal *Physics in Medicine and Biology*, sous le titre : "Quantitative evaluation of regularized phase retrieval algorithms on bone scaffolds seeded with bone cells" (Weber, Langer, Tavella, Ruggiu, & Peyrin, 2016).

D'autre part, nous présentons dans ce chapitre la première contribution technique de cette thèse, à savoir l'automatisation complète du procédé de reconstruction de phase, incluant l'étape d'estimation de phase et celle de reconstruction tomographique. Ce travail a ainsi permis la reconstruction, de manière quasi automatique, de plusieurs dizaines de jeux de données relatives à des échantillons de dents, et acquises en micro-CT de phase par propagation. Ce travail sera valorisé prochainement dans une publication, les résultats des reconstructions étant en cours d'analyse.

La deuxième étude de la thèse (Chapitre IV) porte sur l'étude de la nano-tomographie par contraste de phase, pour l'imagerie haute résolution de l'os, permettant alors la visualisation de son réseau cellulaire. Le système d'acquisition de la nano-CT de phase est présenté à la Figure 9; il est similaire à celui de la micro-CT, à la différence près que le faisceau utilisé est divergent, et non plus parallèle. Des projections sont acquises à différentes distances de propagation, qui impliquent différents facteurs de grossissement.

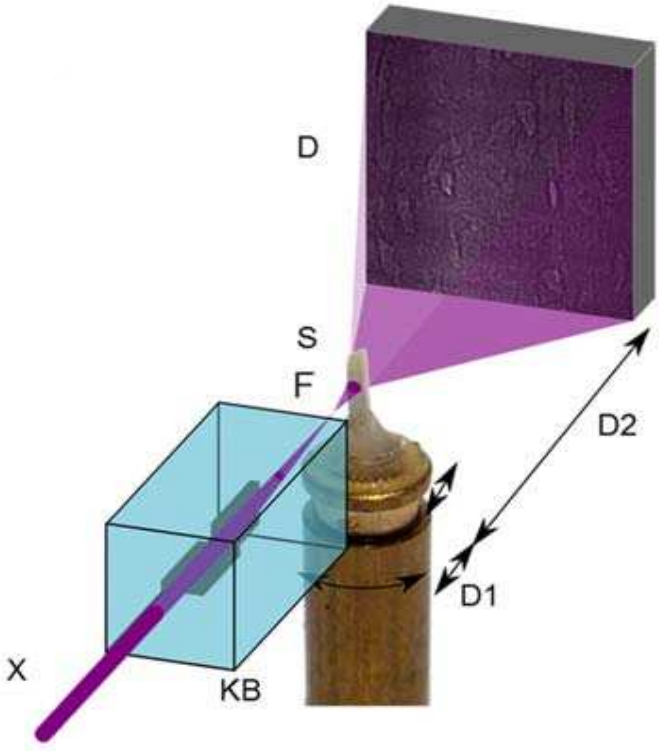

Figure 9: Schéma de l'instrument pour la nano-CT de phase. Le faisceau de rayons X incident (X) est focalisé en un point focal (F), au moyen d'éléments optiques appropriés. $\mathbf{D_1}$ est la distance entre le point focal et l'échantillon (S), et $\mathbf{D_2}$ est la distance de propagation.

Concernant la reconstruction, on utilise classiquement la méthode de Paganin présentée précédemment, adaptée à l'acquisition multi-distance via la méthode des moindres carrés. Par soucis de lisibilité, nous introduisons les deux variables suivantes:

$$\tilde{I}_{norm,k}(\boldsymbol{f}) = \mathcal{F}\left(\frac{I_{D_k}}{I_0}\right)(\boldsymbol{f}) \tag{0.0.18}$$

et

$$\tilde{h}_k(\boldsymbol{f}) = 1 + \frac{D_k \delta_n \lambda\, \pi}{\beta} ||\boldsymbol{f}||^2 \tag{0.0.19}$$

Comme il s'agit d'une acquisition multi-distance, les distances de propagation sont indexées par k, un entier compris entre 1 et K. La formule des moindre carrés, combinée à la formule de Paganin, nous donne l'estimation de la phase, notée $\hat{\varphi}(\boldsymbol{x})$, suivante:

$$\hat{\varphi}(\boldsymbol{x}) = \frac{1}{2}.\frac{\delta_n}{\beta}.\ln(\mathcal{F}^{-1}\left\{\frac{\frac{1}{K}\sum_{k=1}^{K}\tilde{h}_k(\boldsymbol{f}).\tilde{I}_{norm,k}(\boldsymbol{f})}{\left(\frac{1}{K}.\sum_{k=1}^{K}\tilde{h}_k(\boldsymbol{f})^2\right)+\alpha}\right\} \tag{0.0.20}$$

où α est un paramètre de régularisation, fixé arbitrairement.

Cette formule nous sert, en nano-CT de phase, à déterminer une première estimation de la phase, pour chaque angle de projection; ces estimations sont ensuite améliorées via une méthode non-linéaire (gradients conjugués non-linéaires). En effet, les distances de propagation étant relativement longues par rapport à la taille du pixel, la condition de champ proche n'est plus respectée. Ainsi, une contribution non-linéaire de la phase doit être ajoutée.

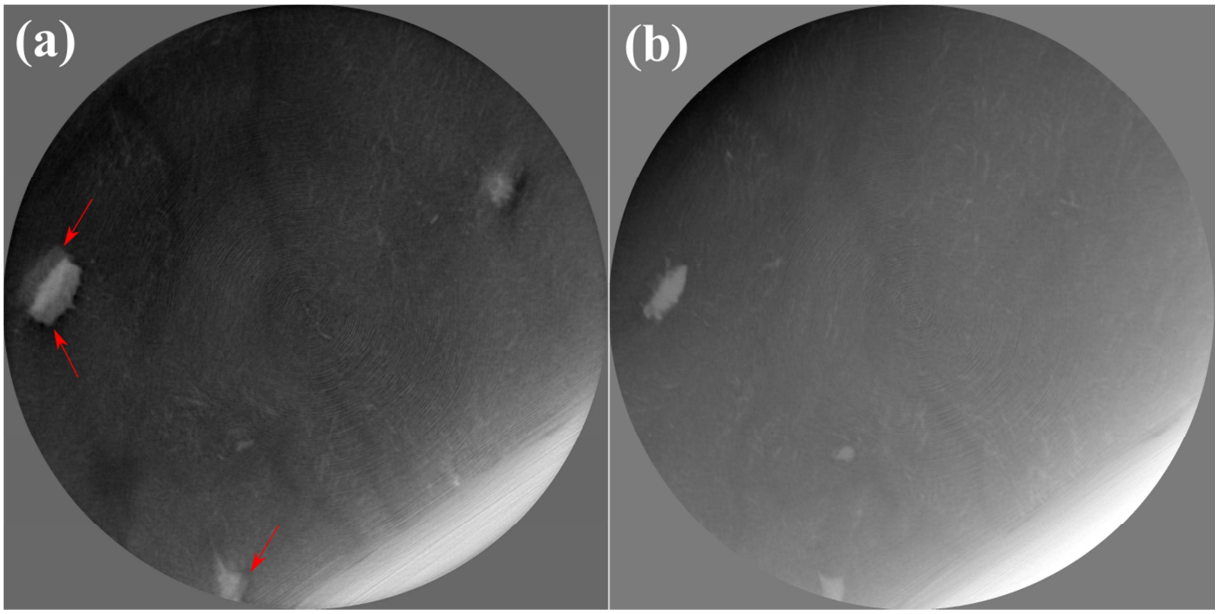

Figure 10: Coupe reconstruite d'un échantillon d'os ostéoporotique, où le recalage des projections à différentes distances a été effectué par (a) une méthode basée sur la corrélation; (b) une méthode basée sur l'information mutuelle. La taille du pixel vaut ici 60nm, et une coupe représente une surface de 122,88µm par 122,88 µm. Les flèches rouges indiquent des artefacts représentatifs d'un mauvais alignement.

Nous présentons également un nouvel outil de recalage des projections, automatique, qui permet d'améliorer efficacement la reconstruction des volumes en nano-tomographie. En effet, pour une acquisition multi-distance, les projections acquises à un même angle doivent être recalées entre elles (et rapportées au même grossissement si besoin). Jusqu'à présent, la méthode de recalage utilisée reposait sur le coefficient de corrélation, qui trouve ses limites en nano-CT, où les images présentent

souvent de nombreuses franges d'interférences (alternance de blanc et de noir). Si les franges sont légèrement décalées, leur contraste sera différent ; un indice reposant sur les niveaux de gris, tel que le coefficient de corrélation, trouve alors ses limites. L'idée ici était d'étudier un indice d'information mutuelle, qui tient plutôt compte de la forme des structures présentes que des niveaux de gris. Comme le montre la Figure 10, cette méthode peut réussir là où la méthode traditionnelle a échoué.

La nano-tomographie de phase s'avère donc être un outil précieux pour étudier la structure fine de l'os, en donnant accès à une imagerie haute-résolution (taille de pixel effective de quelques dizaines de nanomètres) sur un champ de vue de plusieurs dizaines de microns. Différents outils d'analyse (étude du réseau lacuno-canaliculaire, volume et forme des lacunes, gradient de minéralisation autour des lacunes, orientation des fibres de collagènes) ont été appliqués sur les échantillons disponibles : os sain, os souffrant d'ostéoporose et os souffrant d'ostéoarthrite (arthrose). Cette étude visait à démontrer la faisabilité de telles analyses sur l'os, mais aussi d'en discuter leurs limites.

Bien que nos observations soient en accord avec quelques études récentes (Jaiprakash et al., 2012; Prasadam et al., 2013), l'influence d'une pathologie sur la structure de l'os reste controversée.

Van Hove et al. (2009) a observé, grâce à un microscope confocal 3D, des lacunes de forme allongée pour un os ostéoarthritique, contrairement à nous qui les observons plutôt rondes. D'autre part, Mc Creadie *et al.* (2004) a observé une grande diversité dans la forme et la taille des lacunes d'un os ostéoporotique. Il a également été montré que leur forme est influencée par la charge mécanique subie par l'os, et donc, très dépendant de la localisation de l'échantillon. Au travers d'un projet long-terme sur la ligne ID16A de l'ESRF, nous avons l'opportunité d'imager un grand nombre d'échantillons ; cependant, chaque échantillon est très petit par rapport à l'os original dont il est extrait. Il doit de plus être coupé à la main ; il y a donc une variabilité non maîtrisée de la localisation de l'échantillon, ce qui peut limiter les conclusions de nos études.

D'autre part, nous avons remarqué que les reconstructions de nano-CT présentaient un bruit de basses fréquences (fond non-uniforme, voir Figure 11). Ceci peut être un frein à l'analyse, comme par exemple l'analyse des gradients de minéralisation autour des lacunes, qui entrave la quantification de la minéralisation.

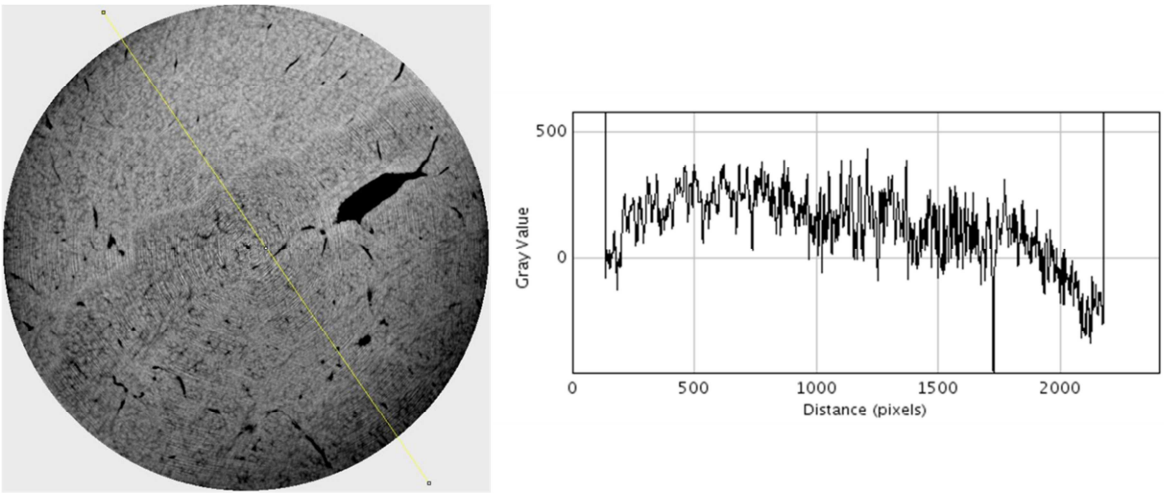

Figure 11: Exemple d'une coupe reconstruite (à gauche), et un profil (à droite). On remarque sur l'image de droite que le profil n'est pas uniforme, ce qui indique la présence de bruit de basse fréquence.

On peut penser que ce type de problème pourrait être compensé par l'emploi d'algorithmes de reconstruction plus avancés, qui font l'objet du chapitre suivant.

Le chapitre V présente le développement d'algorithmes de simulation et de reconstruction de phase. Pour ce qui est de la simulation, un outil de simulation d'images de phase a été implémenté sur la plateforme d'imagerie virtuelle (VIP) de Creatis (Villeurbanne, France). Pour ce qui est de la reconstruction, l'objectif était de développer un algorithme itératif et régularisé, combinant l'estimation de phase et la reconstruction tomographique en une seule étape.

La plateforme VIP a été développée au sein de laboratoire Creatis (Villeurbanne, France). C'est une plateforme d'imagerie versatile, dédiée à la simulation en imagerie médicale. Elle offre actuellement plusieurs modalités (imagerie par résonnance magnétique nucléaire, ultrasons, médecine nucléaire, tomographie par RX, …) (Glatard et al., 2013). L'imagerie par contraste de phase n'était jusqu'alors pas disponible, d'où notre volonté d'en développer un. Cet outil a été porté en libre accès afin d'en faciliter l'utilisation et le développement.

Via une interface graphique, l'utilisateur peut choisir différents paramètres (énergie du faisceau, taille du pixel, distance de propagation), et ainsi simuler les projections qu'il aurait acquises en imagerie par contraste de phase en propagation libre (avec un faisceau parallèle). L'idée est de calculer les transformées de Radon de l'image d'atténuation et l'image du décrément de l'indice de réfraction d'un objet, puis de propager les projections obtenues, selon le modèle de contraste choisi par l'utilisateur. Les simulations ont été faites en 1D (équivalent à un détecteur 1D), puis adaptées en 2D. Pour la 2D, nous proposons une méthode de parallélisation consistant à voir une simulation 2D comme une pile de simulations 1D. Chaque simulation 1D est faite sur un processeur. Le code est distribué via le logiciel Docker, qui permet alors de faire tourner le même programme, avec le même système d'exploitation et les mêmes librairies, bien que les machines puissent être différentes.

Les données simulées sont utilisées pour tester les méthodes de reconstruction de phase développées.

Nous nous sommes intéressés à des algorithmes itératifs combinant estimation de phase et reconstruction tomographique. D'autres algorithmes de ce type ont été proposés par le passé. En 2013, Kostenko *et al*. ont été les premiers à proposer une méthode combinée, alliant la méthode de Paganin à une régularisation (Beck & Teboulle, 2009). Cette méthode nécessite un objet homogène, mais permet de réduire le nombre de projections, et surpasse les méthodes classiques (Kostenko, Batenburg, Suhonen, Offerman, & van Vliet, 2013). Elle a été améliorée par la suite par Kongskov *et al.* (Kongskov, Jørgensen, Poulsen, & Hansen, 2016). Ruhland *et al.* (Ruhlandt, Krenkel, Bartels, & Salditt, 2014) ont proposé un algorithme ne faisant aucune hypothèse restrictive sur l'objet, mais il n'est pas mentionné si cette méthode est robuste à l'enroulement de phase (*phase wrapping*, c'est-à-dire quand la phase excède 2π). En 2016, Anastasio et Chen (Chen et al., 2016) ont développé une méthode combinée qui utilise un opérateur d'estimation de phase non-linéaire, basé sur la dérivée de Fréchet (Davidoiu, Sixou, Langer, & Peyrin, 2011), couplée à une pénalité TV (Variation Totale). Néanmoins, cette méthode n'est pas robuste par rapport au problème de déroulement de phase.

Ici, nous proposons un nouvel algorithme qui utilise d'une part un modèle linéaire du contraste (CTF) pour l'estimation de la phase, et d'autre part l'algorithme itératif SART pour la reconstruction tomographique. Ce type d'algorithme permet l'introduction d'a prioris dans le domaine objet, contrairement aux méthodes mixtes présentées précédemment qui introduisent les a prioris dans le domaine des projections. De plus, nous y ajoutons, à la fin de chaque itération, une contrainte régularisation TV. Nous décrivons le formalisme de la méthode, pour des objets de phase pure (*i.e.*

non atténuants), d'atténuation connue ou inconnue et présentons les premiers résultats sur des données simulées.

Pour aller vers une complexité croissante, nous considérons tout d'abord le cas d'un objet de phase pure, puis d'un objet atténuant d'atténuation connue et enfin le cas plus général d'un objet atténuant d'atténuation inconnue.

- Objet de phase pure (non-atténuant)

En combinant l'expression de la CTF avec l'expression du décalage de phase (Équation (0.0.2)), pour un objet non-atténuant, on obtient dans ce cas :

$$\tilde{I}_{D,\theta}(\boldsymbol{f}) = \delta_{Dirac}(\boldsymbol{f}) + 2\sin(\pi\lambda D|\boldsymbol{f}|^2)\mathcal{F}\left[-\frac{2\pi}{\lambda}\mathcal{R}_\theta\delta_n\right](\boldsymbol{f}) \tag{0.0.21}$$

où $\mathcal{R}_\theta$ est l'opérateur de projection à l'angle θ, et $\mathcal{F}$ est la transformée de Fourier.

Par soucis de clarté, nous notons cette expression comme :

$$\tilde{I}_{D,\theta}(\boldsymbol{f}) = \delta_{Dirac}(\boldsymbol{f}) + A_D(\boldsymbol{f})\mathcal{F}[\mathcal{R}_\theta\delta_n](\boldsymbol{f}) \tag{0.0.22}$$

avec

$$A_D(\boldsymbol{f}) = -\frac{2\pi}{\lambda} \times 2\sin(\pi\lambda D|\boldsymbol{f}|^2) \tag{0.0.23}$$

Dans le domaine réel, cela donne:

$$I_{D,\theta}(\boldsymbol{x}) - 1 = \mathcal{F}^{-1}\{A_D\mathcal{F}[\mathcal{R}_\theta\delta_n]\}(\boldsymbol{x}) \tag{0.0.24}$$

En substituant l'opérateur de contraste à la place de la transformée de Radon, dans l'expression de SART, nous aboutissons à:

$$\begin{aligned}\delta_n{}^{(i)}(\boldsymbol{x}) = \delta_n{}^{(i-1)}(\boldsymbol{x}) + \left[\mathcal{F}^{-1}\{A_D\mathcal{F}\{\mathcal{R}_\theta\}\}\right]^{\mathrm{T}} \\ \times \frac{I_{D,\theta}(\boldsymbol{x}) - 1 - \mathcal{F}^{-1}\left\{A_D\mathcal{F}\left\{\mathcal{R}_\theta\left(\delta_n{}^{(i-1)}\right)\right\}\right\}(\boldsymbol{x})}{\left\|\mathcal{F}^{-1}\{A_D\mathcal{F}\{\mathcal{R}_\theta\}\}\right\|^2}\end{aligned} \tag{0.0.25}$$

Appliquer la transformée de Fourier suivie de son inverse équivaut à l'opérateur identité. De plus, l'opérateur A_D permet de passer de la phase $\tilde{\varphi}_\theta$ à l'intensité $\tilde{I}_{D,\theta}$. L'opérateur ${A_D}^T$peut donc être vu comme l'opérateur d'estimation de phase, permettant de passer de l'intensité $\tilde{I}_{D,\theta}$ à $\tilde{\varphi}_\theta$. Nous le notons A_{-D}, et l'implémentons via la méthode des moindres carrés. Le dénominateur de l'expression est simplifié suite à une étude préliminaire. Nous aboutissons alors à l'expression suivante, pour l'estimation du décrément de l'indice de réfraction:

$$\hat{\delta}_n{}^{(i)}(\boldsymbol{x}) \approx \hat{\delta}_n{}^{(i-1)}(\boldsymbol{x}) + {\mathcal{R}_\theta}^T\left\{\frac{\mathcal{F}^{-1}A_{-D}\mathcal{F}\{I_{D,\theta}(\boldsymbol{x}) - 1\} - \mathcal{R}_\theta\hat{\delta}_n{}^{(i-1)}(\boldsymbol{x})\}}{\|\mathcal{R}_\theta\|^2}\right\} \tag{0.0.26}$$

Cette formulation a été testée sur des données de phase pure simulées (fantôme de Shepp-Logan modifié), présentées à la Figure 12.

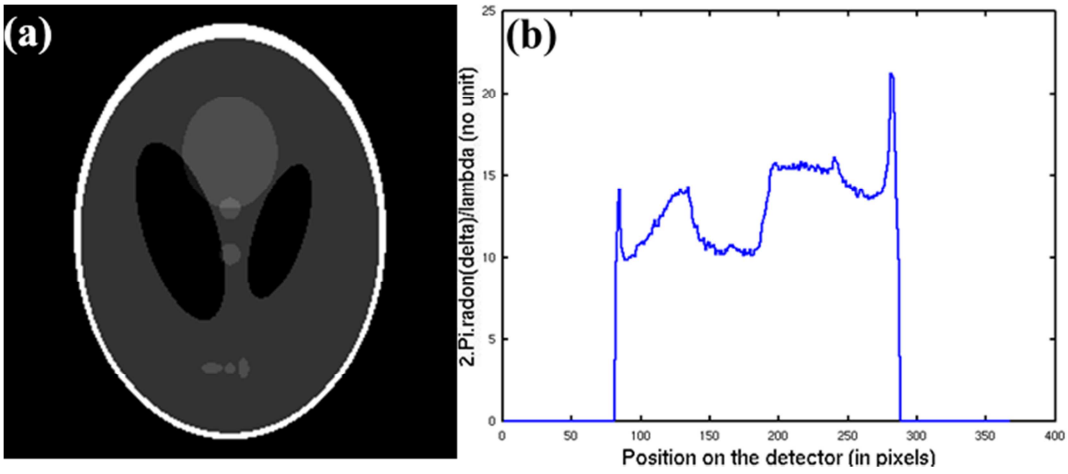

Figure 12: (a) Objet considéré : le fantôme de Shepp-Logan modifié, et (b) une projection de phase. Il est à noter que la phase excède 2π.

Les résultats obtenus, à différentes itérations, sont présentés à la Figure 13.

Ces résultats semblent satisfaisants, à une constante additive près. Si les bords étaient mis à zéro, les valeurs de décrément d'indice de réfraction obtenues seraient très proches des valeurs théoriques attendues. Ceci montre que, dans ce cas, notre algorithme est robuste au bruit et à l'enroulement de phase.

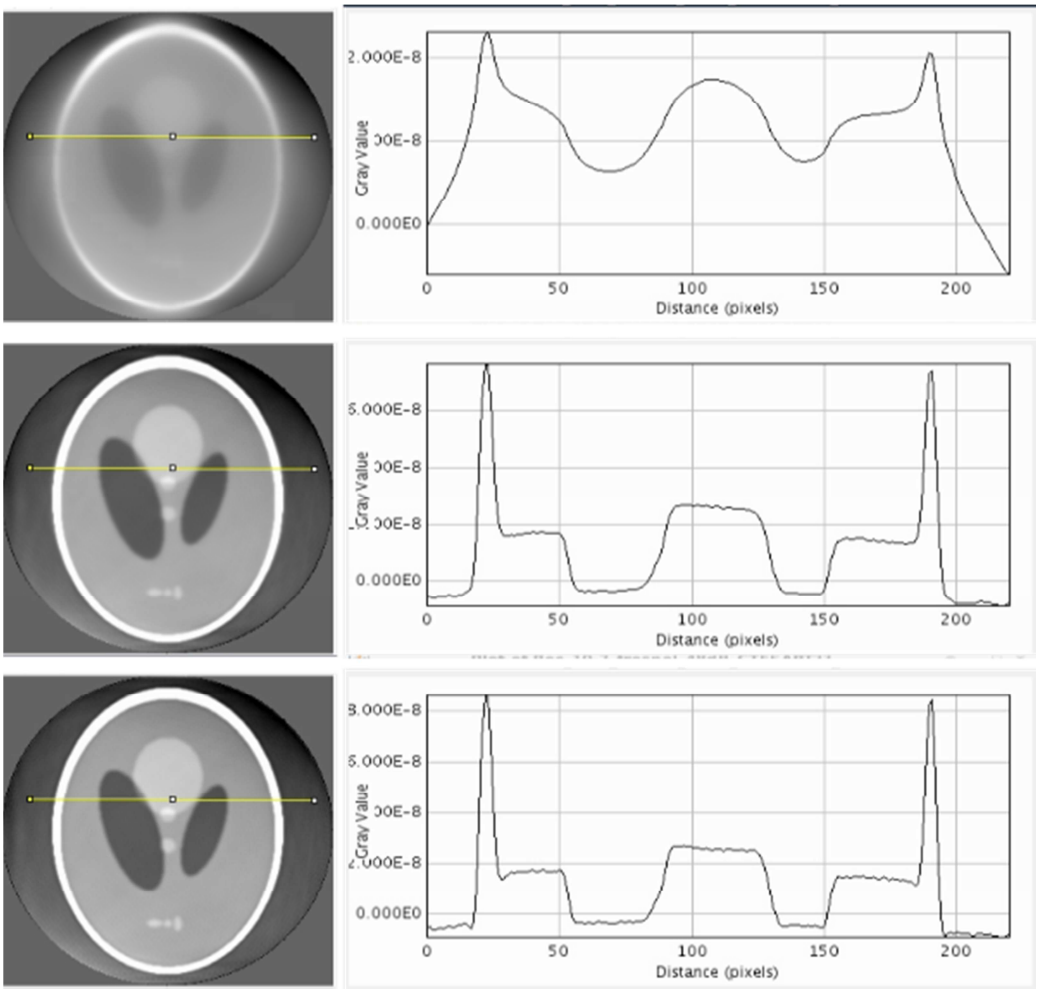

Figure 13: Cartes estimées du décrément de l'indice de réfraction $\boldsymbol{\delta_n}$, à partir de données simulées (modèle de contraste de Fresnel) et bruitées ; la phase est supérieure à 2π. Les cartes résultantes (à gauche), et un profil (à droite) sont présentés à la (a) première, (b) vingtième, (c) quarantième itération de l'algorithme proposé.

- <u>Objet atténuant, d'atténuation connue</u>

Dans ce cas, l'expression de la CTF devient, à un angle θ donné :

$$\tilde{I}_{D,\theta}(\boldsymbol{f}) = k_\theta(\boldsymbol{f}) + A_D(\boldsymbol{f})\mathcal{F}\mathcal{R}_\theta\delta_n(\boldsymbol{f}) \tag{0.0.27}$$

avec

$$A_D(\boldsymbol{f}) = -\frac{4\pi}{\lambda}\sin(\pi\lambda D|\boldsymbol{f}|^2) \tag{0.0.28}$$

et

$$k_\theta(\boldsymbol{f}) = \delta_{Dirac}(\boldsymbol{f}) - 2\cos(\pi\lambda D|\boldsymbol{f}|^2)\,\mathcal{F}\left\{\frac{2\pi}{\lambda}\mathcal{R}_\theta\beta\right\}(\boldsymbol{f}) \tag{0.0.29}$$

De la même manière que précédemment, nous aboutissons à l'expression suivante pour notre algorithme combiné :

$$\hat{\delta}_n{}^{(i)}(\boldsymbol{x}) \approx \hat{\delta}_n{}^{(i-1)}(\boldsymbol{x}) + \mathcal{R}_\theta{}^T \left\{ \frac{\mathcal{F}^{-1}\left\{A_{-D}\{\tilde{I}_{D,\theta} - k_\theta\}\right\}(\boldsymbol{x}) - \left\{\mathcal{R}_\theta \hat{\delta}_n{}^{(i-1)}\right\}(\boldsymbol{x})}{\|\mathcal{R}_\theta\|^2} \right\} \quad (0.0.30)$$

La simulation de données a été faite sur l'objet présenté à la Figure 14, composé de trois fils de matériaux différents (Aluminium, Magnésium, Polyéthylène Téréphtalate).

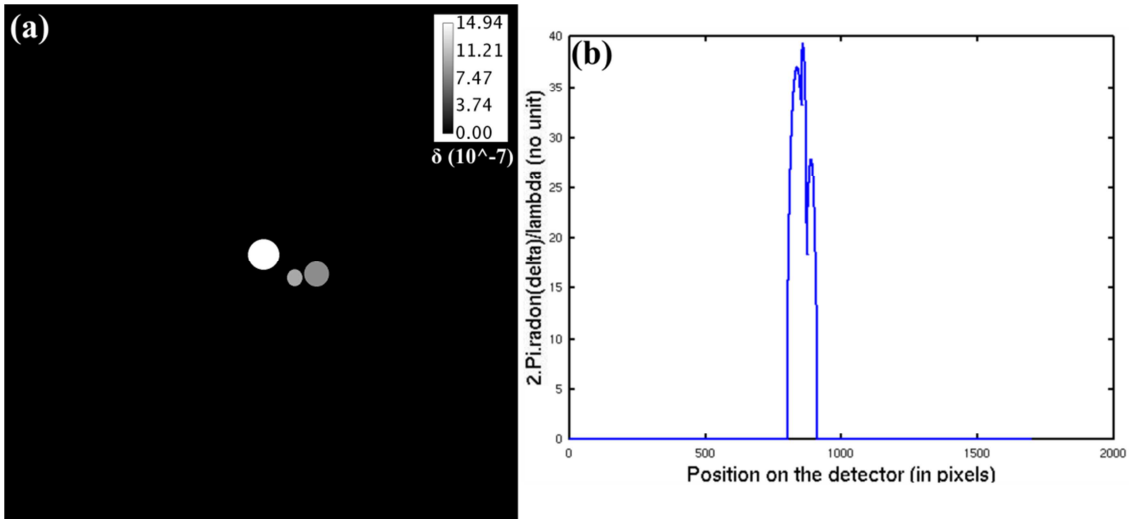

Figure 14: (a) Carte du décrément de l'indice de réfraction $\boldsymbol{\delta_n}$ du fantôme constitué de 3 fils (Al, Mg, PET) utilisé dans l'étude de Frachon *et al.* (Frachon et al., 2015) et (b) une projection de phase.

Supposons d'abord un objet peu atténuant. Pour cela, nous avons réduit l'atténuation de notre fantôme à fils d'un facteur 15. Ainsi, le coefficient d'atténuation linéaire était compris entre 0,08 et 1,07 cm^{-1}, étant ainsi faible, mais non nul.

Les résultats sont présentés à la Figure 15. Les résultats convergent, bien que n'étant pas complétement quantitatifs. Les erreurs normalisées de la reconstruction sont autour de 5% pour un matériau peu atténuant, et autour de 10% pour l'Aluminium, un matériau plus atténuant.

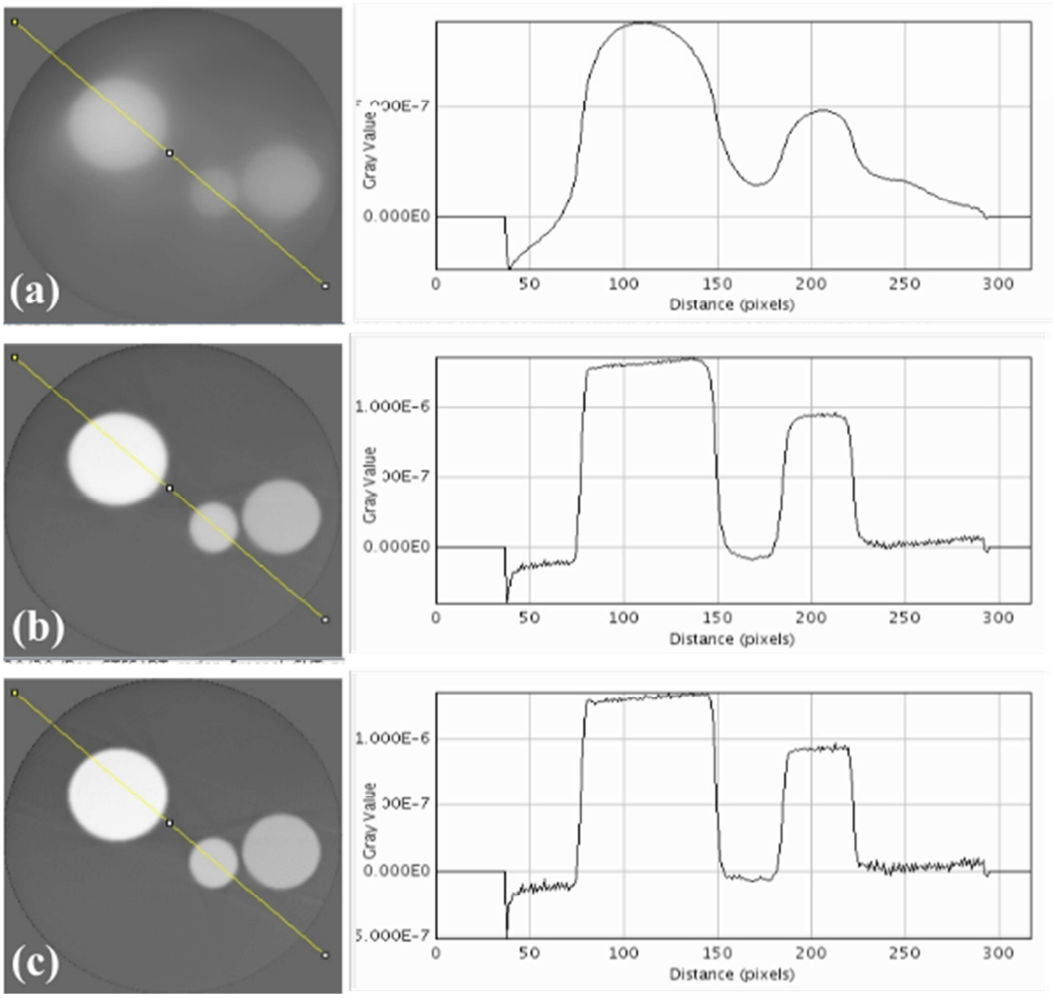

Figure 15: Carte de $\boldsymbol{\delta_n}$ obtenue avec des données simulées (fantôme de 3 fils). Le modèle de Fresnel a été utilisé en tant que modèle de contraste, et aucun bruit n'a été ajouté. L'atténuation a été réduite d'un facteur 15, simulant ainsi un objet peu atténuant. Les cartes résultantes (à gauche), et un profil (à droite) sont présentés à la (a) première, (b) quinzième, (c) trentième itération de l'algorithme proposé.

Pour simuler un objet très atténuant, ce même fantôme a été utilisé, sans aucune réduction d'atténuation. Les résultats correspondant sont présentés à la Figure 16.

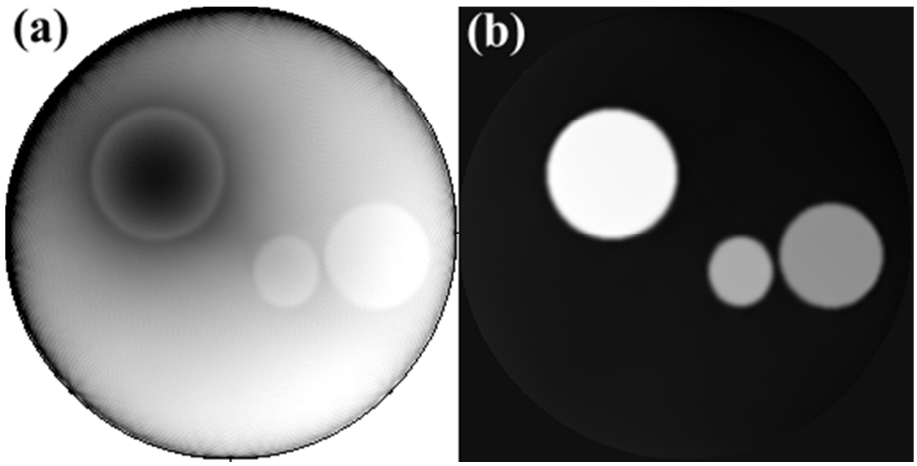

Figure 16: Cartes de $\boldsymbol{\delta_n}$ obtenues pour un objet très atténuant. Les données ont été simulées en utilisant les modèles (a) de Fresnel ou (b) CTF comme modèle de contraste.

On montre donc que les résultats sont satisfaisants si le modèle de contraste utilisé est la CTF, mais le sont beaucoup moins pour un modèle plus réaliste (modèle de Fresnel). On montre ainsi que notre algorithme est plus sensible à l'atténuation qu'à l'enroulement de phase.

- Objet atténuant, d'atténuation inconnue

Enfin, nous pouvons considérer le cas où l'objet imagé est très atténuant, mais son atténuation n'est pas connue. En effet, certaines installations de tomographie de phase, comme la nano-CT de phase, ne rendent pas possible l'acquisition d'une image d'atténuation pure (distance de propagation nulle). Dans ce cas, notre problème a deux inconnues : l'atténuation et la phase.

Dans ce cas, nous itérons tour à tour sur l'atténuation (ou la phase) en supposant l'autre quantité connue, et fixée. Dans le cas où la phase serait connue, on peut réécrire la CTF comme :

$$\tilde{I}_{D,\theta}(\boldsymbol{f}) = l_\theta(\boldsymbol{f}) + C_D(\boldsymbol{f})\mathcal{F}\{\mathcal{R}_\theta\beta\}(\boldsymbol{f}) \tag{0.0.31}$$

avec

$$C_D(\boldsymbol{f}) = -\frac{4\pi}{\lambda}\cos(\pi\lambda D|\boldsymbol{f}|^2) \tag{0.0.32}$$

et

$$l_\theta(\boldsymbol{f}) = \delta_{Dirac}(\boldsymbol{f}) + 2\sin(\pi\lambda D|\boldsymbol{f}|^2)\,\mathcal{F}\left\{-\frac{2\pi}{\lambda}\mathcal{R}_\theta\delta_n\right\}(\boldsymbol{f}) \tag{0.0.33}$$

Ceci nous mène à:

$$I_{D,\theta}(\boldsymbol{x}) - \mathcal{F}^{-1}\{l_\theta\}(\boldsymbol{x}) = \mathcal{F}^{-1}\left\{C_D\mathcal{F}\{\mathcal{R}_\theta\beta\}\right\}(\boldsymbol{x}) \tag{0.0.34}$$

De la même manière que précédemment, on obtient l'expression de l'atténuation :

$$\hat{\beta}^{(i)}(\boldsymbol{x}) \approx \hat{\beta}^{(i-1)}(\boldsymbol{x}) + {\mathcal{R}_\theta}^T\frac{\mathcal{F}^{-1}\left\{A_{-D}\left\{\tilde{I}_{D,\theta} - l_\theta\right\}\right\}(\boldsymbol{x}) - \left\{\mathcal{R}_\theta\hat{\beta}^{(i-1)}\right\}(\boldsymbol{x})}{\|\mathcal{R}_\theta\|^2} \tag{0.0.35}$$

Les tests effectués n'ont pas donné de résultats satisfaisants.

Ce travail ouvre le champ à de multiples perspectives d'amélioration et de recherche : emploi d'autres types de régularisation, ou d'autres modèles de contraste moins restrictifs que la CTF, comme le modèle mixte, par exemple. Les applications et le potentiel de ce type d'algorithme sont divers : reconstruction de données acquises avec peu de projections (qui limiterait ainsi le temps d'acquisition et la dose délivrée), reconstruction de données volumineuses, etc. La possibilité d'une reconstruction quantitative d'objet hétérogènes s'avère également particulièrement intéressante pour l'imagerie de l'articulation du genou par exemple, sans ajout d'agent de contraste, car une telle région comprend des tissus mous, de l'os, du cartilage et des vaisseaux.

Références

Andersen, A. H., & Kak, A. C. (1984). Simultaneous algebraic reconstruction technique (SART): a superior implementation of the art algorithm. *Ultrasonic Imaging*, *6*(1), 81–94.

Beck, A., & Teboulle, M. (2009). A Fast Iterative Shrinkage-Thresholding Algorithm for Linear Inverse Problems. *SIAM Journal on Imaging Sciences*, *2*(1), 183–202. doi:10.1137/080716542

Bonse, U., & Hart, M. (1965). An X-ray interferometer. *Applied Physics Letters*, *6*(8), 155. doi:10.1063/1.1754212

Chapman, D., Thomlinson, W., Johnston, R. E., Washburn, D., Pisano, E., Gmür, N., … Sayers, D. (1997). Diffraction enhanced x-ray imaging. *Physics in Medicine and Biology*, *42*(11), 2015–2025. doi:10.1088/0031-9155/42/11/001

Chen, Y., Wang, K., Gursoy, D., Hoyuelos, C. S., De Carlo, F., & Anastasio, M. A. (2016). Joint reconstruction of absorption and refractive properties in propagation-based x-ray phase-contrast tomography via a non-linear image reconstruction algorithm. In D. Kontos, T. G. Flohr, & J. Y. Lo (Eds.), *SPIE Medical Imaging* (p. 97835H). International Society for Optics and Photonics. doi:10.1117/12.2217443

Cloetens, P., Ludwig, W., Baruchel, J., Van Dyck, D., Van Landuyt, J., Guigay, J. P., & Schlenker, M. (1999). Holotomography: Quantitative phase tomography with micrometer resolution using hard synchrotron radiation x rays. *Applied Physics Letters*, *75*(19), 2912. doi:10.1063/1.125225

Davidoiu, V., Sixou, B., Langer, M., & Peyrin, F. (2011). NON-LINEAR ITERATIVE PHASE RETRIEVAL BASED ON FRECHET DERIVATIVE AND PROJECTION OPERATORS. In *Optics EXPRESS* (Vol. 19, pp. 106–109). Barcelona, Spain. doi:10.1364/OE.19.022809

Dilmanian, F. A., Button, T. M., Le Duc, G., Zhong, N., Pena, L. A., Smith, J. A. L., … Rosen, E. M. (2002). Response of rat intracranial 9L gliosarcoma to microbeam radiation therapy. *Neuro-Oncology*, *4*(1), 26–38. doi:10.1093/neuonc/4.1.26

Dines, K. A., & Lytle, R. J. (1979). Computerized geophysical tomography. *Proceedings of the IEEE*, *67*(7), 1065–1073. doi:10.1109/PROC.1979.11390

Fiedler, S., Bravin, A., Keyriläinen, J., Fernandez, M., Suortti, P., Thomlinson, W., … Karjalainen-Lindsberg, M.-L. (2004). Imaging lobular breast carcinoma: comparison of synchrotron radiation DEI-CT technique with clinical CT, mammography and histology. *Physics in Medicine & Biology*.

Frachon, T., Weber, L., Hesse, B., Rit, S., Dong, P., Olivier, C., … Langer, M. (2015). Dose fractionation in synchrotron radiation x-ray phase micro-tomography. *Physics in Medicine and Biology*, *60*(19), 7543–7566. doi:10.1088/0031-9155/60/19/7543

Glatard, T., Lartizien, C., Gibaud, B., da Silva, R. F., Forestier, G., Cervenansky, F., … Friboulet, D. (2013). A virtual imaging platform for multi-modality medical image simulation. *IEEE Transactions on Medical Imaging*, *32*(1), 110–8. doi:10.1109/TMI.2012.2220154

Gordon, R., Bender, R., & Herman, G. T. (1970). Algebraic Reconstruction Techniques (ART) for three-dimensional electron microscopy and X-ray photography. *J. theor. Biol.*

Guigay, J. P., Langer, M., Boistel, R., & Cloetens, P. (2007). Mixed transfer function and transport of intensity approach for phase retrieval in the Fresnel region. *Optics Letters*, *32*(12), 1617. doi:10.1364/OL.32.001617

Guinier, A. (1994). *X-ray Diffraction in Crystals, Imperfect Crystals, and Amorphous Bodies*. *Acta crystallographica. Section A, Foundations of crystallography* (Vol. 57). New York, NY. doi:10.1021/ja01079a041

Horng, A., Brun, E., Mittone, A., Gasilov, S., Weber, L., Geith, T., … Coan, P. (2014). Cartilage and Soft Tissue Imaging Using X-rays: Propagation-Based Phase-Contrast Computed Tomography of the Human Knee in Comparison With Clinical Imaging Techniques and Histology. *Investigative Radiology*, *49*(9), 627–34. doi:10.1097/RLI.0000000000000063

Izadifar, Z., Chapman, D. L., & Chen, X. (2014). Computed Tomography Diffraction-Enhanced Imaging for In Situ Visualization of Tissue Scaffolds Implanted in Cartilage. *Tissue Engineering Part C: Methods*.

Jaiprakash, A., Prasadam, I., Feng, J. Q., Liu, Y., Crawford, R., & Xiao, Y. (2012). Phenotypic characterization of osteoarthritic osteocytes from the sclerotic zones: a possible pathological role in subchondral bone sclerosis. *International Journal of Biological Sciences*, *8*(3), 406–17. doi:10.7150/ijbs.4221

Keyriläinen, J., Fernández, M., Fiedler, S., Bravin, A., Karjalainen-Lindsberg, M.-L., Virkkunen, P., … Thomlinson, W. (2005). Visualisation of calcifications and thin collagen strands in human breast tumour specimens by the diffraction-enhanced imaging technique: a comparison with conventional mammography and histology. *European Journal of Radiology*, *53*(2), 226–37. doi:10.1016/j.ejrad.2004.03.015

Keyriläinen, J., Fernández, M., Karjalainen-Lindsberg, M.-L., Virkkunen, P., Leidenius, M., von Smitten, K., … Bravin, A. (2008). Toward high-contrast breast CT at low radiation dose. *Radiology*, *249*(1), 321–7. doi:10.1148/radiol.2491072129

Komlev, V. S., Mastrogiacomo, M., Pereira, R. C., Peyrin, F., Rustichelli, F., & Cancedda, R. (2010). Biodegradation of porous calcium phosphate scaffolds in an ectopic bone formation model studied by X-ray computed microtomograph. *European Cells & Materials*, *19*, 136–46.

Kongskov, R. D., Jørgensen, J. S., Poulsen, H. F., & Hansen, P. C. (2016). Noise robustness of a combined phase retrieval and reconstruction method for phase-contrast tomography. *Journal of the Optical Society of America A*, *33*(4), 447. doi:10.1364/JOSAA.33.000447

Kostenko, A., Batenburg, K. J., Suhonen, H., Offerman, S. E., & van Vliet, L. J. (2013). Phase retrieval in in-line x-ray phase contrast imaging based on total variation minimization. *Optics Express*, *21*(1), 710–23. doi:10.1364/OE.21.000710

Labiche, J.-C., Mathon, O., Pascarelli, S., Newton, M. A., Ferre, G. G., Curfs, C., … Carreiras, D. F. (2007). The Fast REadout LOw Noise camera as a versatile x-ray detector for time resolved dispersive extended x-ray absorption fine structure and diffraction studies of dynamic problems in materials science, chemistry, and catalysis. *The Review of Scientific Instruments*, *78*(9), 091301. doi:10.1063/1.2783112

Langer, M., Cloetens, P., Guigay, J.-P., & Peyrin, F. (2008). Quantitative comparison of direct phase retrieval algorithms in in-line phase tomography. *Medical Physics*, *35*(10), 4556. doi:10.1118/1.2975224

Langer, M., Cloetens, P., Pacureanu, A., & Peyrin, F. (2012). X-ray in-line phase tomography of multimaterial objects. *Optics Letters*, *37*(11), 2151–3. doi:10.1364/OL.37.002151

Maire, E., Buffière, J. Y., Mokso, R., Cloetens, P., & Ludwig, W. (2006). Non Destructive Three Dimensional Imaging of Aluminium Alloys. *Materials Science Forum*, *519-521*, 1367–1372. doi:10.4028/www.scientific.net/MSF.519-521.1367

Majumdar, S., Issever, A. S., Burghardt, A., Lotz, J., Arfelli, F., Rigon, L., … Menk, R.-H. (2004). Diffraction enhanced imaging of articular cartilage and comparison with micro-computed tomography of the underlying bone structure. *European Radiology*, *14*(8), 1440–8. doi:10.1007/s00330-004-2355-8

Miao, J., Förster, F., & Levi, O. (2005). Equally sloped tomography with oversampling reconstruction. *Physical Review B*, *72*(5), 052103. doi:10.1103/PhysRevB.72.052103

Mittone, A., Gasilov, S., Brun, E., Bravin, A., & Coan, P. (2015). A single-image method for x-ray refractive index CT. *Physics in Medicine and Biology*, *60*(9), 3433–40. doi:10.1088/0031-9155/60/9/3433

Mollenhauer, J., Aurich, M. E., Zhong, Z., Muehleman, C., Cole, A. A., Hasnah, M., … Chapman, L. D. (2002). Diffraction-enhanced X-ray imaging of articular cartilage. *Osteoarthritis and Cartilage / OARS, Osteoarthritis Research Society*, *10*(3), 163–71. doi:10.1053/joca.2001.0496

Momose, A. (2003). Phase-sensitive imaging and phase tomography using X-ray interferometers. *Optics Express*, *11*(19), 2303. doi:10.1364/OE.11.002303

Momose, A., Takeda, T., Itai, Y., & Hirano, K. (1996). Phase–contrast X–ray computed tomography for observing biological soft tissues. *Nature Medicine*, *2*(4), 473–475. doi:10.1038/nm0496-473

Otsu, N. (1979). A threshold selection method from gray-level histograms. *IEEE Transactions on Systems, Man and Cybernetics*, *9*(1), 62–66.

Paganin, D., Mayo, S. C., Gureyev, T. E., Miller, P. R., & Wilkins, S. W. (2002). Simultaneous phase and amplitude extraction from a single defocused image of a homogeneous object. *Journal of Microscopy*, *206*(1), 33–40. doi:10.1046/j.1365-2818.2002.01010.x

Pfeiffer, F., Weitkamp, T., Bunk, O., & David, C. (2006). Phase retrieval and differential phase-contrast imaging with low-brilliance X-ray sources. *Nature Physics*, *2*(4), 258–261. doi:10.1038/nphys265

Pouyet, E., Fayard, B., & Salomé, M. (2015). Thin-sections of painting fragments: opportunities for combined synchrotron-based micro-spectroscopic techniques. *Heritage* …. Retrieved from http://www.biomedcentral.com/content/pdf/s40494-014-0030-1.pdf

Prasadam, I., Farnaghi, S., Feng, J. Q., Gu, W., Perry, S., Crawford, R., & Xiao, Y. (2013). Impact of extracellular matrix derived from osteoarthritis subchondral bone osteoblasts on osteocytes: role of integrinβ1 and focal adhesion kinase signaling cues. *Arthritis Research & Therapy*, *15*(5), R150. doi:10.1186/ar4333

Raven, C., Snigirev, A., Snigireva, I., Spanne, P., Souvorov, A., & Kohn, V. (1996). Phase-contrast microtomography with coherent high-energy synchrotron x rays. *Applied Physics Letters*, *69*(13), 1826. doi:10.1063/1.117446

Rivard, C., Lanson, B., & Cotte, M. (2015). Phosphorus speciation and micro-scale spatial distribution in North-American temperate agricultural soils from micro X-ray fluorescence and X-ray absorption near-edge spectroscopy. *Plant and Soil*, *401*(1-2), 7–22. doi:10.1007/s11104-015-2494-5

Ruhlandt, A., Krenkel, M., Bartels, M., & Salditt, T. (2014). Three-dimensional phase retrieval in propagation-based phase-contrast imaging. *Physical Review A*, *89*(3), 033847. doi:10.1103/PhysRevA.89.033847

Teague, M. R. (1982). Irradiance moments: their propagation and use for unique retrieval of phase. *Journal of the Optical Society of America*, *72*(9), 1199. doi:10.1364/JOSA.72.001199

Weber, L., Langer, M., Tavella, S., Ruggiu, A., & Peyrin, F. (2016). Quantitative evaluation of regularized phase retrieval algorithms on bone scaffolds seeded with bone cells. *Physics in Medicine and Biology*, *61*(9), N215–N231. doi:10.1088/0031-9155/61/9/N215

Introduction générale

La technique du contraste de phase par rayonnement synchrotron s'avère particulièrement intéressante pour observer des tissus mous (tissus biologiques), dans la gamme d'énergie utilisée en imagerie (10 à 100keV), car elle offre un contraste environ mille fois plus important que l'imagerie d'atténuation conventionnelle. L'imagerie par contraste de phase peut être couplée à une acquisition tomographique. Une telle technique a été rendue possible par l'essor des synchrotrons, dont le rayonnement produit est très cohérent et intense, et dont la taille du faisceau peut être modifiée au moyen d'optiques adaptées. Couplé à des détecteurs de haute technologie (de taille 2048x2048 pixels, et prochainement 4096x4096 pixels), ce faisceau permet une imagerie tridimensionnelle non-destructive, à une résolution micrométrique (ligne ID19), voire nanométrique (ligne ID16), tout en disposant d'un champ de vue relativement large. Par exemple, nous avons pu acquérir des images d'os avec une taille de pixel effective de 25nm et un champ de vue d'une cinquantaine de microns, dans les trois directions de l'espace.

Une imagerie quantitative nécessite néanmoins l'utilisation d'algorithmes d'estimation de phase sur les images acquises ; la plupart de ces algorithmes sont conçus pour des objets homogènes. D'autres algorithmes ont été imaginés pour l'observation d'objets hétérogènes, mais nécessitent plusieurs acquisitions. L'acquisition multiple de données se fait au détriment de la dose délivrée et du temps de scanographie. Ainsi, l'emploi d'algorithmes itératifs régularisés pourrait permettre l'utilisation de moins de données, réduisant alors la dose délivrée et le temps d'acquisition. Les objectifs de ces travaux étaient donc de développer et d'implémenter de tels algorithmes pour la reconstruction tridimensionnelle de la phase. Jusqu'alors, l'introduction d'information a priori et de régularisation était faite dans le domaine des projections, ce qui n'est pas forcément idéal ; par exemple, l'emploi de régularisation TV, qui favorise une image homogène par morceaux, a plus de sens dans le domaine objet que dans celui des projections. Ainsi, le fait d'itérer entre les domaines des projections et de l'objet favorise la régularisation dans le domaine objet, plutôt que dans celui des projections. D'autre part, cette thèse avait pour but l'implémentation d'un outil de simulation d'image en contraste de phase sur la plateforme d'imagerie virtuelle VIP (Creatis, Villeurbanne), jusqu'alors inexistant.

Dans un premier chapitre, nous rappelons les différentes techniques d'imagerie par contraste de phase ; parmi elles, nous nous intéressons ici à l'imagerie par propagation libre, qui consiste à laisser le faisceau se propager librement après avoir traversé l'échantillon. Le détecteur, placé à une certaine distance de l'échantillon (appelée « distance de propagation »), enregistre les franges d'interférences induites par l'échantillon. On mesure ainsi un signal combinant la déviation de phase et l'atténuation du faisceau induites par l'échantillon. Bien que les projections acquises puissent être directement utilisées dans un algorithme de tomographie classique (type rétroprojection filtrée), l'obtention d'une image quantitative nécessite d'appliquer, au préalable, un algorithme d'estimation de phase (*phase retrieval*). Dans ce cas, on estime les projections de phase, que l'on peut traiter grâce à un algorithme de reconstruction tomographique pour obtenir un volume de phase.

Nous présentons dans le second chapitre les différents algorithmes d'estimation de phase. Puisque l'intensité acquise combine, de manière non-linéaire, l'atténuation et la déviation de phase, cette étape peut être vue comme un problème inverse mal posé. Les algorithmes d'estimation de phase se fondent sur différents modèles de contraste, souvent linéarisés, et reposant eux-mêmes sur différentes hypothèses quant à l'objet imagé. Une fois la phase de chaque projection estimée, il s'agit de reconstruire le volume correspondant grâce à une méthode de reconstruction tomographique. Si la

méthode standard est l'algorithme de rétroprojection filtrée, d'autres méthodes, algébriques ou itératives, ont été utilisées. Nous détaillons ici les plus connues (ART, SIRT, SART, EST). Plus récemment, ce type de méthodes a été combiné avec l'estimation de phase dans une seule et même étape. Nous parlons alors d'*algorithmes combinés*, puisqu'ils combinent l'estimation de phase et la reconstruction tomographique, habituellement réalisées en deux étapes indépendantes. Ces méthodes combinées font également appel à la régularisation, souvent nécessaire pour résoudre un problème mal posé. Nous introduisons les méthodes de régularisation les plus utilisées à la fin de ce chapitre.

Dans ce travail, nous nous intéressons aux développements en micro-tomographie et nano-tomographie par contraste de phase, ainsi qu'au développement d'un algorithme itératif innovant visant à reconstruire une carte de phase en 3 dimensions.

La première partie porte sur l'étude de différents algorithmes d'estimation de phase, appliqués à des données biologiques en ingénierie tissulaire osseuse. Ces données ont été acquises en micro-tomographie par contraste de phase sur la ligne ID19 de l'ESRF (Grenoble). Il s'agit ici d'échantillons de biomatériaux ensemencés avec des cellules osseuses (ostéoblastes et ostéoclastes). Ce genre d'échantillons, particulièrement étudiés en médecine régénérative, permet d'observer l'influence des cellules sur la formation ou la résorption de l'os. Nous utilisons ici l'imagerie par contraste de phase, afin de pouvoir quantifier les tissus minéralisés, nouvellement minéralisés et mous, contraste que nous n'aurions pu obtenir en imagerie d'atténuation classique. Grâce à des algorithmes d'estimation de phase utilisant différents types de régularisation, nous montrons que l'emploi d'un certain type de régularisation nous permet d'améliorer la qualité d'image et la quantification de nos échantillons. Nous sommes ainsi capable de différencier trois types de matériaux, et de calculer leur volume : les cellules osseuses, les tissus mous, le tissu osseux synthétique. Une étude statistique a été réalisée pour déterminer l'influence des différentes cellules osseuses sur la formation et la résorption du tissu osseux. Une telle analyse n'avait pas été possible lors d'une précédente étude, qui mettait en œuvre une méthode d'estimation de phase plus basique. D'autre part, nous présentons dans ce chapitre la première contribution technique de cette thèse, à savoir l'automatisation complète du procédé de reconstruction de phase, incluant l'étape d'estimation de phase et celle de reconstruction tomographique.

La deuxième partie présentée ici porte sur l'étude de la nano-tomographie de phase, pour l'imagerie haute résolution de l'os et son réseau cellulaire. Après avoir décrit le système d'acquisition, nous détaillons les méthodes de reconstruction propres à ce système. Nous présentons un nouvel outil de recalage des projections, automatique, qui permet d'améliorer efficacement la reconstruction des volumes en nano-tomographie. D'autre part, la nano-tomographie de phase s'avère un outil précieux pour étudier la structure fine de l'os, en donnant accès à une imagerie haute-résolution (taille de pixel effective de quelques dizaines de nanomètres) sur un champ de vue de plusieurs dizaines de microns. Différents outils d'analyse (étude du réseau lacuno-canaliculaire, minéralisation autour des lacunes et canalicules, orientation des fibres de collagènes) ont été appliqués sur différents échantillons osseux: os sain, os souffrant d'ostéoporose et os souffrant d'ostéoarthrite (arthrose). Cette étude visait à démontrer la faisabilité de telles analyses sur l'os, mais aussi d'en discuter leurs limites.

La dernière partie de cette thèse est consacrée à des développements algorithmiques innovant pour la reconstruction tomographique de la phase. Nous présentons d'abord un outil de simulation d'images par contraste de phase, porté sur la plateforme d'imagerie virtuelle VIP (Creatis, Villeurbanne), en libre accès, afin d'en faciliter l'utilisation et le développement. D'autre part, nous posons les bases théoriques d'un algorithme de reconstruction combinant les étapes d'estimation de phase et de reconstruction tomographique. Il utilise d'une part un modèle linéaire du contraste (appelé Fonction de

Transfert du Contraste, CTF) pour l'estimation de la phase, et d'autre part l'algorithme itératif SART pour la reconstruction tomographique. Nous décrivons le formalisme de la méthode pour différents objets (transparents et atténuants) et présentons les premiers résultats sur des données simulées.

Nous terminons ce manuscrit en rappelant les différents apports de notre travail et en soulignant les perspectives de travaux futurs. Ce travail a permis de développer des méthodes et de mettre en œuvre des outils visant à faciliter la reconstruction de données en micro- et nano-tomographie par contraste de phase, et d'appliquer ces techniques à des échantillons biologiques. D'autre part, nous avons développé un outil de simulation, ainsi qu'un algorithme innovant de reconstruction de phase. Les résultats obtenus sont encourageants, et ouvrent quelques perspectives de recherche pour ce type d'algorithmes, comme par exemple l'emploi d'un autre modèle de contraste (modèle mixte au lieu de la CTF), ou l'étude d'autres types de régularisation.

Chapter I: Physics of X-rays and tomography

This thesis focuses on imaging, using the particular modality of multi-distance in-line X-ray phase tomography. In this chapter, we give the physical context of this work, by introducing some notions about X-rays, how they are characterized and how they interact with their environment. Secondly, phase contrast imaging is presented, its advantages with respect to conventional attenuation imaging and its requirements, as well as existing techniques that enable to perform such an imaging modality. Finally, we present what is tomography, to bridge the gap between phase contrast and phase tomography.

Table of contents

1. X-rays and Synchrotron Radiation

In 1895, Wilhelm Conrad Roentgen discovered a new kind of electromagnetic rays, produced by the collision of electrons on matter, and that can pass through the body (Roentgen, 1896). He called them "X-rays" because of their unknown nature. As an illustration, Figure 1 shows the attenuation of X-rays induced by the hand of Anna Roentgen, the wife of Wilhelm Roentgen, bearing a metal ring. He observed that X-rays are weakly absorbed by soft tissues, but strongly attenuated by bones and metals. X-ray radiography was born. Its great potential in medicine earned W.C. Roentgen to be awarded the Nobel Prize in 1901.

Figure 1: X-ray photograph of the hand of Mrs Roentgen.

A decade later, in 1912, Max Von Laue highlighted that X-rays are not only attenuated by the matter, but also diffracted by crystals. In 1952, Watson and Crick evidenced the double helix structure of DNA by using X-rays diffraction (Watson & Crick, 1953).

Synchrotron radiation (SR) was discovered in 1946 by F. R. Elder, A.M. Gurewitsch, R.V. Langmuir and H.C. Pollock (Elder, Gurewitsch, Langmuir, & Pollock, 1947), in a General Electric synchrotron accelerator. In the early 1960's, synchrotron radiation turned out to have a great potential in medical and material imaging, because of its peculiar properties (developed in the Section 3).

2. The European Synchrotron Radiation Facility (ESRF)

The ESRF is the third 3rd generation synchrotron, built in Europe in the early 1990's, after Spring-8 in Harima (Japan) and the Advanced Photons Source in Argonne (United States). The ESRF, located in Grenoble (France), is an international research institute for cutting-edge science with synchrotron radiation, which offers some peculiar properties, as its high intensity, stability and collimation.

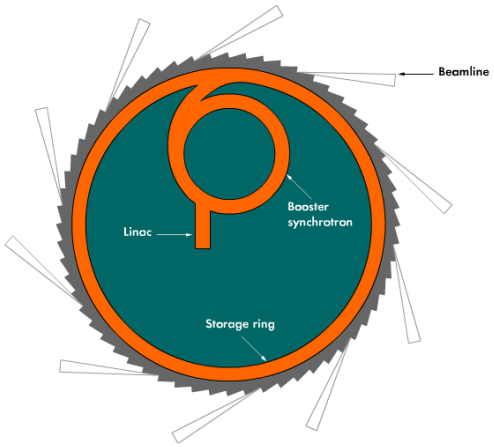

Figure 2: Scheme of the ESRF. Electrons are injected and accelerated in the Linac, re-accelerated in the booster synchrotron, to circulate at a constant speed in the storage ring. Source: *www.esrf.eu.*

The ESRF was created in 1988, thanks to the involvement of 12 countries. It was inaugurated on September 30th 1994 and nowadays employs 600 workers and receives 6000 researchers from all over the world each year to carry out experiments. It is one of the largest 3rd generation synchrotron light sources in the world and the provided X-rays brilliance allows advanced research in many diverse scientific areas including medicine (radiation therapy, imaging), material science (from biomaterials to metals), environment and cultural heritage studies.

The principle of ESRF is depicted in Figure 2: electrons are injected and accelerated in a linear accelerator ("*Linac*"), thanks to a series of radiofrequency cavities. Then, they are transmitted to the *booster synchrotron*, where they are accelerated to reach an energy level of 6GeV. They are finally injected in an 844 meters circumference *storage ring*, in which their kinetic energy is kept constant for several hours. They produced intense SR, when passing through arrays of permanent magnets that deviate them to follow a circulatory trajectory. This SR is directed toward one of the 40 existing beamlines. There are two types of beamlines: BM (for *Bending Magnets*) and ID (for *Insertion Devices*). The bending magnets sources produce a pulsed beam with a wide and continuous spectrum, from microwaves to hard X-rays, and less brilliant than the one produce by insertion devices. The insertion device sources (wigglers and undulators) produce a more brilliant beam and with higher energies. The wigglers, which consist in a periodic series of magnets, produce time-pulsed light of broad energy spectrum, unlike the undulators that produce long-pulses light, with a narrow (monochromatic) but tunable, energy range (Magaritondo, 1988). The ESRF mainly produces hard X-rays, *i.e.* X-rays with energy from 10 to 100keV (in other words, with wavelength from 0.1 to 0.01nm).
As an illustration, the electromagnetic spectrum is depicted in Figure 3, from radiowaves to gamma-rays. The corresponding wavelength, the approximate size and the tool are reported below.

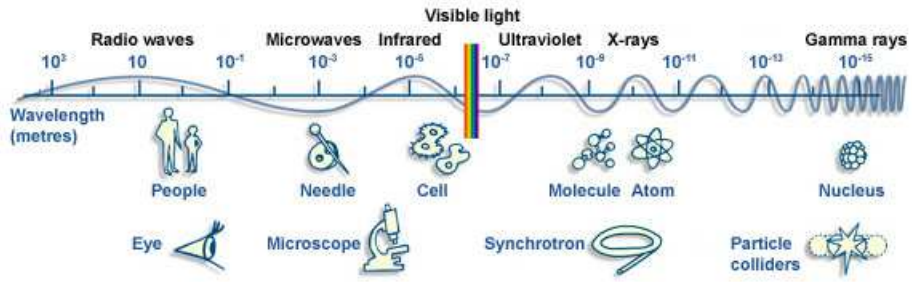

Figure 3: Electromagnetic spectrum, with corresponding wavelengths, and possible objects that can be investigated, with the corresponding technique.

3. X-ray coherence, spectral brightness and requirements for phase-contrast imaging

Synchrotrons potentially produce remarkably bright (10^{13} times more intense than whose produced by a conventional source) and stable X-rays. Their high intensity, stability and coherence allow to perform quantitative X-ray imaging. We give some details on coherence, which is a key property for phase contrast imaging. Two types of coherence can be distinguished: temporal and spatial (Figure 4).

On one hand, the *temporal coherence* length ξ_T (also known as *longitudinal coherence* length) is defined as follows:

$$\xi_T = \lambda \frac{E}{\Delta E} \tag{1.3.1}$$

where $\frac{\Delta E}{E}$ denotes the energy bandwidth and λ the wavelength. The temporal coherence ξ_T is thus related to the monochromaticity of the beam. The more monochromatic the beam is, the more temporally coherent it is. As an example, the energy band pass $\frac{\Delta E}{E}$ at the ESRF ranges between 10^{-4} and 10^{-2}. The corresponding temporal coherence length is about 1µm.

On the other hand, the *spatial coherence* length ξ_S (also known as *transverse coherence* length) is defined as follows:

$$\xi_S = \lambda \frac{\alpha}{\Delta \alpha} \tag{1.3.2}$$

where $\frac{\Delta \alpha}{\alpha}$ denotes the angular acceptance and λ the wavelength. The spatial coherence ξ_S depends on the angular acceptance of the source, *i.e.* on the source size and the distance from the source. The smaller the spot is, the more spatially coherent is the beam. In the same way, the farthest from a small source we are, the more point-like the source is. As an example, for a small spot size (a few micrometers) and long beamlines (100m to 200m), the spatial coherence length is about 100µm.

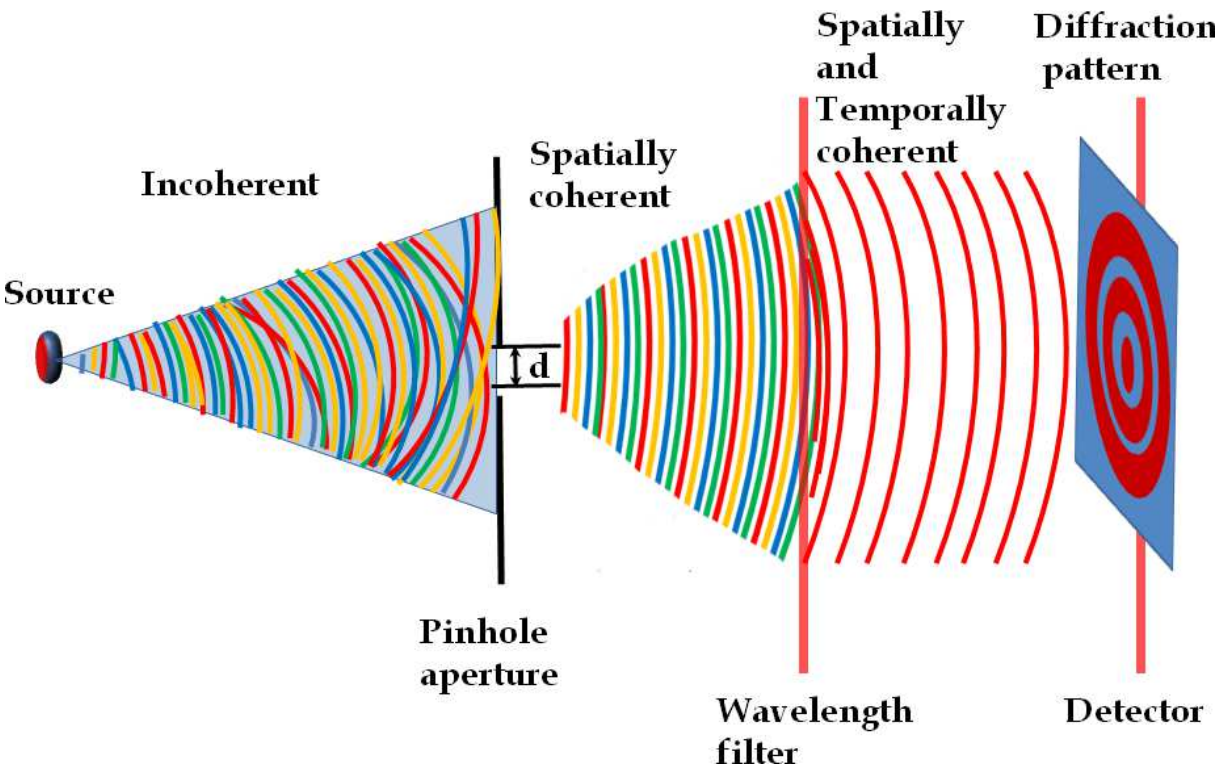

Figure 4: Illustration of spatial and temporal coherences. Image from (Davidoiu, 2013).

Another important property of SR is its spectral brightness. The terms brilliance, brightness and spectral brightness raised ambiguity among the SR community; we choose to adopt the nomenclature defined by Mills et al., (Mills et al., 2005). This spectral brightness is expressed in $\frac{photons}{s.mm^2.mrad^2.0.1\%\frac{\Delta\lambda}{\lambda}}$ and reflects the photon flux (number of photons per second), directed with a certain angular divergence (in mrad²), for a certain the source size (in mm²), with a bandwidth of 0.1% of the central wavelength ($0{,}1\%\frac{\Delta\lambda}{\lambda}$). The more intense and directed the beam is, the more brilliant it is.

As an example, at a given wavelength, the brightness of a light bulb of 60W is about $10^6\,\mathrm{photons/s.mm^2.mrad^2.0.1\%(\Delta\lambda/\lambda)}$, the brightness of the sun $10^{10}\,\mathrm{photons/s.mm^2.mrad^2.0.1\%(\Delta\lambda/\lambda)}$ and the brightness of a 3rd generation synchrotron around $10^{20}\,\mathrm{photons/s.mm^2.mrad^2.0.1\%(\Delta\lambda/\lambda)}$ (Mobilio, Boscherini, & Meneghini, 2015).

Most phase contrast imaging modalities require a temporally coherent (*i.e.* monochromatic) and spatially coherent (*i.e.* parallel) X-ray beam, with a high flux (Peyrin, Cloetens, Salome-Pateyron, Baruchel, & Spanne, 1997), to benefit from the high sensitivity offered by the phase-shift. The SR delivered by the ESRF fulfils these requirements, as explained previously.

Firstly, the temporal coherence (monochromaticity) is required to avoid *beam hardening artefacts* during tomographic reconstruction. The beam hardening is due to the absorption of low energy photons by the sample, and results in a non-uniform grey level in a homogeneous object (Figure 5).

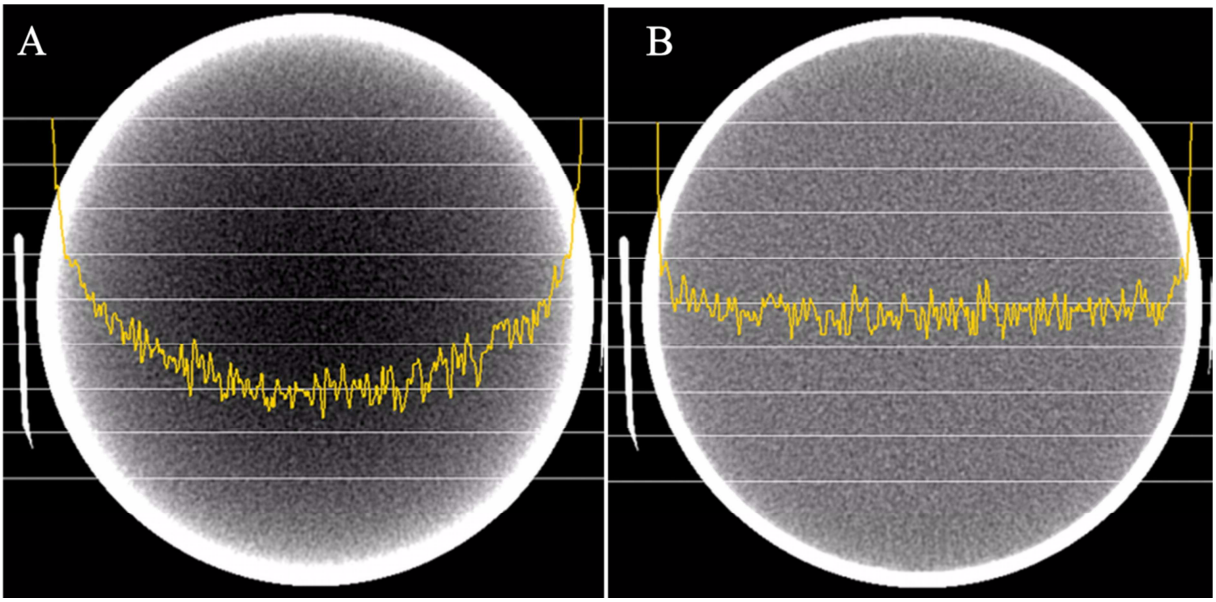

Figure 5: Example of beam-hardening artefact on a tomographic slice of a water cylinder (A) without correction and (B) with correction of the beam hardening. Images from (Barrett & Keat, 2004).

Secondly, the use of highly coherent beams (intrinsically coherent or made coherent) makes it possible to observe Phase Contrast effects. The different techniques that can be used to put in evidence the phase-shift induced by a sample will be detailed in Section 7.

Finally, a highly bright beam allows achieving a good spatial resolution while a sufficient signal-to-noise ratio (SNR) in the image. Actually, the flux is reduced by the monochromator crystal, possible optical elements, and attenuation of the sample. The incoming flux should consequently be large enough so that a sufficient number of photons reach the detector.

4. Interaction of waves with matter: attenuation vs. phase

In this section, we focus on how X-rays interact with the matter. We consider a wave of wavelength λ. If this wave is propagating in vacuum, it is described by its wavenumber k, defined by:

$$k = \frac{2\pi}{\lambda}. \tag{1.4.1}$$

In a medium of refractive index n, this wavenumber becomes k':

$$k' = kn. \tag{1.4.2}$$

The medium can be described by its *complex refractive index* n (Jackson, 1975):

$$n(x, y, z) = 1 - \delta_n(x, y, z) + i\beta(x, y, z) \tag{1.4.3}$$

where δ_n is the *refractive index decrement*, β is the *absorption index* and (x, y, z) are the 3D spatial coordinates.

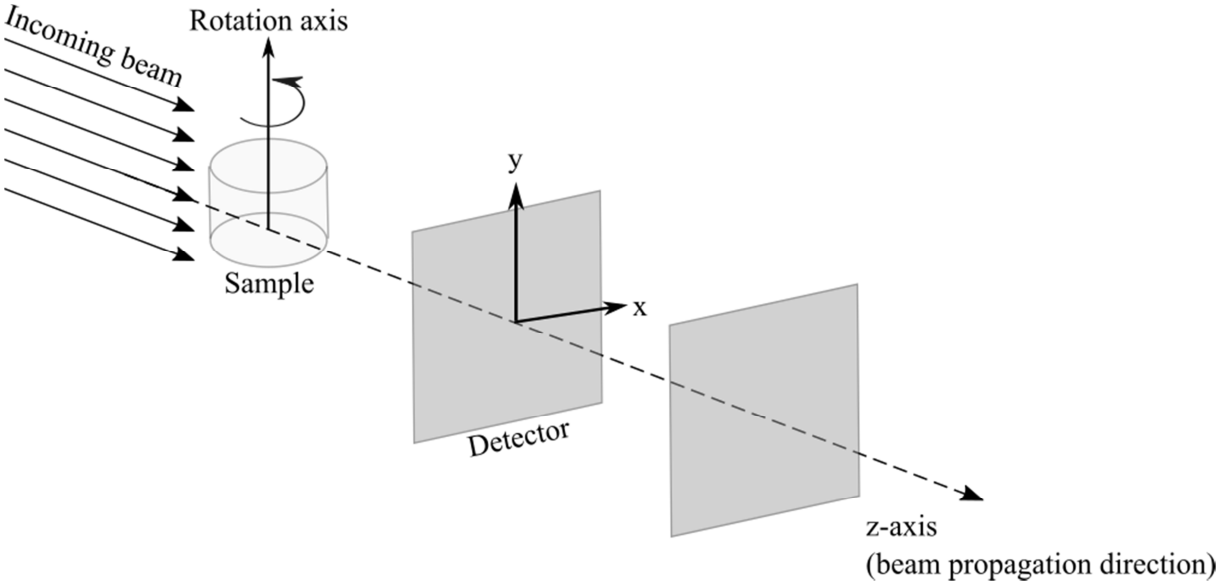

Figure 6: Scheme of the coordinates used in this section.

We consider a wave propagating along the z-direction (Figure 6). The wave front of a planar wave going through the medium becomes:

$$\phi(x,y,z) = \exp(ik'z) = \exp(ikn(x,y,z)z). \tag{1.4.4}$$

Substituting n by its expression (Equation (1.4.3)) leads to:

$$\phi(x,y,z) = \exp\big(ik\big(1-\delta_n(x,y,z)\big)z\big).\exp(-\beta(x,y,z)z). \tag{1.4.5}$$

Consequently, we can observe that an X-ray beam that passes through a medium is both attenuated and phase shifted. δ_n, the refractive index decrement, is related to the phase shift of the incident wave, due to the deflection of the wave front in the medium, and β, the absorption index, is related to the attenuation of the incident beam induced by the medium.

It is worth to note that these two quantities are proportional to the electron density ρ_e of a medium.

First, the refractive index decrement can be expressed as (Jackson 1975)

$$\delta_n = \frac{r_c\lambda^2}{2\pi}\rho_e, \tag{1.4.6}$$

where r_c denotes the classical electron radius, λ the wavelength of the X-ray beam. This formula has been simplified by Guinier (Guinier, 1994), ρ being the density (in g/cm^3) and λ the wavelength (in Å):

$$\delta_n \approx 1.3\cdot 10^{-6}\rho\lambda^2. \tag{1.4.7}$$

The absorption index can be expressed as (Jackson, 1975)

$$\beta = \frac{r_c\lambda^3\rho_e}{4\pi^2 c}\sum_j \frac{f_j\gamma_j}{Z}, \tag{1.4.8}$$

where r_c denotes the classical electron radius, λ the wavelength of the X-ray beam, and $\rho_e$the electron density, c the light velocity, f_j the number of electrons per atom with damping constant $\gamma_j$and Z the atomic number that corresponds to the total number of electrons per atom. Here, j corresponds to an electron in the atom.

5. Attenuation contrast

As seen in the previous section, the amplitude of the wavefront is reduced by a factor $\exp(-\beta z)$, as far as it goes through a medium. β is the imaginary part of the refractive index, related to the linear attenuation coefficient μ through the following relationship (Raven et al., 1996):

$$\mu(x,y,z) = \frac{4\pi}{\lambda}\beta(x,y,z). \tag{1.5.1}$$

The attenuation of X-rays through the matter has been described by the Beer-Lambert law, as mentioned in Section 5.f.

The attenuation of hard X-rays (10-100keV) through the matter is due to the photoelectric effect, Compton scattering (incoherent scattering) and Rayleigh scattering (coherent scattering). At this energy range, pair production is unlikely to occur. The probability of each interaction to occur is described by its *cross section*. It is usually expressed in *barn* ($1\ \text{barn} = 10^{-24}\text{cm}^2$), and depends on the energy of the incident X-ray beam and the atomic number Z of the medium. The cross section is also known as the atomic attenuation coefficient, in cm²/atom.

5.a. Photoelectric effect

The photoelectric effect is illustrated in Figure 7. The incident photon is fully absorbed and dislodges a bound electron close to the nucleus (K-shell electron for example), with a kinetic energy E_{e-}, equal to the energy of the incident photon $h\nu$, minus the binding energy of the electron E_K:

$$E_{e-} = h\nu - E_K, \tag{1.5.2}$$

where h is the Planck constant ($h = 6.62 \times 10^{-34} J.s$) and ν the wave frequency.

The ejected electron (called *photoelectron*) is put in motion following a direction depending on the energy of the incident photon. The atom is thus ionized (an electron of an inner shell is missing), and recovers a stable state by releasing characteristic X-ray (secondary photons), because of the passage of L-/M-shell electrons to the K-shell.

Typically, photoelectrons of energy 20keV are most probably emitted at 70° with respect to the direction of the incident photon, whereas photoelectrons of 500keV are preferentially emitted at 25°.

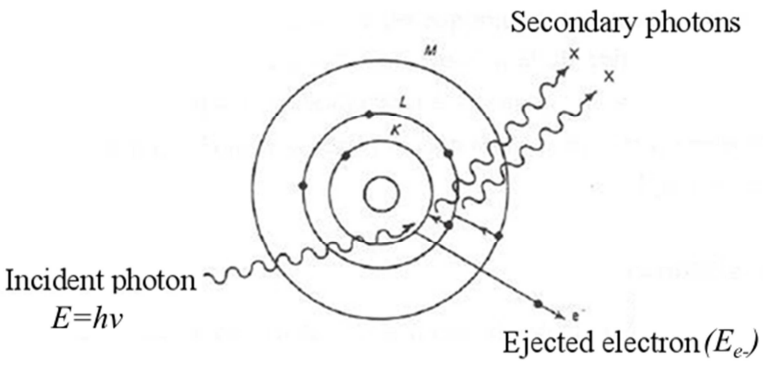

Figure 7: Illustration of the photoelectric effect.

The photoelectric cross-section $\sigma_{photoelectric}$ depends on the energy of the X-ray E and the atomic number Z of the medium as (Wang, 2007):

$$\sigma_{photoelectric} \propto \frac{Z^5}{E^{3.5}}. \tag{1.5.3}$$

5.b. Rayleigh scattering (coherent and elastic scattering)

Rayleigh scattering is elastic and coherent, because there is no change in energy and phase, respectively, between the incident and the scattered photon. The incident photon simply bounces off an atom, and is deviated (Figure 8). This interaction occurs at low energies.

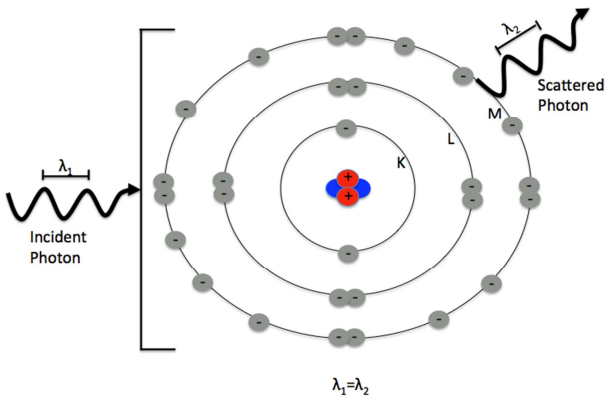

Figure 8: Illustration of Rayleigh scattering.

The Rayleigh cross section $\sigma_{Rayleigh}$ depends on the energy of the incident photon E and the atomic number of the medium Z as (Wang, 2007):

$$\sigma_{Rayleigh} \propto \frac{Z^2}{E^2}. \tag{1.5.4}$$

5.c. Compton interaction (incoherent and inelastic scattering)

The Compton interaction is depicted in Figure 9.

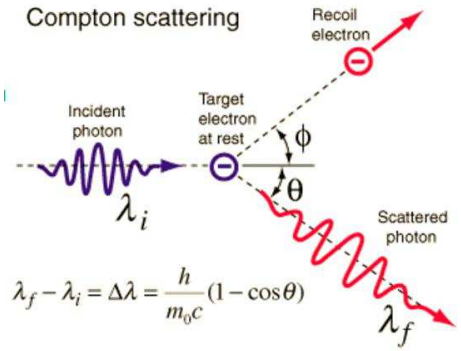

Figure 9: Illustration of the Compton interaction.

The incident photon interacts with an atomic electron of an outer electron shell (low binding energy with respect to the energy of the incident photon); the photon is scattered with an angle θ, and the electron is set in motion, with a kinetic energy E_{e-}, and a direction ϕ:

$$E_{e-} = h\nu - h\nu', \tag{1.5.5}$$

where $h\nu$ is the energy of the incident photon, and $h\nu'$ the energy of the scattered photon.

Using the conservation of energy and the conservation of momentum before and after the interaction, we can express the energy of the scattered photon $h\nu'$, as a function of the energy of the incident photon $h\nu$, and the scattering angle θ:

$$h\nu' = \frac{h\nu}{1 + \frac{h\nu(1-\cos(\theta))}{m_e.c^2}}, \tag{1.5.6}$$

where $m_e.c^2$ denotes the electron rest mass energy ($m_e.c^2 \approx 511\ keV$)

The angular distribution θ of scattered photons and the direction of the recoil electron ϕ, are given by the Klein-Nishina formula (Klein & Nishina, 1929). The angle ϕ never exceeds 90°. Typically, ϕ and θ are likely to decrease when the energy of the incident photon increases. The Compton cross section $\sigma_{Compton}$ decreases with the energy, as (Wang, 2007):

$$\sigma_{Compton} \propto \frac{Zm_e.c^2}{E + m_e.c^2}. \tag{1.5.7}$$

The Compton scattering is incoherent, because the phase of the photon is destroyed (there is a change in the wavelength), and inelastic, because of the transfer of energy between the photon and the recoil electron.

5.d. Pair production

The pair production is illustrated in Figure 10a. It required an incident photon whose energy is higher than 1.022MeV, which is not the case of hard X-rays (10 to 100keV). Briefly, the photon is absorbed near the nucleus, and produces an *electron-positron* pair. The positron quickly annihilates with an electron of the medium, to produce the so-called annihilation radiation, namely two photons γ of 511keV each, emitted in opposite direction (Figure 10b).

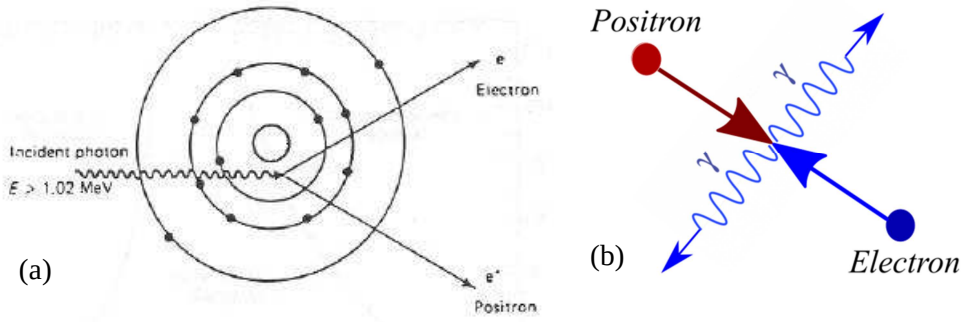

Figure 10: (a) Pair production mechanism; (b) annihilation of a positron with an electron.

The cross section of pair production typically increases with the energy E of the incident photons. It also depends on the atomic number of the medium Z as (Wang, 2007):

$$\sigma_{pair} \propto \frac{Z^2 \left(E-2m_e.c^2\right)^3 \left(E+2m_e.c^2\right)^3}{E^6}. \tag{1.5.8}$$

5.e. Total attenuation coefficient

The total cross section σ_{TOT} of the X-rays with matter is the combination of all the previously described effects. Nevertheless, for hard X-rays (10 to 100keV), the pair production is unlikely to occur, so it can be neglected.

$$\sigma_{TOT} = \sigma_{photoelectric} + \sigma_{Compton} + \sigma_{Rayleigh} + \sigma_{pair} \tag{1.5.9}$$

As an illustration, Figure 11 shows the predominant effect for energies ranging from 10keV to 100MeV and atomic numbers ranging from 1 to 100.

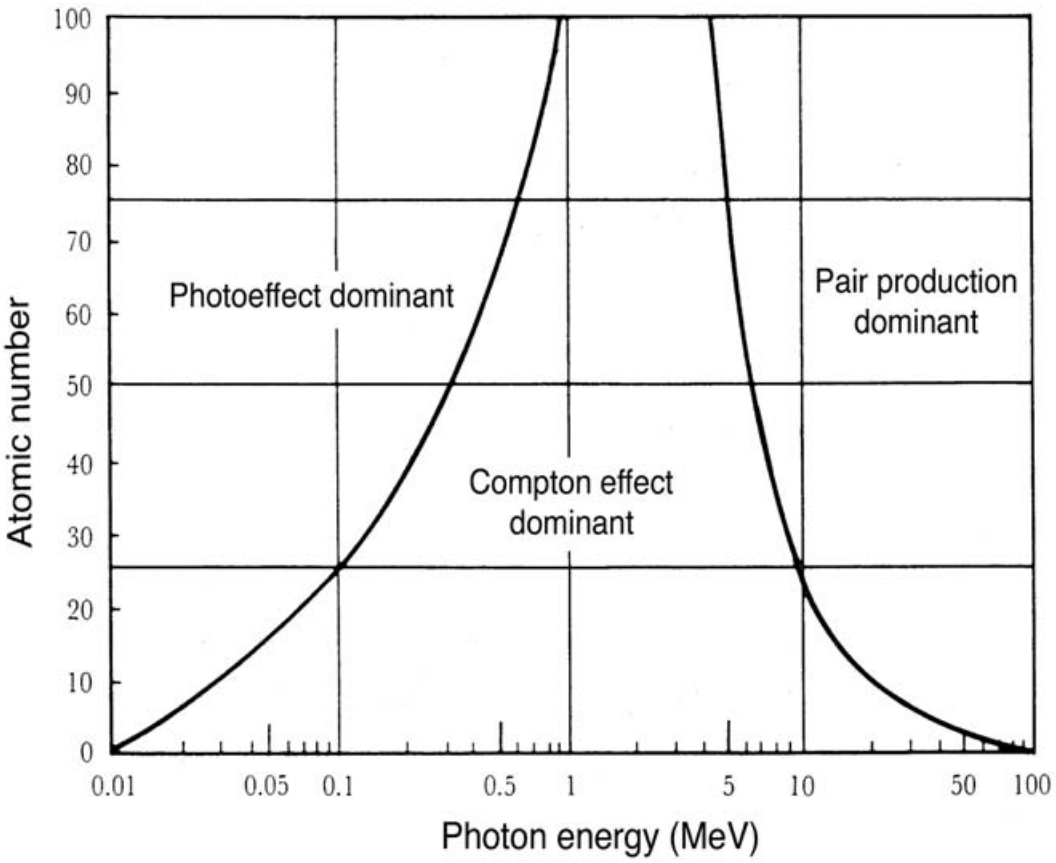

Figure 11: Predominant effect, as a function of the atomic number of the material Z and the photon energy, in MeV. Figure from (Podgorsak, 2005).

The linear attenuation coefficient μ, usually expressed in cm^{-1}, is related to the total cross section σ_{TOT} through:

$$\mu = \frac{N_A . \rho . \sigma_{TOT}}{A}, \tag{1.5.10}$$

where N_A denotes the Avogadro's constant ($N_A \approx 6.022.10^{23} mol^{-1}$), ρ the mass density of the material and A the atomic mass number of the medium. Figure 13 shows the linear attenuation coefficient of several materials, as a function of the energy.

The mass attenuation coefficient, $\frac{\mu}{\rho}$, expressed in cm^2/g, is also often used. At the ESRF, it could be, as well as other physical and optical indexes, calculated using the software XOP (del Río & Dejus, 2004). Figure 12 illustrates the mass attenuation coefficient of water for each interaction (coherent Rayleigh scattering, incoherent Compton scattering, photoelectric effect and pair production), and the resulting total mass attenuation coefficient, as a function of the energy of the incident photon.

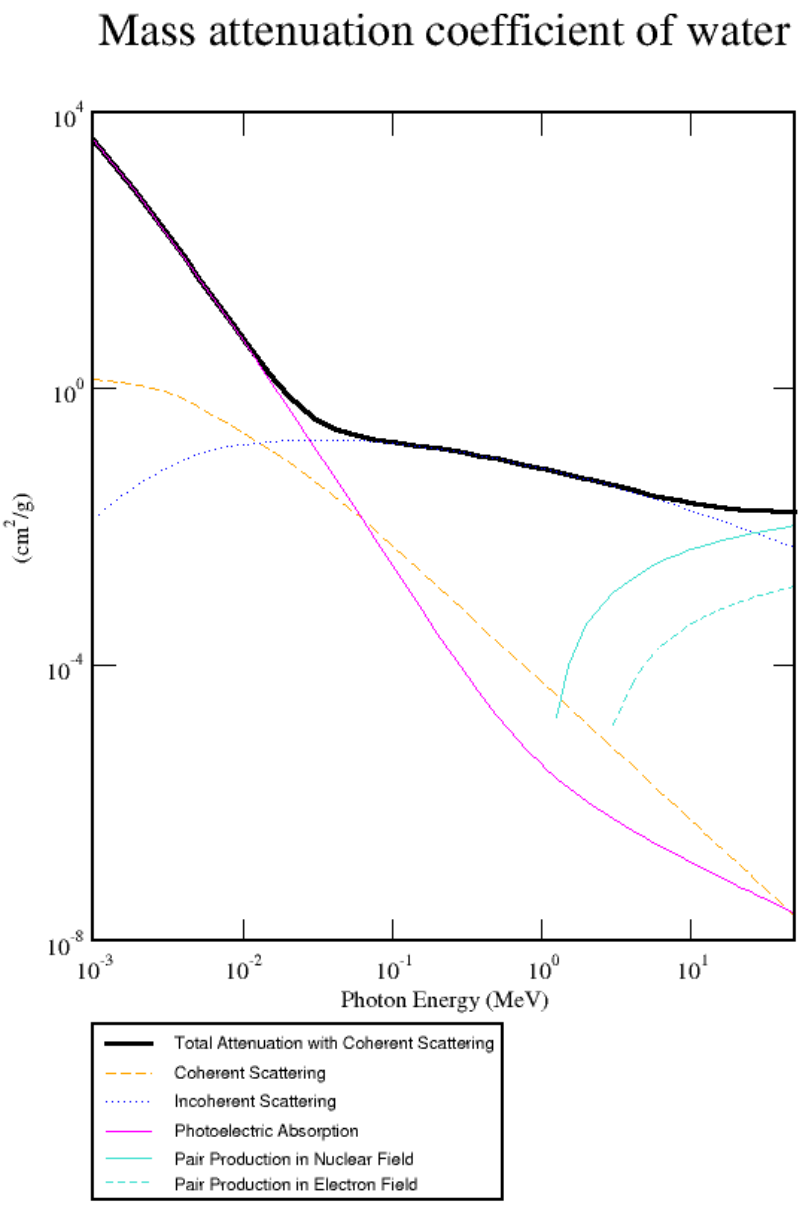

Figure 12: Total mass attenuation coefficient (cm^2/g), for energies from 1keV to 50MeV (bold). Each thinner curve corresponds to the attenuation coefficient for a specific interaction, mentioned below the graph.

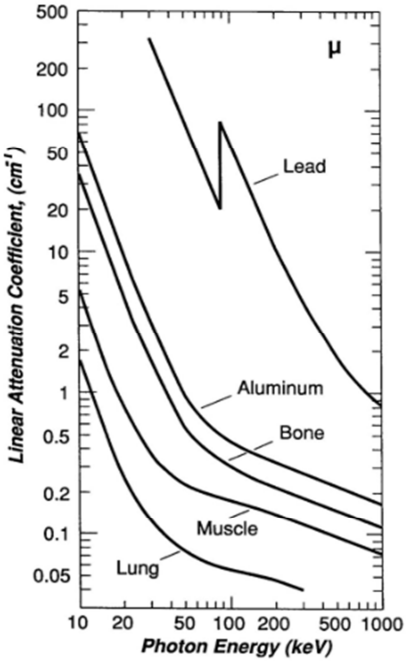

Figure 13: Linear attenuation coefficients (in cm^{-1}) of different materials, as a function of the photon energy (in keV). Note the presence of an abrupt jump in the linear attenuation coefficient of the lead, around 88keV; it is the K-absorption edge of the lead, and it corresponds to the energy of the electrons on the K-shell of the lead, which are ejected when the incoming energy exceeds the one of the K-edge.

5.f. Beer-Lambert law

The Beer-Lambert law describes the attenuation of the photons in a medium. We consider an incident beam composed of N_0 photons of energy E, going through a homogeneous material, of linear attenuation coefficient μ (in cm^{-1}), and thickness t (in cm) along the z-direction. The number of transmitted photons N_t is given by:

$$N_t(E) = N_0(\mathrm{E}).\exp(-\mu(E).t) \tag{1.5.11}$$

If the object is inhomogeneous, its attenuation coefficient varies spatially. The number of transmitted photons N_t is then expressed as:

$$N_t(E) = N_0(\mathrm{E})\exp(-\int_{path} \mu(z,E)dz) \tag{1.5.12}$$

Usually, the data are transformed in order to get directly the integral of the attenuation coefficient. The recorded intensity I is (Mobilio et al., 2015):

$$I = \ln\left(\frac{N_0(E)}{N_t(E)}\right) = \int_{path} \mu(z,E)dz \tag{1.5.13}$$

6. Phase contrast

During the past three decades, there has been a growing interest in X-ray phase contrast imaging (PCI). Unlike conventional absorption-based imaging, which is only sensitive to the attenuation of the incoming X-ray beam, PCI also relies on the phase shift of X-rays occurring when they pass through a medium. The real $(1-\delta_n)$ and imaginary (β) parts of n are respectively related to the phase-shift and the absorption. This modality offers a better sensitivity than conventional radiology, since for hard X-rays (10-100 keV) and low-Z materials (such as soft tissues), refraction is at least two or three orders of magnitude higher than absorption at typical imaging energies (Momose, Takeda, Itai, & Hirano, 1996), as illustrated on Figure 14.

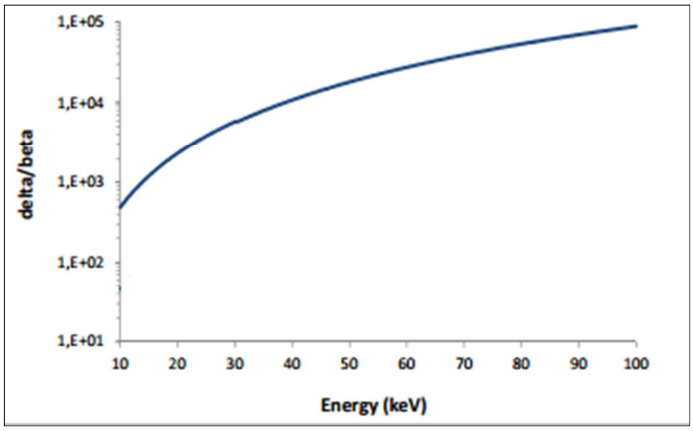

Figure 14: δ_n/β ratio of soft tissues, as a function of the energy (in the range of hard X-rays).

Nevertheless, phase contrast is not directly measurable, and needs to be put in evidence by the mean of various experimental techniques, described in the next section.

7. Phase contrast techniques

Since the emergence of phase contrast, several techniques have been developed. They enable to measure the phase shift, induced by the sample, of the wave front, or a signal related to the phase-shift (*e.g.* its gradient or Laplacian). To this aim, they take advantages of various physical phenomena, as refraction, diffraction, etc.

7.a. Crystal interferometry

One of the first set-up designed for phase contrast measurements was the Laue-Laue-Laue interferometer (Bonse & Hart, 1965). It uses three crystals with Laue geometry[1]. Momose *et al.* demonstrated the high potential of phase contrast by imaging soft-tissue with a high sensitivity (Momose et al., 1996).

[1] The Laue geometry (transmission geometry) refers to the diffraction of the beam from the opposite surface it hit the crystal. This is opposed to the Bragg geometry (reflection geometry), where the beam is refracted from the same surface it entered the crystal.

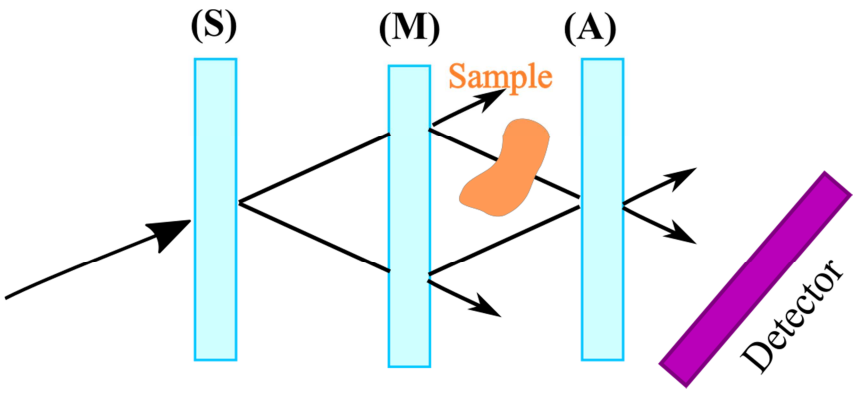

Figure 15: Laue-Laue-Laue interferometer (Bonse & Hart, 1965). (S), (M) and (A) are respectively the splitter, mirror and analyser crystals.

As depicted in Figure 15, a monochromatic beam is split into two coherent beams using the (S) splitter crystal. They are transmitted by the crystal mirror (M), so that they converge on the analyzer crystal (A). One beam is phase-shifted when passing through the sample, unlike the other. This results in interference patterns that are recorded by the detector downstream to the interferometer. These images are directly proportional to the phase itself.

7.b.Analyzer-based phase contrast

A phase contrast imaging modality, using a crystal analyzer in Bragg geometry[1], was introduced by Chapman et al., in 1997 (Chapman et al., 1997). This phase contrast modality is also known as "Diffraction-Enhanced Imaging" (DEI), or "Analyzer-Based Imaging" (ABI). The incident X-ray beam is monochromatized using a typically Si(111) double crystal monochromator, that is deviated when passing through the sample. A second crystal (usually Si(333)), called the analyzer crystal, selects the refracted beams at certain angles (Figure 16a).

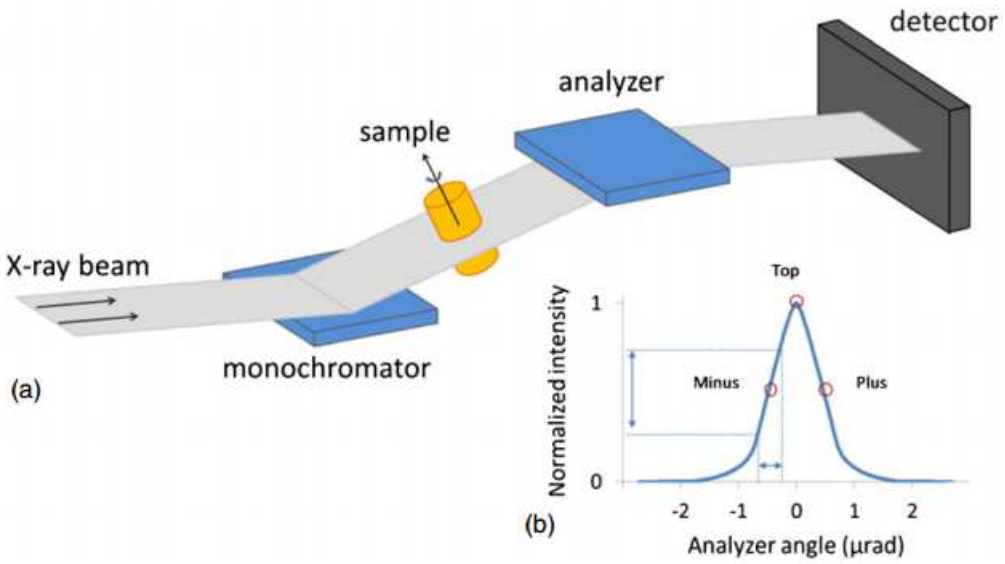

Figure 16: Analyzer-based imaging set-up (a), and Rocking-Curve (RC) of a Si(333) crystal analyzer (b). Illustrations from (Sztrókay et al., 2012).

The analyzer acts as an angular filter, which selects a narrow beam satisfying the Bragg's condition:

$$k\lambda = 2d.\sin(\theta), \tag{1.7.1}$$

where d is distance between two adjacent lattice planes of the crystal, θ is the angle of the incident beam, λ is the wavelength of the incoming beam, and k is an integer (diffraction order).

The analyzer crystal is characterised by its Rocking Curve (RC), which represents the normalized transmitted intensity as a function of the angle of the analyzer. Typically, for a Si(333) crystal operating at 70 keV, the full-width at half-maximum of the RC is about 0.95 µrad. Thus, the ABI set-up requires a high spatial stability.

A dataset consists in acquiring images at several angular positions of the sample, for two positions of the analyzer crystal, usually "Plus" and "Minus" positions on the RC (see Figure 16b), corresponding to the angles where 50% of the intensity is transmitted. By combining the recorded intensities at two positions of the RC, the apparent absorption image and the refraction angle (angular deviation) can be retrieved.

The angular deviation is directly related to the phase gradient, through:

$$\Delta\alpha_x = -\frac{\lambda}{2\pi}\frac{\partial\varphi}{\partial x} \tag{1.7.2}$$

Thus, ABI is sensitive to beam deflection in one direction (the direction parallel to the diffracted beam), and permits the direct measurement of local beam deflection using a monochromatic and parallel X-ray beam, under small refraction angle condition.

The major drawbacks of this technique are the requirement of perfect crystals and high spatial stability. Moreover, acquisitions are known to be time-consuming because the photon flux is drastically reduced by the crystals.

This technique has mainly been applied in biomedical research, and particularly in mammography (Fiedler et al., 2004; Keyriläinen et al., 2005), cartilage and bone imaging (Izadifar, Chapman, & Chen, 2014; Majumdar et al., 2004; Mollenhauer et al., 2002), and more recently in biomaterial imaging (Appel et al., 2015). Recently, some efforts have been devoted in reducing the delivered dose towards clinically compatible dose (Keyriläinen et al., 2008; Mittone, Gasilov, Brun, Bravin, & Coan, 2015).

7.c. Grating-based phase contrast

The grating-based technique is also called Differential Phase Contrast Imaging (DPCI) (David, Nöhammer, Solak, & Ziegler, 2002; Momose, 2003). It is based on Fresnel diffraction in a periodic grating system (Weitkamp et al., 2005), also known as the *self-imaging phenomenon*. It requires a spatially coherent beam (or made spatially coherent by a source grating).

Because of beams interference, the image of the grating is then repeated regularly, at multiple of the Talbot distance (Lord Rayleigh, 1881). The Talbot distance d_T is defined as:

$$d_T = \frac{2g^2}{\lambda} \tag{1.7.3}$$

where g is the period of the grating, and λ the wavelength of the incident beam.

7.c.i. Talbot distances and fractional Talbot distances

For an absorbing periodic grating (of period g), illuminated by a monochromatic beam of wavelength λ, self-imaging (*i.e.* repetition of the grating pattern, transversally to the propagation axis) occurs at multiples of the Talbot distance d_T, defined in Equation (1.7.3).

If the grating is not absorbing, but induces a substantial phase shift α of the illuminating wavefront, the self-imaging occurs at multiples of fractional Talbot distance f_T (Arrizón & Ibarra, 1996):

$$f_T = \frac{g^2}{2\eta^2\lambda}, \text{with } \eta = \begin{cases} 1 \text{ if } \alpha = \pi/2 \\ 2 \text{ if } \alpha = \pi \end{cases} \tag{1.7.4}$$

7.c.ii. Set-up

The grating interferometry set-up is depicted in Figure 17.

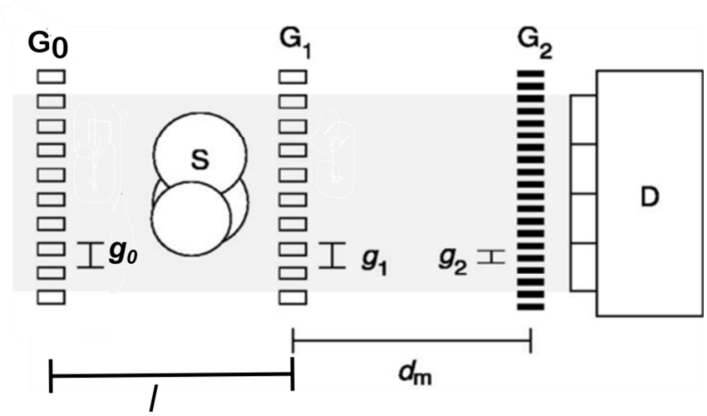

Figure 17: Scheme of the interferometry set-up. G_0 is the source grating (of a g_0-period), G_1 the phase grating (of a g_1-period), and G_2 the absorption grating (of a g_2-period), placed just before the detector D. The distance between G_0 and G_1 is l, and the distance between G_1 and G_2 is d_m. Figure adapted from (Pfeiffer, Weitkamp, Bunk, & David, 2006; Zanette, 2011).

A so-called *phase grating* G_1 is placed after the sample, and induces a consequent phase shift on the wavefront without attenuating the beam. This results in periodic intensity modulation (wavefront interferences) at fractional Talbot distance f_T. The *absorption grating* G_2 (also known as *analyzer grating*), usually placed at $d_m = f_T$, constructs the image.

When using a divergent and polychromatic beam, a *source grating* G_0 is added close to the source, to make a series of coherent sources from the incoming incoherent source. This enables phase contrast imaging with conventional lab sources (Pfeiffer et al., 2006).

It is noteworthy that the periods of G_0 and G_2 are interdependent, and the distances separating each grating are related by:

$$g_0 = g_2 \cdot \frac{l}{d_m} \tag{1.7.5}$$

7.c.iii. Phase stepping

The phase-stepping method, which consists in recording the signal at several (usually 3 to 6) positions of the analyzer grating, allows to quantify the absorption, the phase-shift and the small-angle scattering (SAXS) (also called "dark-field") induced by the sample. For the reconstruction, the stepping curves (intensity recorded in each point as a function of the phase step) with and without the sample, are fitted with a sine curve, and enable to reconstruct the absorption, the phase and the dark-field. The decrease in intensity of the wavefront (in the presence of the sample, with respect to without sample), its lateral shift and its decrease in visibility are related to the attenuation, the refraction and the scattering of the sample, respectively. The detailed reconstruction process is explained in (Thüring, Modregger, Pinzer, Wang, & Stampanoni, 2011).

Grating interferometry offers a moderate spatial resolution, which depends on the size source, the grating pitch size, and the distances d_m and l separating each grating. Its compatibility with conventional lab sources offers it great applications in biomedical imaging. A recent investigation has been devoted to optimizing the acquisition of a phase contrast clinical scanner using grating interferometry (Müller et al., 2015). Current research is mainly focused on breast imaging (Anton, Bayer, & Beckmann, 2013; Stampanoni, Wang, & Thüring, 2011; Sztrókay et al., 2013; Willner et al., 2014), and aims at reducing the delivered dose in mammography (Gromann et al., 2016; Scherer et al., 2015). Grating-based imaging has also been used in bone imaging (Potdevin et al., 2012) and brain imaging (Pinzer et al., 2012). Its clinical potential has been demonstrated by the development of a laboratory set-up for phase micro-tomography (Pfeiffer et al., 2006), and applied to soft-tissue imaging (Bech et al., 2009).

7.d.Edge-illumination technique

This technique, firstly introduced by Olivo and Speller (Olivo & Speller, 2008), is also known as coded-aperture. It does not require a spatially or temporally coherent beam (*i.e.* suitable for a divergent polychromatic beam).

The principle of this technique is the following: wavefront distortions induced by the sample are converted into intensity variations. The detector is not placed in the direction of the sample but slightly below or above (see Figure 18), so that a beam that would not be detected is detected because of the deviation caused by the sample. In the same way, a beam that would have been detected without the presence of the sample is not detected, because of the deviation caused by the presence of the sample.

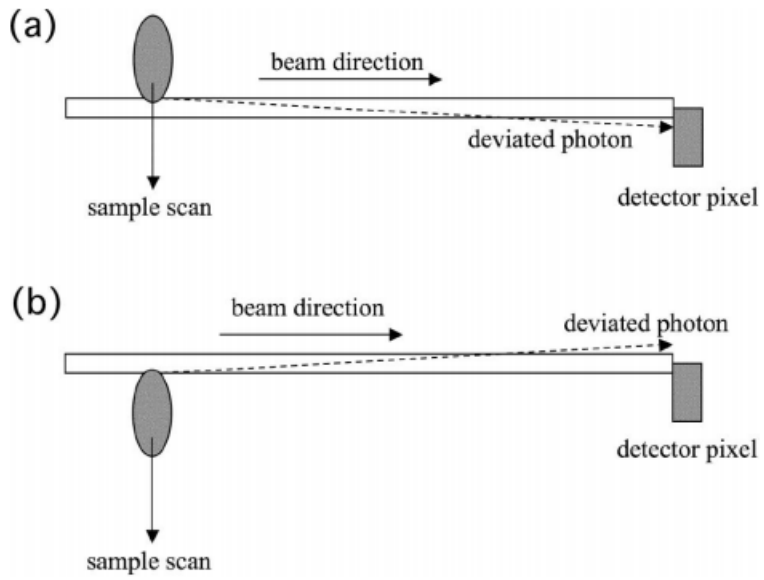

Figure 18: Edge-illumination principle: (a) a beam that would have been undetected is actually detected, and (b) vice-versa.

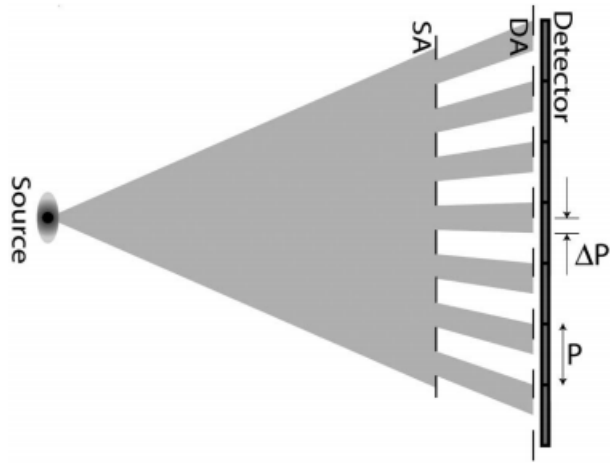

Figure 19: Coded-aperture set-up (from [Olivo, 2011]). The Sample Aperture (SA) mask is placed just upstream to the sample. The Detector Aperture (DA) mask is placed just before the detector. P denotes the detector pixel size, and ΔP the illuminated fraction of a pixel.

The set-up of this technique is depicted on Figure 19. The incoming beam created by the source is divided into multiple beams, using a sample aperture (SA) mask. The detector aperture (DA) mask, placed just before the detector, is positioned so that each beam impinges partially (ΔP) on a single pixel detector (of size P). The recorded intensity thus depends on the illuminated fraction of the pixel, and on the refraction angle (Endrizzi et al., 2014).

This low-dose non-interferometric technique (C. K. Hagen, Munro, Endrizzi, Diemoz, & Olivo, 2014) has been successfully applied to cartilage imaging (Marenzana et al., 2012), and scaffolds (C. Hagen et al., 2015), with an effective pixel size of 3.5μm.

7.e. Propagation-based phase contrast

The simplest phase contrast set-up is propagation-based phase contrast imaging (PB-PCI) (Snigirev, Snigireva, Kohn, Kuznetsov, & Schelokov, 1995; Wilkins, Gureyev, Gao, Pogany, & Stevenson, 1996), also known as *free space propagation* phase contrast. It consists in letting a spatially coherent beam propagate after passing through a sample. If the detector is close to the sample "at contact plane", an absorption image of the object is recorded. Phase contrast can be achieved by moving the detector downstream.

This technique can be easily extended to tomographic imaging, by acquiring projections at several angular positions of the object, using a high-resolution detector (Fast REadout LOw Noise [FReLoN] camera (Labiche et al., 2007)), to image the propagation fringes at a sufficient precision. The recorded measurements are directly related to the Laplacian of the phase, $\nabla^2\varphi$, in the near-fileld regime approximation

This technique has been refined by Cloetens *et al.* (P. Cloetens et al., 1999) to a multiple distances acquisition (Figure 20). This particular method is called *holotomography*, and consists in acquiring projections for a complete rotation of the sample, at different sample to detector distances. This enables to cover well the Fourier domain (the Fresnel transform, mentioned in the Chapter II, can have zero crossing at certain distances), and thus improving the phase reconstruction. Recently, a quite exhaustive experimental study about acquisition optimization, with respect to dose delivering and image quality, has been published by (Frachon et al., 2015).

These two methods (single-distance and multiple-distance) benefit from the coherence of the beam and its high flux. Actually, they do not require any optical elements such as analyser crystals, which make them free from photon losses and optical aberrations. The signal intensity depends on the propagation distance, as shown in Figure 21.

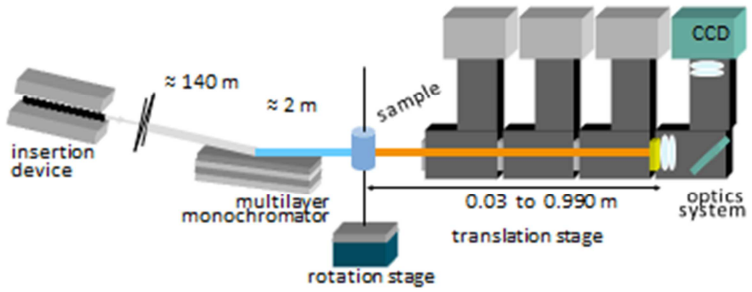

Figure 20: Set-up for multiple propagation distances acquisition (holotomography). Image from (Langer, Cloetens, & Peyrin, 2010).

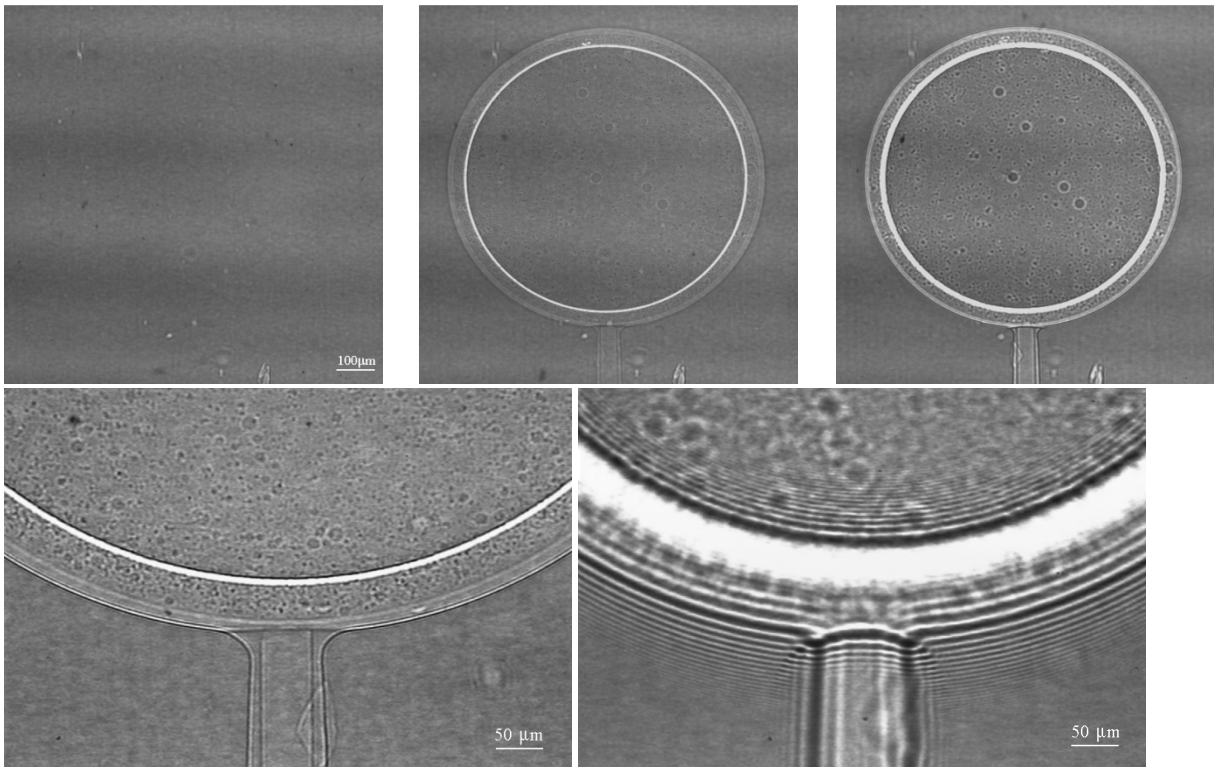

Figure 21: Recorded intensities of a non-attenuation object (a polystyrene sphere of 30µm thick, covered by a 15µm-thick parylene sphere), at (a) 3mm; (b) 190mm; (c) 830mm propagation distance. Zoomed-in details of the sample at (d) 0.15m and (e) 3.08m propagation distance. Energy beam is about 17.7keV. Images from (P. Cloetens et al., 1999).

Regardless of the number of distances used, a classical reconstruction process consists in performing phase retrieval at each projection angle, followed by tomographic reconstruction. The existing phase retrieval algorithms of propagation-based phase contrast imaging will be further developed in the Chapter II).

Because of its simplicity, and the high spatial resolution achievable (up to 20nm with magnified in-line phase contrast), PBI has been widely used in various domains, such as material science (P. Cloetens et al., 1997), plant imaging (Peter Cloetens, Mache, Schlenker, & Lerbs-Mache, 2006; Rousseau et al., 2015), cartilage and bone imaging (Horng et al., 2014; Kampschulte et al., 2016; Maggiano et al., 2016) and brain imaging (Bartels, Krenkel, Cloetens, Möbius, & Salditt, 2015; Rositi et al., 2014). Very recently, a lab source set-up has been applied to lung imaging, achieving a resolution up to a few micrometers (Krenkel, Töpperwien, Dullin, Alves, & Salditt, 2016).

8. Tomography

Now we have defined the phase contrast, we introduce the basic principle of computed tomography (CT), because they are both combined in phase-contrast CT.

8.a. Data acquisition and Radon transform

Data acquisition in X-ray 2D parallel beam CT can be described as follows. The detector is placed opposite to the source. Each ray of the source is attenuated by the sample, positioned between the source and the detector, and is recorded by one element on the detector. The attenuated intensity is recorded, for each angle θ, and each element of the detector. The resulting dataset of projections is named *sinogram* (Figure 22).

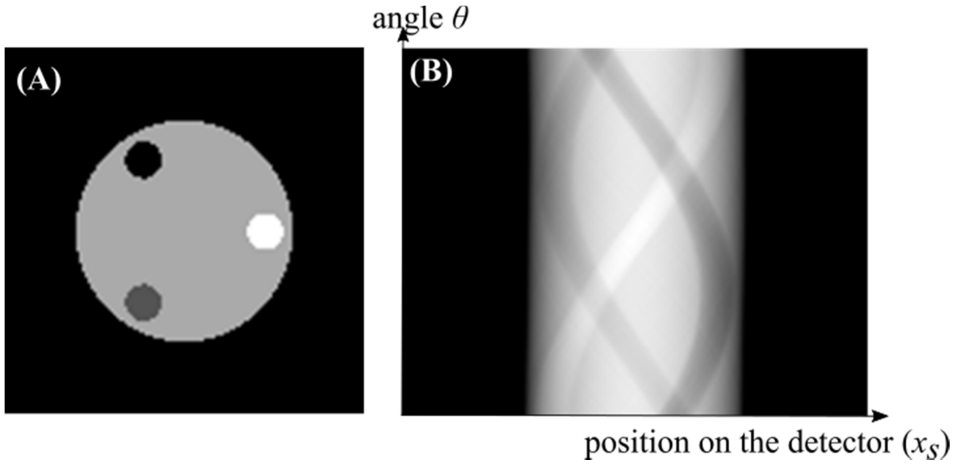

Figure 22: (A) Synthetic image and (B) its corresponding sinogram, for θ ranging between 0 and π. Courtesy of F. Peyrin.

The sinogram can be modeled thanks to the Radon transform, which was defined and studied by Johann Radon, in 1917. This mathematical transform relates an n-D function to the set of its integrals over hyper planes. In the 2D case, it corresponds to the set of projections of the image at angles θ, p_θ (Figure 23).

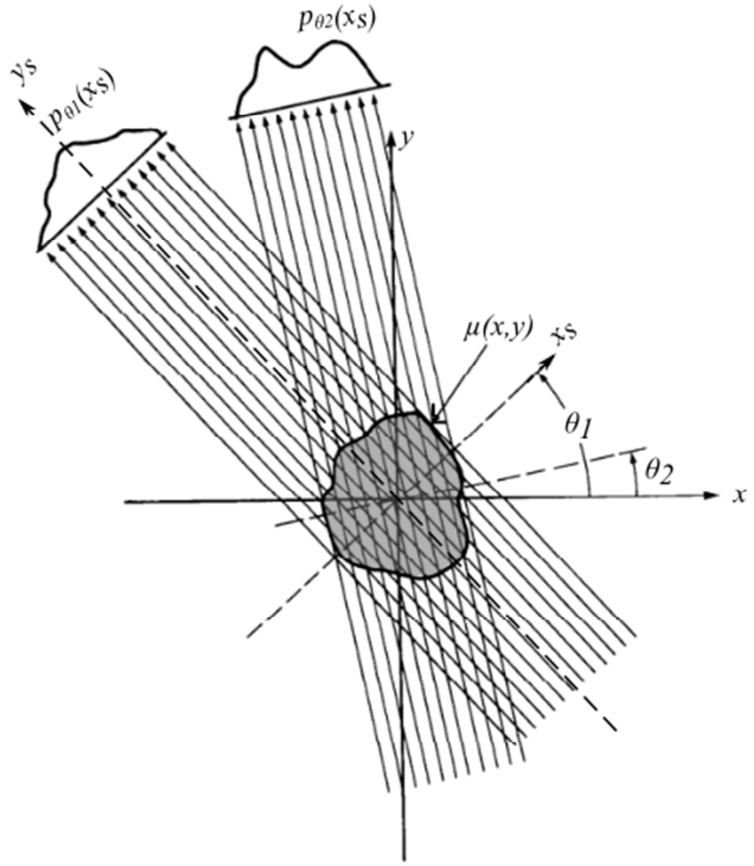

Figure 23: Principle of the Radon transform. Image modified from (Kak & Slaney, 1988).

The object is described in the Cartesian coordinate system (x, y) by its linear attenuation coefficient 2D-map $\mu(x, y)$. The coordinate system attached to the beam, *i.e.* the system (x, y) rotated with an angle θ is denoted by the system (x_s, y_s), as shown in Figure 23. These two systems are linked through the following relationship:

$$\begin{pmatrix} x_s \\ y_s \end{pmatrix} = \begin{pmatrix} \cos\theta & \sin\theta \\ -\sin\theta & \cos\theta \end{pmatrix} . \begin{pmatrix} x \\ y \end{pmatrix}. \tag{1.8.1}$$

In the same way, the system (x, y) is the system (x_s, y_s), rotated of an angle $-\theta$. Consequently:

$$\begin{cases} x = x_s \cos\theta - y_s \sin\theta \\ y = x_s \sin\theta + y_s \cos\theta \end{cases}. \tag{1.8.2}$$

The projection is expressed as

$$p_\theta(x_s) = \int_{-\infty}^{+\infty} \mu(x, y)\, dy_s\,, \tag{1.8.3}$$

which is equivalent, in the rotated coordinate system (x_s, y_s), to:

$$p_\theta(x_s) = \int_{-\infty}^{+\infty} \mu(x_s \cos\theta - y_s \sin\theta\,, x_s \sin\theta + y_s \cos\theta)\, dy_s. \tag{1.8.4}$$

8.b.Fourier slice theorem

The Fourier slice theorem, also known as the *central slice theorem*, is fundamental in the theory of image reconstruction. It states that the 1D Fourier transform of a projection of an object at angle θ, p_θ, is equal to the 2D Fourier transform of the object on a line at angle θ passing through the origin. A scheme of this theorem is depicted in Figure 24. This theorem is a key point to understand tomographic reconstruction. Its mathematical demonstration is given below.

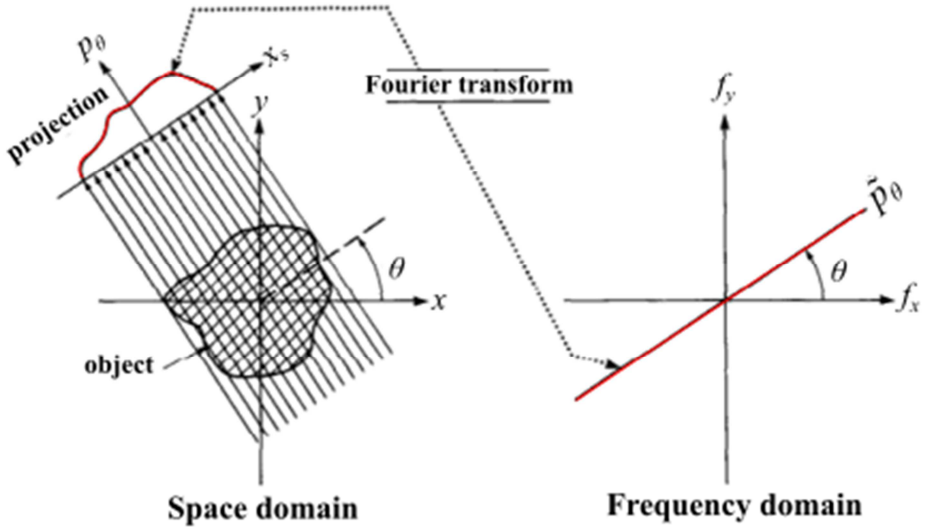

Figure 24: Illustration of the Fourier slice theorem. Figure modified from (Kak & Slaney, 1988).

Let (f_x, f_y) be the equivalent coordinate system of (x, y) in the Fourier domain.

By definition of the Fourier transform, the 2D Fourier transform of $\mu, \mathcal{F}_{2D}\{\mu\}$, also denoted $\tilde{\mu}$ is:

$$\mathcal{F}_{2D}\{\mu\}(f_x, f_y) = \tilde{\mu}(f_x, f_y) = \iint \mu(x, y).\, exp(-2\pi i(x\, f_x + y f_y))\, dx\, dy. \qquad (1.8.5)$$

Let $p_\theta(x_s)$ be a projection of angle θ, and $\tilde{p}_\theta(f_x)$ its 1D Fourier transform:

$$\mathcal{F}_{1D}\{p_\theta\}(f_x) = \tilde{p}_\theta(f_x) = \int p_\theta(x_s)\, exp(-2\pi i x_s f_x)\, dx_s. \qquad (1.8.6)$$

Subsituting Equation (1.8.4) in Equation (1.8.6) leads to:

$$\tilde{p}_\theta(f_x) = \iint \mu(x_s\, cos\, \theta - y_s\, sin\, \theta\, , x_s\, sin\, \theta + y_s\, cos\, \theta).\, exp(-2\pi i x_s f_x)\, dx_s\, dy_s. \qquad (1.8.7)$$

Substituting (x_s, y_s) by their equivalent in the fixed Cartesian grid (x, y) leads to:

$$\tilde{p}_\theta(f_x) = \iint \mu(x, y).\, exp(-2\pi i(x\, cos\, \theta\, f_x + y\, sin\, \theta\, f_x))\, dx\, dy \qquad (1.8.8)$$

$$\tilde{p}_\theta(f_x) = \tilde{\mu}(f_x \cos\theta\,, f_x \sin\theta). \tag{1.8.9}$$

Note that $f_x\,cos\,\theta$ and $f_x\,sin\,\theta$ are the Cartesian coordinates of a straight line passing through the origin, rotated of an angle θ with respect to the abscissa of the coordinate system.

Then μ can be inferred from an infinite number of projections by doing an inverse Fourier transform of $\tilde{\mu}$, expressed as follows:

$$\mu(x,y) = \iint \tilde{\mu}\left(f_x, f_y\right) exp\left(2i\pi\,(f_x x + f_y y)\right) df_x df_y. \tag{1.8.10}$$

8.c. Filtered back projection

Retroprojection, or Back-projection, consists in "spreading" the projections, according to:

$$\mu_{BP}(x,y) = \int_0^\pi p_\theta(x\cos\theta + y\sin\theta, \theta)\, d\theta \tag{1.8.11}$$

The simple retroprojection of all projections results in a blurred reconstruction, and star-like artefacts, as depicted in Figure 25A. This blurring can be alleviated by the use of a high-pass filter prior to back projection.

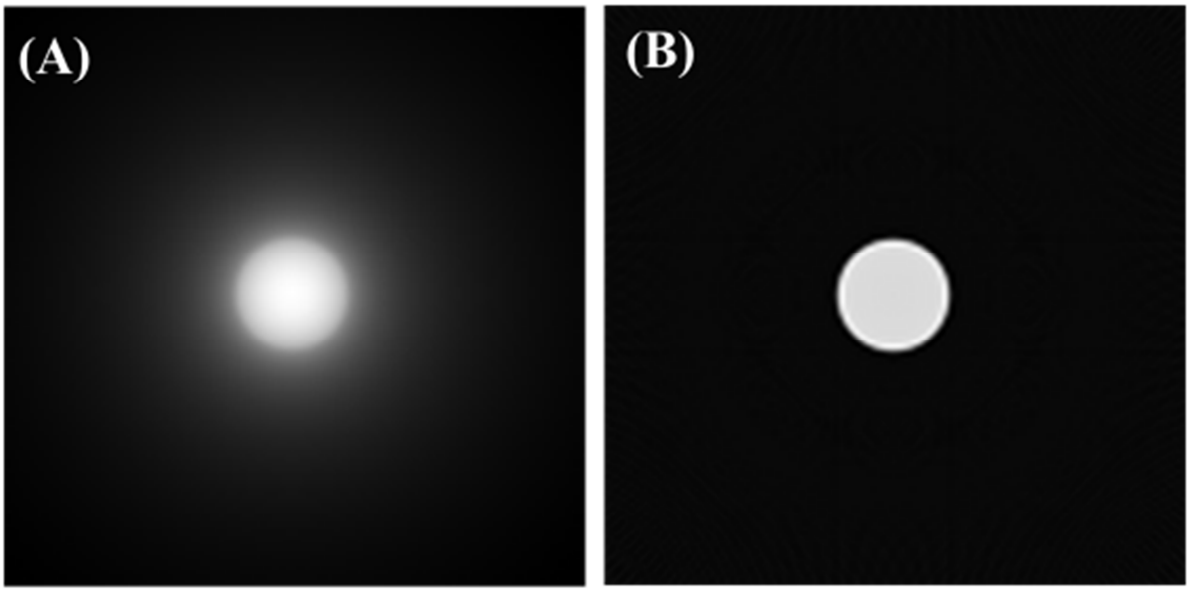

Figure 25: Backprojection (A) and filtered backprojection (B) of the sinogram of a circle.

Filtered back-projection, usually shortened to FBP, consists in filtering the projections using a ramp filter before backprojection. The mathematical demonstration of this reconstruction method is given below.

The expression of Cartesian coordinates of the Fourier domain (f_x, f_y) as a function of their equivalents in the polar coordinates (u, θ) is : $\begin{cases} f_x = u\cos\theta \\ f_y = u\sin\theta \end{cases}$.

Recall the expression of the inverse Fourier transform in Equation (1.8.10), and express it in the polar system:

$$\mu(x,y) = \frac{1}{2}\int_{\theta=0}^{\theta=2\pi}\int_{u=-\infty}^{u=+\infty}\tilde{\mu}(u,\theta)\exp(2i\pi\big(u(x\cos\theta + y\sin\theta)\big)|u|\,du\,d\theta. \quad (1.8.12)$$

The integral of the linear attenuation coefficient at $+\pi$, $p_{\theta+\pi}$, is the same than the integral at θ, p_θ, except the sign because of the reverse direction:

$$p_{\theta+\pi}(x_s) = -p_\theta(x_s). \quad (1.8.13)$$

According to the central slice theorem, developed in Section 8.b (Page 55), we have the following equality in terms of linear attenuation coefficient:

$$\tilde{\mu}(u,\theta+\pi) = \tilde{\mu}(-u,\theta). \quad (1.8.14)$$

Consequently, the integral over 2π of *u* in Equation (1.8.12) is equivalent to an integral over π of the absolute value of *u*:

$$\mu(x,y) = \int_{\theta=0}^{\theta=\pi}\int_{u=-\infty}^{u=+\infty}\tilde{\mu}(u,\theta)\exp(2i\pi u(\cos\theta\,x + \sin\theta\,y))|u|\,du\,d\theta \quad (1.8.15)$$

We apply the Fourier slice theorem in Equation (1.8.15) :

$$\mu(x,y) = \int_{\theta=0}^{\theta=\pi}\int_{u=-\infty}^{u=+\infty}\tilde{p}_\theta(u)|u|\exp\big(2i\pi u(\cos\theta\,x + \sin\theta\,y)\big)\,du\,d\theta. \quad (1.8.16)$$

Note the filtered projection at an angle θ by Q_θ:

$$\mu(x,y) = \int_\theta Q_\theta(x\cos\theta + y\sin\theta)\,d\theta, \quad (1.8.17)$$

with

$$Q_\theta(x\cos\theta + y\sin\theta) = \int_{-\infty}^{+\infty}\tilde{p}_\theta(u)|u|\exp(2i\pi u(\cos\theta\,x + \sin\theta\,y))du. \quad (1.8.18)$$

In $|u|$ we recognize the ramp filter. In practice, the integrale is not performed on the whole Fourier space, but on a limited bandwidth [-u_{max}; u_{max}]:

$$Q_\theta(x\cos\theta + y\sin\theta) = \int_{-u_{max}}^{+u_{max}}\tilde{p}_\theta(u)|u|\exp\big(2i\pi u(\cos\theta\,x + \sin\theta\,y)\big)\,du. \quad (1.8.19)$$

Computing the integral on a limited bandwidth instead of the whole space is equivalent to apply an apodization filter *ρ(u)* defined by:

$$\rho(u) = \begin{cases} 1, & -u_{max} \leq u \leq +u_{max} \\ 0, & \text{otherwise} \end{cases} \tag{1.8.20}$$

Since the ramp filter boosts the high frequencies, and thus the noise, it is usually followed by low-pass filtering (as the Hann filter).In practice, this apodization filter is a Gaussian-like filter, which leads to reconstruction filter (ramp filter + apodization filter) as those depicted in Figure 26.

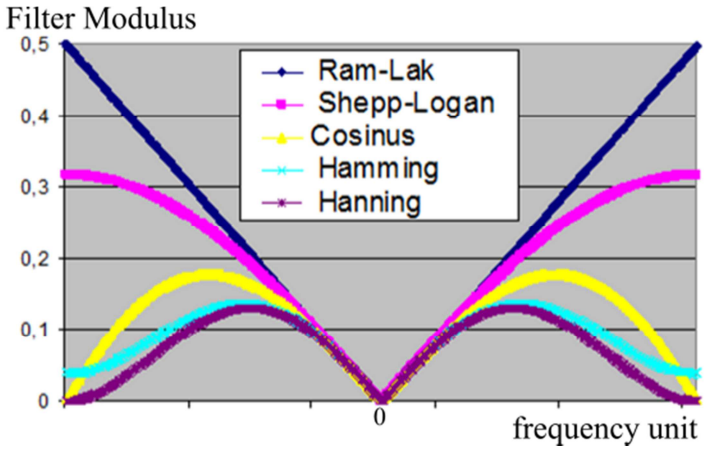

Figure 26: Examples of classical reconstruction filters.

The FBP is the standard and most popular reconstruction algorithm for parallel beam CT. It usually gives satisfying results while reasonable computation time, at least if the data are correctly sampled. Moreover, it has been extended to fan- and cone-beam CT. Some further mathematical developments about it are given in the book of (Kak & Slaney, 1988).

At the ESRF, the tomographic reconstruction is based on FBP (Salomé et al., 1999). The software currently used, called PyHST (Python High Speed Tomography), has been developed by A. Hammersley and later optimized by A. Mirone (Mirone, Brun, Gouillart, Tafforeau, & Kieffer, 2014).

8.d.Sampling theorem

One key-point of the reconstruction using FBP is to have a sufficient number of projections. Recall the Shannon theorem (also known as *sampling theorem*):

$$f_s \geq 2u_{max}, \tag{1.8.21}$$

where f_s is the sampling frequency, and u_{max} the maximal frequency of the signal. Let consider a projection of size D, sampled at a frequency f_s. The number of samples N_s in one projection is

$$N_s = f_s D. \tag{1.8.22}$$

It is admitted that the minimal number of projections N_p that ensures a good reconstruction using FBP is about:

$$N_p \approx \frac{\pi}{2} N_s. \tag{1.8.23}$$

The number of projections is always a tradeoff between image quality and delivered dose. An insufficient number of projections will result in star-like artefacts in the reconstructed image, but a too large number of projections will lead to a high delivered dose.

8.e. 3D – CBCT

Because conventional X-ray sources are commonly divergent, the FBP has been extended to fan- and cone-beam geometries. These geometries, as well as the classical parallel beam configuration used at the ESRF, are depicted in Figure 27.

Planar fan beam geometry is used in the 2nd scanner generation; the beam is divergent and the detector a line array. The sample rotates and translates to get a complete dataset of projections of the volume to image (Peyrin & Engelke, 2012).

Cone-beam CT (CBCT) appeared in the early 90's, and is nowadays broadly used in dental imaging, radiotherapy and interventional radiology. By acquiring 2D projections (*i.e.* including all the field of view), the sample only needs to rotate to get a complete data set of projections.

Tuy's data consistency condition (Tuy, 1983) states that every plane intersecting the object must also intersects the source at least once. This is non-valid for a circular trajectory of the source for example. Exact reconstruction algorithms have then been proposed by Grangeat (Grangeat, 1987) and Defrise and Clack (Defrise & Clack, 1994) for acquisitions satisfying Tuy's condition. It is based on the same principle than the FBP, but the data are either rebinned to parallel configuration or filtered by a 2D shift-variant filter.

The classical reconstruction algorithm used in CBCT is the Feldkamp-Davis-Kress method (shortened to FDK method), where a weighting step is performed prior to the FBP (Feldkamp, Davis, & Kress, 1984). This weighting step gives more importance to the rays that are close to the cone axis. Although this method is non-exact, it enables to reconstruct data acquired for a circular trajectory of the source. Only the slice in the plane of the source is reconstructed exactly. Nevertheless, FDK method has led to satisfying results, and has been widely used as a starting point to further developments (Turbell, 2001).

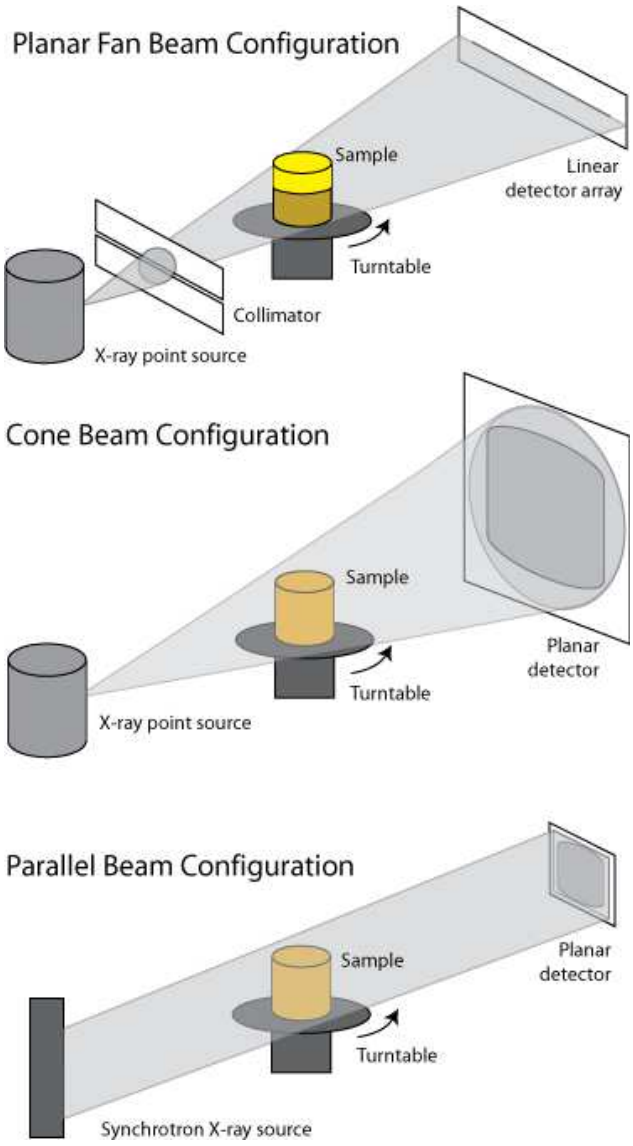

Figure 27: Planar fan beam, cone beam and parallel beam configurations for tomography. Figure from *http://serc.carleton.edu/research_education/geochemsheets/techniques/CT.html*

Conclusions

This thesis focuses on phase contrast imaging, because its offers an enhanced contrast with respect to conventional attenuation imaging. Coupled to high resolution detector and synchrotron radiation beam, it enables to image from soft tissues to bone with a high precision. In this first chapter, we present the physical context of this work, by introducing X-rays properties, and their interactions with the matter, as well as the requirement for phase contrast imaging. We present the different set-ups to do phase contrast imaging; the simplest of them is the propagation-based imaging, which is the set-up we used in this work. Since we are dealing with 3D phase contrast imaging, we finish by a section presenting the theoretical part of tomography, from data acquisition to volume reconstruction. The Cone-Beam Computed Tomography is also mentioned, as it is widely used in conventional tomography.

References

Anton, G., Bayer, F., & Beckmann, M. (2013). Grating-based darkfield imaging of human breast tissue. *Zeitschrift Für Medizinische Physik*.

Appel, A. A., Larson, J. C., Jiang, B., Zhong, Z., Anastasio, M. A., & Brey, E. M. (2015). X-ray Phase Contrast Allows Three Dimensional, Quantitative Imaging of Hydrogel Implants. *Annals of Biomedical Engineering*. doi:10.1007/s10439-015-1482-5

Arrizón, V., & Ibarra, J. G. (1996). Self-imaging of discrete gratings at fractions of the Talbot distance: an eigenvalue problem. *Optics Letters*, *21*(6), 378. doi:10.1364/OL.21.000378

Barrett, J. F., & Keat, N. (2004). Artifacts in CT: recognition and avoidance. *Radiographics : A Review Publication of the Radiological Society of North America, Inc*, *24*(6), 1679–91. doi:10.1148/rg.246045065

Bartels, M., Krenkel, M., Cloetens, P., Möbius, W., & Salditt, T. (2015). Myelinated mouse nerves studied by X-ray phase contrast zoom tomography. *Journal of Structural Biology*, *192*(3), 561–8. doi:10.1016/j.jsb.2015.11.001

Bech, M., Jensen, T. H., Feidenhans'l, R., Bunk, O., David, C., & Pfeiffer, F. (2009). Soft-tissue phase-contrast tomography with an x-ray tube source. *Physics in Medicine and Biology*, *54*(9), 2747–53. doi:10.1088/0031-9155/54/9/010

Beltran, M. A., Paganin, D. M., Siu, K. K. W., Fouras, A., Hooper, S. B., Reser, D. H., & Kitchen, M. J. (2011). Interface-specific x-ray phase retrieval tomography of complex biological organs. *Physics in Medicine and Biology*, *56*(23), 7353–69. doi:10.1088/0031-9155/56/23/002

Bonse, U., & Hart, M. (1965). An X-ray interferometer. *Applied Physics Letters*, *6*(8), 155. doi:10.1063/1.1754212

Chapman, D., Thomlinson, W., Johnston, R. E., Washburn, D., Pisano, E., Gmür, N., … Sayers, D. (1997). Diffraction enhanced x-ray imaging. *Physics in Medicine and Biology*, *42*(11), 2015–2025. doi:10.1088/0031-9155/42/11/001

Cloetens, P., Ludwig, W., Baruchel, J., Van Dyck, D., Van Landuyt, J., Guigay, J. P., & Schlenker, M. (1999). Holotomography: Quantitative phase tomography with micrometer resolution using hard synchrotron radiation x rays. *Applied Physics Letters*, *75*(19), 2912. doi:10.1063/1.125225

Cloetens, P., Mache, R., Schlenker, M., & Lerbs-Mache, S. (2006). Quantitative phase tomography of Arabidopsis seeds reveals intercellular void network. *Proceedings of the National Academy of Sciences of the United States of America*, *103*(39), 14626–30. doi:10.1073/pnas.0603490103

Cloetens, P., Pateyron-Salomé, M., Buffière, J. Y., Peix, G., Baruchel, J., Peyrin, F., & Schlenker, M. (1997). Observation of microstructure and damage in materials by phase sensitive radiography and tomography. *Journal of Applied Physics*, *81*(9), 5878. doi:10.1063/1.364374

David, C., Nöhammer, B., Solak, H. H., & Ziegler, E. (2002). Differential x-ray phase contrast imaging using a shearing interferometer. *Applied Physics Letters*, *81*(17), 3287. doi:10.1063/1.1516611

Davidoiu, V. (2013). Nonlinear approaches for phase retrieval in the Fresnel region for hard X-ray imaging. INSA de Lyon.

Defrise, M., & Clack, R. (1994). A cone-beam reconstruction algorithm using shift-variant filtering and cone-beam backprojection. *IEEE Transactions on Medical Imaging*, *13*(1), 186–95. doi:10.1109/42.276157

del Río, M. S., & Dejus, R. J. (2004). XOP 2.1: A new version of the X-ray optics software toolkit. *Proc. Synchrotron Radiation Instrumentation: Eighth International Conference, (Edited by T. Warwick et Al.)*, (American Institute of Physics, San Fransisco), 784–787.

Elder, F. R., Gurewitsch, A. M., Langmuir, R. V., & Pollock, H. C. (1947). Radiation from Electrons in a Synchrotron. *Physical Review*, *71*(11), 829–830. doi:10.1103/PhysRev.71.829.5

Endrizzi, M., Diemoz, P. C., Millard, T. P., Louise Jones, J., Speller, R. D., Robinson, I. K., & Olivo, A. (2014). Hard X-ray dark-field imaging with incoherent sample illumination. *Applied Physics Letters*, *104*(2), 024106. doi:10.1063/1.4861855

Feldkamp, L. A., Davis, L. C., & Kress, J. W. (1984). Practical cone-beam algorithm. *Journal of the Optical Society of America A*, *1*(6), 612. doi:10.1364/JOSAA.1.000612

Fiedler, S., Bravin, A., Keyriläinen, J., Fernandez, M., Suortti, P., Thomlinson, W., … Karjalainen-Lindsberg, M.-L. (2004). Imaging lobular breast carcinoma: comparison of synchrotron radiation DEI-CT technique with clinical CT, mammography and histology. *Physics in Medicine & Biology*.

Frachon, T., Weber, L., Hesse, B., Rit, S., Dong, P., Olivier, C., … Langer, M. (2015). Dose fractionation in synchrotron radiation x-ray phase micro-tomography. *Physics in Medicine and Biology*, *60*(19), 7543–7566. doi:10.1088/0031-9155/60/19/7543

Grangeat, P. (1987). *Analyse d'un systeme d'imagerie 3d par reconstruction a partir de radiographies x en geometrie conique*. ENST.

Gromann, L. B., Bequé, D., Scherer, K., Willer, K., Birnbacher, L., Willner, M., … Cozzini, C. (2016). Low-dose, phase-contrast mammography with high signal-to-noise ratio. *Biomedical Optics Express*, *7*(2), 381. doi:10.1364/BOE.7.000381

Guinier, A. (1994). *X-ray Diffraction in Crystals, Imperfect Crystals, and Amorphous Bodies*. *Acta crystallographica. Section A, Foundations of crystallography* (Vol. 57). New York, NY. doi:10.1021/ja01079a041

Hagen, C. K., Munro, P. R. T., Endrizzi, M., Diemoz, P. C., & Olivo, A. (2014). Low-dose phase contrast tomography with conventional x-ray sources. *Medical Physics*, *41*(7), 070701. doi:10.1118/1.4884297

Hagen, C., Maghsoudlou, P., Totonelli, G., Diemoz, P., Endrizzi, M., Rigon, L., … Olivo, A. (2015). High contrast microstructural visualisation of natural acellular matrices by means of phase-based x-ray tomography. *Scientific Reports*. Nature Publishing Group.

Horng, A., Brun, E., Mittone, A., Gasilov, S., Weber, L., Geith, T., … Coan, P. (2014). Cartilage and Soft Tissue Imaging Using X-rays: Propagation-Based Phase-Contrast Computed Tomography of the Human Knee in Comparison With Clinical Imaging Techniques and Histology. *Investigative Radiology*, *49*(9), 627–34. doi:10.1097/RLI.0000000000000063

Izadifar, Z., Chapman, D. L., & Chen, X. (2014). Computed Tomography Diffraction-Enhanced Imaging for In Situ Visualization of Tissue Scaffolds Implanted in Cartilage. *Tissue Engineering Part C: Methods*.

Jackson, J. D. (1975). *Classical Electrodynamics*.

Kak, A. C., & Slaney, M. (1988). Principles of computerized tomographic imaging.

Kampschulte, M., Langheinirch, A. C., Sender, J., Litzlbauer, H. D., Althöhn, U., Schwab, J. D., … Krombach, G. A. (2016). Nano-Computed Tomography: Technique and Applications. *RoFo : Fortschritte Auf Dem Gebiete Der Rontgenstrahlen Und Der Nuklearmedizin*, *188*(2), 146–154. doi:10.1055/s-0041-106541

Keyriläinen, J., Fernández, M., Fiedler, S., Bravin, A., Karjalainen-Lindsberg, M.-L., Virkkunen, P., … Thomlinson, W. (2005). Visualisation of calcifications and thin collagen strands in human breast tumour specimens by the diffraction-enhanced imaging technique: a comparison with conventional mammography and histology. *European Journal of Radiology*, *53*(2), 226–37. doi:10.1016/j.ejrad.2004.03.015

Keyriläinen, J., Fernández, M., Karjalainen-Lindsberg, M.-L., Virkkunen, P., Leidenius, M., von Smitten, K., … Bravin, A. (2008). Toward high-contrast breast CT at low radiation dose. *Radiology*, *249*(1), 321–7. doi:10.1148/radiol.2491072129

Klein, O., & Nishina, Y. (1929). Über die Streuung von Strahlung durch freie Elektronen nach der neuen relativistischen Quantendynamik von Dirac. *Zeitschrift Für Physik*, *52*(11-12), 853–868.

doi:10.1007/BF01366453

Krenkel, M., Töpperwien, M., Dullin, C., Alves, F., & Salditt, T. (2016). Propagation-based phase-contrast tomography for high-resolution lung imaging with laboratory sources. *AIP Advances*, *6*(3), 035007. doi:10.1063/1.4943898

Labiche, J.-C., Mathon, O., Pascarelli, S., Newton, M. A., Ferre, G. G., Curfs, C., … Carreiras, D. F. (2007). The Fast REadout LOw Noise camera as a versatile x-ray detector for time resolved dispersive extended x-ray absorption fine structure and diffraction studies of dynamic problems in materials science, chemistry, and catalysis. *The Review of Scientific Instruments*, *78*(9), 091301. doi:10.1063/1.2783112

Langer, M., Cloetens, P., & Peyrin, F. (2010). Regularization of phase retrieval with phase-attenuation duality prior for 3-D holotomography. *IEEE Transactions on Image Processing : A Publication of the IEEE Signal Processing Society*, *19*(9), 2428–36. doi:10.1109/TIP.2010.2048608

Magaritondo, G. (1988). *Introduction to Synchrotron Radiation*. *Oxford University Press* (1st Editio.). New York, NY.

Maggiano, I. S., Maggiano, C. M., Clement, J. G., Thomas, C. D. L., Carter, Y., & Cooper, D. M. L. (2016). Three-dimensional reconstruction of Haversian systems in human cortical bone using synchrotron radiation-based micro-CT: morphology and quantification of branching and transverse connections across age. *Journal of Anatomy*. doi:10.1111/joa.12430

Majumdar, S., Issever, A. S., Burghardt, A., Lotz, J., Arfelli, F., Rigon, L., … Menk, R.-H. (2004). Diffraction enhanced imaging of articular cartilage and comparison with micro-computed tomography of the underlying bone structure. *European Radiology*, *14*(8), 1440–8. doi:10.1007/s00330-004-2355-8

Marenzana, M., Hagen, C. K., Das Neves Borges, P., Endrizzi, M., Szafraniec, M. B., Ignatyev, K., & Olivo, A. (2012). Visualization of small lesions in rat cartilage by means of laboratory-based x-ray phase contrast imaging. *Physics in Medicine and Biology*, *57*(24), 8173–84. doi:10.1088/0031-9155/57/24/8173

Mills, D. M., Helliwell, J. R., Kvick, A., Ohta, T., Robinson, I. A., & Authier, A. (2005). Report of the Working Group on Synchrotron Radiation Nomenclature - brightness, spectral brightness or brilliance? *Journal of Synchrotron Radiation*, *12*(Pt 3), 385. doi:10.1107/S090904950500796X

Mirone, A., Brun, E., Gouillart, E., Tafforeau, P., & Kieffer, J. (2014). The PyHST2 hybrid distributed code for high speed tomographic reconstruction with iterative reconstruction and a priori knowledge capabilities. *Nuclear Instruments and Methods in Physics Research Section B: Beam Interactions with Materials and Atoms*, *324*, 41–48. doi:10.1016/j.nimb.2013.09.030

Mittone, A., Gasilov, S., Brun, E., Bravin, A., & Coan, P. (2015). A single-image method for x-ray refractive index CT. *Physics in Medicine and Biology*, *60*(9), 3433–40. doi:10.1088/0031-9155/60/9/3433

Mobilio, S., Boscherini, F., & Meneghini, C. (Eds.). (2015). *Synchrotron Radiation: Basics, Methods and Applications*. Berlin, Heidelberg: Springer Berlin Heidelberg. doi:10.1007/978-3-642-55315-8

Mollenhauer, J., Aurich, M. E., Zhong, Z., Muehleman, C., Cole, A. A., Hasnah, M., … Chapman, L. D. (2002). Diffraction-enhanced X-ray imaging of articular cartilage. *Osteoarthritis and Cartilage / OARS, Osteoarthritis Research Society*, *10*(3), 163–71. doi:10.1053/joca.2001.0496

Momose, A. (2003). Phase-sensitive imaging and phase tomography using X-ray interferometers. *Optics Express*, *11*(19), 2303. doi:10.1364/OE.11.002303

Momose, A., Takeda, T., Itai, Y., & Hirano, K. (1996). Phase–contrast X–ray computed tomography for observing biological soft tissues. *Nature Medicine*, *2*(4), 473–475. doi:10.1038/nm0496-473

Müller, M., Yaroshenko, A., Velroyen, A., Bech, M., Tapfer, A., Pauwels, B., … Pfeiffer, F. (2015). Contrast-to-noise ratio optimization for a prototype phase-contrast computed tomography scanner. *The Review of Scientific Instruments*, *86*(12), 123705. doi:10.1063/1.4938163

Olivo, A., & Speller, R. (2008). Image formation principles in coded-aperture based x-ray phase contrast imaging. *Physics in Medicine and Biology*, *53*(22), 6461–6474. doi:10.1088/0031-9155/53/22/012

Peyrin, F., Cloetens, P., Salome-Pateyron, M., Baruchel, J., & Spanne, P. (1997). Reconstruction 3D en tomographie par rayonnement synchrotron coherent. *Gretsi*, 423–426.

Peyrin, F., & Engelke, K. (2012). CT imaging: Basics and new trends. In C. Grupen & I. Buvat (Eds.), *Handbook of Particle Detection and Imaging* (pp. 883–915). Berlin, Heidelberg: Springer Berlin Heidelberg. doi:10.1007/978-3-642-13271-1

Pfeiffer, F., Weitkamp, T., Bunk, O., & David, C. (2006). Phase retrieval and differential phase-contrast imaging with low-brilliance X-ray sources. *Nature Physics*, *2*(4), 258–261. doi:10.1038/nphys265

Pinzer, B. R., Cacquevel, M., Modregger, P., McDonald, S. A., Bensadoun, J. C., Thuering, T., … Stampanoni, M. (2012). Imaging brain amyloid deposition using grating-based differential phase contrast tomography. *NeuroImage*, *61*(4), 1336–46. doi:10.1016/j.neuroimage.2012.03.029

Podgorsak, E. B. (2005). Radiation Oncology Physics: A Handbook for Teachers And Students.

Potdevin, G., Malecki, A., Biernath, T., Bech, M., Jensen, T. H., Feidenhans'l, R., … Pfeiffer, F. (2012). X-ray vector radiography for bone micro-architecture diagnostics. *Physics in Medicine and Biology*, *57*(11), 3451–61. doi:10.1088/0031-9155/57/11/3451

Raven, C., Snigirev, A., Snigireva, I., Spanne, P., Souvorov, A., & Kohn, V. (1996). Phase-contrast microtomography with coherent high-energy synchrotron x rays. *Applied Physics Letters*, *69*(13), 1826. doi:10.1063/1.117446

Roentgen, W. C. (1896). On a new kind of rays. *Science (New York, N.Y.)*, *3*(59), 227–231.

Rositi, H., Frindel, C., Wiart, M., Langer, M., Olivier, C., Peyrin, F., & Rousseau, D. (2014). Computer vision tools to optimize reconstruction parameters in x-ray in-line phase tomography. *Physics in Medicine and Biology*, *59*(24), 7767–75. doi:10.1088/0031-9155/59/24/7767

Rousseau, D., Widiez, T., Di Tommaso, S., Rositi, H., Adrien, J., Maire, E., … Rogowsky, P. (2015). Fast virtual histology using X-ray in-line phase tomography: application to the 3D anatomy of maize developing seeds. *Plant Methods*, *11*(1), 55. doi:10.1186/s13007-015-0098-y

Salomé, M., Peyrin, F., Cloetens, P., Odet, C., Laval-Jeantet, A.-M., Baruchel, J., & Spanne, P. (1999). A synchrotron radiation microtomography system for the analysis of trabecular bone samples. *Medical Physics*, *26*(10), 2194. doi:10.1118/1.598736

Scherer, K., Willer, K., Gromann, L., Birnbacher, L., Braig, E., Grandl, S., … Pfeiffer, F. (2015). Toward Clinically Compatible Phase-Contrast Mammography. *Plos One*, *10*(6), e0130776. doi:10.1371/journal.pone.0130776

Snigirev, A., Snigireva, I., Kohn, V., Kuznetsov, S., & Schelokov, I. (1995). On the possibilities of x-ray phase contrast microimaging by coherent high-energy synchrotron radiation. *Review of Scientific Instruments*, *66*(12), 5486. doi:10.1063/1.1146073

Stampanoni, M., Wang, Z., & Thüring, T. (2011). The first analysis and clinical evaluation of native breast tissue using differential phase-contrast mammography. *Investigative Radiology*.

Sztrókay, A., Diemoz, P. C., Schlossbauer, T., Brun, E., Bamberg, F., Mayr, D., … Coan, P. (2012). High-resolution breast tomography at high energy: a feasibility study of phase contrast imaging on a whole breast. *Physics in Medicine and Biology*, *57*(10), 2931–42. doi:10.1088/0031-9155/57/10/2931

Sztrókay, A., Herzen, J., Auweter, S., Liebhardt, S., Mayr, D., Willner, M., … Bamberg, F. (2013). Assessment of grating-based X-ray phase-contrast CT for differentiation of invasive ductal carcinoma and ductal carcinoma in situ in an experimental ex vivo set-up. *European Radiology*.

Thüring, T., Modregger, P., Pinzer, B. R., Wang, Z., & Stampanoni, M. (2011). Non-linear regularized phase retrieval for unidirectional X-ray differential phase contrast radiography. *Optics Express*,

19(25), 25545–58. doi:10.1364/OE.19.025545

Turbell, H. (2001). *Cone-Beam Reconstruction Using Filtered Backprojection*.

Tuy, H. K. (1983). An Inversion Formula for Cone-Beam Reconstruction. *SIAM Journal on Applied Mathematics*, *43*(3), 546–552. doi:10.1137/0143035

Wang, Y. (2007). Intuitive dimensional analyses of the energy and atomic number dependences of the cross sections for radiation interaction with matter. *Journal of X-Ray Science and Technology*, *15*, 169–175.

Watson, J. D., & Crick, F. H. C. (1953). Molecular Structure of Nucleic Acids: A Structure for Deoxyribose Nucleic Acid. *Nature*, *171*(4356), 737–738. doi:10.1038/171737a0

Weitkamp, T., Diaz, A., David, C., Pfeiffer, F., Stampanoni, M., Cloetens, P., & Ziegler, E. (2005). X-ray phase imaging with a grating interferometer. *Optics Express*, *13*(16), 6296. doi:10.1364/OPEX.13.006296

Wilkins, S. W., Gureyev, T. E., Gao, D., Pogany, A., & Stevenson, A. W. (1996). Phase-contrast imaging using polychromatic hard X-rays. *Nature*, *384*(6607), 335–338. doi:10.1038/384335a0

Willner, M., Herzen, J., Grandl, S., Auweter, S., Mayr, D., Hipp, A., … Pfeiffer, F. (2014). Quantitative breast tissue characterization using grating-based x-ray phase-contrast imaging. *Physics in Medicine and Biology*, *59*(7), 1557–71. doi:10.1088/0031-9155/59/7/1557

Zanette, I. (2011, December 16). Interférométrie X à réseaux pour l’imagerie et l'analyse de front d'ondes au synchrotron. Université de Grenoble.

Chapter II: Image formation and phase retrieval in phase contrast tomography

In this chapter, we first introduce the different image formation models of propagation-based phase contrast tomography (direct problem) existing in the literature. These models describe the recorded intensity of phase contrast projections, as a function of the attenuation and the phase information, usually entangled. These phase contrast projections can be directly used as input to tomographic reconstruction algorithms, as explained in the Section 2. But more generally, the quantitative reconstruction of the refractive index of an object given measured phase contrast images requires phase and attenuation detangling. This step is called *phase retrieval* (inverse problem), and is performed for each angular projection. In Section 3, we present several phase retrieval methods existing in the literature, used in single- or multi-distance in-line phase contrast tomography. Phase retrieval is followed by tomographic reconstruction of the obtained phase projections. This can be done using Filtered Back-Projection (Chapter I), or algebraic tomographic reconstruction algorithms. The latter are presented in Section 4, because they are gaining ground when it comes to solving the tomographic inverse problem. Then, we introduce different regularisation methods, since regularisation has been extensively used to solve the inverse problem of phase retrieval, or in tomographic reconstruction. Finally, recent developments on "combined methods", *i.e.* methods that combine phase retrieval and tomographic reconstruction into a single step, are presented in Section 6.

Table of contents

1. Image formation and modelling in propagation-based imaging

In this section, we consider propagation-based phase contrast imaging. The propagation of diffracted waves in the near-field region is known as *Fresnel diffraction* (near-field diffraction). The corresponding set-up is extensively described in Chapter I. We introduce the notations that will be used in the manuscript. We consider a parallel beam configuration, propagating in the z-direction. The projection plane (x, y) can also be referred by $\boldsymbol{x} = (x, y)$. The sample can be rotating by an angle θ around the *y*-axis, in a 2π-angular range. The distance between the sample and the detector is *D*.

1.a. Fresnel diffraction

In propagation-based imaging (PBI), the contrast is due to free space propagation in the near-field regime of a highly spatially coherent beam, after passing through the object. It creates interference patterns (*Fresnel fringes*), recorded by the detector. The phase information is encoded in these fringes (J.-P. Guigay, 1977).

At each angle θ, the interaction between the object and the X-ray wave can be described as a transmittance function T_θ, involving the projections of the attenuation and the phase shift at the angle θ, respectively B_θ and φ_θ:

$$T_\theta(\boldsymbol{x}) = \exp\big(-B_\theta(\boldsymbol{x}) + i\varphi_\theta(\boldsymbol{x})\big), \tag{2.1.1}$$

where $B_\theta(\boldsymbol{x})$ and $\varphi_\theta(\boldsymbol{x})$ are projections of the absorption index and refractive index decrement, respectively, perpendicular to the propagation direction of the beam:

$$B_\theta(\boldsymbol{x}) = \frac{2\pi}{\lambda}\int \beta(\boldsymbol{x}, z)\, dz \tag{2.1.2}$$

$$\varphi_\theta(\boldsymbol{x}) = -\frac{2\pi}{\lambda}\int \delta_n(\boldsymbol{x}, z)\, dz \tag{2.1.3}$$

Thus, if $u_{inc}(\boldsymbol{x})$ denotes the incident wave front, and $u_{0,\theta}(\boldsymbol{x})$ the wave front right after the sample (*i.e.* at contact plane), we obtain:

$$u_{0,\theta}(\boldsymbol{x}) = T_\theta(\boldsymbol{x}) u_{inc}(\boldsymbol{x}). \tag{2.1.4}$$

The corresponding intensity recorded by the detector, without any propagation, is:

$$I_{0,\theta}(\boldsymbol{x}) = \left|u_{0,\theta}(\boldsymbol{x})\right|^2 \tag{2.1.5}$$

$$I_{0,\theta}(\boldsymbol{x}) = \left|T_\theta(\boldsymbol{x}) u_{inc}(\boldsymbol{x})\right|^2 \tag{2.1.6}$$

By substituting Equation (2.1.1) in Equation (2.1.6), we obtain:

$$I_{0,\theta}(\boldsymbol{x}) = \left|e^{-B_\theta(x)} e^{i\,\varphi_\theta(x)} u_{inc}(\boldsymbol{x})\right|^2 = \left|e^{-B_\theta(x)}\right|^2 \left|e^{i\,\varphi_\theta(x)}\right|^2 |u_{inc}(\boldsymbol{x})|^2. \tag{2.1.7}$$

The second term of the product can be dropped, because $\varphi_\theta(\boldsymbol{x})$ is real. This leads to:

$$I_{0,\theta}(\boldsymbol{x}) = e^{-2.B_\theta(\boldsymbol{x})}|u_{inc}(\boldsymbol{x})|^2 = e^{-2B_\theta(\boldsymbol{x})}I_{inc}(\boldsymbol{x}), \tag{2.1.8}$$

which corresponds to the standard Beer-Lambert law used in attenuation CT.

In the case of propagation, the free space propagation over a distance *D* can be modelled by the Fresnel transform involving the propagator P_D (Goodman, 2005):

$$P_D(\boldsymbol{x}) = \frac{1}{i\lambda D}\exp\left(i\frac{\pi}{\lambda D}|\boldsymbol{x}|^2\right), \tag{2.1.9}$$

or equivalently by its Fourier transform $\tilde{P}_D$:

$$\tilde{P}_D(\boldsymbol{f}) = \exp(-i\pi\lambda D|\boldsymbol{f}|^2), \tag{2.1.10}$$

where $\boldsymbol{f} = (f, g)$ are the frequency variables corresponding to (x, y) (*i.e.* the coordinates in the Fourier space).

The Fresnel transform can be written as the convolution of the exit wave front $u_{0,\theta}(\boldsymbol{x})$ with the propagator $P_D(\boldsymbol{x})$. If $u_D(\boldsymbol{x})$ denotes the wave front at a distance *D* from the sample, we obtain:

$$u_D(\boldsymbol{x}) = P_D(\boldsymbol{x}) * u_0(\boldsymbol{x}). \tag{2.1.11}$$

Usually, in computer implementations, the propagator is applied in the Fourier domain, since there it becomes a multiplication instead of a convolution in the spatial domain. The equivalent of Equation (2.1.11) in the Fourier domain is:

$$\tilde{u}_D(\boldsymbol{f}) = \tilde{P}_D(\boldsymbol{f})\tilde{u}_0(\boldsymbol{f}). \tag{2.1.12}$$

Since u_D usually stays in the real domain, and the propagator is applied in the Fourier domain, we get:

$$u_D(\boldsymbol{x}) = \mathcal{F}^{-1}(\tilde{P}_D\mathcal{F}[u_0])(\boldsymbol{x}) \tag{2.1.13}$$

where $\mathcal{F}$and $\mathcal{F}^{-1}$ respectively denote the Fourier transform and the inverse Fourier transform.

The operator $\mathcal{F}r_{\mathrm{D}}$, also known as the Fresnel transform at a propagation distance *D*, can then be expressed as:

$$\mathcal{F}r_D = \mathcal{F}^{-1}\tilde{P}_D\mathcal{F}. \tag{2.1.14}$$

If we assume a unitary wave front, which means that $u_{inc}(\boldsymbol{x}) = 1$, the interaction between the incident wave front and the sample, followed by free space propagation over a distance *D* can thus be modelled as:

$$u_{\theta,D}(\boldsymbol{x}) = T_{\theta,D}(\boldsymbol{x}) = (T_\theta * P_D)(\boldsymbol{x}). \tag{2.1.15}$$

The intensity recorded by the detector at a distance *D* is:

$$I_{\theta,D}(\boldsymbol{x}) = |u_{\theta,D}(\boldsymbol{x})|^2. \tag{2.1.16}$$

Its equivalent in the Fourier domain can be expressed as (J.-P. Guigay, 1977):

$$\widetilde{I_D}(\boldsymbol{f}) = \int T\left(\boldsymbol{x} - \frac{\lambda D\boldsymbol{f}}{2}\right) T^*\left(\boldsymbol{x} + \frac{\lambda D\boldsymbol{f}}{2}\right) \exp(-i2\pi\boldsymbol{x}.\boldsymbol{f})\, d\boldsymbol{x}, \tag{2.1.17}$$

which is useful as a starting point for contrast linearisation. Thus, intensities recorded by the detector are quantitatively, but non-linearly, related to the phase shift of the wave induced by the object.

1.b.TIE Model and WTIE

The Transport of Intensity Equation (TIE) (Teague, 1982) not only describes, for a monochromatic beam propagating along an axis *z*, the intensity recorded in the projection plane $\boldsymbol{x}$, $I_D(\boldsymbol{x})$, but also it phase φ:

$$\nabla_{\boldsymbol{x}}[I_0(\boldsymbol{x})\nabla_{\boldsymbol{x}}\varphi(\boldsymbol{x})] = -\frac{2\pi}{\lambda}\frac{\partial I_0(\boldsymbol{x})}{\partial z}. \tag{2.1.18}$$

$\nabla_{\boldsymbol{x}}$ denotes the gradient operator (first derivative) in the plane (x, y), namely:

$$\nabla_{\boldsymbol{x}} s = \left(\frac{\partial s}{\partial x}; \frac{\partial s}{\partial y}\right) \tag{2.1.19}$$

and $\nabla_{\boldsymbol{x}} \cdot$ is the divergence operator:

$$\nabla_{\boldsymbol{x}} \cdot \boldsymbol{s} = \frac{\partial s_x}{\partial x} + \frac{\partial s_y}{\partial y}. \tag{2.1.20}$$

This model is valid for non-interferometric measurements (such as PBI), large Fresnel number (equivalent to small propagation distances), and paraxial approximation (parallel beam). By Taylor expanding the transmittance function in Equation (2.1.17), which is possible because of small propagation distances, we get:

$$T\left(\boldsymbol{x} + \frac{\lambda D\boldsymbol{f}}{2}\right) \approx T(\boldsymbol{x}) + \frac{1}{2}\lambda D\boldsymbol{f}\nabla_{\boldsymbol{x}}T(\boldsymbol{x}). \tag{2.1.21}$$

This leads to

$$I_D(\boldsymbol{x}) = I_0(\boldsymbol{x}) - \frac{\lambda D}{2\pi}\nabla_{\boldsymbol{x}}\big(I_0(\boldsymbol{x})\nabla_{\boldsymbol{x}}\varphi(\boldsymbol{x})\big). \tag{2.1.22}$$

The quantity $(I_D(\boldsymbol{x}) - I_0(\boldsymbol{x}))/D$ can be approximated by the partial derivative of I_D in the propagation direction (the *z*-axis), yielding:

$$-\frac{2\pi}{\lambda}\frac{\partial I_0(\boldsymbol{x})}{\partial z} = \nabla_{\boldsymbol{x}}\big(I_0(\boldsymbol{x})\nabla_{\boldsymbol{x}}\varphi(\boldsymbol{x})\big). \tag{2.1.23}$$

A symbolic solution of this TIE was proposed by Paganin (D. M. Paganin, 2006):

$$\varphi(\boldsymbol{x}) = -\frac{2\pi}{\lambda}\nabla_{\boldsymbol{x}}{}^{-2}\left(\nabla_{\boldsymbol{x}}\left\{\frac{1}{I_0(\boldsymbol{x})}\nabla_{\boldsymbol{x}}\left(\nabla_{\boldsymbol{x}}{}^{-2}\frac{\partial I_0(\boldsymbol{x})}{\partial z}\right)\right\}\right), \tag{2.1.24}$$

where $\nabla_{\boldsymbol{x}}{}^{-2}$denotes the inverse Laplacian.

The Weak absorption Transport of Intensity Equation (WTIE) has been derived from the TIE (Equation (2.1.22)) by Bronnikov (Andrei V. Bronnikov, 2002), under weak absorption conditions (*i.e.* if $I_0(\boldsymbol{x})$ varies relatively little with respect to the projection plane (x, y), it can be taken out of the gradient operator). The intensity is then expressed as:

$$I_D(\boldsymbol{x}) = I_0(\boldsymbol{x})\left[1 - \frac{\lambda D}{2\pi}\nabla_x^2\varphi(\boldsymbol{x})\right]. \tag{2.1.25}$$

A solution of the WTIE can be expressed using the inverse Laplacian (D. M. Paganin, 2006):

$$\varphi(\boldsymbol{x}) = -\frac{2\pi}{\lambda D}\nabla_x^{-2}\left(\frac{I_D(\boldsymbol{x})}{I_0(\boldsymbol{x})} - 1\right). \tag{2.1.26}$$

1.c. CTF model

The Contrast Transfer Function (CTF) is a model valid for slowly varying phase (SVP) and weakly attenuating object (Born-type approximation). These assumptions are summarized as follows:

$$\begin{cases} B(\boldsymbol{x}) \ll 1 \\ |\varphi(\boldsymbol{x}) - \varphi(\boldsymbol{x} - \lambda D\boldsymbol{f})| \ll 1 \end{cases} \tag{2.1.27}$$

To achieve the CTF expression, the transmittance function (Equation (2.1.1)) is linearized to the 1st order, using classic Taylor's development:

$$T(\boldsymbol{x}) \approx 1 - B(\boldsymbol{x}) + i\varphi(\boldsymbol{x}) \tag{2.1.28}$$

By substituting this equation in the Equation (2.1.17), and given the shift property of the Fourier transform and Euler's formula, the CTF expression is obtained (Cloetens et al., 1999):

$$\tilde{I}_D(\boldsymbol{f}) = \delta_{Dirac}(\boldsymbol{f}) - 2\cos(\pi\lambda D|\boldsymbol{f}|^2)\,\tilde{B}(\boldsymbol{f}) + 2\sin(\pi\lambda D|\boldsymbol{f}|^2)\tilde{\varphi}(\boldsymbol{f}), \tag{2.1.29}$$

where ~ denotes the Fourier transform, and δ_{Dirac} is the Dirac distribution.

1.d. Mixed model

This model was developed in the early 2000's by Guigay *et al.* (J. P. Guigay, Langer, Boistel, & Cloetens, 2007). It is valid for slowly varying phase and weakly or strongly absorbing object. This model originally aimed at finding a formulation, valid for all objects (even strongly attenuating), that made both the CTF and the TIE coincide at small propagation distances. Using this model, the Fourier transform of the intensity is expressed as:

$$\begin{aligned} \tilde{I}_D(\boldsymbol{f}) \approx \tilde{I}_D^{\varphi=0}(\boldsymbol{f}) &+ 2\sin(\pi\lambda D|\boldsymbol{f}|^2)\,.\mathcal{F}\{I_0\varphi\}(\boldsymbol{f}) \\ &+ \cos(\pi\lambda D|\boldsymbol{f}|^2)\frac{\lambda D}{2\pi}\mathcal{F}\{\nabla_{\boldsymbol{x}}\cdot(\varphi\nabla_{\boldsymbol{x}}I_0)\}(\boldsymbol{f}) \end{aligned} \tag{2.1.29}$$

where $\tilde{I}_D^{\varphi=0}$ is the Fourier transform of the intensity at a propagation distance *D*, assuming there is no phase shift.

It is noticeable that in this expression, the phase shift φ is coupled to the attenuation intensity I_0. A new variable ψ is thus introduced as the product of the attenuation image I_0 with the phase shift φ:

$$\psi(\boldsymbol{x}) = I_0(\boldsymbol{x}).\varphi(\boldsymbol{x}) \tag{2.1.30}$$

Moreover, we have:

$$\varphi\nabla_{\boldsymbol{x}} I_0 = I_0\varphi\nabla_{\boldsymbol{x}}\ln(I_0) = \psi\nabla_{\boldsymbol{x}}\ln(I_0). \tag{2.1.31}$$

The expression of the diffraction pattern becomes:

$$\begin{aligned}\tilde{I}_D(\boldsymbol{f}) = \tilde{I}_D^{\varphi=0}(\boldsymbol{f}) + 2\sin(\pi\lambda D|\boldsymbol{f}|^2).\tilde{\psi}(\boldsymbol{f}) \\ + \cos(\pi\lambda D|\boldsymbol{f}|^2)\frac{\lambda D}{2\pi}\mathcal{F}\{\nabla_{\boldsymbol{x}}\cdot(\psi\nabla_{\boldsymbol{x}}\ln(I_0))\}(\boldsymbol{f})\end{aligned} \tag{2.1.32}$$

For clarity, the following variables are introduced:

$$A_D(\boldsymbol{f}) = 2\sin(\pi\lambda D|\boldsymbol{f}|^2) \tag{2.1.32}$$

and

$$\Delta_D(\boldsymbol{f}) = \cos(\pi\lambda D|\boldsymbol{f}|^2)\frac{\lambda D}{2\pi}\mathcal{F}\{\nabla_{\boldsymbol{x}}\cdot(\psi\nabla_{\boldsymbol{x}}\ln(I_0))\}(\boldsymbol{f}) \tag{2.1.33}$$

The Mixed model expression becomes:

$$\tilde{I}_D(\boldsymbol{f}) = \tilde{I}_D^{\varphi=0}(\boldsymbol{f}) + A_D(\boldsymbol{f})\tilde{\psi}(\boldsymbol{f}) + \Delta_D(\boldsymbol{f}) \tag{2.1.34}$$

This new expression can be seen as a linear problem, with a perturbation term due to the partial differential equation. Intuitively, $\tilde{\psi}(\boldsymbol{f})$ can be retrieved from $\tilde{I}_D(\boldsymbol{f})$, and thus the phase shift φ. This phase retrieval step is further developed in the Section 3.a.

2. Phase contrast tomography

In this section, we briefly recall phase contrast tomography, which consists in using the projections directly as input of tomographic reconstruction, without any phase retrieval step. In the considered system, an object can be described by its complex refractive index *n*:

$$n(\boldsymbol{x}, z) = 1 - \delta_n(\boldsymbol{x}, z) + i\beta(\boldsymbol{x}, z). \tag{2.2.1}$$

The real part of n, $(1-\delta_n)$, is related to the phase shift induced by the object, and the imaginary part of n, β, is related to the attenuation. Further details on the refractive index decrement δ_n and the absorption index β have been given in the Chapter I.

The absorption index β is related to the linear attenuation coefficient μ by the following relationship (Raven et al., 1996):

$$\mu(\boldsymbol{x}, z) = \frac{4\pi}{\lambda}\beta(\boldsymbol{x}, z) \tag{2.2.2}$$

Attenuation B and phase shift φ induced by the object can be described as projections perpendicular to the propagation direction of the beam:

$$B(\boldsymbol{x}) = \frac{2\pi}{\lambda}\int \beta(\boldsymbol{x}, z)\, dz \tag{2.2.3}$$

$$\varphi(\boldsymbol{x}) = -\frac{2\pi}{\lambda}\int \delta_n(\boldsymbol{x}, z)\, dz. \tag{2.2.4}$$

When the attenuation projections are used as input of tomographic reconstruction, one gets a 3D-map of the linear attenuation coefficient. If the tomographic reconstruction algorithm is applied to the phase contrast images, without any phase retrieval, one obtains a 3D volume that encodes attenuation and phase information. We detail below how this resulting volume can be interpreted under some assumptions.

We first assume that the weak defocusing conditions are respected (near-field diffraction):

$$\lambda D|\boldsymbol{f}|^2 \ll 1 \tag{2.2.5}$$

In this case, the Fresnel propagator in Fourier space can be linearized (Cowley, 1995), and the intensity is thus expressed as:

$$\begin{aligned} I_D(\boldsymbol{x}) = I_0(\boldsymbol{x})\left[1 - \frac{\lambda D}{2\pi}\nabla_{\boldsymbol{x}}^2\varphi(\boldsymbol{x})\right] \\ -\frac{\lambda D}{\pi}\exp\big(-B(\boldsymbol{x})\big).\nabla_{\boldsymbol{x}}(\exp -B(\boldsymbol{x}))\,.\nabla_{\boldsymbol{x}}\varphi(\boldsymbol{x}) \end{aligned} \tag{2.2.6}$$

where $\nabla_{\boldsymbol{x}}$ denotes the gradient operator in the projection plane and $\nabla_{\boldsymbol{x}}^2$ is the Laplacian operator:

$$\nabla_{\boldsymbol{x}}^2 s = \frac{\partial^2 s}{\partial x^2} + \frac{\partial^2 s}{\partial y^2}. \tag{2.2.7}$$

Assuming that the attenuation varies slowly with respect to the phase, the last term can be neglected, which leads to (AV Bronnikov, 1999):

$$I_D(\boldsymbol{x}) = I_0(\boldsymbol{x})\left[1 - \frac{\lambda D}{2\pi}\nabla_{\boldsymbol{x}}^2\varphi(\boldsymbol{x})\right]. \tag{2.2.8}$$

Considering that the last term $\frac{\lambda D}{2\pi}\nabla_{\boldsymbol{x}}^2\varphi(\boldsymbol{x})$ is much lower than 1, we get:

$$I_D(\boldsymbol{x}) = I_0(\boldsymbol{x})\exp\left(-\frac{\lambda D}{2\pi}\nabla_{\boldsymbol{x}}^2\varphi(\boldsymbol{x})\right). \tag{2.2.9}$$

As mentioned in Chapter I, the intensity recorded at contact plane is:

$$I_0(\boldsymbol{x}) = \exp\left(-2.B(\boldsymbol{x})\right). \quad (2.2.10)$$

By combining Equations (2.2.9) and (2.2.10), replacing B and φ by their expressions (Equations (2.2.3) and (2.2.4)), and defining a projection as the natural logarithm of the recorded intensity, we obtain:

$$-\ln\left(I_D(x,y)\right) = \frac{4\pi}{\lambda}\int \beta(x,y,z)\,dz - D\left(\frac{\partial^2}{\partial x^2}+\frac{\partial^2}{\partial y^2}\right)\int \delta_n(x,y,z)\,dz \quad (2.2.11)$$

The integral over z in Equation (2.2.11) corresponds to the Radon transform (defined in Chapter I). Consequently, the quantities can be retrieved by a tomographic reconstruction method, such as the filtered back-projection (FBP), which yields:

$$g(x,y,z) = \mu(x,y,z) - D\left(\frac{\partial^2}{\partial x^2}+\frac{\partial^2}{\partial y^2}+\frac{\partial^2}{\partial z^2}\right)\delta_n(x,y,z). \quad (2.2.12)$$

The first term of the 3D reconstructed object correspond to the linear attenuation coefficient, in 3D. This is related to the attenuation induced by the object. The second term is related to the second derivative of the refractive index decrement. It reflects the variations of the sharp changes in the refractive index. It is noticeable that when no propagation ($D = 0$) only the attenuation contributes to the image (Cloetens et al., 1997; Peyrin, Cloetens, Salome-Pateyron, Baruchel, & Spanne, 1997).

3. Phase retrieval

The intensity recorded by the detector is equal to the squared modulus of this wavefield, and entangles phase and attenuation information. Retrieving the phase information from recorded data is thus a non-linear inverse problem. Over the last three decades, many phase retrieval methods have been developed for all the phase contrast modalities. Here, we focus on PBI-related phase retrieval, involving one (single-distance acquisition) or several (holotomography) propagation distances.

3.a. Single distance acquisition

Single distance X-ray PCI acquisition consists in acquiring only one tomographic dataset recorded at a single propagation distance *D*. It is convenient since it is as fast as standard attenuation CT acquisition and, the data pre-processing is easier than the one in multi-distance acquisitions. The article of Burvall *et al.* (2011) gives a large overview and comparison of existing phase retrieval methods for single-distance in-line phase contrast tomography (Burvall, Lundström, Takman, Larsson, & Hertz, 2011).

3.a.i. Bronnikov method

The methods developed by Bronnikov (Andrei V. Bronnikov, 2002; AV Bronnikov, 1999) were avant-garde of the methods that combine phase retrieval and tomographic reconstruction. They are valid for near-field diffraction (Fresnel diffraction), weak defocusing conditions (Equation (2.2.5)) and slowly varying attenuation. In other words, the absorption is weak and homogeneous.

The intensity can be written as:

$$I_{D,\theta}(\boldsymbol{x}) = I_{0,\theta}(\boldsymbol{x})\left[1 - \frac{\lambda D}{2\pi}\nabla_{\boldsymbol{x}}^2\varphi_\theta(\boldsymbol{x})\right]. \tag{2.3.1}$$

By introducing the variable g_θ, defined as:

$$g_\theta(\boldsymbol{x}) = \frac{I_{D,\theta}(\boldsymbol{x})}{I_{0,\theta}(\boldsymbol{x})} - 1, \tag{2.3.2}$$

the author rewrote the Equation (2.3.1) as:

$$\nabla_{\boldsymbol{x}}^2\varphi_\theta(\boldsymbol{x}) = -\frac{2\pi}{\lambda D}g_\theta(\boldsymbol{x}). \tag{2.3.3}$$

If $\mathcal{R}$ denotes the Radon transform and s the variable equal to $x.\sin(w) + y.\cos(w)$, we get:

$$\frac{\partial^2}{\partial s^2}\mathcal{R}\delta_n(s,\theta,w) = -\frac{1}{d}\mathcal{R}g_\theta(s,w). \tag{2.3.4}$$

This method uses the FBP algorithm with a modified ramp filter, multiplied by a filter related to the phase retrieval step. It is derived from the WTIE and from the relationship between the 3D Radon transform of the object and the 2D Radon transform of the phase projections (Equation (2.3.4)). It enables to retrieve the 3D refractive index of the object into one step, by a 2D low-pass filtering:

$$\delta_n(\boldsymbol{x}, z) = \frac{1}{4\pi^2 d}\int_0^\pi q * g_\theta \, d\theta, \tag{2.3.5}$$

where * denotes the 2D-convolution and q is a low pass filter:

$$q(x,y) = \frac{|y|}{x^2 + y^2}. \tag{2.3.6}$$

For a pure phase object, Bronnikov showed that a single plane acquisition is sufficient, whereas two-plane acquisition is needed if the object induces both amplitude and phase shifts.

3.a.ii. Modified Bronnikov method

A few years later, a so-called "Modified Bronnikov Approach" (MBA) emerged from Groso *et al.* (Groso, Abela, & Stampanoni, 2006). Whereas weakly and homogeneously absorbing objects need intensities at two acquisition planes in the Bronnikov method, MBA gets rid of the residual absorption, providing it is almost constant. The residual absorption is taken into account by adding an absorption term in the low-pass filtering:

$$q(x,y) = \frac{|y|}{x^2 + y^2 + \alpha_{abs}} \tag{2.3.7}$$

The absorption correction factor α_{abs} is determined semi-empirically (*i.e.* using simulation and experiment). First, projections of non-absorbing to weakly absorbing and known objects are simulated.

Phase retrieval from a single intensity is imperfect, due to the residual absorption. A correction term is determined, because the object is perfectly known. This yields a calibration curve that expresses the correction to be applied as a function of the attenuation induced by the object. The final correction parameter to apply for the imaged object is determined from both this calibration curve and a ratio between simulated and experimental intensities. Note that this method also combines the tomographic reconstruction with the phase retrieval step.

3.a.iii. Phase attenuation-duality

The so-called Phase-Attenuation Duality (PAD) method was proposed by Wu and Liu in 2005 (Wu, Liu, & Yan, 2005). It makes possible to retrieve the phase and the absorption from a single-image. It is valid for inhomogeneous soft tissues imaged at energies between 60 and 500keV (*i.e.* energy range where the Compton effect is predominant). Unlike in the previously described methods, this method does not take into account the tomographic step.

Briefly, the PAD method expresses the attenuation and the phase as a function of the electron density of the material, given the Compton cross-section determined using the Klein-Nishina formula (Klein & Nishina, 1929). The electron density is then expressed as a function of the recorded intensity using the Fresnel-Kirschoff diffraction theory. Therefore, under the cited conditions of material and energy, the attenuation and the phase can be derived from the recorded intensity.

Recently, a generalized PAD method (valid for long propagation distances) has been applied to fish heads imaging in phase contrast micro-tomography (Liu, Wu, & Xiao, 2015).

3.a.iv. Homogeneous Paganin's method

In the early 2000's, Paganin *et al.* proposed a method valid for single-distance acquisition in the near-field approximation, under the assumption of an homogeneous object (D. Paganin, Mayo, Gureyev, Miller, & Wilkins, 2002). For the considered material, the ratio between the real and complex part of the refractive index, δ_n/β, is supposedly known. Note that δ_n/β also depends on the energy of the beam, which should thus preferentially be well-calibrated and monochromatic.

This method relies on the TIE model and explicitly uses the relationship between phase and absorption with the ratio δ_n/β yielding the following inversion formula:

$$\varphi(\boldsymbol{x}) = \frac{\delta_n}{2\beta}\ln\left(\mathcal{F}^{-1}\left\{\frac{\mathcal{F}\left(\frac{I_D(\boldsymbol{x})}{I_0(\boldsymbol{x})}\right)}{1+\lambda D\pi\frac{\delta_n}{\beta}\left|\left|\boldsymbol{f}\right|\right|^2}\right\}\right). \tag{2.3.7}$$

This phase retrieval method is largely employed at the ESRF, because of its simple implementation. The theoretical values of the physical parameters of the material (δ_n and β) are calculated using the X-ray Optics software XOP (del Río & Dejus, 2004), given its composition. The ratio δ_n/β can also be optimized by visual observation or using other computer vision tools (Rositi et al., 2014).

3.a.v. Two-material object

In the vein of Paganin's method, Beltran *et al.* proposed a phase retrieval method valid for single-distance acquisition of a "spatially-quantized object", in the near-field approximation (Beltran, Paganin, Uesugi, & Kitchen, 2010).

The imaged object is supposed to be composed of two homogeneous materials, where a first material embeds a second material. The total attenuation and phase is described by the Beer-Lambert's law. Absorption index and refractive index decrement of each material should be known, as previously. Under the hypothesis that the thickness of the embedding material varies slowly, and that the total projected thickness is known, the thickness of the embedded material is retrieved, and thus the corresponding phase is untangled from the measured intensity.

3.b. Multi-distance acquisition with parallel-beam

In this subsection, we consider phase retrieval using an acquisition performed with the parallel beam holotomography (multi-distances acquisition) set-up, as described in Chapter I. We show here how the phase is retrieved using this model, adding possibly prior knowledge on the object. The various methods of creating a prior of the reconstructed phase, depending on composition assumption on the object (homogeneous, multi-material, and heterogeneous) is detailed.

3.b.i. General mixed approach

A commonly used phase retrieval method when it comes to multi-distances acquisition is the mixed approach. The global idea of this phase retrieval algorithm is to see the inverse problem as a minimization problem, considering the Mixed approach developed by Guigay *et al.* (J. P. Guigay et al., 2007) as the contrast model.

Recall the simplified expression of the diffraction pattern, using the mixed model:

$$\tilde{I}_D(\boldsymbol{f}) = \tilde{I}_D^{\varphi=0}(\boldsymbol{f}) + A_D(\boldsymbol{f})\tilde{\psi}(\boldsymbol{f}) + \Delta_D(\boldsymbol{f}), \tag{2.3.8}$$

with

$$A_D(\boldsymbol{f}) = 2\sin(\pi\lambda D|\boldsymbol{f}|^2) \tag{2.3.9}$$

and

$$\Delta_D(\boldsymbol{f}) = \cos(\pi\lambda D|\boldsymbol{f}|^2)\frac{\lambda D}{2\pi}\mathcal{F}\{\nabla_{\boldsymbol{x}} \cdot [\psi(\boldsymbol{x}).\nabla_{\boldsymbol{x}}\ln(I_0(\boldsymbol{x}))]\}(\boldsymbol{f}). \tag{2.3.10}$$

Retrieving ψ from several measurements I_D can be done using a least-square minimization approach:

$$\tilde{\psi}(\boldsymbol{f}) = \min_{\tilde{\psi}} \sum_D \left|A_D(\boldsymbol{f})\tilde{\psi}(\boldsymbol{f}) - [\tilde{I}_D(\boldsymbol{f}) - \tilde{I}_D^{\varphi=0}(\boldsymbol{f}) - \Delta_D(\boldsymbol{f})]\right|^2 \tag{2.3.11}$$

A first estimate of the phase is either set to zero, $\varphi^{(0)}(x,y) = 0$, leading to $\psi^{(0)}(x,y) = 0$ or determined using a least-square approach , given that the term Δ_D is neglected:

$$\psi^{(0)}(\boldsymbol{x}) = \mathcal{F}^{-1}\left\{\frac{\sum_D A_D(\boldsymbol{f}).\left[\tilde{I}_D(\boldsymbol{f}) - \tilde{I}_D^{\varphi=0}(\boldsymbol{f})\right]}{\sum_D A_D(\boldsymbol{f})^2}\right\}. \quad (2.3.12)$$

In practice, $\tilde{\psi}(\boldsymbol{f})$ is solved iteratively:

$$\tilde{\psi}^{(i+1)}(\boldsymbol{f}) = \frac{\sum_D A_D(\boldsymbol{f})[\tilde{I}_D(\boldsymbol{f}) - \tilde{I}_D^{\varphi=0}(\boldsymbol{f}) - {\Delta_D}^{(i)}(\boldsymbol{f})]}{\sum_D A_D(\boldsymbol{f})^2} \quad (2.3.13)$$

The term ${\Delta_D}^{(i)}(\boldsymbol{f})$ is updated iteratively following:

$${\Delta_D}^{(n)}(\boldsymbol{f}) = \cos(\pi\lambda D|\boldsymbol{f}|^2)\frac{\lambda D}{2\pi}\mathcal{F}\{\nabla_x \cdot [\psi^{(i)}(\boldsymbol{x}).\nabla_x \ln(I_0(\boldsymbol{x}))]\}(\boldsymbol{f}) \quad (2.3.14)$$

3.b.ii. Regularised mixed approach for homogeneous object

In the paper (Langer, Cloetens, & Peyrin, 2010), the authors proposed the resolution of the phase retrieval inverse problem, by introducing a regularisation term in the mixed approach, since A_D is close to zero in the low-frequency range:

$$\begin{aligned}&\tilde{\psi}(\boldsymbol{f})\\ &= \arg\min_{\tilde{\psi}} \sum_D \left|A_D(\boldsymbol{f})\tilde{\psi}(\boldsymbol{f}) - [\tilde{I}_D(\boldsymbol{f}) - \tilde{I}_D^{\varphi=0}(\boldsymbol{f}) - \Delta_D(\boldsymbol{f})]\right|^2 + \alpha\left|\tilde{\psi}(\boldsymbol{f})\right.\\ &\left. - \tilde{\psi}_0(\boldsymbol{f})\right|^2\end{aligned} \quad (2.3.15)$$

The phase can then be retrieved iteratively (3 to 5 iterations are required for convergence), taking into account the a priori $\tilde{\psi}_0$:

$$\psi^{(i+1)}(\boldsymbol{x}) = \mathcal{F}^{-1}\left\{\frac{\sum_D A_D(\boldsymbol{f}).\left[\tilde{I}_D(\boldsymbol{f}) - \tilde{I}_D^{\varphi=0}(\boldsymbol{f}) - {\Delta_D}^{(i)}(\boldsymbol{f}) + \alpha\tilde{\psi}_0(\boldsymbol{f})\right]}{\sum_D A_D(\boldsymbol{f})^2 + \alpha}\right\} \quad (2.3.16)$$

and the term ${\Delta_D}^{(i)}(\boldsymbol{f})$ is updated according to Equation (2.3.14).

The parameter α is a regularisation parameter that can be determined using a L-curve criterion (Hansen & O'Leary, 1993; Hansen, 1999), as explained in detail in (Langer et al., 2010). The residual error of the fidelity term, $\sum_D\left|A_D(\boldsymbol{f})\tilde{\psi}_\alpha(\boldsymbol{f}) - [\tilde{I}_D(\boldsymbol{f}) - \tilde{I}_D^{\varphi=0}(\boldsymbol{f}) - \Delta_D(\boldsymbol{f})]\right|$, is plotted as a function of the regularisation term $\left|\tilde{\psi}_\alpha(\boldsymbol{f}) - \tilde{\psi}_0(\boldsymbol{f})\right|$, to get the so-called "L-curve". The corner of the L-curve corresponds to the optimal value of α that minimizes the data fidelity error, and the regularization error.

For homogeneous object, the a priori of the phase is designed by converting the attenuation projections I_0 into phase projections given the ratio δ_n/β:

$$\tilde{\psi}_0(\boldsymbol{f}) = \ell(\boldsymbol{f}).\mathcal{F}\left\{\frac{\delta_n}{2\beta} I_0 \ln(I_0)\right\}(\boldsymbol{f}), \quad (2.3.17)$$

where ℓ is a low-pass filter.

The major drawback of this method is that it requires an attenuation scan, which is not trivial for all samples and set-ups, from an experimental point of view, because it implies to put the camera very close to the sample, while letting it rotate.

This mixed phase retrieval method was successfully applied to *Crossdactylodes bookermani* frog, a sample that contains biological tissues and bones (weakly and strongly absorbing respectively). Fine structures in the soft tissue were visible, although it was surrounding strongly absorbing bone. Nevertheless, the presence of artefacts around bone showed the need to go beyond homogeneous objects.

3.b.iii. Regularised mixed approach for multi-material objects

To fit with larger classes of objects, it is possible to assume a multi-material object composition. The main change lies in the design of the prior ψ_0. The different materials should be identified, and the projected length of each material should be known. This requires a passage to the object domain, before projections creation. The attenuation volume is thus reconstructed, in order to get the 3D distribution of the absorption index $\beta(x, y, z)$, prior to conversion into a phase volume using two or several δ_n/β ratios (corresponding to the different materials). Once the phase a priori volume $\delta_{n,0}$ is created, the priors phase projections $\varphi_0(\boldsymbol{x})$ are obtained by a simple Radon transform, multiplied by $-2\pi/\lambda$ (Equation (2.2.4)). The phase is finally retrieved as described in Equation (2.3.16).

For bi-material object, the attenuation volume is thresholded, so that we obtain an approximation of a bi-material volume (Langer, Cloetens, Pacureanu, & Peyrin, 2012). Finally, the absorption volume is turned into a phase volume by applying a certain δ_n/β value to each segmented part. Mathematically, the a priori of the refractive index decrement distribution δ_0 can be expressed as follows:

$$\delta_{n,0}(\boldsymbol{x}, z) = m(\boldsymbol{x}, z).\beta(\boldsymbol{x}, z), \tag{2.3.18}$$

such that

$$m(\boldsymbol{x}, z) = \begin{cases} \delta_{n,a}/\beta_a\,, & \beta(\boldsymbol{x}, z) < t \\ \delta_{n,b}/\beta_b\,, & \beta(\boldsymbol{x}, z) \geq t \end{cases} \tag{2.3.19}$$

where t denotes the threshold, usually chosen using Otsu's method (Otsu, 1979).

Most interesting samples, for example in biology, are heterogeneous, meaning that δ_n and β vary continuously in the sample. To convert the attenuation volume into a phase volume, a functional relationship between the δ_n/β ratio and the attenuation coefficient μ is determined given the caracteristics of the material. In a recent paper, the authors focused on bone, where it was shown that the relationship between μ and δ_n/β follows a power-law trend (Langer et al., 2014).

3.c. Summary

The Table 1 sums up the various phase retrieval algorithms, specifying some relevant parameters for each. The reference of the corresponding article is cited in the first column, followed by the direct model it employs, in the second column. The models are those presented in Section 1: the Transport of

Intensity (*TIE*), the weak Transport of Intensity Equation (*WTIE*), the Contrast Transfer Function (*CTF*) and the mixed approach (*Mixed*). In the third column, the assumption(s) on the object are mentioned. Assumptions can be related to the attenuation of the object: non-attenuating (*pure phase*), *weakly absorbing*, *homogeneous*, *bi-material*, *heterogeneous*, slowly-varying attenuation (*SVA*). They can also restrict the object to have a slowly varying phase (*SVP*). The regime (fourth column) corresponds to the validity conditions of the methods. In most cases, the weak defocusing conditions (*WDC*) should be respected (*i.e.* near-field diffraction, equivalent to large Fresnel numbers). One method (Liu et al., 2015) has been extended to long propagation distances. The fifth column refers to the acquisition method: single-plane (*single*), two-plane (*two*) or multiple-plane (*multiple*) acquisition. Finally, the last column specifies if the method is a phase retrieval method (*PR*) or if it couples phase retrieval and tomographic reconstruction (*combined*).

Reference paper	**Direct contrast model**	**Assumptions on the object**	**Regime**	**Acquisition planes**	**Phase retrieval only (*PR*) or coupled to tomographic reconstruction (*combined*)**
(Andrei V. Bronnikov, 2002; AV Bronnikov, 1999)	WTIE	pure phase SVA	WDC	single two	combined
(Groso et al., 2006)	WTIE	weakly absorbing	WDC	single	combined
(Wu et al., 2005)	WTIE	Soft tissues from 60 to 500 keV	WDC	Single	PR
(Liu et al., 2015)	WTIE	Soft tissues from 60 to 500 keV	long propagation distances	single	PR
(D. Paganin et al., 2002)	TIE	homogeneous	WDC	single	PR
(Beltran et al., 2010)	TIE	bi-material	WDC	single	PR
(Cloetens et al., 1999)	CTF	pure phase SVP	WDC	multiple	PR
(Langer et al., 2010)	Mixed	homogeneous SVA SVP	WDC	multiple	PR
(Langer et al., 2012)	Mixed	bi-material SVA SVP	WDC	multiple	PR
(Langer et al., 2014)	Mixed	heterogeneous SVA SVP	WDC	multiple	PR

Table 1: Summary of the different phase retrieval algorithms used in in-line phase contrast imaging. In the third column, *pure phase* refers to a non-attenuating object, *SVA* to an object with slowly-varying attenuation, and *SVP* to an object with slowly varying phase. The weak defocusing conditions are

abbreviated by *WDC*. In the last column, *PR* refers to phase retrieval only, while *combined* refers to methods that couple phase retrieval and tomographic reconstruction.

4. Algebraic and iterative tomographic reconstruction methods

Iterative algorithms originally raised interest in Nuclear Medicine, where the data usually suffer from noise and low counts. Later, the Algebraic Reconstruction Technique (ART) and the Simultaneous Iterative Reconstruction Technique (SIRT) have been used in electron tomography (Weyland & Midgley, 2004; Yates et al., 2006), where the data are under-sampled and noisy, to limit the sustained exposition of the sample to radiation. Actually, the interests of using such iterative algorithms mainly lies in the possibility of dose and acquisition time reduction (by acquiring less projections), and the possibility of reconstructing volumes from noisy projections and adding constraints.

Consider the following tomographic reconstruction problem:

$$\boldsymbol{p} = \boldsymbol{R}\boldsymbol{f} + \boldsymbol{n} \tag{2.4.1}$$

where $\boldsymbol{p}$ represents the measurements (e. g. projections), $\boldsymbol{f}$ the unknown (e. g. the attenuation coefficient) and $\boldsymbol{R}$ the transformation (e. g. Radon transform), and $\boldsymbol{n}$ an additive noise. Note that variables in bold refer to matrices, so that the problem is discretised.

Although $\boldsymbol{f}$ is an image it is represented as a column vector, where each element (pixel) of $\boldsymbol{f}$ is indexed by the integer j, leading to $\boldsymbol{f}_j$, s.t. $j \in [1:N]$. The projections are likewise represented by a column vector, for which each element is indexed by the integer i, leading to $\boldsymbol{p_i}$, s.t. $i \in [1:M]$. Consequently, the projection operator matrix $\boldsymbol{R}$ is of dimensions $M \times N$, usually non-square.

As explained in Chapter I, $\boldsymbol{f}$ can be retrieved from the measured projections $\boldsymbol{p}$ using the FBP. This method solves the tomographic reconstruction problem by using an *approximation* of the inverse Radon transform; actually the Radon transform is mathematically non-invertible when using discrete or a limited number of projections.

Nevertheless, if the tomographic problem suffers from missing or noisy projections, iterative tomographic reconstruction algorithms are classical alternatives to the FBP. In this case, the tomographic problem is seen as an optimization problem, aiming at minimizing the $\ell 2$-norm of the cost function $\boldsymbol{R}\boldsymbol{f} - \boldsymbol{p}$, as explained in Section 5.

In the following sections, we presented three iterative methods, widely used in tomographic reconstruction. The three of these methods use a gradient descent, to minimize iteratively the cost function. The gradient of the residual term is $\boldsymbol{R}^*(\boldsymbol{R}\boldsymbol{f} - \boldsymbol{p})$, where $\boldsymbol{R}^*$ is the adjoint of $\boldsymbol{R}$, *i.e.* the backprojection operator (described in Chapter I).

4.a. ART algorithm

The Algebraic Reconstruction Technique, ART in its abbreviated form, (Gordon, Bender, & Herman, 1970) is an iterative method that enables to solve linear problems, by minimizing the cost function of the residual with the Kaczmarz method (Kaczmarz, 1937).

ART requires a first estimate of f, $f^{(0)}$. The unknown f can be initialized with zeros. In this case, the solution will converge to the solution of minimal norm. At the k^{th} iteration, $f^{(k)}$ is estimated element by element from the difference between the estimated projections $Rf^{(k-1)}$ and the measurement p. The update of the j^{th} element of f, at the k^{th} iteration, $f_j^{(k)}$, is mathematically expressed as:

$$f_j^{(k)} = f_j^{(k-1)} + \lambda_R \frac{(p_i - R_i f^{(k-1)})}{\|R_i\|^2} R_{ij} \tag{2.4.2}$$

λ_R is the relaxation parameter ranging from 0 to 2.

In ART, the solution is updated element by element (pixel by pixel) for every ray, a ray being one element of a projection. One iteration is completed when all the rays have been processed. In practice, it converges in about 5 to 10 iterations. ART is known to provide noisy results if the projection matrix $\boldsymbol{R}$ does not describe the geometry accurately enough (Kak & Slaney, 1988).

4.b. SIRT algorithm

Considering that a pixel can be crossed by several rays, Dines and Lytle developed the Simultaneous Iterative Reconstruction Technique (SIRT) (Dines & Lytle, 1979). Unlike ART which processes ray by ray, SIRT considers all rays that pass through an element simultaneously. The correction of each pixel is calculated by averaging the correction brought by each ray. Compared to the ART method, it produces smoother images at the end, but it needs more memory, and is longer to converge. One iteration is completed once all the rays have been processed.

4.c. SART algorithm

The Simultaneous Algebraic Reconstruction Technique (SART) was derived from ART and SIRT by Andersen and Kak in 1984 (Andersen & Kak, 1984). The idea of this efficient iterative technique is to update the image at every projection, thus considering all rays of a certain projection. The SART converges faster than the SIRT, and requires less memory. It has been shown to benefit from ART and SIRT advantages, while alleviating their drawbacks (Kak & Slaney, 1988).

4.d. Equally-Sloped Tomography

The Equally-Slopped Tomography (EST) algorithm, an iterative tomographic reconstruction method, was first proposed by Miao *et al.* in 2005 (Miao, Förster, & Levi, 2005).

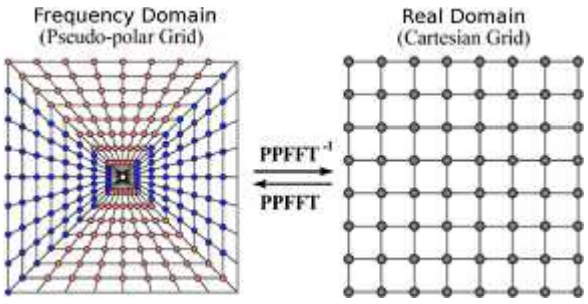

Figure 1: Pseudo-Polar Fast Fourier Transform bridges the gap between real domain and frequency domain. Image from (Miao et al., 2005).

Numerical images usually lie on a Cartesian grid, whereas its Fourier transform is describes in a polar grid, if the angular step is constant (*cf.* Central Slice Theorem, described in Chapter I). However, no exact Fourier transform between Cartesian and polar grids exists. Therefore, the idea of a "pseudo-polar" grid emerges: it consists in creating a polar-like grid, which enables an exact Fourier transform between it and the Cartesian grid. This transformation is called Pseudo Polar Fast Fourier Transform (PPFFT) (Figure 1). Compared to the traditional polar grid, the pseudo polar grid is made of equally-sloped lines (not equally-angled lines anymore). Samples of the object Fourier transform can thus be made to lie on a pseudo-polar grid by varying the angle between projections to instead have equally sloped lines.

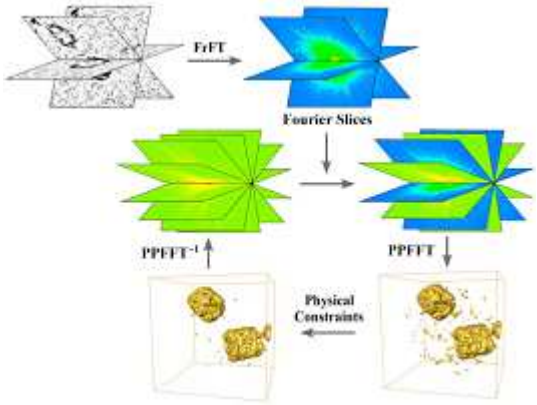

Figure 2: Scheme of the Equally-Sloped Tomography. Image from (Miao et al., 2005).

The schematic layout of EST algorithm is depicted on Figure 2. It is initiated by transforming the acquired projections in Fourier slices, by applying a Fourier transform. These measured slices are deemed as constraints for the iterative loop. Missing slices (colored in green in Figure 2) are made of random values. The forward PPFFT is applied to convert these slices in the real domain. After that, physical constraints are enforced in the real domain: the reconstructed volume is forced to be positive, and null outside a defined support. Finally, this iterative algorithm iterates back and forth between object and Fourier domain, where data are updated by measured Fourier slices (frequency constraint). Moreover, iterations are monitored by an error function, which represents the difference between the measured Fourier slices and corresponding calculated ones. Iterations tend to reduce this error function. This method successfully achieves significant dose reduction (Fahimian, Mao, Cloetens, & Miao, 2010), up to 74% for high resolution (92 µm pixel size) 3D imaging of human breast (Zhao et al., 2012), using ABI.

4.e. Applications to phase contrast tomography

More recently, algebraic algorithms such as ART and SIRT were largely employed in Diffraction Contrast Tomography (DCT) with for example some applications to crystallography (Johnson, King, Honnicke, Marrow, & Ludwig, 2008; Reischig et al., 2013), but also in Differential Phase Contrast Tomography (DPCT) (Wang et al., 2011). Other statistical (Koehler, Brendel, & Roessl, 2011) or regularised iterative methods (Cong, Yang, & Wang, 2012; Nilchian, Vonesch, Modregger, Stampanoni, & Unser, 2013; Sun, 2015) appeared recently. They enable to drastically reduce the number of acquired projections, up to a factor of 4. This is a great improvement for DPCT that usually suffers from long acquisition time.

In 2015, Fu *et al.* proposed a 3D algebraic Iterative Reconstruction (AIR) for cone-beam DPCT (Fu et al., 2015). While FDK (Feldkamp, Davis, & Kress, 1984) is usually used for tomographic reconstruction of cone-beam data, although it suffers from artifacts at large cone angles, the authors propose an new dedicated Algebraic Iterative Reconstruction (AIR) method. ART is here combined with a derivative operation (on forward projections), to take into account the nature of phase projections in DPCT. The proposed algorithm was tested on a numerical "Defrise phantom" (*i.e.* a multidisk phantom), as well as on experimental data. The authors show that AIR outperforms FDK, even when the aperture of the cone beam angle increases. Nevertheless, this obtained result is still not perfect, and takes long time to converge.

5. Introduction to ill-posed inverse problems and regularization

In the following, we consider a linear and discrete problem. The variables, written in bold, thus refer to vectors and matrices. Recall the considered forward problem for operator $\boldsymbol{R}$:

$$\boldsymbol{p} = \boldsymbol{R}\boldsymbol{f}. \tag{2.5.1}$$

The corresponding inverse problem consists in retrieving $\boldsymbol{f}$ from data $\boldsymbol{p}$.
The well-posedness of an inverse problem has been defined by Hadamard in 1923, according to the three following conditions:

- a solution of the problem exists
- the solution of the problem is unique
- the solution of the problem is continuous with respect to the input data.

In such a well-posed problem, $\boldsymbol{f}$ can be directly accessed by inverting $\boldsymbol{R}$:

$$\boldsymbol{f} = \boldsymbol{R}^{-1}\boldsymbol{p}. \tag{2.5.2}$$

In practice, most of inverse problems are ill-posed (A.N. Tikhonov & Arsenin, 1977), because they do not satisfy one or several of the Hadamard conditions, previously mentioned. This ill-posedness can be due to the fact that there is no existence of a solution (e.g. presence of noise or any other perturbations), or conversely a limited amount of data can cause the problem to have more than one solution. Finally, a discontinuity in the problem can made the solution vary considerably with respect to small perturbation on input data.

We can also consider the direct problem in presence of additive noise $\boldsymbol{n}$:

$$\boldsymbol{p} = \boldsymbol{R}\boldsymbol{f} + \boldsymbol{n} \tag{2.5.3}$$

To solve such linear problems, the least-square method can be used; this will gives the solution with the smallest norm, by using different methods (e.g. Singular Value Decomposition, gradient descent, …). Nevertheless, the solution can highly derive from the optimum in the presence of noise, or other outliers. To alleviate this ill-posedness, regularization is commonly employed. It consists in introducing a priori information on the solution, for example by setting boundary condition.

5.a. Least-square minimization and pseudo-inverse

The general idea of a minimization problem is to minimize a data fidelity term, *i.e.* supporting solutions that are the closest to the measurements (images). On the top of that, an additional term is often added. This can be the ℓ2-, ℓ1- (LASSO) or TV-norm of the estimated solution.

A classic regularization method for solving ill-posed inverse problems is the least square minimization. It consists in finding $\boldsymbol{f}$ that minimizes the square difference between $\boldsymbol{p}$ and $\boldsymbol{Rf}$. We denote $|\boldsymbol{Rf}-\boldsymbol{p}|$ the Euclidian norm, also known as the ℓ2-norm, of $\boldsymbol{Rf}-\boldsymbol{p}$. This can be seen as minimizing a data fidelity function, and, in others words, finding an estimate $\hat{\boldsymbol{f}}$ of $\boldsymbol{f}$, for which $\boldsymbol{R}\hat{\boldsymbol{f}}$ is as close as possible to the data $\boldsymbol{p}$.

$$\hat{\boldsymbol{f}} = \arg\min_{\boldsymbol{f}}(|\boldsymbol{Rf}-\boldsymbol{p}|^2) \tag{2.5.4}$$

If the columns of $\boldsymbol{R}$ are linearly independent, and by denoting $\boldsymbol{R}^*$ its adjoint (also known as conjugate transpose), the matrix $\boldsymbol{R}^*\boldsymbol{R}$ is invertible. This leads to:

$$\hat{\boldsymbol{f}} = (\boldsymbol{R}^*\boldsymbol{R})^{-1}\boldsymbol{R}^*\boldsymbol{p}. \tag{2.5.5}$$

This can be written as

$$\hat{\boldsymbol{f}} = \boldsymbol{R}^{\dagger}\boldsymbol{p}, \tag{2.5.6}$$

where $\boldsymbol{R}^{\dagger}$ is a generalized inverse, namely the Moore-Penrose pseudo-inverse of $\boldsymbol{R}$ (Bjerhammar, 1951; Moore, 1920; Penrose, 1955). In practice, the pseudo-inverse $\boldsymbol{R}^{\dagger}$ is the solution of the least-square problem (Equation (2.5.3)).

This method is usually used to solve an over-determined problem, for example a problem containing one unknown and K equations, as it is the case in holotomography, since we recorded images at K distances to determine the phase. We may write our problem as follows:

$$\boldsymbol{p}_k = \boldsymbol{R}_k\boldsymbol{f} + \boldsymbol{n}_k, \tag{2.5.7}$$

where k is an integer, such that $k \in [1{:}K]$.
The estimate of f, referred by $\hat{f}$, using the linear least square method verifies:

$$\frac{1}{N}\sum_{i=1}^{N}\boldsymbol{R}_i^2\,\hat{\boldsymbol{f}} = \frac{1}{N}\sum_{i=1}^{N}\boldsymbol{R}_i\boldsymbol{p}_i. \tag{2.5.8}$$

5.b. Tikhonov regularization and its generalization

The Tikhonov regularization (Andrei N Tikhonov, 1963) consists in searching for a solution with a bounded energy. This constraint may be expressed by using the Euclidian norm of the solution, also called the ℓ2-norm, and mathematically defined as:

$$\|\boldsymbol{f}\|_2^2 = \sqrt{\sum_{i=1}^{N}\sum_{j=1}^{M}|f_{i,j}|^2}. \tag{2.5.9}$$

Minimizing the ℓ2-norm of the solution encourages solution with the smallest ℓ2-norm, and thus excludes noise and outliers. The solution can be expressed as a minimizer of a functional:

$$\hat{\boldsymbol{f}} = \arg\min_{\boldsymbol{f}}(|\boldsymbol{R}\boldsymbol{f} - \boldsymbol{p}|^2 + \alpha|\boldsymbol{\Gamma}\boldsymbol{f}|^2) \tag{2.5.9}$$

where $\boldsymbol{\Gamma}$ denotes the Tikhonov matrix and α the regularisation parameter. The latter parameter reflects a compromise between data fidelity and noise sensitivity. Actually, if chosen too small, the estimated solution would be close to the collected data, but unstable if the problem is ill-conditioned. If chosen too large, on the contrary, the estimated solution is stable but inaccurate.

There exist several and various ways to obtain an optimal value of the regularization parameter. Among them, the Morozov discrepancy principle (Morozov, 1984) is worth citing; it chooses alpha so that the norm of the data fidelity term approaches the norm of the noise. The L-curve criterion (Hansen & O'Leary, 1993) is another method, described in Section 3.b.

Using the Tikhonov regularization, a solution of the problem can be explicitly expressed as:

$$\hat{\boldsymbol{f}} = (\boldsymbol{R}^T\boldsymbol{R} + \alpha\boldsymbol{\Gamma}^T\boldsymbol{\Gamma})^{-1}\boldsymbol{R}^T\boldsymbol{p}. \tag{2.5.10}$$

The generalised Tikhonov regularisation consists in adding a regularisation parameter that compares the solution with an a priori solution.

$$\arg\min_{\boldsymbol{f}}(|\boldsymbol{R}\boldsymbol{f} - \boldsymbol{p}|^2 + \alpha|\boldsymbol{\Gamma}(\boldsymbol{f} - \boldsymbol{f_0})|^2) \tag{2.5.11}$$

where $\boldsymbol{f_0}$ is the a priori of $\boldsymbol{f}$, α is a regularization parameter and $\boldsymbol{\Gamma}$ is the Thikonov matrix. If the Tikhonov matrix is the identity matrix the problem can be analyzed through the Singular Value Decomposition (SVD), a matrix factorization method.

5.c. L1 regularization

The Tikhonov regularization is derived from the ℓ2-minimization problem, because it involves ℓ2-norm calculation. ℓ1-regularization involves the ℓ1-norm of a matrix, defined as the sum of the absolute values of its elements:

$$\|\boldsymbol{f}\|_1 = \sum_{i=1}^{N}\sum_{j=1}^{M}|f_{i,j}| \tag{2.5.12}$$

Minimizing the objective function J containing a ℓ1-penalty encourages sparsity of the solution, while being convex; strictly speaking, the ℓ0-norm, defined by the number of non-zero entries, encourages sparsity of the solution, by inciting the fewest non-zero entries in the solution, but it is non-convex and discontinuous. Moreover, the ℓ1-norm is less sensitive to outliers and noise than the ℓ2-norm.

Several methods to find the solution *f* that minimizes the functional *J* (also known as cost function) exist. As an example, the LASSO method (Least Absolute Shrinkage and Selection Operator (Tibshirani, 1996)) used the ℓ1-norm of the estimated as a constraint:

$$J(\boldsymbol{f}) = \|\boldsymbol{Rf} - \boldsymbol{p}\|_2^2 + \alpha\|\boldsymbol{f}\|_1 \tag{2.5.13}$$

This method is used when the number of observations is about the number of unknowns, while least square method (involving ℓ2-norm) is used when the number of observations exceeds the number of unknowns.

5.d. TV Minimization

TV-minimisation is one the most famous regularization method, with the Tikhonov regularisation. It consists in minimizing the Euclidian norm of the residual data fidelity term, in addition to the TV-norm of the solution.

The TV-norm is defined as the ℓ1-norm of the amplitude of the gradient (first derivative, denoted as ∇):

$$\|\boldsymbol{f}\|_{TV} = \sum_{i=1}^{N}\sum_{j=1}^{M}\left\|\nabla f_{i,j}\right\|_1 \tag{2.5.14}$$

The solution *f* is thus the minimizer of the functional *J*, expressed as:

$$J(\boldsymbol{f}) = \|\boldsymbol{Rf} - \boldsymbol{p}\|_2^2 + \alpha\|\boldsymbol{f}\|_{TV} \tag{2.5.15}$$

It encourages solutions that have sparse gradient and thus piecewise constant regions.

Such TV-minimization is particularly used to reconstruct signal from incomplete datasets, and has been demonstrated to outperform the classic ℓ2-regularisation in several applications (Bresson & Chan, 2008; Marquina & Osher, 2008).

As an example, it has been applied to inverse problems such as denoising, deblurring, and inpainting (A Beck & Teboulle, 2009; Dahl, Hansen, Jensen, & Jensen, 2010), but also to phase retrieval more recently (Kostenko, Batenburg, Suhonen, Offerman, & van Vliet, 2013). In the latter, three phase contrast models were considered: CTF, Mixed approach and phase-attenuation duality models. This enables to retrieve the phase from single-, but also multiple-distance acquisitions.

5.e. Summary of objective functions

Here is a summary of the previously mentioned methods to solve linear ill-posed inverse problem.

Consider the following direct and discrete problem:

$$\boldsymbol{p} = \boldsymbol{Rf} + \boldsymbol{n} \tag{2.5.16}$$

where $\boldsymbol{f}$ is the unknown quantity we want to retrieve, $\boldsymbol{p}$ the measurement, $\boldsymbol{n}$ a perturbation term (noise) and $\boldsymbol{R}$ the linear operator, non inversible. A solution $\hat{\boldsymbol{f}}$ can be estimated by minimizing different objective functions, summed up below.

Least Squares:

$$\hat{\boldsymbol{f}} = arg\min_{\boldsymbol{f}}(\|\boldsymbol{R}\boldsymbol{f} - \boldsymbol{p}\|_2^2) \tag{2.5.17}$$

Tikhonov:

$$\hat{\boldsymbol{f}} = arg\min_{\boldsymbol{f}}(\|\boldsymbol{R}\boldsymbol{f} - \boldsymbol{p}\|_2^2 + \alpha\|\boldsymbol{\Gamma}\boldsymbol{f}\|_2^2) \tag{2.5.18}$$

L1-regularization:

$$\hat{\boldsymbol{f}} = arg\min_{\boldsymbol{f}}(\|\boldsymbol{R}\boldsymbol{f} - \boldsymbol{p}\|_2^2 + \alpha\|\boldsymbol{f}\|_1) \tag{2.5.19}$$

TV-regularization:

$$\hat{\boldsymbol{f}} = arg\min_{\boldsymbol{f}}(\|\boldsymbol{R}\boldsymbol{f} - \boldsymbol{p}\|_2^2 + \alpha\|\boldsymbol{\nabla}\boldsymbol{f}\|_1) \tag{2.5.20}$$

6. Combined methods

Very recently, some efforts have been devoted to combined methods, *i.e.* methods that combine phase retrieval and tomographic reconstruction into one single step. This aims at reducing data manipulation, while processing iteratively allows the introduction of constraints on the object, in the iterative loop. Designing such an algorithm was also an aim of this thesis. For this reason, this section is dedicated to the state of art of combined methods.

In 2013, Kostenko *et al.* (Kostenko, Batenburg, King, Offerman, & van Vliet, 2013) first presented a combined method using the CTF as the direct contrast model; in this case, retrieving the phase from the intensity is a linear problem, solved in the least-square sense. The Radon transform is considered as the projection operator, to solve the tomographic inverse problem. Both phase retrieval and tomographic reconstruction are thus regarded as linear problems, entangled, and solved iteratively, with additional TV regularisation, by the use of FISTA (Amir Beck & Teboulle, 2009). This innovative algorithm was designed for in-line PCT of homogeneous objects. It takes advantages of redundancy between the projections in parallel beam acquisition, known as the Helgason-Ludwig consistency conditions, (Helgason, 1965; Ludwig, 1966). In this paper, the authors compared decombined, but regularized, steps (i.e. simple phase retrieval with additional TV-regularisation, and simple tomographic reconstruction with additional TV-regularisation) to the presented method. The authors show that the combined regularised method outperforms the others in most cases, for piecewise constant objects, on both experimental and real data.

A few years later, Kongskov *et al.* (Kongskov, Jørgensen, Poulsen, & Hansen, 2016) proposed further improvements of this method by solving the optimization problem using a primal-dual method (Chambolle & Pock, 2010) instead of FISTA. This turns out to be more robust to noise.

In 2014, Ruhlandt *et al.* proposed a three-dimensional phase retrieval for propagation-based phase-contrast imaging (A. Ruhlandt, Krenkel, Bartels, & Salditt, 2014). The authors observed that most of existing phase retrieval algorithms for PBI require restrictive assumptions on the object (low-absorption, slowly varying phase, phase and absorption relationship), or restrictions on the experimental acquisition scheme (multiple distance acquisition) (Cloetens et al., 1999; D. Paganin et al., 2002; Wu et al., 2005).

The authors tackle the challenge of reconstructing single-distance in-line phase contrast data, without any restrictive assumption, on real and noisy data. They combine an iterative phase retrieval algorithm (Gerchberg & Saxton, 1972) with an algebraic tomographic reconstruction technique (ART), to stabilize the low frequency problem.

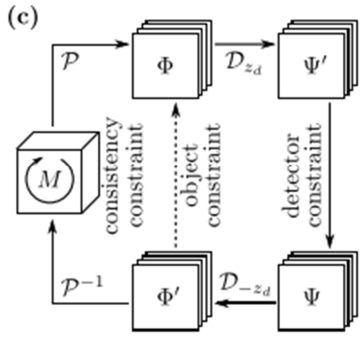

Figure 3: Scheme of the method proposed by Ruhlandt *et al.* (2014). Figure from (A. Ruhlandt et al., 2014).

The scheme of this algorithm is depicted on Figure 3. The outer loop (on the right) is related to the phase retrieval, and the inner loop (on the left) relates to the tomographic reconstruction. In the outer loop, D_{z_d} and D_{-z_d} respectively denotes the forward and inverse Fresnel propagators, at a propagation distance z_d; propagators are applied on projection of a certain angle. Ψ represents the modulus of the holographic images, and ϕ a complex projection, which can be easily separated into the phase shift and the attenuation. The mentioned object constraints are positivity of the absorption index β and refractive index decrement δ_n, valid for any object. The inner loop, performed on δ_n and β separately, is composed of projection and retroprojection operators P and P^{-1}, respectively.

The authors present the results of this method, tested on simulated data, of 130^3 voxel objects, using 90 projections over 180°, with additive Gaussian noise. They showed that this algorithm outperformed classical two-step methods, while requiring less a priori information on the sample.

In 2016, Ruhlandt and Salditt (Aike Ruhlandt & Salditt, 2016) proposed to do first the tomographic reconstruction and thus perform the phase retrieval in 3D. They showed that propagating the Radon transform of an object is equivalent to do the Radon transform of the propagated object in 3D. This turns out to be also computationnally efficient.

This innovative kind of combined methods were the object of this thesis work (see Chapter V), where we proposed a new algorithm that entangles phase retrieval and tomographic reconstruction.

7. Conclusion

In this chapter, we introduced the different models of phase contrast, and their assumptions, before describing in details some phase retrievals methods, particularly used in PBI. This step is usually followed by tomographic reconstruction, involving either the FBP (presented in Chapter I), or, more recently, algebraic or iterative algorithms, presented in Section 4. Phase retrieval, as well as tomographic reconstruction, aim at solving an inverse problem. To this aim, advanced methods have been developed, involving more and more the use of regularization, which is the topic of Section 5. Finally, we focused on new methods that combine phase retrieval and tomographic reconstruction, as one goal of this thesis is to develop and implement such an algorithm.

References

Andersen, A. H., & Kak, A. C. (1984). Simultaneous algebraic reconstruction technique (SART): a superior implementation of the art algorithm. *Ultrasonic Imaging*, *6*(1), 81–94.

Beck, A., & Teboulle, M. (2009). A Fast Iterative Shrinkage-Thresholding Algorithm for Linear Inverse Problems. *SIAM Journal on Imaging Sciences*, *2*(1), 183–202. doi:10.1137/080716542

Beck, A., & Teboulle, M. (2009). Gradient-based algorithms with applications to signal recovery. *Convex Optimization in Signal Processing …*.

Beltran, M. A., Paganin, D. M., Uesugi, K., & Kitchen, M. J. (2010). 2D and 3D X-ray phase retrieval of multi-material objects using a single defocus distance. *Optics Express*, *18*(7), 6423–36.

Bjerhammar, A. (1951). Application of calculus of matrices to method of least squares; with special references to geodetic calculations. *Trans. Roy. Inst. Tech. Stockholm*, *49*.

Bresson, X., & Chan, T. (2008). Fast dual minimization of the vectorial total variation norm and applications to color image processing. *Inverse Problems and Imaging*.

Bronnikov, A. V. (2002). Theory of quantitative phase-contrast computed tomography. *Journal of the Optical Society of America A*, *19*(3), 472. doi:10.1364/JOSAA.19.000472

Bronnikov, A. (1999). Reconstruction formulas in phase-contrast tomography. *Optics Communications*.

Burvall, A., Lundström, U., Takman, P. A. C., Larsson, D. H., & Hertz, H. M. (2011). Phase retrieval in X-ray phase-contrast imaging suitable for tomography. *Optics Express*, *19*(11), 10359–76. doi:10.1364/OE.19.010359

Chambolle, A., & Pock, T. (2010). A First-Order Primal-Dual Algorithm for Convex Problems with Applications to Imaging. *Journal of Mathematical Imaging and Vision*, *40*(1), 120–145. doi:10.1007/s10851-010-0251-1

Cloetens, P., Ludwig, W., Baruchel, J., Van Dyck, D., Van Landuyt, J., Guigay, J. P., & Schlenker, M. (1999). Holotomography: Quantitative phase tomography with micrometer resolution using hard synchrotron radiation x rays. *Applied Physics Letters*, *75*(19), 2912. doi:10.1063/1.125225

Cloetens, P., Pateyron-Salomé, M., Buffière, J. Y., Peix, G., Baruchel, J., Peyrin, F., & Schlenker, M. (1997). Observation of microstructure and damage in materials by phase sensitive radiography and tomography. *Journal of Applied Physics*, *81*(9), 5878. doi:10.1063/1.364374

Cong, W., Yang, J., & Wang, G. (2012). Differential phase-contrast interior tomography. *Physics in Medicine and Biology*, *57*(10), 2905–14. doi:10.1088/0031-9155/57/10/2905

Cowley, J. M. (1995). *Diffraction Physics*.

Dahl, J., Hansen, P., Jensen, S., & Jensen, T. (2010). Algorithms and software for total variation image reconstruction via first-order methods. *Numerical Algorithms*.

del Río, M. S., & Dejus, R. J. (2004). XOP 2.1: A new version of the X-ray optics software toolkit. *Proc. Synchrotron Radiation Instrumentation: Eighth International Conference, (Edited by T. Warwick et Al.)*, (American Institute of Physics, San Fransisco), 784–787.

Dines, K. A., & Lytle, R. J. (1979). Computerized geophysical tomography. *Proceedings of the IEEE*, *67*(7), 1065–1073. doi:10.1109/PROC.1979.11390

Fahimian, B. P., Mao, Y., Cloetens, P., & Miao, J. (2010). Low-dose x-ray phase-contrast and absorption CT using equally sloped tomography. *Physics in Medicine and Biology*, *55*(18), 5383–400. doi:10.1088/0031-9155/55/18/008

Feldkamp, L. A., Davis, L. C., & Kress, J. W. (1984). Practical cone-beam algorithm. *Journal of the Optical Society of America A*, *1*(6), 612. doi:10.1364/JOSAA.1.000612

Fu, J., Hu, X., Velroyen, A., Bech, M., Jiang, M., & Pfeiffer, F. (2015). 3D algebraic iterative reconstruction for cone-beam x-ray differential phase-contrast computed tomography. *PloS One*,

10(3), e0117502. doi:10.1371/journal.pone.0117502

Gerchberg, R. W., & Saxton, W. O. (1972). A practical algorithm for the determination of the phase from image and diffraction plane pictures. *Optik*, *35*, 237–246.

Goodman, J. W. (2005). *Introduction to Fourier Optics*. New York: Roberts and Company Publishers.

Gordon, R., Bender, R., & Herman, G. T. (1970). Algebraic Reconstruction Techniques (ART) for three-dimensional electron microscopy and X-ray photography. *J. theor. Biol.*

Groso, A., Abela, R., & Stampanoni, M. (2006). Implementation of a fast method for high resolution phase contrast tomography. *Optics Express*, *14*(18), 8103. doi:10.1364/OE.14.008103

Guigay, J. P., Langer, M., Boistel, R., & Cloetens, P. (2007). Mixed transfer function and transport of intensity approach for phase retrieval in the Fresnel region. *Optics Letters*, *32*(12), 1617. doi:10.1364/OL.32.001617

Guigay, J.-P. (1977). Fourier transform analysis of Fresnel diffraction patterns and in-line holograms. *Optik*, *49*, 121–125.

Hansen, P. (1999). The L-curve and its use in the numerical treatment of inverse problems.

Hansen, P., & O'Leary, D. (1993). The use of the L-curve in the regularization of discrete ill-posed problems. *SIAM Journal on Scientific Computing*.

Helgason, S. (1965). The Radon transform on Euclidean spaces, compact two-point homogeneous spaces and Grassmann manifolds. *Acta Mathematica*, *113*(1), 153–180. doi:10.1007/BF02391776

Johnson, G., King, A., Honnicke, M. G., Marrow, J., & Ludwig, W. (2008). X-ray diffraction contrast tomography: a novel technique for three-dimensional grain mapping of polycrystals. II. The combined case. *Journal of Applied Crystallography*, *41*(2), 310–318. doi:10.1107/S0021889808001726

Kaczmarz, S. (1937). Angenäherte auflösung von systemen linearer gleichungen. *Bulletin International de l'Academie Polonaise Des …*.

Kak, A. C., & Slaney, M. (1988). Principles of computerized tomographic imaging.

Klein, O., & Nishina, Y. (1929). Über die Streuung von Strahlung durch freie Elektronen nach der neuen relativistischen Quantendynamik von Dirac. *Zeitschrift Für Physik*, *52*(11-12), 853–868. doi:10.1007/BF01366453

Koehler, T., Brendel, B., & Roessl, E. (2011). Iterative reconstruction for differential phase contrast imaging. Theory and initial results. In *Fully3D*.

Kongskov, R. D., Jørgensen, J. S., Poulsen, H. F., & Hansen, P. C. (2016). Noise robustness of a combined phase retrieval and reconstruction method for phase-contrast tomography. *Journal of the Optical Society of America A*, *33*(4), 447. doi:10.1364/JOSAA.33.000447

Kostenko, A., Batenburg, K. J., King, A., Offerman, S. E., & van Vliet, L. J. (2013). Total variation minimization approach in in-line x-ray phase-contrast tomography. *Optics Express*, *21*(10), 12185–96. doi:10.1364/OE.21.012185

Kostenko, A., Batenburg, K. J., Suhonen, H., Offerman, S. E., & van Vliet, L. J. (2013). Phase retrieval in in-line x-ray phase contrast imaging based on total variation minimization. *Optics Express*, *21*(1), 710–23. doi:10.1364/OE.21.000710

Langer, M., Cloetens, P., Hesse, B., Suhonen, H., Pacureanu, A., Raum, K., & Peyrin, F. (2014). Priors for X-ray in-line phase tomography of heterogeneous objects. *Philosophical Transactions of the Royal Society A: Mathematical, Physical and Engineering Sciences*, *372*(2010), 20130129–20130129. doi:10.1098/rsta.2013.0129

Langer, M., Cloetens, P., Pacureanu, A., & Peyrin, F. (2012). X-ray in-line phase tomography of multimaterial objects. *Optics Letters*, *37*(11), 2151–3. doi:10.1364/OL.37.002151

Langer, M., Cloetens, P., & Peyrin, F. (2010). Regularization of phase retrieval with phase-attenuation

duality prior for 3-D holotomography. *IEEE Transactions on Image Processing : A Publication of the IEEE Signal Processing Society*, *19*(9), 2428–36. doi:10.1109/TIP.2010.2048608

Liu, H., Wu, X., & Xiao, T. (2015). Synchrotron-based high-energy x-ray phase sensitive microtomography for biomedical research. *Medical Physics*, *42*(10), 5595–603. doi:10.1118/1.4929551

Ludwig, D. (1966). The radon transform on euclidean space. *Communications on Pure and Applied Mathematics*, *19*(1), 49–81. doi:10.1002/cpa.3160190105

Marquina, A., & Osher, S. J. (2008). Image Super-Resolution by TV-Regularization and Bregman Iteration. *Journal of Scientific Computing*, *37*(3), 367–382. doi:10.1007/s10915-008-9214-8

Miao, J., Förster, F., & Levi, O. (2005). Equally sloped tomography with oversampling reconstruction. *Physical Review B*, *72*(5), 052103. doi:10.1103/PhysRevB.72.052103

Moore, E. H. (1920). On the reciprocal of the general algebraic matrix. *Bulletin of the American Mathematical Society*, *26*(9), 394–395. doi:10.1090/S0002-9904-1920-03322-7.

Morozov, V. A. (1984). *Methods for Solving Incorrectly Posed Problems*. New York, NY: Springer New York. doi:10.1007/978-1-4612-5280-1

Nilchian, M., Vonesch, C., Modregger, P., Stampanoni, M., & Unser, M. (2013). Fast iterative reconstruction of differential phase contrast X-ray tomograms. *Optics Express*, *21*(5), 5511–28. doi:10.1364/OE.21.005511

Otsu, N. (1979). A threshold selection method from gray-level histograms. *IEEE Transactions on Systems, Man and Cybernetics*, *9*(1), 62–66.

Paganin, D. M. (2006). *Coherent X-Ray Optics*.

Paganin, D., Mayo, S. C., Gureyev, T. E., Miller, P. R., & Wilkins, S. W. (2002). Simultaneous phase and amplitude extraction from a single defocused image of a homogeneous object. *Journal of Microscopy*, *206*(1), 33–40. doi:10.1046/j.1365-2818.2002.01010.x

Penrose, R. (1955). A generalized inverse for matrices. *Proceedings of the Cambridge Philosophical Society*, *51*, 406–413. doi:10.1017/S0305004100030401

Peyrin, F., Cloetens, P., Salome-Pateyron, M., Baruchel, J., & Spanne, P. (1997). Reconstruction 3D en tomographie par rayonnement synchrotron coherent. *Gretsi*, 423–426.

Raven, C., Snigirev, A., Snigireva, I., Spanne, P., Souvorov, A., & Kohn, V. (1996). Phase-contrast microtomography with coherent high-energy synchrotron x rays. *Applied Physics Letters*, *69*(13), 1826. doi:10.1063/1.117446

Reischig, P., King, A., Nervo, L., Viganó, N., Guilhem, Y., Palenstijn, W. J., … Ludwig, W. (2013). Advances in X-ray diffraction contrast tomography: flexibility in the setup geometry and application to multiphase materials. *Journal of Applied Crystallography*, *46*(2), 297–311. doi:10.1107/S0021889813002604

Rositi, H., Frindel, C., Wiart, M., Langer, M., Olivier, C., Peyrin, F., & Rousseau, D. (2014). Computer vision tools to optimize reconstruction parameters in x-ray in-line phase tomography. *Physics in Medicine and Biology*, *59*(24), 7767–75. doi:10.1088/0031-9155/59/24/7767

Ruhlandt, A., Krenkel, M., Bartels, M., & Salditt, T. (2014). Three-dimensional phase retrieval in propagation-based phase-contrast imaging. *Physical Review A*, *89*(3), 033847. doi:10.1103/PhysRevA.89.033847

Ruhlandt, A., & Salditt, T. (2016). Three-dimensional propagation in near-field tomographic X-ray phase retrieval. *Acta Crystallographica Section A Foundations and Advances*, *72*(2). doi:10.1107/S2053273315022469

Sun, F. (2015). An Iterative Image Reconstruction for Differential X-ray Phase-contrast Computed Tomography. *Journal of Fiber Bioengineering and Informatics*, *8*(3), 521–528. doi:10.3993/jfbim00125

Teague, M. R. (1982). Irradiance moments: their propagation and use for unique retrieval of phase. *Journal of the Optical Society of America*, *72*(9), 1199. doi:10.1364/JOSA.72.001199

Tibshirani, R. (1996). Regression shrinkage and selection via the lasso. *J. Royal. Statist. Soc B., Vol. 58, No. 1*.

Tikhonov, A. N. (1963). Solution of incorrectly formulated problems and the regularization method. *Soviet Mathematics*, *4*, 501–504.

Tikhonov, A. N., & Arsenin, V. Y. (1977). *Solution of Ill-posed Problems*.

Wang, Z., Huang, Z., Zhang, L., Chen, Z., Kang, K., Yin, H., … Marco, S. (2011). Low dose reconstruction algorithm for differential phase contrast imaging. *Journal of X-Ray Science and Technology*, *19*(3), 403–15. doi:10.3233/XST-2011-0303

Weyland, M., & Midgley, P. A. (2004). Electron tomography. *Materials Today*, *7*(12), 32–40. doi:10.1016/S1369-7021(04)00569-3

Wu, X., Liu, H., & Yan, A. (2005). X-ray phase-attenuation duality and phase retrieval. *Optics Letters*, *30*(4), 379. doi:10.1364/OL.30.000379

Yates, T. J. V., Thomas, J. M., Fernandez, J.-J., Terasaki, O., Ryoo, R., & Midgley, P. A. (2006). Three-dimensional real-space crystallography of MCM-48 mesoporous silica revealed by scanning transmission electron tomography. *Chemical Physics Letters*, *418*(4-6), 540–543. doi:10.1016/j.cplett.2005.11.031

Zhao, Y., Brun, E., Coan, P., Huang, Z., Sztrókay, A., Diemoz, P. C., … Bravin, A. (2012). High-resolution, low-dose phase contrast X-ray tomography for 3D diagnosis of human breast cancers. *Proceedings of the National Academy of Sciences of the United States of America*, *109*(45), 18290–4. doi:10.1073/pnas.1204460109

Chapter III: Phase-contrast micro-tomography of scaffolds seeded with bone cells

In the field of regenerative medicine, there has been a growing interest in studying the combination of bone scaffolds and cells that can maximize newly formed bone when used as artificial bone grafts. In-line phase-contrast X-ray tomography was used to image porous bone scaffolds (Skelite©), seeded with bone forming cells. This technique allows the quantification of both mineralized and soft tissue, unlike with classical X-ray micro-computed tomography. Phase contrast images were acquired at four distances. The reconstruction is typically performed in two successive steps: phase retrieval and tomographic reconstruction. In this work, different regularisation methods were applied to the phase retrieval process. The application of a priori terms for heterogeneous objects enables quantitative 3D imaging of not only bone morphology, mineralization, and soft tissue formation, but also cells trapped in the pre-bone matrix. A statistical study was performed to derive statistically significant information on the different culture conditions. Such analysis was not possible in the previous study, since it employed homogeneous object assumptions. By the mean of heterogeneous assumption on the object, the reconstruction is now quantitative in soft tissues, as well as in bone, which enable to separate the cells from other tissues. In addition, the automation of the reconstruction process, which was done during this thesis, is also presented.

A slightly different version of this chapter was published in *Phys Med Biol*, 2016, under the title: “Quantitative evaluation of regularized phase retrieval algorithms on bone scaffolds seeded with bone cells”. (Weber, Langer, Tavella, Ruggiu, & Peyrin, 2016)

Table of contents

1. Introduction

In the field of regenerative medicine, studying the combination of bone scaffolds and cells that can maximize newly formed bone has been of paramount importance. Research has been focused on scaffolds themselves (Hutmacher, 2000), as well as on cell development (Tortelli et al., 2009) and cell culture techniques (Holy, Shoichet, & Davies, 2000). The classical imaging method for cells is histology, but more recently attention has been drawn on real 3D and non-destructive imaging techniques. FIB-SEM (Focused Ion Beam–Scanning Electron Microscope) has, for instance, been successfully employed to study the interaction between bone cells and nanofiber membranes (Stachewicz et al., 2015). 3D imaging techniques using synchrotron radiation, such as SR-microtomography and SR-microdiffraction, have been applied to bone tissue engineering (Cancedda et al., 2007). Since SR benefits from high flux and monochromaticity, it enables quantitative and non-destructive attenuation-based tomography. This was used to study bone resorption and quantify porosity and local thickness of scaffolds in 3D (Komlev et al., 2010). As mentioned in Chapter 1, SR also enables an even more powerful imaging technique: phase contrast imaging.

During the past two decades, X-ray phase-contrast imaging has been of a growing interest for biological samples, because it enables enhancing contrast in biological tissues compared to conventional attenuation imaging, for hard X-rays (10 to 100keV) (Momose, Takeda, Itai, & Hirano, 1996). Several methods have been developed for phase contrast imaging and tomography, namely analyser-based imaging (Chapman et al., 1997), grating interferometry (David, Nöhammer, Solak, & Ziegler, 2002), coded-aperture technique (Olivo & Speller, 2007) and propagation-based imaging (Snigirev, Snigireva, Kohn, Kuznetsov, & Schelokov, 1995). Propagation-based imaging (PBI) is the simplest set-up among the other existing set-ups since it only requires a partially coherent beam, without extra optical element in the beam. Coupled with a high-resolution detector, for example that available at ESRF (FReLoN camera, Labiche et al., 2007), this modality achieves a sub-micrometric resolution.

PBI can be coupled to tomography by imaging a sample using this coherent beam, after rotating it over a 180° or 360° range. This yields a tomographic technique that has very high sensitivity, but in which contrast is present mainly on material interfaces (edge enhancement effect), and is usually called *phase contrast tomography*. In this case both the projections and the tomographic reconstruction contain phase and attenuation information (Cloetens et al., 1997). The phase shift can be extracted from such projection images, using a so-called *phase retrieval* algorithm. We output a 3D image of the refractive index decrement distribution in the sample by using these phase images as input to a tomographic reconstruction algorithm (Cloetens et al., 1999). This has two major advantages: the contrast is quantitative area contrast (as opposed to the edge contrast), facilitating interpretation and analysis of the images, and the contrast is proportional to the local mass density in the sample (Guinier, 1994).

The phase retrieval process from Fresnel diffraction patterns is nevertheless sensitive to noise in the low spatial frequency range, because of the weak transfer of low frequency information in the phase shift by the Fresnel transform. This can result in spurious slowly varying patterns in the background of the reconstructed images. To alleviate this problem, regularisation of the phase retrieval has been introduced, either by assuming homogeneous objects (Max Langer, Cloetens, & Peyrin, 2010a; Paganin, Mayo, Gureyev, Miller, & Wilkins, 2002), or heterogeneous objects (Langer et al., 2014; Langer, Cloetens, Pacureanu, & Peyrin, 2012).

Previously, bone scaffolds made of Skelite©, a material composed of Silicon stabilized tricalcium phosphate (Si-TCP) and β-tricalcium phosphate/hydroxyapatite (β-TCP/HA), were imaged. These scaffolds were seeded with bone cells, namely osteoblasts (OBs) and pre-osteoclasts (pre-OCs). A study lead by Mastrogiacomo et al. (2007), using a homogeneous object phase retrieval approach, showed that OBs and pre-OCs respectively induced new bone formation and bone resorption.

Here, we use these data to compare several regularised phase retrieval algorithms. This is the first comparison on experimental data that does not use phantom objects. After choosing the most appropriate algorithm based on quantitative criteria, quantitative analyses of samples were performed, such as volume calculations of the different fractions, particularly the fraction containing cells. We show that the bone cells segmentation becomes possible if using appropriate a priori knowledge for the reconstruction. Characteristic 3D-features of the cells such as size and volume are measured in the segmented volumes. These calculations were not possible with other reconstruction algorithms.

2. Materials & Methods

2.a. Imaged samples

Scaffolds used in this study are made of Skelite© (MilleniumBiologix Corp., Kingston, Canada), a material that mimics the structure of trabecular bone. This bone-like material is roughly composed of 67% Si-TCP (Silicon stabilized tricalcium phosphate) and 33% β-TCP/HA (β-tricalcium phosphate/Hydroxyapatite). Nine samples of 9 mm-diameter and 1.2 mm-height were seeded with bone cells. Three of them were seeded with osteoblasts (cells that form new bone and control mineral deposition), three others were seeded with pre-osteoclasts (cells that dissolve the bone), and the last three scaffolds were seeded with both OBs and pre-OCs. OBs induce bone formation, and pre-OCs activated by the presence of OBs should induce bone resorption and creation of mineralized bone tissue. No data of empty scaffolds were available, but the pre-OCs samples are comparable to empty scaffolds, since pre-OCs are activated by the presence of osteoblasts (Mastrogiacomo et al., 2007). Cells were cultivated in the scaffolds for 8 weeks. Then, the samples were washed in PBS, fixed in paraformaldehyde and stored in 70% ethanol. Samples were finally dried before imaging.

2.b. Phase tomography

2.b.i. Phase contrast

A 3D object can be described by its complex refractive index:

$$n(x,y,z) = 1 - \delta_n(x,y,z) + i\beta(x,y,z), \qquad (3.2.1)$$

where (x, y, z) denotes the coordinates in the real space, z corresponds to the propagation axis, and (x,y) the coordinates of a projection parallel to the propagation direction, as depicted in the Chapter I. The real $(1-\delta_n)$ and imaginary (β) parts of n are respectively related to the phase-shift and the absorption. For hard X-ray and low-Z tissues, δ_n is three orders of magnitude higher than β, which offers a better sensitivity for phase-contrast imaging than conventional attenuation imaging (Momose et al., 1996).

2.b.ii. Propagation-based imaging

Propagation-based imaging (Snigirev et al., 1995) presents the simplest set-up for phase-contrast imaging. Phase contrast is achieved by letting a spatially coherent beam to propagate after passing through the sample. Phase contrast increases as the detector moves further away, because of the growing of the interference patterns. Nevertheless, intensity recorded by the detector contains both attenuation and phase information. Phase information is then inferred from images acquired by the detector at one (Paganin et al., 2002) or several (Cloetens et al., 1999) distances. Phase retrieval from recorded intensities is a non-linear inverse problem that requires simplifications and regularisation to be solved.

2.b.iii.Image formation

At each angle θ, the interaction between the objet and the X-ray wave can be described as a transmittance function:

$$T_\theta(\boldsymbol{x}) = \exp[-B_\theta(\boldsymbol{x}) + i\varphi_\theta(\boldsymbol{x})]. \tag{3.2.2}$$

Attenuation B_θ and phase shift φ_θ induced by the object at an angle θ can be described as projections perpendicular to the propagation direction (here, the z_θ-axis; note that **x** denotes the vector (x, y)).

$$B_\theta(\boldsymbol{x}) = \frac{2\pi}{\lambda}\int \beta(\boldsymbol{x}, z_\theta)\, dz_\theta \tag{3.2.3}$$

and

$$\varphi_\theta(\boldsymbol{x}) = -\frac{2\pi}{\lambda}\int \delta_n(\boldsymbol{x}, z_\theta)\, dz_\theta. \tag{3.2.4}$$

If $u_{inc}(\mathbf{x})$ denotes the incident wave front, the wave front right after the sample $u_0(\mathbf{x})$ is written as:

$$u_0(\boldsymbol{x}) = T_\theta(\boldsymbol{x})u_{inc}(\boldsymbol{x}). \tag{3.2.5}$$

The free space propagation over a distance D can be modeled by the Fresnel transform involving the propagator P_D (Goodman, 2005), defined in the Chapter II:

$$u_{\theta,D}(\boldsymbol{x}) = P_D(\boldsymbol{x}) * u_0(\boldsymbol{x}), \tag{3.2.6}$$

which leads to:

$$u_{\theta,D}(\boldsymbol{x}) = P_D(\boldsymbol{x}) * \big(T_\theta(\boldsymbol{x})u_{inc}(\boldsymbol{x})\big). \tag{3.2.7}$$

We consider a unitary wavefront, which means that $u_{inc}(\mathbf{x}) = 1$. We note $T_{\theta,D}$ the operator that combines the transmission of the object at an angle θ and the free-space propagation over a distance D

$$u_{\theta,D}(\boldsymbol{x}) = T_{\theta,D}(\boldsymbol{x}) = (T_\theta * P_D)(\boldsymbol{x}) \tag{3.2.8}$$

The intensity recorded by the detector at a distance D is:

$$I_{\theta,D}(\boldsymbol{x}) = \left|T_{\theta,D}(\boldsymbol{x})\right|^2. \tag{3.2.9}$$

2.b.iv. Phase retrieval

Phase retrieval consists in calculating the phase shift $\varphi_\theta(\boldsymbol{x})$ from the phase contrast images at one or several different propagation distances $\{I_{\theta,D}(\boldsymbol{x})/D = D_1 \dots D_n\}$.

In Paganin's method (Paganin et al., 2002) the phase is directly expressed as a function of the intensity recorded at one distance *D*, using the following formula :

$$\varphi_\theta(\boldsymbol{x}) = \frac{\delta_n}{2\beta}\ln\left(\mathcal{F}^{-1}\left\{\frac{\mathcal{F}\left(I_{\theta,D}(\boldsymbol{x})\right)}{1+\lambda D\pi.\frac{\delta_n}{\beta}\left|\left|\boldsymbol{f}\right|\right|^2}\right\}\right). \tag{3.2.10}$$

where $\mathcal{F}$ and $\mathcal{F}^{-1}$ denotes the Fourier transform and its inverse, respectively; $I_{\theta,D}(\mathbf{x})$, the intensity recorded at a distance *D*, the sample being rotated at an angle θ; λ, the wavelength of the beam; $\boldsymbol{f}$, the coordinates in the Fourier domain (f_x, f_y); δ_n the refractive index decrement and β the absorption index of the object.

However this formula relies on the Transport of Intensity Equation that assumes a small propagation distance *D*, and on a strictly homogeneous object (Turner et al., 2004). In this study, we used the mixed approach (Guigay, Langer, Boistel, & Cloetens, 2007) for phase retrieval. This approach relies on the expression of the intensity recorded by the detector at each distance using a combination of the Contrast Transfer Function (CTF) and the Transport of Intensity Equation (TIE). This mixed approach is valid for strongly absorbing object and approaches the TIE for small propagation distances, and enables to retrieve the phase from measured intensity.

2.b.v. Regularisation

Retrieving the phase from this model is an ill-posed inverse problem due to zero-crossings in the Fresnel transform transfer function, which can be solved by introducing regularisation techniques. The phase can then be expressed as the solution of the following minimization problem:

$$\hat{\varphi}_\theta(\boldsymbol{x}) = \text{argmin}_\varphi \sum\left(\left|\hat{I}_{\theta,D,\varphi}(\boldsymbol{x}) - I_{\theta,D}(\boldsymbol{x})\right|^2 + \alpha\left|\varphi_\theta(\boldsymbol{x}) - \varphi_{\theta,0}(\boldsymbol{x})\right|^2\right) \tag{3.2.11}$$

where $\hat{\varphi}_\theta(\boldsymbol{x})$ is an estimate of the phase projection at angle θ
$\hat{I}_{\theta,D,\varphi}(\boldsymbol{x})$ denotes the calculated intensity (*e.g.* using the mixed approach)
$I_{\theta,D}(\boldsymbol{x})$ is the measured intensity
α is a regularisation parameter, determined using a L-curve criterion
$\varphi_{\theta,0}(\boldsymbol{x})$ is an initial guess of the phase.

Two types of regularisation, determining the construction of the $\varphi_{\theta,0}(\boldsymbol{x})$, were used in this study.

On one hand, the object is assumed to be homogeneous (Langer et al., 2010a). In this case, the attenuation is supposed to be proportional to the phase shift (*i.e.* the ratio δ_n/β is constant). The proportionality coefficient between phase and attenuation is inferred from both the chemical composition of the sample and the energy of the beam, using XOP software (Del Río & Dejus, 2004). This relationship is then applied on each attenuation projections, in order to get a prior estimate of the phase shift, $\varphi_{\theta,0}(\mathbf{x})$, in the Radon domain, expressed as:

$$\varphi_{\theta,0}(\boldsymbol{x}) = l(\boldsymbol{x}) \times \frac{\delta_n}{2\beta} \ln\left[I_{\theta,D}(\boldsymbol{x})\right], \tag{3.2.12}$$

where $I_{\theta,D}(\boldsymbol{x})$ the intensity measured at a distance D from the sample, $l(\boldsymbol{x})$ a low-pass filter, δ_n the refractive index decrement and β the absorption index of the object.

In case of multi-distance acquisition, the absorption distance is used to design the prior. This prior knowledge is then introduced in the Tikhonov regularisation, weighted by the regularisation parameter α. This parameter is determined using a L-curve criterion, as explained in details in (Max Langer et al., 2010a). Basically, it consists in plotting the model errors as a function of the regularisation errors, for some values of α. This usually leads to an L-shape curve. The point at the corner of the "L" corresponds to the point of maximum curvature, but also gives the value of α that offers the best trade-off between reducing the model and the regularisation errors.

On the other hand, the object is assumed to be heterogeneous, as it is often the case for experimental biological samples. In this case, the prior is designed in the object domain, *i.e.* that the 3D phase prior is designed from the 3D reconstructed attenuation object, using a relationship between the attenuation and the phase. This relationship could be a simple threshold (attenuation volume is segmented and the corresponding part below and above the threshold are associated with one δ_n/β value), or a functional relationship, as described in (Langer et al., 2014). The estimated phase volume is eventually backprojected to get, at each angular position, an initial guess of the phase in the Radon domain.

2.b.vi. Reconstruction algorithms

The ratio δ_n/β for Skelite at 30keV was calculating using XOP software (del Río & Dejus, 2004). It is equal to 335. Note that this value differs from the one used in the previous study (M Langer et al., 2010b), namely 380. This is due to the fact that the authors did not take into account the cross section of the elastic Rayleigh scattering, which influences the linear attenuation coefficient, and thus the δ_n/β ratio. The experimental data were reconstructed using the several regularised phase retrieval algorithms ("methods") mentioned below.

The so-called "Method P" corresponds to Paganin's algorithm (Equation (3.2.10) and (Paganin et al., 2002)). This method is considered as a gold standard when it comes to phase retrieval. For this reconstruction method, only one distance acquisition was used. This distance was judiciously chosen, among the four available, to avoid zero-crossing in the contrast transfer function (namely the fourth).

"Method A" corresponds to the mixed approach using homogeneous regularisation (Max Langer et al., 2010a). This method uses the four distances acquisitions, with the δ_n/β ratio determined previously.

"Method B" corresponds to the mixed approach with heterogeneous regularisation (Langer et al., 2012); the attenuation scan is thresholded and each resulting part of the histogram is associated with

the δ_n/β value of the Skelite (335 at 30keV) or soft tissue (2000 at 30keV). Here, since the histogram of the attenuation scan is trimodal (see Figure 1), we have two possibilities for thresholding. Threshold between the 1st mode (air) and the 2nd mode (soft tissue) of the histogram amounts to consider the sample as homogeneous, since it consists in separating the sample from the air. Thus, in the "Method B" (Figure 1), we choose to threshold between the second and the third mode, which consists in assuming the sample as bi-material.

"Method C" designates the mixed approach using functional relationship between attenuation and δ_n/β ratio to creates a priori knowledge on the phase map (Langer et al., 2014). The function was created by plotting the δ_n/β value (at 30keV) as a function of the attenuation (Figure 3), for different materials that composed the samples (namely collagen, fully-mineralized bone and pure Skelite). Bone part was interpolated using an exponential relationship, as described in (Langer et al., 2014).

All these methods are summarised in Table 1.

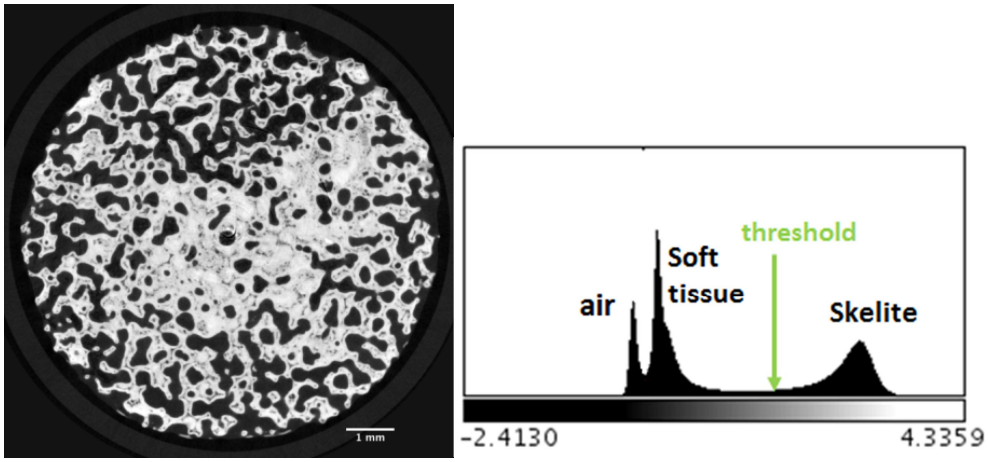

Figure 1: Example of a filtered slice of the attenuation scan, and the corresponding histogram; the histogram is clearly tri-modal, so that 2 different thresholds are possible. We used the second threshold for method B.

	Phase retrieval method	Assumption on the sample	Characteristics	Number of distances	Reference
Method A	Mixed	Homogeneous		4	Langer *et al.*, 2010a
Method B	Mixed	Multimaterial	Threshold between soft tissue and scaffold	4	Langer *et al.*, 2012
Method C	Mixed	Heterogeneous	Functional relationship between μ and δ/β	4	Langer *et al.*, 2014
Method P	Paganin	Homogeneous		1	Paganin *et al.*, 2002

Table 1: Summary of the different phase retrieval methods applied.

Figure 2 shows a plot of the linear attenuation coefficient μ as a function of the δ_n/β ratio of tissues. This function aims at relating all types of imaged material, from unmineralized soft tissues (collagen and immature bone) to mineralized hard tissues (mature bone and scaffold). In-between, the mineralization is progressively increased, to cover the transition between soft and hard parts.
Immature bone is composed of collagen and hydroxyapatite (HA), in variable proportions. As the (immature) bone gets mineralized, the proportion of HA increases, the proportion of collagen remaining constant (~30%). This was used to calculate the points depicted on Figure 2. This part of the curve shows a power-law trend, with a good correlation coefficient ($R^2 > 0.999$).

The Skelite is roughly composed of Si-$TCP_{saturated}$ (67%) and of a mix of HA and β-TCP (33%). Another formula was reported in the literature, namely the Skelite being composed of α-TCP (78%), HA (21%) and β-TCP (1%) (Gillespie, 2007). Both compositions give very similar results whether concerning the linear attenuation coefficient or the δ_n/β-ratio.

For completeness, the chemical formulas of the different material are reported in Table 2.

Material	Chemical formula
Si-TCP saturated	$Ca_3(Si_{0.1}P_{0.9}O_{3.95})_2$
Hydroxyapatite (HA)	$Ca_5(PO_4)_3OH$
β-TCP	$Ca_3(PO_4)_2$
collagen	C_2H_5NO-C_5H_9NO-$C_5H_{10}NO_2$
α-TCP	$Ca_3(PO_4)_2$

Table 2: Chemical formulas of material used in this study.

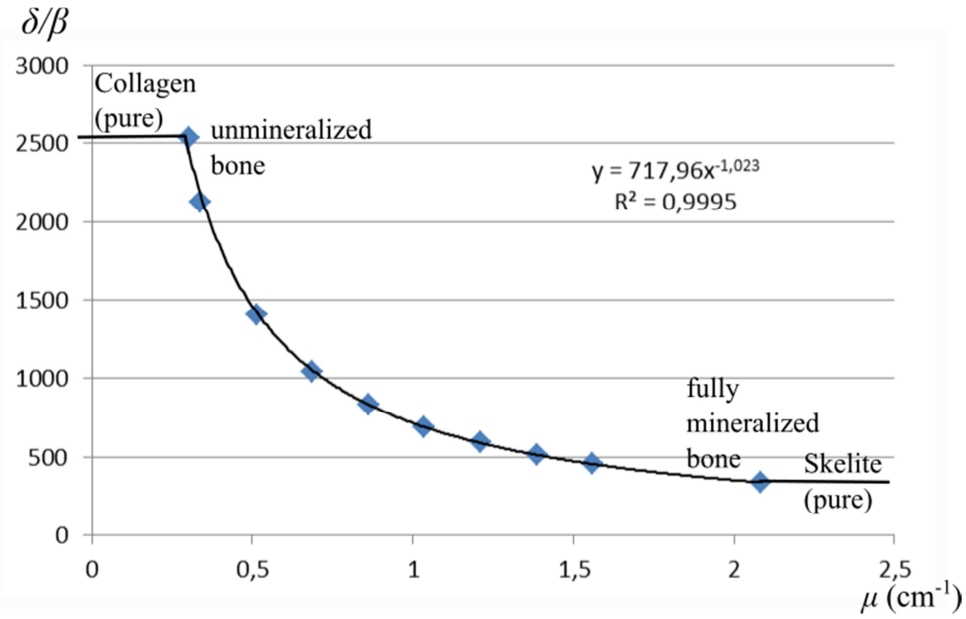

Figure 2: Functional relationship between the attenuation and the δ_n/β values at 30keV, used in method C.

2.b.vii. Phase tomography

Projections are acquired at several angles, for several sample-to-detector distances, using a high-resolution detector (Fast Readout Low Noise [FReLoN] camera). Phase retrieval is performed to extract the phase shift at each angular position. Then, a usual tomographic reconstruction algorithm (Filtered-Back Projection) enables to get a 3D-map of the refractive index of the object. It is performed using PyHST software developed at the ESRF, Grenoble, France (Mirone, Brun, Gouillart, Tafforeau, & Kieffer, 2014; Mirone, Wilcke, Hammersley, & Ferrero, 2008).

2.c. Data acquisition

Images were recorded at the ID19 beamline, ESRF (Grenoble, France). Beam energy was set at 30keV using a double-Si crystal monochromator. After passing through the sample, the X-ray beam is converted into visible light using a Gadox scintillator. This light is then recorded by a FReLoN camera, with a CCD of size 2048 x 2048 pixels (Labiche et al., 2007). For each of the nine samples, 2000 projections were acquired over a 360° range, with an exposure time of 0.4s, at four different sample-to-detector distances (namely 0.01, 0.33, 0.45, and 0.99m). The effective pixel size is here equal to 5µm. The field-of-view, of 10mm x 7mm, was limited by the monochromator in the vertical direction.

2.d. Data Reconstruction

Holotomographic acquisition results in a large amount of data: usually several thousands of projections, multiplied by 3 or 4 propagation distances. Classically, the workflow of the reconstruction of a single phase volume is the following:

- **Dark- and flat-fielding**

  Each acquired projection is first corrected, using the flat-field and the dark-field signals.

The flat-field corresponds to the image created by illuminating the detector with the beam, while removing the sample from the field of view. This aims at correcting the beam inhomogeneity and beam current variations. Depending on how long is the tomographic scan, several flat fields are recorded during a single scan.
The dark-field corresponds to the image produced when there is no beam and no sample. It aims at correcting the detector read-out dark-current background-noise. Several dark-current images are recorded once per tomographic scan, and the average signal is called the dark-field. The applied correction is:

$$I_{\text{corrected}} = \frac{I_{\text{acquired}} - I_{\text{dark}}}{I_{\text{flat}} - I_{\text{dark}}} \tag{3.2.13}$$

where $I_{\text{acquired}}$is the acquired signal,
$I_{\text{corrected}}$is the corrected signal,
I_{dark} is the average dark-current signal, and
I_{flat} is the flat-field signal.

- **Registration step**

Prior to the acquisition, the translation stage with the detector is aligned with the beam so that the sample remains in the same position in the image at each propagation distance. Nevertheless, residual shifts (a few pixels) can remain between the projections at different propagation distances, due to set-up vibrations or sample stage motor drift. To alleviate this misalignment, a registration of projections is required. This is performed at selected angles (usually every 100 projections or less), using a correlation-based method (maximization of the correlation coefficient), to determine the shifts between each distance, every 100 projections. For in-between projections, shift values are interpolated. As a result, one gets values of residual shifts between a propagation plane and the other propagation planes.

- **Selection of the reference plane**

The most stable propagation plane is deemed as the reference plane. It is determined by registering images taken during the scan to images taken at a few angles after the scan is complete, regarding how large are these shifts. Then, every single projection is shifted with the calculated value before the phase retrieval, so that the whole dataset is well-registered.

- **Choice of regularisation parameter**

Phase retrieval is first performed at one projection angle, for several regularisation parameters. The L-curve is automatically plotted. Then, the user should select the optimal regularisation value, before launching phase retrieval on every projection.

- **Phase retrieval**

The phase retrieval is parallelised with respect to the projection angle, which reduces computation time to a couple of minutes, depending on the number of projections to process, the size of the images, the number of distances used, and the availability of computing resources.

- **Tomographic reconstruction**

  Once all the phase projections are collected, the user should launch the tomographic reconstruction. This step has also been parallelised, and could take up to a few hours.

As one can see, this phase volume reconstruction requires several interventions of the user. For each reconstructed sample, the user should launch several Matlab scripts, while tuning parameters, to get a first phase map. Thus, a shell script is launched the phase retrieval on several machines, in parallel. This parallelisation is of paramount importance to save time in the reconstruction process. After making sure that all the phase maps are retrieved, the user should launch a shell script to have the whole volume reconstructed, on a GPU (Graphics Processing Unit).

In order to alleviate the reconstruction workload, the first contribution of this thesis was to automate the reconstruction workflow, so that no human intervention is required. All the steps described above were transparently linked, so that each step is executed automatically in sequence. The reference plane and the regularisation parameter are automatically estimated. One single Matlab script should be launched to get the final phase volume. This enables to faster reconstruct data, and possibly process larger amount of data. As an example, a large amount of teeth samples were imaged at the ID19 beamline, and reconstructed using this automated code (collaboration with Dr P. Zaslansky, Julius Wolff Institute, Charité-Universitätsmedizin Berlin, Berlin). The analysis of the reconstructed volumes is currently in progress, and become possible thanks to this automation.

2.e. Comparison of reconstruction algorithms

Comparison of the four reconstruction methods was performed on one slice from a scaffold seeded with cells. Each algorithm was assessed with respect to the others qualitatively (regarding image quality) and quantitatively (regarding the histograms of the reconstructed image). Hence, the reconstruction method that offers the best combination of image quality and accuracy was used to determine quantitative parameters of the samples.

2.f. Quantitative 3D-parameters extraction

The reconstructed volumes were segmented based on the histogram, so that each fraction (Skelite, soft tissue, cells, air) of the sample can be separated from the others. To this aim, we modeled each modes of the histogram by a Gaussian function. Each threshold was chosen by determining the intersection of two fits. For the peak corresponding to the cell, the fit was sometimes difficult. In such case, we found the local minimum around the peak to determine the thresholds. Then, 3D quantitative parameters were extracted from each segmented part. The volume fractions were determined by simple calculation of the number of voxels in each compartment. Thanks to this, we can access the total sample volume (**TV**), the mineralized volume (**MV**), the immature bone volume (**IBV**), the cells volume (**CV**), and some volume filling fractions such as the fraction of mineralized volume (**MV/TV**), the fraction of immature bone volume in the scaffold pore space (**IBV/(TV-MV)**) and the fraction of the scaffold pore space volume filled with cells (**CV/(TV-MV))**.

Additionally, the local thickness (Hildebrand & Ruegsegger, 1997; Martín-Badosa et al., 2003) of the different fractions that composed the samples were calculated. This yields measurements of the mean thickness of the mineralized scaffold (**M.Th**), the mean thickness of immature bone (**IB.Th**), and also the mean thickness of the cells (**C.Th**).

3. Results

3.a. Qualitative comparison of regularized algorithms, on a slice of the sample seeded with OBs in a sufficient quantity

In this section, we compared qualitatively the presented regularised phase retrieval methods. The results are presented on a slice of a sample, seeded with osteoblasts, where the bone cells are clearly visible.

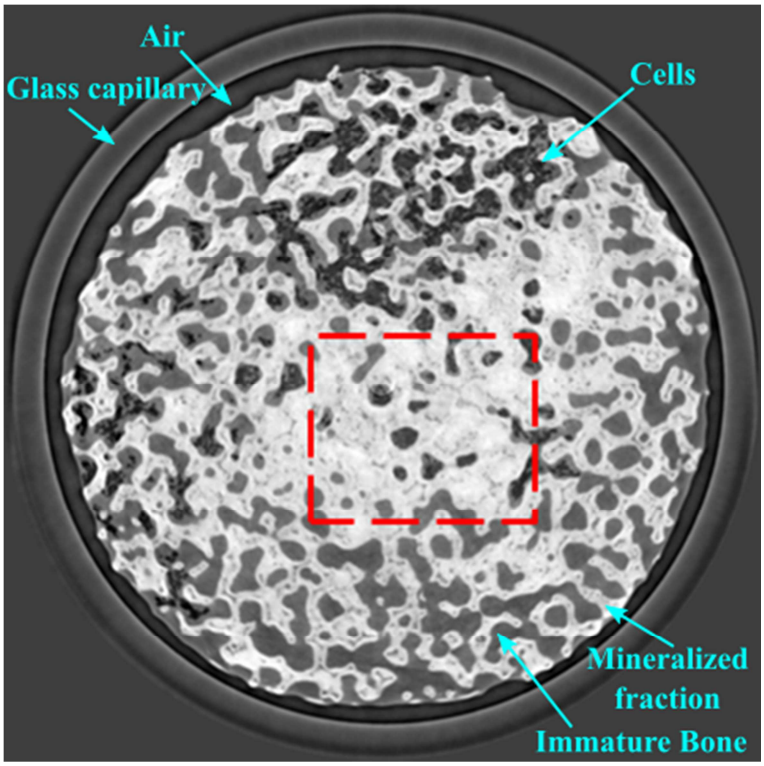

Figure 3: Reconstructed slice of a sample filled with OBs, using method A (homogeneous mixed approach). The dashed selection corresponds to the crop in Figure 4.

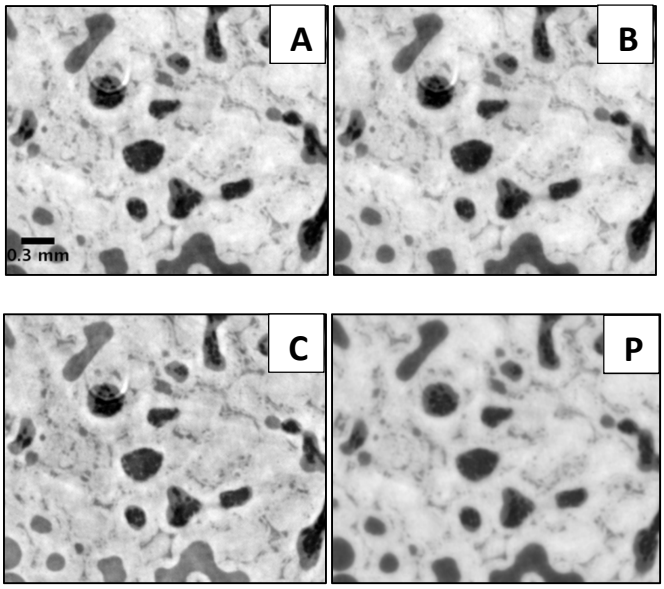

Figure 4: Crop of a reconstructed slice, using [A] homogeneous mixed approach, [B] heterogeneous mixed approach with thresholding, [C] heterogeneous mixed approach with functional relationship and [P] Paganin's algorithm. The scale bar corresponds to 0.3mm. The dimensions of the crop are 2.90mm by 2.42mm.

Figure 4 shows a crop (2.90mm x 2.42mm) of a reconstructed slice (Figure 3), using the homogeneous regularisation [A], the heterogeneous regularisation with the threshold [B], using the functional relationship between attenuation and phase [C], or using Paganin's method [P] (see Section 2.b.vi). Undesired phase contrast fringes around immature bone (collagen) are noticeable in reconstructions performed using methods **A** and **C**. Method **P** gives a reconstruction blurred with respect to those obtained using other regularized methods. From a visual point of view, method B seems the best since it avoids undesired remaining phase contrast fringes, while providing a sharp image.

3.b.Quantitative comparisons of regularized algorithms, on a slice of the sample seeded with OBs in a sufficient quantity (histogram-based study)

We reconstruct grey level images that correspond to $-\frac{2\pi}{\lambda}\delta_n$. The grey values were shifted in order to set air to zero (due to a slight offset also present in the attenuation tomograms), and then converted into mass densities, using the formula of (Guinier, 1994)

$$\delta_n \approx 1.35 \times 10^{-6} \rho \times \lambda^2 \qquad (3.3.1)$$

The mass density ρ is expressed in g/cm^3, and the wavelength λ in Å.

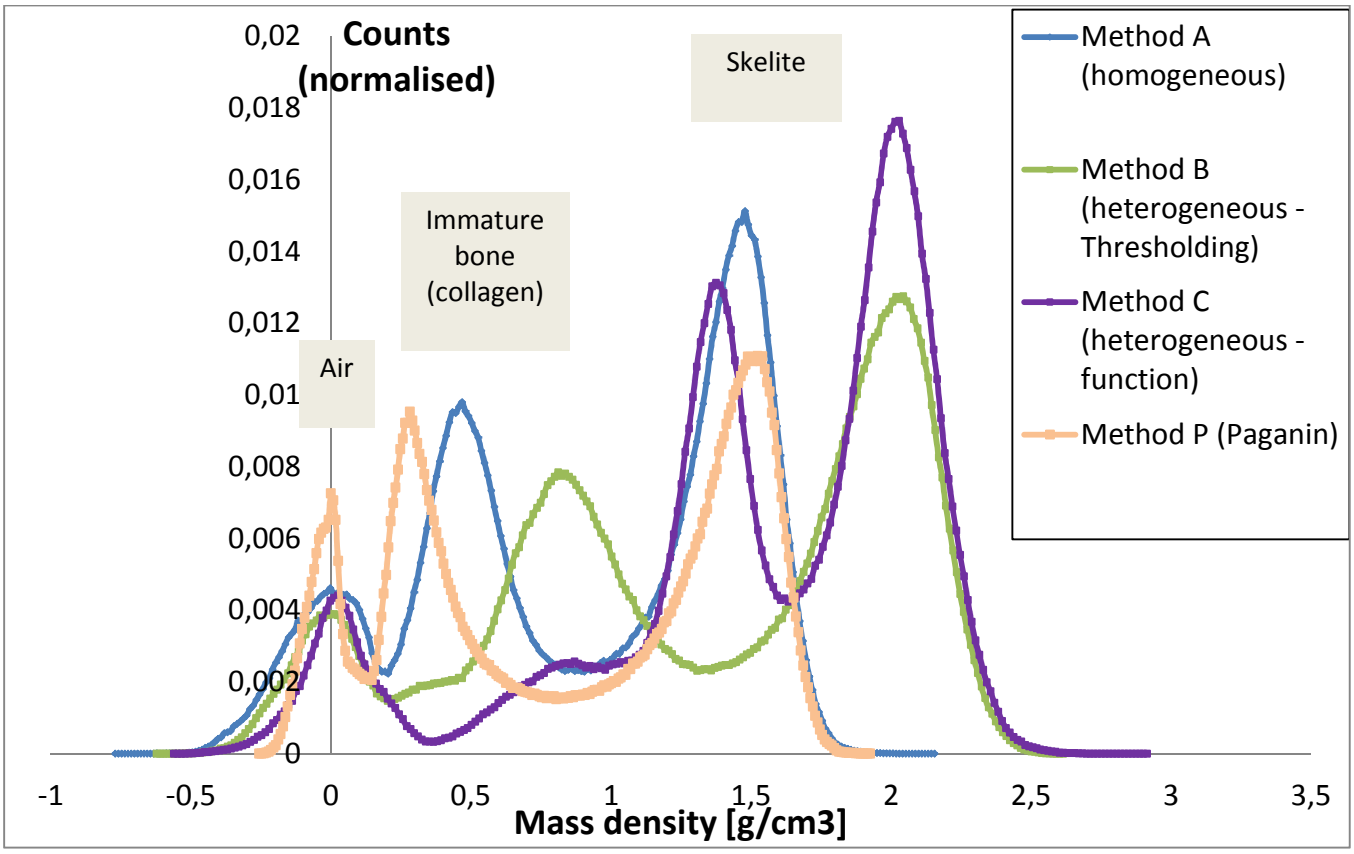

Figure 5: Histograms of the mass density, for the same reconstructed slice, using the four methods describe above (see *Materials and Methods*). Grey levels histograms were converted into mass density and readjust to set air to zero. The studied slice corresponds to a sub-volume equal to 0.33mm^3.

Figure 5 shows histograms of the mass density, for one same slice of a sample seeded with OBs, using the four methods describe above (see Section 3.b.vi). Using methods A and P, only 3 modes are distinguishable in the histogram, while this studied slice contains 4 major materials: Skelite©, immature bone, cells (OBs) and air. Four modes are actually visible using methods B and C, but method B appears more quantitative. Actually, immature bone (similar to collagen or soft tissue) has a theoretical mass density of 1.06g/cm^3 [ICRU-44] and Skelite© a mass density around 1.80g/cm^3. Thus, we choose method B to perform quantitative parameters extraction. Actually, as we showed in the last two parts, this method appears as the best trade-off between qualitative and quantitative reconstruction.

3.b.i. Comparison between samples, using the same reconstruction method ("method B")

Using method B, we reconstructed all of the nine volumes. Then, we compute their histograms, as showed in Figures 6, 7 and 8.

The histograms of samples seeded with OBs (Figure 6) present 4 peaks: the first corresponds to the air. The second (small, and not present in sample A) corresponds to the osteoblasts, that we can

see by eyes in the 3D reconstruction, and whose quantity is varying from one sample to another. The third and fourth mode of the histogram corresponds respectively to the immature bone, and the Skelite. Corresponding mass densities are in good agreement with our expectations: for this group, we found an average mass density for the immature bone of 0.699 ± 0.02 g/cm^3 and an average mass density for Skelite equal to 1.865 ± 0.03 g/cm^3 (to be compared to the theoretical values of 1.80g/cm^3 for Skelite, and around 1.00g/cm^3 for soft tissues).

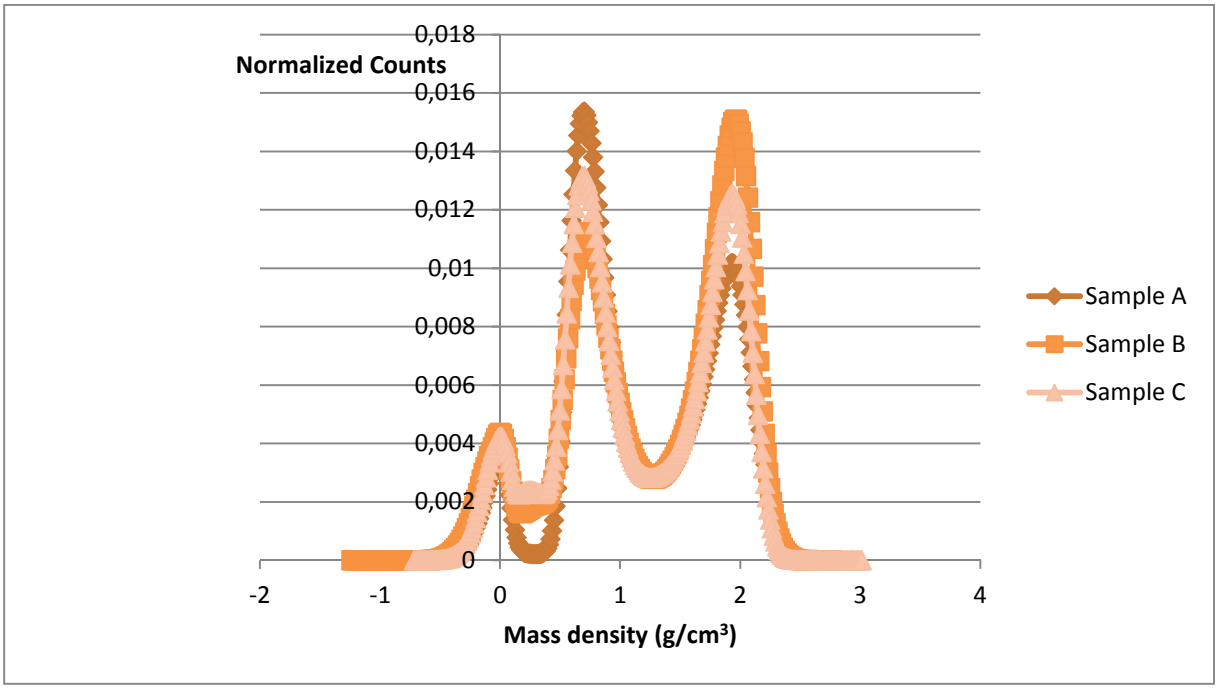

Figure 6: Histograms of the three samples containing OBs.

The samples seeded with pre-OCs are considered as control samples, since pre-OCs only cannot induce bone resorption by themselves. The second peak does not correspond to the immature bone, because the corresponding mass density is really too low. For this group, we found an average density for Skelite equal to 1.831 ± 0.10 g/cm^3. The lowest peak has a mass density of 0.209 ± 0.10 g/cm^3 (Figure 7). For this group of samples, we noticed a high variability of scaffolds mass densities, unlike in the two other groups.

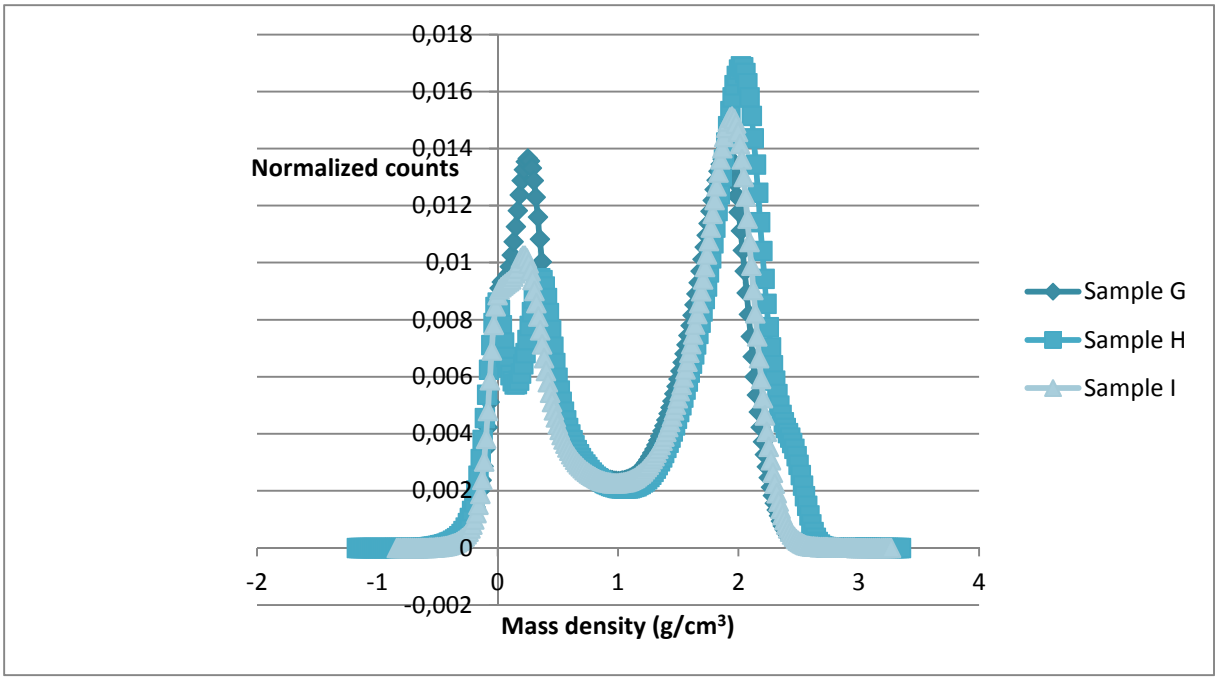

Figure 7: Histograms of the three samples containing pre-OCs.

Figure 8 shows the mass densities histograms of samples seeded with both OBs and pre-OCs. We observed that, unlike in scaffolds seeded with OBs, very few cells are visible in these samples. For this group, we found an average mass density for immature bone of 0.688 ± 0.05 g/cm^3 and an average density for Skelite equal to 1.811 ± 0.02 g/cm^3. We expect that pre-OCs balance minerals quantity between Skelite and immature bone, so that the Skelite becomes fairly less mineralized, contrary to the soft tissues that become more mineralized.

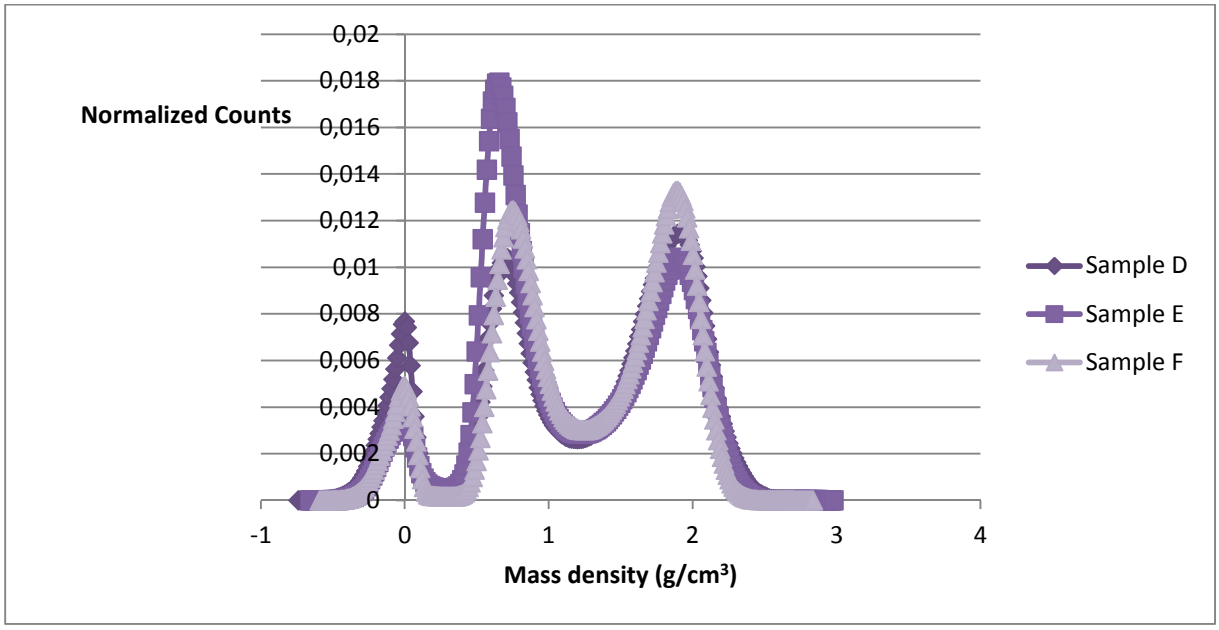

Figure 8: Histograms of the three samples containing OBs and pre-OCs.

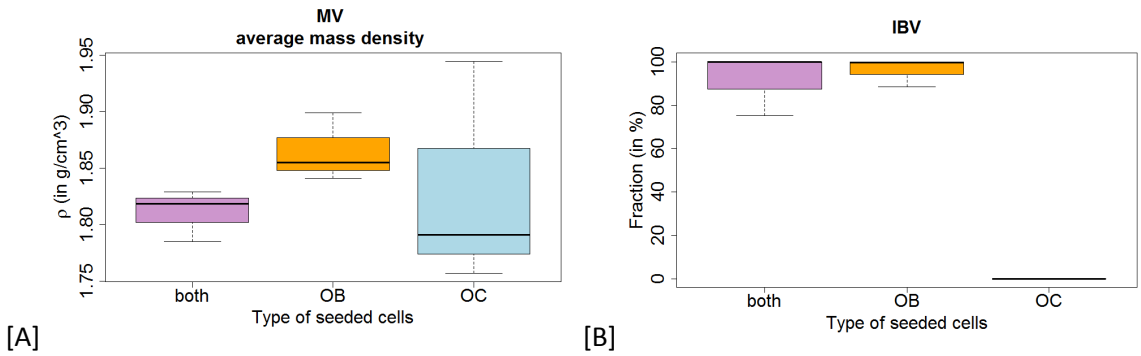

Figure 9: Mineralized volume average mass density (in g/cm^3) [A] and Immature Bone fraction (in %) [B] for each group, as a function of the type of seeded cells (OBs+pre-OCs, OBs and pre-OCs respectively).

This trend can be confirmed by the average mass density of mineralized fraction (Figure 9A), but not by mineralized volume fraction (Figure 9A). These results should be taken with caution regarding the high standard deviations of the measurements, and the small amount of samples for a meaningful statistical study.

3.c. Quantitative parameters extracted from reconstruction using a heterogeneous regularisation

The 3D images were segmented into 4 phases: air, cells (C), soft tissue composed of collagen or immature bone (IB), scaffold or mineral (M). The following parameters were computed:

TV: Total Volume
MV: Mineralized Volume
IBV: Immature Bone volume
MV/TV: Mineralized volume fraction (fraction of Skelite in the sample)
IBV / (TV – MV): Volume filled with soft tissue, when extracting hard parts.
CV / (TV – MV): Volume filled with cells, when extracting hard parts – available space for cells.
M.Th, IB.Th, C.Th: average 3D local thickness of each phase.

	Fraction (in %)			Local thickness (in µm)		
Sample	**MV/TV**	**IBV/(TV-MV)**	**CV/(TV-MV)**	**M.Th**	**IB.Th**	**C.Th**
OBs	44.7 +/- 5.0	98.2+/-8.9	5.1 +/- 4.3	121.4 +/- 20.3	176.0 +/- 29.0	60.8 +/- 2.1
OBs + pre-OCs	46.4 +/- 1.9	91.7 +/- 14.3	0.45 +/- 0.60	123.66 +/- 20.27	206.23 +/- 43.38	64.71 +/- 26.26
pre-OCs	48.5 +/- 2.7	0 +/- 0	0 +/- 0	150.4 +/- 13.8	0 +/- 0	0 +/- 0

Table 3: Summary of the measurements (fractions and local thickness) for each group.

Table 3 summarizes the different parameters extracted for each group. The column “MV/TV” represents the mineralized volume fraction, “IBV / (TV – MV)” the volume fraction filled with soft tissue, when extracting hard parts, and “CV/ (TV – MV)” the volume fraction filled with cells, when extracting hard parts. The mean thickness and thickness distribution of each part were computed according to a method specifically developed to this aim for trabecular bone characterization (Hildebrand & Ruegsegger, 1997). The cells were included into the immature bone part, before thickness calculation of immature bone part, to avoid irrelevant holes left by cells.

The average mass density of each part was computed after the thresholding. Grey levels images correspond to the quantity $-\frac{2\pi}{\lambda}\delta_n$, and were converted into mass densities using the Equation (3.3.1).

As an example, Figure 10 shows a 3D rendering of a scaffold, in grey levels, seeded with OBs (in pink).

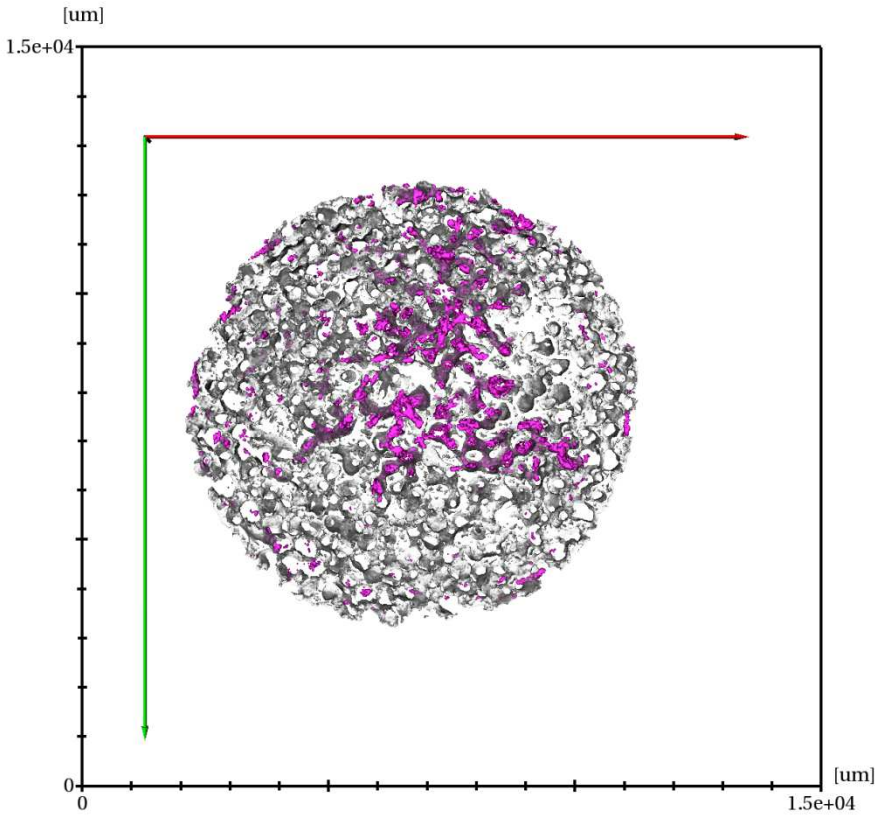

Figure 10: 3D rendering of a scaffold (in grey level), seeded with OBs (in pink).

3.d.ANOVA

The ANOVA test (ANalysis Of Variance) is statistical test used to determine, in this example, if the type of seeded cells has actually a significant influence on the different measured parameters (volumes and thicknesses). If a difference is detected, the Tukey’s HSD (Honest Significant Difference) test is employed post-hoc to determine which groups were different from each other on a selected measured parameter.

For each measurement, we performed an ANOVA to determine if the volumes or thickness are significantly related to the type of the samples (seeded with OBs, seeded with pre-OCs, seeded with bot OBs and pre-OCs). We call "group" all the scaffolds that are seeded with the same type of cells. Thus, in our study, we have 3 groups (scaffolds seeded with OBs, scaffolds seeded with pre-OCs and scaffolds seeded with both OBs and pre-OCs).

There appeared to be some differences in the volumes of Skelite, soft tissues and cells, the thickness of the Skelite, soft tissue and cells, between the groups. We want to determine if these differences are significant, by performing an ANOVA (with a confidence level of 95%).

Parameter of interest	P-value	Confidence
Mass density of MV	0.5833	
Mass density of IBV	0.7328	
MV	0.448	
IBV	2.831 *10^-5	***
CV / (TV - MV)	0.1861	
M.Th	0.1808	
IB.Th	0.1024	

Table 4: p-values and confidence determined by the ANOVA, for different parameters of interest. *** stands for a confidence level higher than 95%.

From the results given by the ANOVAs (Table 4), we can deduce that none of the parameters are significantly related to the type of seeded cells, except the volume of Immature Bone. This is to be expected since OBs are responsible for new bone formation.

3.d.i. Outlier detection

On Figure 9, the average mineralized fraction mass density of one sample seeded with pre-OCs seems to be an outlier, because a bit higher than the other values. To verify this numerically, we compute the first quartile (Q1), the third quartile (Q3) and the interquartile range (IQR). We chose to define an outlier as a value lying above Q1+1.5xIQR or below Q3-1.5xIQR, according to a widespread statistical definition. For this dataset, the quartiles are the following:

Quartile	0%	25%	50%	75%	100%
Average mineralized fraction mass density (g/cm^3)	1.76	1.79	1.83	1.85	1.94

We found that the IQR was equal to 0.064, thus, the highest value of this dataset, 1.94, is not an outlier according to this definition. Nevertheless, being detected as an outlier is not sufficient argument to be excluded from a study. In the latter case, the image quality of the reconstruction is also worth considering.

4. Discussion

In this chapter, we compared several quantitative phase retrieval methods for the analysis of bone scaffolds seeded with bone cells. In most studies, the single distance Paganin's phase retrieval algorithm is used (Hesse et al., 2014; Marinescu et al., 2013; Mohammadi et al., 2014). In a previous work, we discussed how to select the best δ_n/β parameter in the Paganin's algorithm according to the feature of interest in the image (Rositi et al., 2013, 2014). Some other studies compare different phase retrieval methods (Burvall, Lundström, Takman, Larsson, & Hertz, 2011; Langer, Cloetens, Guigay, & Peyrin, 2008; Yan, Wu, & Liu, 2011), with different contrast models. However, our results show that the choice of the phase retrieval algorithms and regularisation has a great impact both on the qualitative and quantitative analysis of the image. This work allowed the selection of the best algorithm in the sense that it provides the best separation between different material components in the object as well as sharp details in the image. To our knowledge, there has not been such study in the past.

The method selected in this study is based on a more sophisticated model since it assumes a multi-material prior on the object, built from the attenuation scan. It enables to distinguish the cells from the soft tissue and from the Skelite. Nevertheless, only OBs are visible using this method, not the pre-OCs. We cannot tell at this stage if the pre-OCs are present or if contrast is insufficient, however, since radiation damage to the samples has prevented us from validating this by performing histological analysis on the same samples.

We expected Skelite porosity to be roughly the same in every sample. In practice, it was not the case: we observed a much higher thickness of the Skelite in some samples, and with a high variability. These variations could be attributed to the manufacturing process. The number of samples is also very low in this study. Nevertheless, mean thicknesses of the scaffolds are in good agreement with those reported in (M Langer et al., 2010b). Here, the ANOVA did not reveal any significant difference in the thickness of the mineralized phase due to the different cell cultures. However, we should be careful with these results, since we only have 3 samples per group. To achieve more accurate statistics, more samples would have to be included, so that there are around 10 samples per group. The limitation in number of samples has mainly been due to limited access to synchrotron radiation X-rays for phase contrast imaging. Using the protocol described here, more data can be added to the statistical analysis as more images of this kind of scaffolds become available.

Concerning the diameter of the cells, according to literature, the human osteoblasts are supposed to be around 20-30µm in diameter. Here, the average diameter is close to 60µm. This can be explained by the facts that the cells are clustered. Moreover, the OBs are well visible because they are trapped in the bone matrix. We did not attempt to separate osteoblasts from their neighbors, since this is a difficult problem in itself, and it is outside the scope and purpose of this work.

Human pre-OCs are multi-nuclei cells that contain around five nuclei, for a total diameter around 150-200µm. In the images presented here, we cannot distinguish pre-OCs from other tissues. This might be

due to the pre-OCs either getting washed out from the scaffolds during the different steps of culture and imaging, or alternatively they are also embedded in the immature bone matrix but the contrast is not sufficient to distinguish them.

In the OCs group, we see (Figure 10A) that the Mineralized fraction density is a bit lower, but not significantly so, than in the other groups. This could be explained by the reconstructed image quality that seems to be worst for this group. It could be due to samples moving during the acquisition, since each samples of a group were scanned simultaneously.

Immature bone volume fractions closed to 100% correspond to samples that are very filled with newly formed bone and cells. This confirms the activity of OBs. Bone resorption would have been expected for (OBs + pre-OCs) samples, but not really visible here. We can see that the control group, seeded with pre-OCs, was not at all filled with newly formed bone, which is in good agreement with our expectation.

5. Conclusion

This chapter presents the comparison of several regularised phase reconstruction methods for propagation-based phase tomography.

In this work, we showed that the design of the prior is crucial for the quality of the reconstruction (reduction of some artefacts). Although there is not a unique solution to design the prior, it influences the quality of the reconstruction.

With respect to the previous work (M Langer et al., 2010b), more advanced regularised methods enables to see and quantify the cells, which were not visible in the previous study. We were able to separate them from the rest of the sample.

We presented a framework for statistical analysis of this kind of cell cultures. Nevertheless, the limited number of samples did not enable to find any significant differences in the different tested culture conditions. Acquisition of further data is mainly limited by a restricted access to synchrotron radiation facilities. However, the whole imaging and analysis protocol should allow completing the dataset used for statistical analysis, and thus improving it, as soon as new experimental data becomes available.

References

Burvall, A., Lundström, U., Takman, P. A. C., Larsson, D. H., & Hertz, H. M. (2011). Phase retrieval in X-ray phase-contrast imaging suitable for tomography. *Optics Express*, *19*(11), 10359–76. doi:10.1364/OE.19.010359

Cancedda, R., Cedola, A., Giuliani, A., Komlev, V., Lagomarsino, S., Mastrogiacomo, M., … Rustichelli, F. (2007). Bulk and interface investigations of scaffolds and tissue-engineered bones by X-ray microtomography and X-ray microdiffraction. *Biomaterials*, *28*(15), 2505–24. doi:10.1016/j.biomaterials.2007.01.022

Chapman, D., Thomlinson, W., Johnston, R. E., Washburn, D., Pisano, E., Gmür, N., … Sayers, D. (1997). Diffraction enhanced x-ray imaging. *Physics in Medicine and Biology*, *42*(11), 2015–2025. doi:10.1088/0031-9155/42/11/001

Cloetens, P., Ludwig, W., Baruchel, J., Van Dyck, D., Van Landuyt, J., Guigay, J. P., & Schlenker, M. (1999). Holotomography: Quantitative phase tomography with micrometer resolution using hard synchrotron radiation x rays. *Applied Physics Letters*, *75*(19), 2912. doi:10.1063/1.125225

Cloetens, P., Pateyron-Salomé, M., Buffière, J. Y., Peix, G., Baruchel, J., Peyrin, F., & Schlenker, M. (1997). Observation of microstructure and damage in materials by phase sensitive radiography and tomography. *Journal of Applied Physics*, *81*(9), 5878. doi:10.1063/1.364374

David, C., Nöhammer, B., Solak, H. H., & Ziegler, E. (2002). Differential x-ray phase contrast imaging using a shearing interferometer. *Applied Physics Letters*, *81*(17), 3287. doi:10.1063/1.1516611

del Río, M. S., & Dejus, R. J. (2004). XOP 2.1: A new version of the X-ray optics software toolkit. *Proc. Synchrotron Radiation Instrumentation: Eighth International Conference, (Edited by T. Warwick et Al.)*, (American Institute of Physics, San Fransisco), 784–787.

Gillespie, P. A. (2007). *Silicon complexes in silicon doped calcium phosphate biomaterials*. Queen's University, Kingston, Ontario, Canada.

Goodman, J. W. (2005). *Introduction to Fourier Optics*. New York: Roberts and Company Publishers.

Guigay, J. P., Langer, M., Boistel, R., & Cloetens, P. (2007). Mixed transfer function and transport of intensity approach for phase retrieval in the Fresnel region. *Optics Letters*, *32*(12), 1617. doi:10.1364/OL.32.001617

Guinier, A. (1994). *X-ray Diffraction in Crystals, Imperfect Crystals, and Amorphous Bodies*. *Acta crystallographica. Section A, Foundations of crystallography* (Vol. 57). New York, NY. doi:10.1021/ja01079a041

Hesse, B., Langer, M., Varga, P., Pacureanu, A., Dong, P., Schrof, S., … Peyrin, F. (2014). Alterations of mass density and 3D osteocyte lacunar properties in bisphosphonate-related osteonecrotic human jaw bone, a synchrotron µCT study. *PloS One*, *9*(2), e88481. doi:10.1371/journal.pone.0088481

Hildebrand, T., & Ruegsegger, P. (1997). A new method for the model-independent assessment of thickness in three-dimensional images. *Journal of Microscopy*, *185*(1), 67–75. doi:10.1046/j.1365-2818.1997.1340694.x

Holy, C. E., Shoichet, M. S., & Davies, J. E. (2000). Engineering three-dimensional bone tissue in

vitro using biodegradable scaffolds: investigating initial cell-seeding density and culture period. *Journal of Biomedical Materials Research*, *51*(3), 376–82.

Hutmacher, D. W. (2000). Scaffolds in tissue engineering bone and cartilage. *Biomaterials*, *21*(24), 2529–2543. doi:10.1016/S0142-9612(00)00121-6

Komlev, V. S., Mastrogiacomo, M., Pereira, R. C., Peyrin, F., Rustichelli, F., & Cancedda, R. (2010). Biodegradation of porous calcium phosphate scaffolds in an ectopic bone formation model studied by X-ray computed microtomograph. *European Cells & Materials*, *19*, 136–46.

Labiche, J.-C., Mathon, O., Pascarelli, S., Newton, M. A., Ferre, G. G., Curfs, C., … Carreiras, D. F. (2007). Invited article: the fast readout low noise camera as a versatile x-ray detector for time resolved dispersive extended x-ray absorption fine structure and diffraction studies of dynamic problems in materials science, chemistry, and catalysis. *The Review of Scientific Instruments*, *78*(9), 091301. doi:10.1063/1.2783112

Langer, M., Cloetens, P., Guigay, J.-P., & Peyrin, F. (2008). Quantitative comparison of direct phase retrieval algorithms in in-line phase tomography. *Medical Physics*, *35*(10), 4556. doi:10.1118/1.2975224

Langer, M., Cloetens, P., Hesse, B., Suhonen, H., Pacureanu, A., Raum, K., & Peyrin, F. (2014). Priors for X-ray in-line phase tomography of heterogeneous objects. *Philosophical Transactions of the Royal Society A: Mathematical, Physical and Engineering Sciences*, *372*(2010), 20130129–20130129. doi:10.1098/rsta.2013.0129

Langer, M., Cloetens, P., Pacureanu, A., & Peyrin, F. (2012). X-ray in-line phase tomography of multimaterial objects. *Optics Letters*, *37*(11), 2151–3. doi:10.1364/OL.37.002151

Langer, M., Cloetens, P., & Peyrin, F. (2010). Regularization of phase retrieval with phase-attenuation duality prior for 3-D holotomography. *IEEE Transactions on Image Processing : A Publication of the IEEE Signal Processing Society*, *19*(9), 2428–36. doi:10.1109/TIP.2010.2048608

Langer, M., Liu, Y., Tortelli, F., Cloetens, P., Cancedda, R., & Peyrin, F. (2010). Regularized phase tomography enables study of mineralized and unmineralized tissue in porous bone scaffold. *Journal of Microscopy*, *238*(3), 230–9. doi:10.1111/j.1365-2818.2009.03345.x

Marinescu, M., Langer, M., Durand, A., Olivier, C., Chabrol, A., Rositi, H., … Wiart, M. (2013). Synchrotron radiation X-ray phase micro-computed tomography as a new method to detect iron oxide nanoparticles in the brain. *Molecular Imaging and Biology : MIB : The Official Publication of the Academy of Molecular Imaging*, *15*(5), 552–9. doi:10.1007/s11307-013-0639-6

Martín-Badosa, E., Amblard, D., Nuzzo, S., Elmoutaouakkil, A., Vico, L., & Peyrin, F. (2003). Excised bone structures in mice: imaging at three-dimensional synchrotron radiation micro CT. *Radiology*, *229*(3), 921–8. doi:10.1148/radiol.2293020558

Mastrogiacomo, M., Papadimitropoulos, A., Cedola, A., Peyrin, F., Giannoni, P., Pearce, S. G., … Cancedda, R. (2007). Engineering of bone using bone marrow stromal cells and a silicon-stabilized tricalcium phosphate bioceramic: evidence for a coupling between bone formation and scaffold resorption. *Biomaterials*, *28*(7), 1376–84. doi:10.1016/j.biomaterials.2006.10.001

Mirone, A., Brun, E., Gouillart, E., Tafforeau, P., & Kieffer, J. (2014). The PyHST2 hybrid distributed code for high speed tomographic reconstruction with iterative reconstruction and a priori knowledge capabilities. *Nuclear Instruments and Methods in Physics Research Section B: Beam Interactions with Materials and Atoms*, *324*, 41–48. doi:10.1016/j.nimb.2013.09.030

Mirone, A., Wilcke, R., Hammersley, A., & Ferrero, C. (2008). PyHST—high speed tomographic reconstruction. *SciSoftlast Visit March*.

Mohammadi, S., Larsson, E., Alves, F., Dal Monego, S., Biffi, S., Garrovo, C., … Dullin, C. (2014). Quantitative evaluation of a single-distance phase-retrieval method applied on in-line phase-contrast images of a mouse lung. *Journal of Synchrotron Radiation*, *21*(Pt 4), 784–9. doi:10.1107/S1600577514009333

Momose, A., Takeda, T., Itai, Y., & Hirano, K. (1996). Phase–contrast X–ray computed tomography for observing biological soft tissues. *Nature Medicine*, *2*(4), 473–475. doi:10.1038/nm0496-473

Olivo, A., & Speller, R. (2007). A coded-aperture technique allowing x-ray phase contrast imaging with conventional sources. *Applied Physics Letters*, *91*(7), 074106. doi:10.1063/1.2772193

Paganin, D., Mayo, S. C., Gureyev, T. E., Miller, P. R., & Wilkins, S. W. (2002). Simultaneous phase and amplitude extraction from a single defocused image of a homogeneous object. *Journal of Microscopy*, *206*(1), 33–40. doi:10.1046/j.1365-2818.2002.01010.x

Rositi, H., Frindel, C., Langer, M., Wiart, M., Olivier, C., Peyrin, F., & Rousseau, D. (2013). Information-based analysis of X-ray in-line phase tomography with application to the detection of iron oxide nanoparticles in the brain. *Optics Express*, *21*(22), 27185–96. doi:10.1364/OE.21.027185

Rositi, H., Frindel, C., Wiart, M., Langer, M., Olivier, C., Peyrin, F., & Rousseau, D. (2014). Computer vision tools to optimize reconstruction parameters in x-ray in-line phase tomography. *Physics in Medicine and Biology*, *59*(24), 7767–75. doi:10.1088/0031-9155/59/24/7767

Snigirev, A., Snigireva, I., Kohn, V., Kuznetsov, S., & Schelokov, I. (1995). On the possibilities of x-ray phase contrast microimaging by coherent high-energy synchrotron radiation. *Review of Scientific Instruments*, *66*(12), 5486. doi:10.1063/1.1146073

Stachewicz, U., Qiao, T., Rawlinson, S. C. F., De Macedo Almeida, F. V., Li, W.-Q., Cattell, M., & Barber, A. H. (2015). 3D imaging of cell interactions with electrospun PLGA nanofiber membranes for bone regeneration. *Acta Biomaterialia*. doi:10.1016/j.actbio.2015.09.003

Tortelli, F., Pujic, N., Liu, Y., Laroche, N., Vico, L., & Cancedda, R. (2009). Osteoblast and osteoclast differentiation in an in vitro three-dimensional model of bone. *Tissue Engineering. Part A*, *15*(9), 2373–83. doi:10.1089/ten.tea.2008.0501

Turner, L. D., Dhal, B. B., Hayes, J. P., Mancuso, A. P., Nugent, K. A., Paterson, D., … Peele, A. G. (2004). X-ray phase imaging: Demonstration of extended conditions for homogeneous objects. *Optics Express*, *12*(13), 2960. doi:10.1364/OPEX.12.002960

Weber, L., Langer, M., Tavella, S., Ruggiu, A., & Peyrin, F. (2016). Quantitative evaluation of regularized phase retrieval algorithms on bone scaffolds seeded with bone cells. *Physics in Medicine and Biology*, *61*(9), N215–N231. doi:10.1088/0031-9155/61/9/N215

Yan, A., Wu, X., & Liu, H. (2011). Robustness of phase retrieval methods in X-ray phase contrast imaging: a comparison. *Medical Physics*, *38*(9), 5073–80. doi:10.1118/1.3618731

Chapter IV: Phase nano-tomography of bone

In this chapter, we focus on phase nano-tomography, with applications in bone imaging. We present the entire imaging process, from the set-up to the reconstruction method. We present a new registration tool, enabling an efficient, and automated, registration of the projections acquired at different distances that is more robust than previous methods. We experimentally demonstrate its efficiency on real data, acquired on the ID16A beamline. Then, we show that the nanometric resolution provided by this beamline is a precious tool to analyze the structure of the bone, through a feasibility study combining several analysis tools.

Table of contents

1. Phase-contrast nano-tomography

X-ray phase contrast tomography has been of a growing interest in biology and medical fields, because it enables non-destructive 3D imaging of samples with a very high sensitivity and sub-millimetric resolution. This sensitivity and resolution are also due to the relatively large propagation distances (phase contrast increases as the propagation distance increases), and the cutting-edge instrumentation and detectors employed. Nevertheless, some structures can only be resolved at a nanometric scale. Even if phase-contrast micro-tomography has been widely used, nano-tomography has only emerged during the last few years, using magnified phase contrast imaging (Langer et al. 2012b). Like phase contrast micro-tomography, it uses multiple distance propagation-based imaging, except that the incoming beam is not parallel but divergent. Beam divergence and different sample-to-detector distances induce different magnification factors of the projections recorded by the detector. In practice, the projections are rescaled to the highest magnification factor that gives the smallest pixel size. Phase retrieval is finally performed according to the presented scheme: a linear least-squares method to roughly assess roughly the phase, and a non-linear conjugate gradient (NLCG) method to refine it.

1.a. Set-up of phase nano-CT

The set-up of phase nano-CT is depicted in Figure 1. Kirkpatrick-Baez (KB) mirrors, curved reflective optics, focus the incoming parallel X-ray beam (X) horizontally and vertically onto a focal spot (F). D_1 is the distance between the focal spot and the sample (S), and D_2 is the propagation distance, *i.e.* the distance between the sample and the detector.

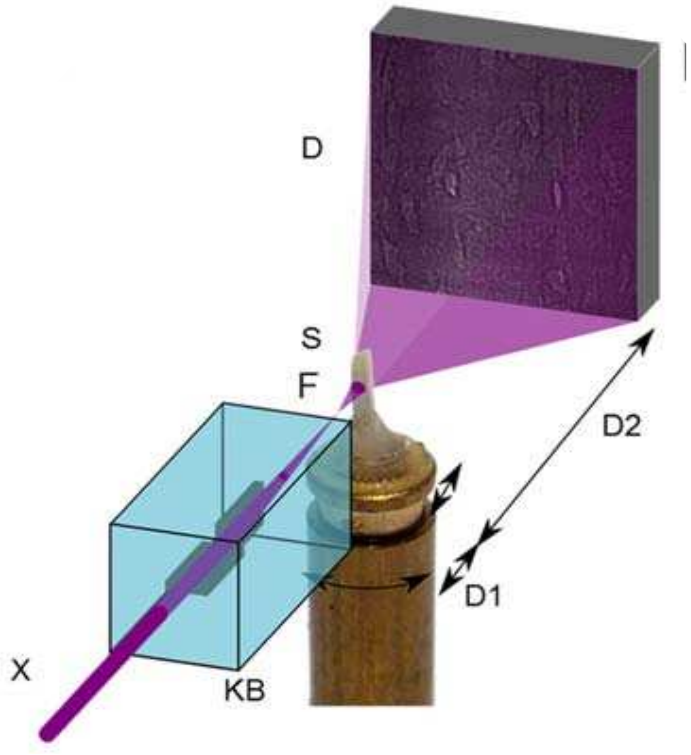

Figure 1: Set-up of phase nano-CT. The incoming parallel X-ray beam (X) is focused onto a focal spot (F) using specific optical elements. D_1 is the distance between the spot (F) and the sample (S), and D_2 is the propagation distance.

Since the beam is spatially divergent, recording an image at sample-to-detector distance D_2 also induces, apart from phase contrast, magnification of the projections (Figure 1). The magnification M is expressed using the well-known Thales' theorem:

$$M = \frac{D_1 + D_2}{D_1}. \tag{4.1.1}$$

We obtain projections with different magnification by modifying the propagation distance. In practice, the detector and the focus point are fixed, *i.e.* $D_1 + D_2$ is kept constant. It means that the sample is moving along a translation stage to get images with different magnifications, unlike in the parallel set-up, where the detector moves further from the sample.

It is noteworthy that in this case of divergent beam, the wave front is spherical; the spherical wave Fresnel diffraction phenomenon can be seen as a plane wave illumination problem at the defocusing distance D (Guigay, 1977), defined by:

$$\frac{1}{D} = \frac{1}{D_1} + \frac{1}{D_2}, \tag{4.1.2}$$

which is equivalent to:

$$D = \frac{D_1 D_2}{D_1 + D_2} = \frac{D_2}{M}. \tag{4.1.3}$$

In a few words, this defocusing distance D is an equivalent of the propagation distance that takes into account the magnification. The distances $[D_1, D_2, \dots, D_k, \dots, D_K]$ denote the equivalent propagation distances, and are indexed by k, with K the total number of distances used. We write:

$$\forall k \in [1{:}K], D_k = \frac{D_{1,k} \,.\, D_{2,k}}{D_1 + D_2}, \tag{4.1.4}$$

with:

$$\forall k \in [1{:}K], \;\; D_{1,k} + D_{2,k} = D_1 + D_2 = \text{constant}. \tag{4.1.5}$$

In practice, we acquire projections for a complete rotation of the sample, at different propagation distances D_k.

1.b. Phase nano-CT workflow

As an introduction, we present the workflow of phase nano-imaging, a bit similar to phase micro-CT, from the data acquisition to the analysis.

ACQUISITION:

a. Projections of the sample are acquired for a complete range of tomographic angle (from 0 to 180°).
b. At the end of the scan, projections are recorded at 0, 90 and 180°.
c. The acquisition step is repeated K times, K being the number of propagation distances.

PRE-PROCESSING:

d. Images are flat-fielded.
e. One check if the sample moved during the scan, by comparing images during and after the scan, for every distance (also called “planes”). The most stable plan is considered as the “reference plane”.
f. The projections are rescaled to the same smallest pixel size (in other words, to the highest magnification).
g. The projections of different propagation planes, at every 100th projection angle, are registered.
h. To get the shifts values for every projection angles, a polynomial interpolation of the shifts is performed.
i. Application of the shifts to every projections.

PHASE RETRIEVAL:

j. First estimate using a chosen linear least-squares method (presented in Section 2.b)
k. Refinement using non-linear conjugate gradient method (presented in Section 2.c)

TOMOGRAPHIC RECONSTRUCTION

It can be done using the FBP, or an algebraic reconstruction method.

POST-PROCESSING

As an example, one can perform filtering, segmentation, etc.

DATA ANALYSIS

1.c. Experiments

During my thesis, I was involved in ten experiments, for a total of 128 *shifts*. A shift being 8 hours of beamtime, this represents 6 months of working days. Among all these experiments, one was running on ID16A, through the Long-Term Project MD830. From February 2014 to May 2016, we were allocated 56 shifts, enabling the imaging of bone samples, for research in various fields:

- bone micro- and nano-structure description (Lacuno-Canalicular Network morphology, extracellular matrix mineralization and collagen fibril arrangement) for bone undergoing particular pathology (osteoporosis, osteoarthritis, osteonecrosis) or mechanical stress (in collaboration with K. Raum and P. Varga, both from Charité, Berlin, Germany)
- bone quantitative ultrasound imaging and bone biomechanics (in collaboration with P. Laugier and Q. Grimal, both from LIB, Paris, France)
- effects of compression tests on bone micro-pillars (in collaboration with Ph. Zysset from EPFL, Lausanne and U. Wolfram & Jakob Schwiedrzik, both from ISTB, Berne, Switzerland)
- nano-architecture of bone, in normal, immobilized and disease-affected bone (in collaboration with H. Birkedal from Aarhus University, Aarhus, Denmark)
- gravity effect (and mechanical strain) on bone micro- and nano-structure, and, more recently, bone microvascularization (in collaboration with L. Vico and M.-H. Lafage-Proust, both from LBTO, Saint-Etienne, France) on ID19.

2. Phase retrieval in phase nano-CT

The phase retrieval process is similar to the one in phase micro-CT, described in the Chapter III. As pre-processing, the projections at different propagation distances are dark- and flat-fielded before being registered. In the case of phase nano-CT, the registration is harder: the projections should first being rescale to the same magnification factor, and the presence of multilayers monochromators induce strong regular patterns, which can make the registration fail. The non-linear contributions to the phase make the use of non-linear iterative algorithm mandatory, to improve the resolution of the retrieved phase maps.

2.a. Direct contrast model

To retrieve the phase information from the image recorded by the detector (which is a non-linear problem), and since we are still in the Fresnel diffraction regime, we can use the Contrast Transfer Function (CTF) (see Equation (2.1.19) in Chapter II). Nevertheless, for nano-tomography, propagation distances are relatively long compared to the pixel size. The near-field condition is not met any longer, so that the non-linear contribution of the phase cannot be neglected. In this case, the CTF is rewritten by adding a non-linear term to the measured intensity, leading to:

$$\tilde{I}_D(\boldsymbol{f}) = \delta_{Delta}(\boldsymbol{f}) - 2\cos(\pi\lambda D|\boldsymbol{f}|^2)\,\tilde{B}(\boldsymbol{f}) + 2sin(\pi\lambda D|\boldsymbol{f}|^2)\tilde{\varphi}(\boldsymbol{f}) + \tilde{I}_{NL,D}(\boldsymbol{f}). \tag{4.2.1}$$

Phase retrieval is thus performed in two stages. A first initial guess of the phase is determined using a classical linear least-squares method, described in Section 5 of Chapter II, and recall in the next section. This first guess corresponds to the linear part of the retrieved phase, but is not sufficient to provide good image quality at such high resolution. Consequently, the non-linear term is determined recursively, using a non-linear conjugate gradient algorithm, described in Section 2.c. It improves the recovery of the high frequencies of the phase, and thus its resolution.

2.b. Linear least squares method

2.b.i. General method

We consider a global image formation model:

$$\tilde{I}_{D_k}(\boldsymbol{f}) = \tilde{c}_k(\boldsymbol{f}).\tilde{\chi}(\boldsymbol{f}) \tag{4.2.2}$$

Where I_{D_k} is the recorded intensity, c_k a contrast transfer function, χ the quantity to be retrieved and $\tilde{}$ denotes the Fourier transform.

The Wiener filtering gives, for the previous problem, an estimate of $\tilde{\chi}(\boldsymbol{f})$, noted $\hat{\tilde{\chi}}(\boldsymbol{f})$, that minimizes the mean quadratic error:

$$\hat{\tilde{\chi}}(\boldsymbol{f}) = \frac{\tilde{c}_k{}^*(\boldsymbol{f}).\tilde{I}_{D_k}(\boldsymbol{f})}{\tilde{c}_k{}^*(\boldsymbol{f}).\tilde{c}_k(\boldsymbol{f}) + \alpha_{Wiener}}, \tag{4.2.3}$$

where $\tilde{c}_k{}^*$ denotes the conjugate of $\tilde{c}_k$, and α_{Wiener} is a regularization parameter, related to the spectral density of the noise.

In the multi-distance acquisition, the least-squares method consists in minimizing the quantity quadratic error ε, with:

$$\varepsilon = \sum_{k=1}^{K} \int \left\| \tilde{c}_k(\boldsymbol{f}).\hat{\tilde{\chi}}(\boldsymbol{f}) - \tilde{I}_{D_k}(\boldsymbol{f}) \right\|^2 d\boldsymbol{f}. \tag{4.2.4}$$

This leads to:

$$\hat{\tilde{\chi}}(\boldsymbol{f}) = \frac{\frac{1}{K}\sum_{k=1}^{K} \tilde{c}_k(\boldsymbol{f}).\tilde{I}_{D_k}(\boldsymbol{f})}{\left(\frac{1}{K}.\sum_{k=1}^{K} \tilde{c}_k{}^*(\boldsymbol{f}).\tilde{c}_k(\boldsymbol{f})\right) + \alpha}. \tag{4.2.5}$$

2.b.ii. Homogeneous CTF model

The least-squares method, described previously can be applied on the CTF model, in order to solve the phase from recorded intensities. If we consider a pure phase object (*i.e.* no absorption), in the near-field regime, the Fourier transform of the intensity recorded by the detector at a distance D_k from the sample can be expressed as:

$$\tilde{I}_{D_k}(\boldsymbol{f}) = \delta_{Delta}(\boldsymbol{f}) + 2\sin(\pi\lambda D_k|\boldsymbol{f}|^2)\tilde{\varphi}(\boldsymbol{f}). \tag{4.2.6}$$

In most cases, we cannot assume a pure phase object, so that the absorption term cannot be neglected. In this case, our problem will have two unknowns: the absorption and the phase. However, the problem can be rewritten as a "one unknown-problem" by assuming that the sample is composed of one homogeneous material. The absorption is consequently proportional to the phase (*i.e.* the δ_n/β ratio is constant). In this case, the attenuation can be written as:

$$B(\boldsymbol{x}) = \frac{2\pi}{\lambda}\frac{1}{\delta_n/\beta}\int \delta_n(\boldsymbol{x}, z)\, dz = -\frac{1}{\delta_n/\beta}\varphi(\boldsymbol{x}) \tag{4.2.7}$$

leading to:

$$\tilde{I}_{D_k}(\boldsymbol{f}) = \delta_{Delta}(\boldsymbol{f}) + \left[2\frac{1}{\delta_n/\beta}\cos(\pi\lambda D_k|\boldsymbol{f}|^2) + 2\sin(\pi\lambda D_k|\boldsymbol{f}|^2)\right]\tilde{\varphi}(\boldsymbol{f}). \tag{4.2.8}$$

This is the expression of the intensity recorded by the detector at a distance D_k from the sample, assuming that the near-field condition is fulfilled, and the imaged object is homogeneous. The least-squares formulation becomes:

$$\begin{aligned} &\frac{1}{K}\sum_{k=1}^{K} 2\left(\frac{1}{\delta_n/\beta}\cos(\pi\lambda D_k|\boldsymbol{f}|^2) + \sin(\pi\lambda D_k|\boldsymbol{f}|^2)\right)^2 \hat{\tilde{\varphi}}(\boldsymbol{f}) \\ &\qquad = \frac{1}{K}\sum_{k=1}^{K}\left[\frac{1}{\delta_n/\beta}\cos(\pi\lambda D_k|\boldsymbol{f}|^2) + \sin(\pi\lambda D_k|\boldsymbol{f}|^2)\right]\tilde{I}_{D_k}(\boldsymbol{f}) \end{aligned} \tag{4.2.9}$$

This method can be used on phase nano-CT data, to determine the first estimate of the phase, which will be refined using a non-linear method.

2.b.iii. Extension of the Paganin's method to multi-distance acquisition

The Paganin's method (Paganin, Mayo, Gureyev, Miller, & Wilkins, 2002) expresses the phase shift, for an homogeneous object:

$$\varphi(\boldsymbol{x}) = \frac{1}{2}.\frac{\delta_n}{\beta}.\ln\left(\mathcal{F}^{-1}\left\{\frac{\mathcal{F}\left(\frac{I_{D_k}(\boldsymbol{x})}{I_0(\boldsymbol{x})}\right)}{1+\frac{D_k\delta_n\lambda\pi}{\beta}||\boldsymbol{f}||^2}\right\}\right), \tag{4.2.10}$$

where $I_{D_k}(\boldsymbol{x})$ is the intensity at a propagation distance D_k, $\mathcal{F}$ and $\mathcal{F}^{-1}$ denote the Fourier transform and its inverse respectively, $I_0(\boldsymbol{x})$ is the intensity at contact plane, δ_n/β is the ratio of the refractive index decrement to the absorption index, and λ is the wavelength of the beam.

For readability, we introduce the three following variables:

$$\tilde{I}_{norm,k}(\boldsymbol{f}) = \mathcal{F}\left(\frac{I_{D_k}}{I_0}\right)(\boldsymbol{f}) \tag{4.2.11}$$

$$\tilde{h}_k(\boldsymbol{f}) = 1+\frac{D_k\delta_n\lambda\,\pi}{\beta}||\boldsymbol{f}||^2 \tag{4.2.12}$$

and

$$\tilde{A}(\boldsymbol{f}) = \mathcal{F}\left\{\exp\left(\frac{2\beta}{\delta_n}\varphi(\boldsymbol{x})\right)\right\}(\boldsymbol{f}). \tag{4.2.13}$$

Combining Equations (4.2.10), (4.2.11) and (4.2.13) leads to:

$$\tilde{I}_{norm,k}(\boldsymbol{f}) = \tilde{A}(\boldsymbol{f}).\tilde{h}_k(\boldsymbol{f}). \tag{4.2.14}$$

Retrieving the phase from multi-distance measurements using the least squares method to the Paganin formula leads to the following estimate of the phase shift:

$$\hat{\varphi}(\boldsymbol{x}) = \frac{1}{2}.\frac{\delta_n}{\beta}.\ln\left(\mathcal{F}^{-1}\left\{\frac{\frac{1}{K}\sum_{k=1}^{K}\tilde{h}_k(\boldsymbol{f}).\tilde{I}_{norm,k}(\boldsymbol{f})}{\left(\frac{1}{K}.\sum_{k=1}^{K}\tilde{h}_k(\boldsymbol{f})^2\right)+\alpha}\right\}\right), \tag{4.2.15}$$

where α is an arbitrary regularization parameter.

In phase nano-CT, a first estimate of the phase can be determined using this Equation (4.2.15), before being refined using a non-linear method, for every projection.

2.c. Non-linear conjugate gradient methods

The idea behind conjugate gradient (CG) methods is to find a solution for quadratic functions. We showed previously that the least-squares method was employed to solve the linearized phase retrieval problem. Nevertheless, in the context of phase nano-CT, the non-linear contributions in the expression of the recorded intensity are greater due to the fact that the near-field condition is not met any longer. The first estimate of the phase, given by the least-squares method, is thus refined iteratively using a non-linear conjugate gradient (NLCG) method.

2.c.i. Principle of the method

The aim of a non-linear conjugate gradient algorithm is to minimize iteratively a non-linear function $J(r)$. This minimum can be a local minimum. The value of the local minimum is updated iteratively, according to:

$$r_{k+1} = r_k + \alpha_k s_k \tag{4.2.16}$$

where α_k is the steplength and s_k the conjugate gradient direction (search direction), updated recursively.

An iteration of such NLCG algorithm is designed as follow:

1. Find the steepest search direction
   The gradient gives the direction of the maximal increase of the function. Consequently, the steepest direction we choose is set as the opposite direction of the gradient direction, where we have the maximal decrease of the function:
   $$-g_k = -\nabla_r J(r_k) \tag{4.2.17}$$

2. Calculate the conjugate direction (*i.e.* the search direction) s_k, where β_k is calculated according to a chosen method described below.
   $$s_k = \begin{cases} -g_k & \text{if } k = 0 \\ -g_k + \beta_k s_{k-1} & \text{if } k \geq 1 \end{cases} \tag{4.2.18}$$

3. Get the optimal value for the step length α_k, by performing a line search:
   $$\alpha_k = \underset{\alpha}{\operatorname{argmin}} J(r_k + \alpha s_k) \tag{4.2.19}$$
   This will minimizes J along a line

4. Update of the solution r:
   $$r_{k+1} = r_k + \alpha_k s_k \tag{4.2.20}$$

2.c.ii. Calculation of the parameter β_k

Several formulas have been designed to compute the value of the parameter β_k, used in Equation (4.2.18), that allows to update the conjugate direction. Among all the existing formulas, four are well-known and widely employed, and a first one was specifically designed for phase retrieval in phase nano-CT. Originally, a conjugate gradient (CG) method was proposed by Hestenes and Stiefel to solve linear systems (Hestenes & Stiefel, 1952):

$$\beta_k^{HS} = \frac{g_k^T (g_k - g_{k-1})}{s_{k-1}^T (g_k - g_{k-1})} \tag{4.2.21}$$

Then, Fletcher and Reeves proposed the first non-linear CG method (Fletcher, 1964):

$$\beta_k^{FR} = \frac{\|g_k\|^2}{\|g_{k-1}\|^2} \tag{4.2.22}$$

A few years later, Polak and Ribière (Polak & Ribiere, 1969) and Polyak (Polyak, 1969) designed the following expression of β_k:

$$\beta_k^{PRP} = \frac{g_k^T(g_k - g_{k-1})}{\|g_{k-1}\|^2} \tag{4.2.23}$$

All these three methods are equivalent when applied to linear problem. For non-linear problems, it is admitted that the Fletcher-Reeves method is the easiest to implement, while the Polar-Ribière-Polak method converges faster and turns out to be quite efficient.

More recently, Dai and Yuan (Dai & Yuan, 1999) proposed a formula that presents a stronger convergence, with respect to the previous proposed methods:

$$\beta_k^{DY} = \frac{\|g_k\|^2}{s_{k-1}^T(g_k - g_{k-1})} \tag{4.2.24}$$

A few time later, P. Cloetens (unpublished) designed a formula that is based on the orthogonality of s_{k-1}:

$$\beta_k^{Clo} = \frac{g_k^T . s_{k-1}}{s_{k-1}^T . s_{k-1}} \tag{4.2.25}$$

More details on the conjugate gradient method can be found in the article of Shewchuk (1994) (Shewchuk, 1994). Whatever the formula used for the calculation of the value of β_k, it is admitted than the more optimal method has to be selected experimentally, depending on the data.

2.c.iii. Application to phase nano-CT

In this section, we present how the non-linear conjugate gradients are implemented at the ESRF.

All these five methods for β_k calculation, presented in the previous section, are implemented in the reconstruction code available at the ESRF. Experimentally, the last method (Equation (4.2.25)) is usually used and provides very satisfying results in most cases.

In our case, the functional $J(r)$ can be expressed as:

$$J(r) = \frac{1}{KR}\sum_{k=1}^{K}\sum_{r=1}^{R}\left|I_{D_k,meas}(r) - I_{D_k,calc}(r)\right|^2 \tag{4.2.26}$$

where K is the total number of distances, R is the total number of pixels of a projection, and $I_{D_k,meas}$ is the recorded intensity at a propagation distance D_k. $I_{D_k,calc}$ is the calculated intensity at a propagation distance D_k, using:

$$I_{D_k,calc}(r) = \left|T(r) * P_{D_k}(r)\right|^2 * j_0(r) \tag{4.2.27}$$

where P_{D_k} is the Fresnel propagator, defined in the Chapter II, Equation (2.1.9), T is the transmittance function of the object (see Chapter II, Equation (2.1.1)), and j_0 models the transfer function of the optics (determined experimentally).

The gradient of J is calculated as:

$$-g_k = -\frac{dJ(r)}{dT(r)} \tag{4.2.28}$$

We used typically 8 to 10 iterations for NLCG.

3. Registration of recorded images using mutual information

A well-known drawback of multi-distance acquisition is, as shown in step *g*. of the workflow (section 1.b), the need for projection registration within the distances. Actually, due to a possible misalignment of the camera and the sample through the beam axis, and possible vibrations of the moving motors, the projections are usually misaligned a few pixels. To perform the registration, we can use different methods, presented in this section. In phase nano-CT, we consider *rigid* registration (*i.e.* only translation and rotation) of multi-resolution images (*i.e*. different magnifications), and we limit to translation only (in both vertical and horizontal directions).

3.a. Correlation-based methods

Usually, correlation-based methods are employed at the ESRF, to perform the registration of the projections. Beforehand, the data are flat-fielded, and rescale to the same magnification factor, using the theoretical values of the magnification (Equation (4.1.1)). Then, the horizontal and vertical drifts of the projections are determined. In order to have the shift value for every single projection, without performing the registration for every projection, the calculated shifts are fitted with a polynomial function (Figure 2).

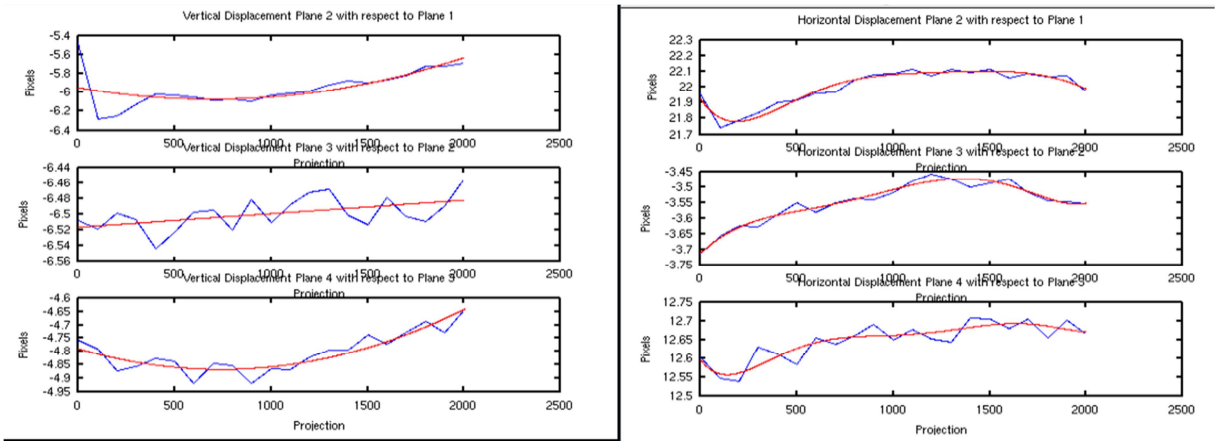

Figure 2: Example of shifts curves. The projection number is reported on the abscissa, and the shift value (in pixels) on the ordinate. The blue line is drawn from the measurements every 100 projections and the red curve corresponds to the polynomial fit. Note that the difference between measured and fitted values is less than one pixel in all plots, which is characteristic for a successful registration, and a stable scan.

Correlation-based methods consist in determining the shifts for which the correlation coefficient of the different projections is the highest. It performs quite well when it comes to phase micro-CT data. In phase nano-CT, the images usually suffer from strong and regular lines artefacts (due to the KB mirrors), as shown on Figure 3. In this case, the correlation-based method could fail (Figure 4), because of these regular strong patterns, still visible despite the flat-fielding.

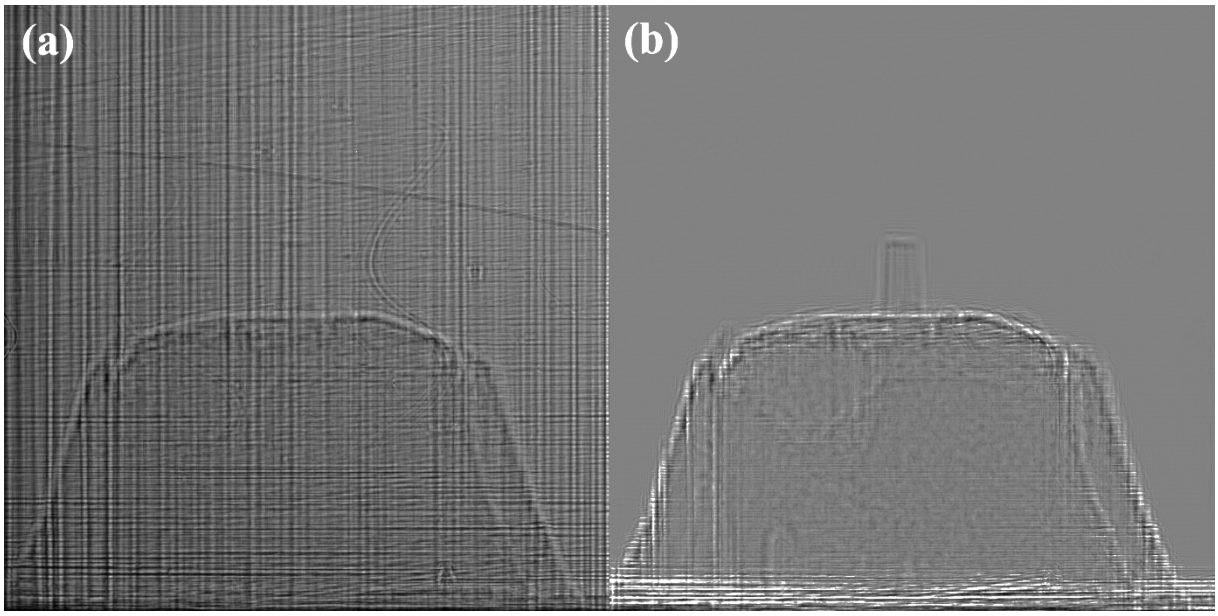

Figure 3: Projection of a bone micro-pillar (a) without and (b) with flat-fielding. The lines artefacts from the KB mirrors are clearly visible on (a), and attenuated on (b), but still visible. A projection is 2048 * 2048pixels. The effective pixel size, taking into account the magnification, is 39.27nm.

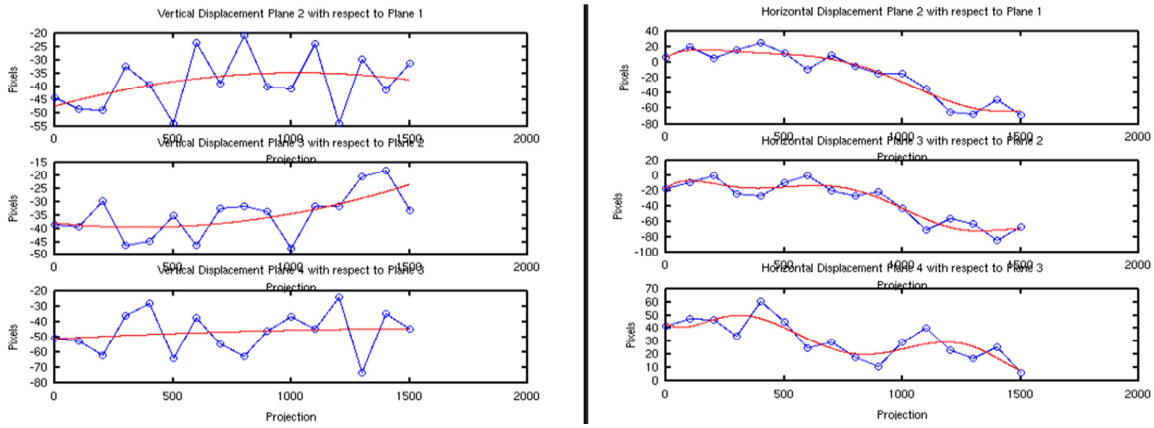

Figure 4: Example of the Figure 3, where the registration using a correlation-based method fails, most probably because of the artefacts induced by the KB mirrors. The vertical shifts are reported on the left, and the horizontal shifts on the right. We notice differences up to several tens of pixels between the measured (blue line) and the calculated (red line) values.

If the correlation-based method reveals unsuccessful, there is still a possibility to perform the registration automatically, by using the ImageJ plugin "Turbo Reg"[1], which performs a multi-resolution registration based on intensity (Thévenaz, Ruttimann, & Unser, 1998).

[1] http://bigwww.epfl.ch/thevenaz/turboreg/

Otherwise, the registration can be done manually, which makes it possible to align some projections by hand. Nevertheless, this method is still very time-consuming and operator-dependant, which is not convenient.

3.b.Mutual information-based method

Given the limitations of the intensity-based registration methods, we investigated another approach for the registration of Fresnel diffraction patterns, in collaboration with a trainee (Annika Hänsch). This new method is based on mutual information (MI), usually employed in multi-modality imaging, where the contrast can be different (Moddemeijer, 1989). The mutual information has the major advantage to be invariant to intensity changes, as inversion contrast.

Consider two images A and B. Their pixels are indexed by a and b, respectively. The MI index of A and B is expressed:

$$MI(A,B) = \sum_{a\epsilon A}\sum_{b\epsilon B} p_{AB}(a,b).\log\left(\frac{p_{AB}(a,b)}{p_A(a).p_B(b)}\right) \quad (4.3.1)$$

where $p_{AB}(a,b)$ is the joint probability distribution function of A and B, $p_A(a)$ and $p_B(b)$ the marginal probability distribution functions of A and B, respectively.

The MI index of two images can be null or positive; it is equal to 0 if the two images are independent, and increases with the similarity of the two images.

In our case, we can have different contrast because of remaining interference fringes. The idea behind this method was to lie on a morphological, geometry-based criterion, rather than an intensity-based criterion (as the correlation coefficient).

The software *Elastix* (Klein, Staring, Murphy, Viergever, & Pluim, 2010; Shamonin et al., 2013) was used to align, automatically and in parallel, the projections. Even if being not successful every time, this method has the major advantage of being fully automated. *Elastix* enables to use different similarity indexes, such as the MI, and can handle multi-resolution images. It was thus possible to take into account the magnification of the images, inherent to phase nano-CT projections. In this case, the magnification factor determined from the images, and not from the theoretical values. This method was integrated to the reconstruction process, and called via a new approach for shifts determination. Then, the shift determination of every projection is done by polynomial interpolation, as mentioned in the workflow.

As an example, Figure 5 shows an example where this new method outperforms the classical correlation approach. On the slice reconstructed with the classical approach (a), misalignment artefacts are clearly visible. On the contrary, the use of MI-based method improves a lot the image quality (b).

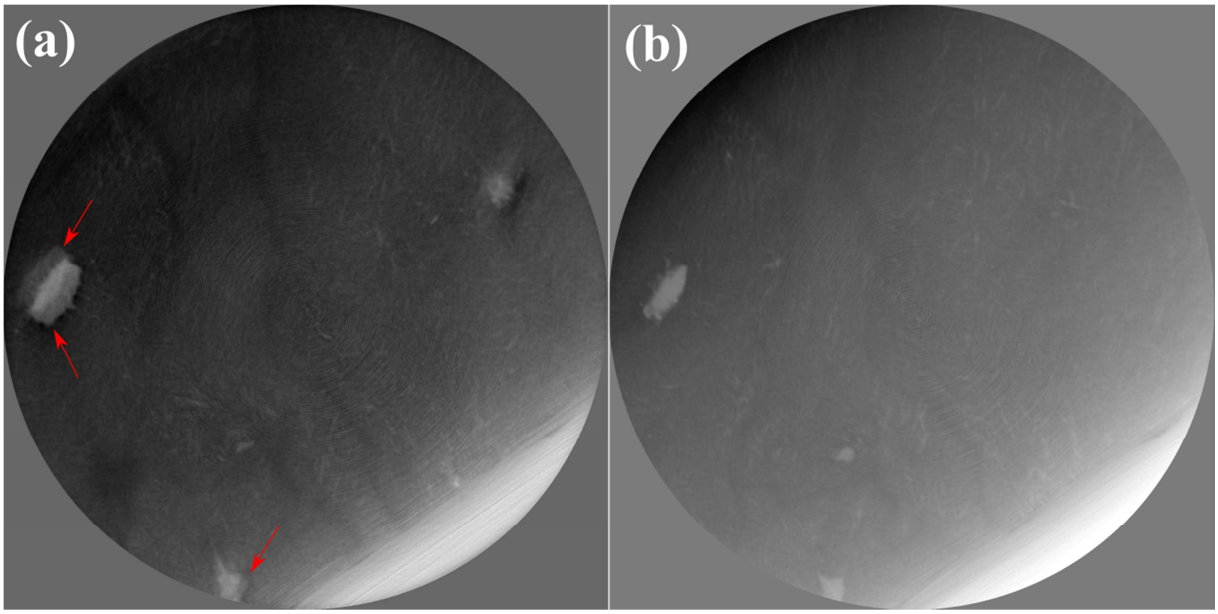

Figure 5: Reconstructed nano-CT slice of an osteoporotic sample, where registration of multiple distance projections were registered using (a) a correlation-based method, (b) a MI-based method. The pixel size is 60nm, and a slice is of size 122.88µm x 122.88µm. The red arrows highlight typical misalignments artefacts.

3.c. Application to bone micro-pillars

The bone micro-pillar samples were prepared at the Institute of Surgical Technology and Biomechanics (ITSB, Bern, Switzerland). A micro-pillar was cut out of a piece of ovine bone (Schwiedrzik et al., 2014). The acquisition was made at ID16A beamline (ESRF, Grenoble), in July 2015. The energy of the beam was set to 33.6keV. 2000 projections were acquired over a 180° range, with an exposure time of 0.4s per projection. The effective pixel size was equal to 25nm.

We reconstructed a 3D phase map of the sample using the Paganin's method, extended to multi-distance acquisitions using least-squares, followed by a 10-iteration NLCG. The δ_n/β ratio was set to 645, as calculated for cortical bone at 33.6keV. On this scan, we compared the classical correlation based method and the registration method using MI, described in Section 3. The results are shown on Figure 6, for two different heights. To better understand the presented slice, a 3D rendering of the whole sample is visible in Figure 7. We can see the micro-pillar on top of a larger base.

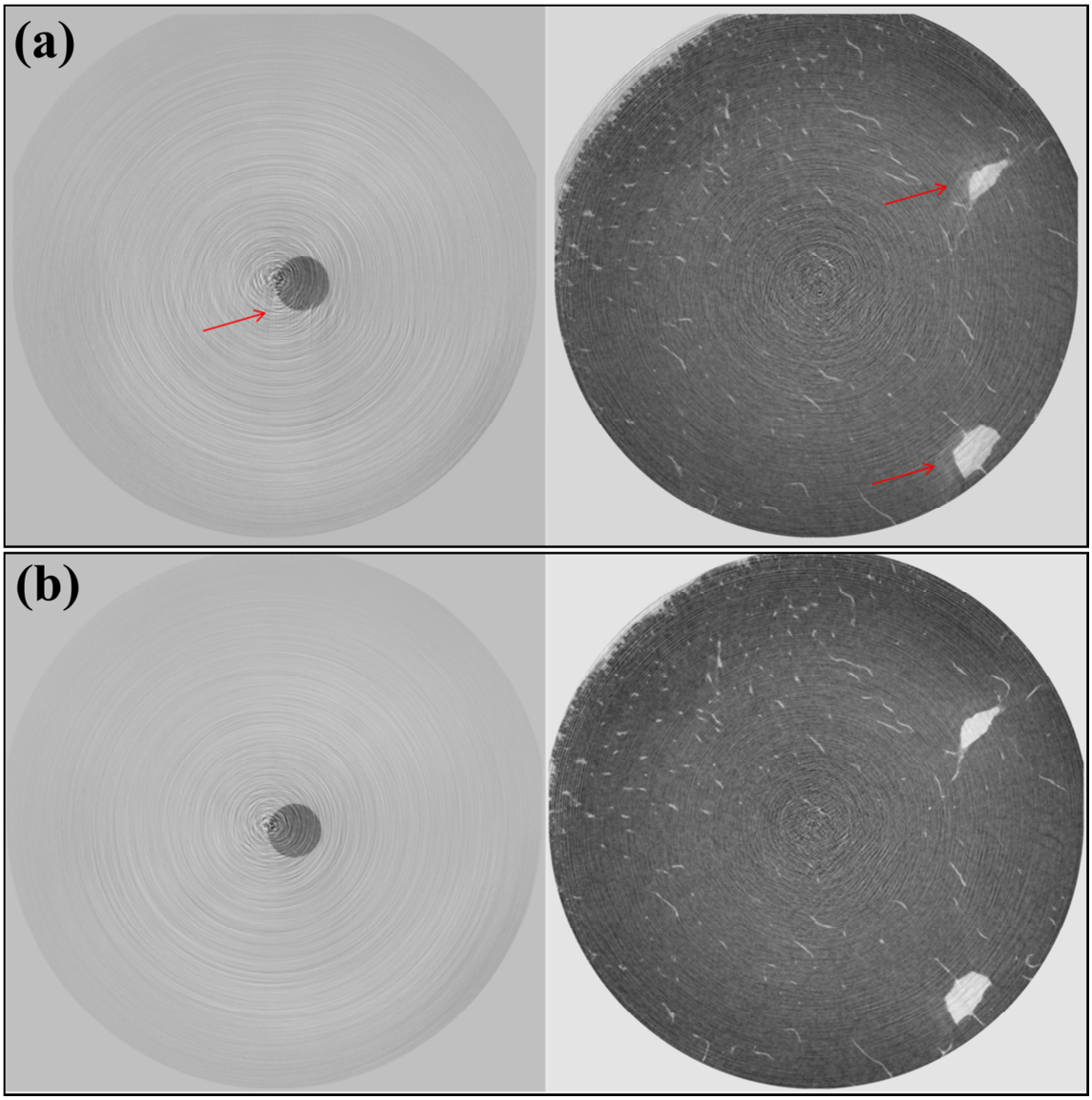

Figure 6: Example of phase δ_n volume after registering the projections using (a) a correlation-based method; (b) the MI-based method (*Elastix*). The left column shows a slice in the micro-pillar part, and the right column a slice in the base of the micro-pillar, made of bone. The red arrows highlight typical misalignments artefacts.

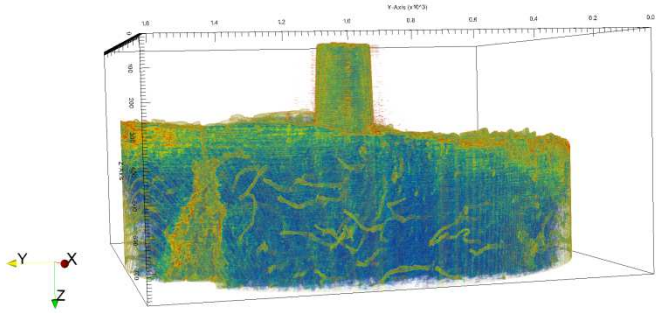

Figure 7: Volume rendering of the micro-pillar (*'istb_mp5_25nm_tomo3'*). The box is 51µm (X) by 51µm (Y) by 19.9µm (Z). A lacuna is visible on the bottom left of the base.

We see that the MI-based method clearly improve the registration, in addition to be fully automated. Nevertheless, it fails when registering projections containing only the micro-pillar, because of the interferences fringes (Figure 8). Thus, it is required, to correctly image this kind of samples, to keep the base of the pillar in the field of view, because bone lacunae are useful for registration.

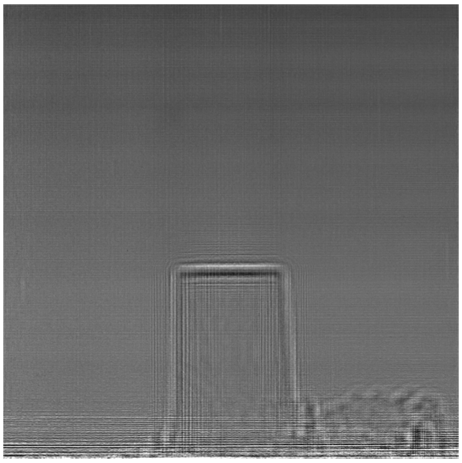

Figure 8: Acquired projection of the micro-pillar only, a more difficult case when it comes to registration.

4. Application of phase nano-CT to bone imaging

4.a. Introduction to the bone structure

To better understand the images presented in this chapter, we first introduce the human bone structure.

At the microscopic scale, human mature bone is composed of two types of bone, as depicted on Figure **9**:

- compact bone, also known as *cortical bone*, is dense. Its functional unit is the *osteon*.
- spongy bone, also known as *trabecular bone*, or cancellous bone, is porous (from 30% to 90% porosity). The functional unit of trabecular bone is the *trabecula*.

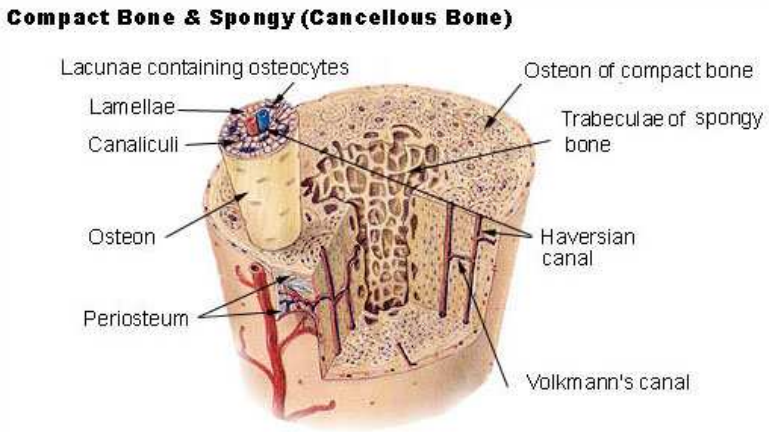

Figure 9: Macroscopic structure of bone (image from an online biological textbook, *boundless.com*.)

Here, we are mainly interested in human cortical bone, since it is the most important in strength and failure. As depicted in Figure 10 (left), human cortical bone is composed of *osteons*, basic constituting units created during bone remodelling around a Haversian canal containing nerves and vessels. The osteons are connected by interstitial lamellae. Osteonal and interstitial regions are separated by a so-called *cement line* (visible in Figure 12). A *lacuna* is a small space containing one bone cell (*osteocyte*). Lacunae are interconnected by small canals called *canaliculi*, as shown on Figure 10 (right). The system composed of the lacunae and the canaliculi is called the *lacuno-canalicular network* (LCN).

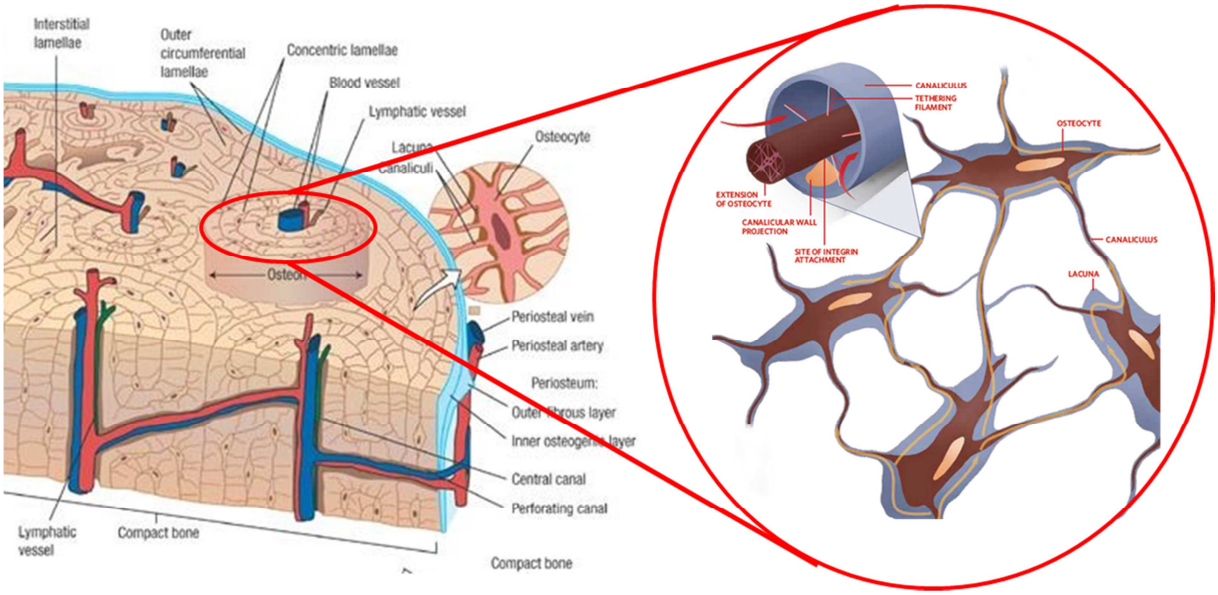

Figure 10: Macroscopic structure of bone (left), and zoom in on an osteon (right). Figure modified from (Taylor, Hazenberg, & Lee, 2007).

Chemically speaking, mature bone is composed by 70% of inorganic material (mainly hydroxyapatite), and 30% of organic material (90 % of which is collagen). The hydroxyapatite (HA) ensures the rigidity of bone, while the *collagen fibrils* ensure its flexibility.

4.b.Bone imaging with phase nano-CT

As a first exploratory investigation into changes of the bone ultrastucture, samples from a donor diagnosed with osteoarthritis, with osteoporosis and without diagnosis as control, were imaged.

The healthy samples were obtained from the diaphysis part of human femurs removed during multi-organ collection, which complied with the requirements of the French Transplant Administration. The donors were women aged from 85 to 92 years old. The diaphysis is the middle section of a long bone, made of cortical bone. Bone samples underwent a treatment (Biobank ®) consisting of supercritical carbon dioxide for delipidation, chemical bath in order to eliminate medullary proteins and gamma irradiation for sterilization. They were provided by the Laboratoire d'Imagerie Biomédicale (LIB, Paris, France), through the involvement of Dr P. Laugier and Dr Q. Grimal.

The osteoporotic and osteoarthritic bone samples were obtained from human femoral heads, removed during hip arthroplasty of donors performed at the Orthopedic Department of the Hospital of Orleans (CHR d'Orléans), within the involvement of Dr C.L. Benhamou.

All these samples (healthy, osteoporotic, osteoarthritic) were imaged using magnified phase nano-CT at the ID22-beamline (ESRF, Grenoble) in 2010, through the allocated beamtime MD-431. CT scans were acquired at 4 sample-to-detector distances. The energy of the X-ray beam was set to 17keV, and the effective pixel size varied from 35nm to 60nm, leading to a field-of-view from about 70 to 120µm, respectively. The detector was a FReLoN camera of size 2048 x 2048pixels. The smallest pixel size (35nm) was used to image healthy samples, while the larger pixel size (60nm) was used for the imaging of pathological samples. A set of 2500projections, over a 360° range, was acquired for healthy samples, with a counting time of 0.1s per projection. For osteoporotic and osteoarthritic samples, the number of projections was 3000, over the same range, with a counting time of 0.1s per projection. The average number of counts in the reference image, for each condition, is given in Table 1.

The data were reconstructed using the method detailed in Section 2. The registration was performed using the classical correlation-based method, or, later, MI-based method when appropriate. A first estimate of the phase map at each projection angle was determined using a linear least-square method, assuming a homogeneous composition (linear least-squares extended to Paganin's method). The δ_n/β value for these samples was set to 202, as calculated for cortical bone at 17keV. Then, the phase maps were refined using 10 iterations of the NLCG method. Finally, a filtered back-projection of these maps output the 3D phase volume.

4.c. Observations of the LCN

The high spatial resolution provided by phase nano-CT, with relatively large field-of-view, enables a precise observation of the LCN, in 3D. The LCN was segmented using a region growing (hysteresis thresholding) algorithm (Canny, 1986): a first threshold is applied on the image to select the lacunae from the rest of the volume. Then, the lacunae volume is refined by adding pixels that are connected to this volume, provided that they are below a second and higher threshold. Once the lacunae are segmented, they were analysed by determining the number of lacunae in a volume (and the volume fraction of bone occupied by lacunae), as well as the lacunae volume, shape and orientation, using tools developed by the team (Dong et al., 2014). As in this paper, small structures due to noise (less than 82µm^3) were removed.

4.c.i. Healthy sample

The total imaged volume is about 72µm x 72µm x72µm; we count 5 lacunae in this volume, which represents 0.34% of the total volume. A 3D rendering of the raw reconstructed volume, made using the software *Paraview* (Ahren, Geveci, & Law, 2005), is shown in Figure 11. This volume is similar, in terms of visible features, to the one found in the literature (Langer et al., 2012). The cement line is also distinguishable, and highlighted on the slice in Figure 12. The orientation analysis of the lacunae indicates elongated lacunae, with orientation vector $\vec{u} = 0\vec{X} + 1\vec{Y} + 4\vec{Z}$, *i.e.* lacunae principally oriented in the *z*-direction, as obvious on the rendering.

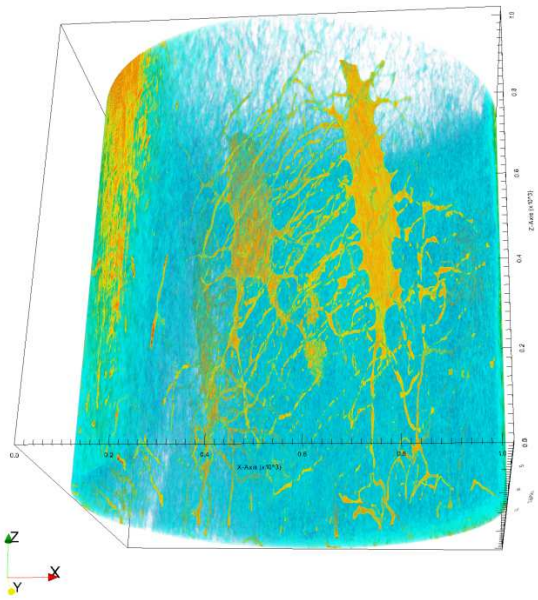

Figure 11: 3D rendering of the reconstructed phase volume (*'felip_228D_35nm_')* of size 71.68µm x 71.68µm x 71.68µm. The lacunae and the canaliculi are depicted in shades of yellow-orange.

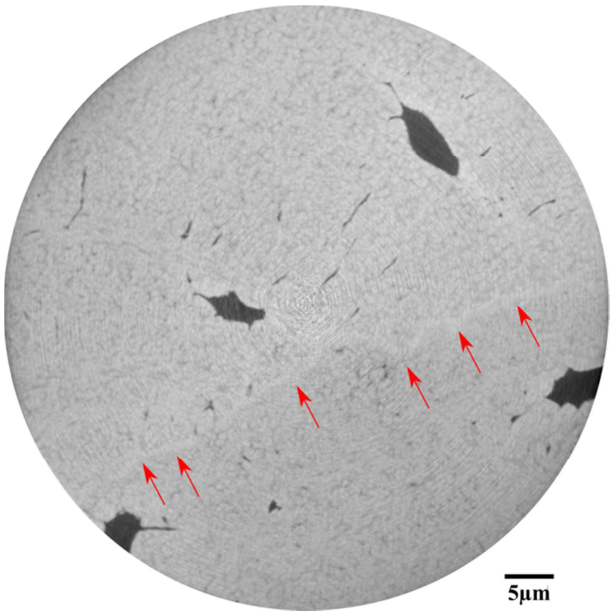

Figure 12: Reconstructed slice of a healthy sample. The image is 2048x2048 pixels, which corresponds to a physical size of 71.68µm x 71.68µm. The red arrows indicate the cement line.

4.c.ii. Osteoporotic sample

For the osteoporotic sample, we count 27 lacunae, representing 0.66% of the total volume. On the 3D rendering presented in Figure 13, we can observe ellipsoidal lacunae, as well as the presence of soft tissue in some lacunae, more visible in the reconstructed slice in Figure 14. The orientation analysis predicates elongated lacunae, oriented along the vector $31\vec{X} + 3\vec{Y} + 6\vec{Z}$, *i.e.* mainly oriented in the x-direction, as visible on the 3D rendering.

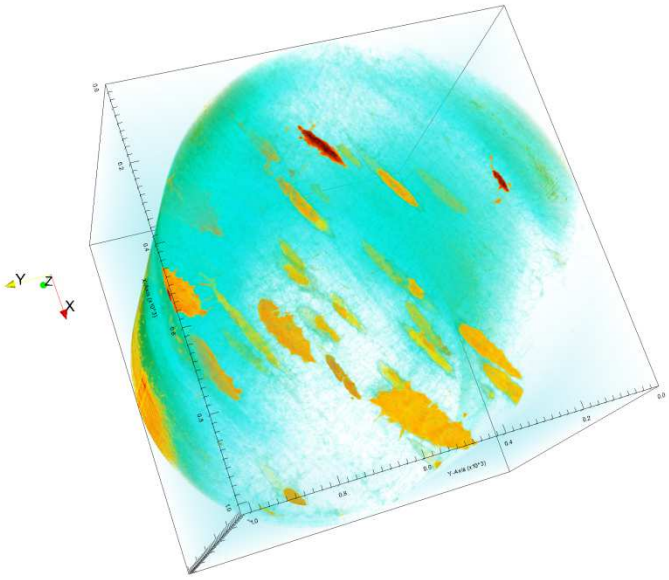

Figure 13: 3D rendering of the raw reconstructed volume (*'nano_OP237_a1_'*). It is rotated so that the elongate structure of the lacunae appears clearly. The box is of size 122.88µm x 122.88µm x 122.88 µm.

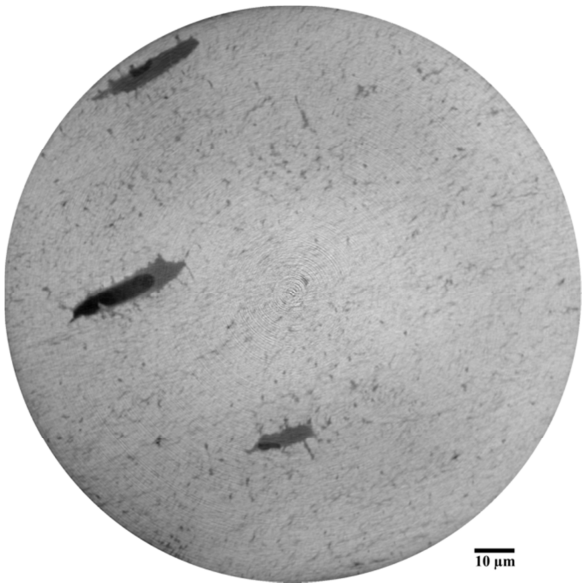

Figure 14: Reconstructed slice of an osteoporotic sample. The pixel size is 60 nm, and the scale bar represents 10µm. Grey, corresponding to remaining soft tissues, is visible inside lacunae, as well as their elongated shape.

4.c.iii. Osteoarthritic sample

Even if osteoarthritis is known as an inflammatory pathology of the cartilage, there has been little work on its effects on the bone cellular structure. As visible on Figure 15 and Figure 16, this sample presents mostly round lacunae. We count about 49 lacunae, representing 1.49% of the total volume. Moreover, we can observe the presence of mineralized tissue in some lacunae, as well as degraded lacunae. These observation were confirmed in several studies: Prasadam *et al.* (2013) showed that

osteocytes grown on OA matrices tend to be rounded (Prasadam et al., 2013), by using scanning electron microscopy. Moreover, Jaiprakash *et al.* (2012) also highlighted this rounded shape, as well as an increased lacunae density in osteoarthritic bone, and a disorganized mineral distribution, which could be compatible with our observation of mineral-containing lacunae (Jaiprakash et al., 2012).

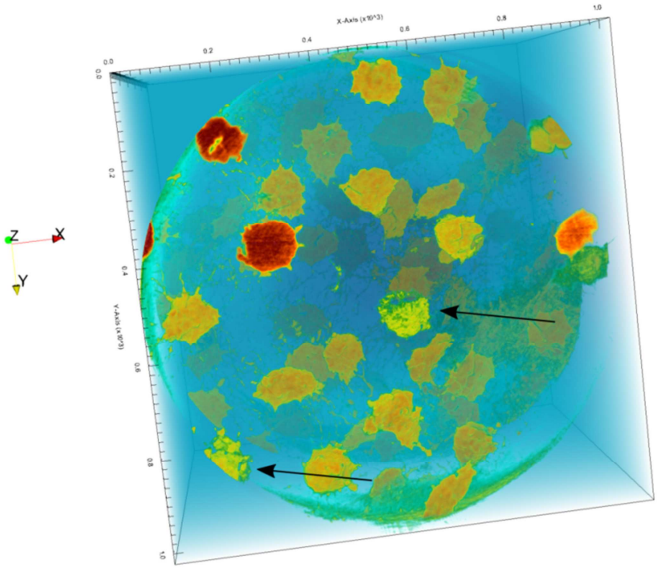

Figure 15: 3D rendering of the reconstructed osteoarthritic sample (*'nano_A95_1_1a_'*). The black arrows indicate visibly degraded lacunae. The rounded shape of the lacunae is also noticeable. The box is of size 122.88µm x 122.88µm x 122.88 µm.

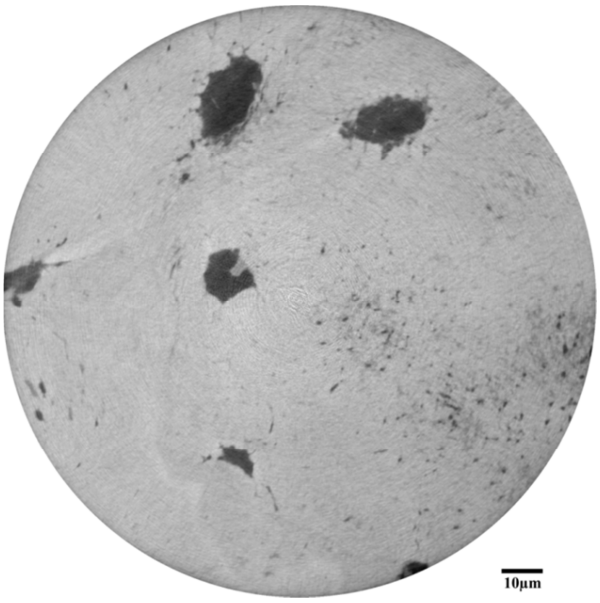

Figure 16: Reconstructed slice of an osteoarthritic sample. The pixel size is 60nm, and the scale bar represents 10µm.

4.c.iv. Summary

The Table 1 summarizes our observations, for the three presented samples. The first part is dedicated to the acquisition conditions. The second part relates the total studied volume (TV). The third part expresses the bone volume (BV), as well as the bone fraction (BV/TV). The fourth part is dedicated to the segmented lacunae: their number (Lc.number), the total volume of lacunae (Lc.TV), and the lacunae fraction (Lc.TV/TV), as well as the average volume of a lacuna (Lc.V). Each lacuna is fitted

with an ellipsoid; the average length (Lc.L1), width (Lc.L2), and depth (Lc.L3) is precised, as well as the ratios Lc.L1/Lc.L2 and Lc.L2/Lc.L3, and the global orientation of lacunae (Orientation).

Sample	Healthy	Osteoporotic	Osteoarthritic
Pixel size (nm)	35	60	60
Energy (keV)	17	17	17
Number of projections	2500	3000	3000
Exposure time (s)	0.1	0.1	0.1
Average counts in the reference (a.u.)	1430	1190	1235
TV (μm^3)	209604,81	1442891,17	1457251,48
BV (μm^3)	208616.27	1433403.67	1435606.22
BV/TV (%)	99.53	99.34	98.51
Lc.number	5	27	49
Lc.TV (µm3)	988.54	9487.50	21645.26
Lc.TV / TV (%)	0.47	0.66	1.49
Lc.V (in μm^3)	197.71	351.39	441.74
Lc.L1 (in µm)	18.87	20.75	16.99
Lc.L2 (in µm)	7.36	9.21	12.15
Lc.L3 (in µm)	3.74	4.04	6.03
Lc.L1/Lc.L2	2.56	2.25	1.40
Lc.L2/Lc.L3	1.97	2.28	2.01
Orientation	4Z / 1Y	31X / 3Y / 6Z	X23 / Y17 / Z1

Table 1: Summary of the results. The acquisition conditions are recall in the first part, followed by the descriptive parameters. TV is the total studied volume, BV is the bone volume, Lc.TV is the total lacunae volume, Lc.V is the average lacuna volume. Lc.L1, Lc.L2, and Lc.L3 denote the average length, width, and depth, respectively, and Orientation the global orientation of the lacunae.

4.c.v. Discussion and conclusion

We presented the first observations of osteocyte lacunae from human bone in 3D using phase nano-CT, enabling high resolution imaging of a relatively large field-of-view. Actually, other techniques such as transmission X-ray microscopy provides a good resolution (40nm) but has a very limited field of view (5.5µm x 5.5µm x 5.5 µm) (Andrews et al., 2010).

Qualitatively, we observed large differences between osteoporotic, osteoarthritic and healthy tissue. Although our observations are in good agreements with some recent studies (Jaiprakash et al., 2012; Prasadam et al., 2013), the influence of pathology on bone structure remains controversial. Van Hove et al. (2009) observed, using 3D confocal microscopy, elongated osteocytes in osteoarthritic bone (van Hove et al., 2009). Moreover, Mc Creadie *et al.* (2004) observed a large diversity in sizes and shape of osteocytes, in osteoporotic samples (McCreadie, Hollister, Schaffler, & Goldstein, 2004). It is also evidenced that the shape of osteocytes is influenced by mechanical load of the bone, and is thus highly dependent of sample location.

The descriptive parameters, summed up in Table 1, are quite in good agreement with a previous study (Dong et al., 2014). In this paper, the authors assess an average size of lacuna of 18.9 ± 4.9µm in length, 9.2 ± 2.1µm in width and 4.8 ± 1.1µm in depth. Our results are in these ranges, and the anisotropic ratio length:width:depth is also around 4:2:1. Nevertheless, the average lacuna volume of the healthy sample seems quite small with respect to the previous study, and the results of the two other samples. This is probably inherent to the sample, which contains much less lacunae than the others. Nevertheless, the imperfect automatic segmentation is worth mentioning. It sometimes segments some canaliculi with the lacuna, and split some others in two (due to image artefacts). This could be responsible for results variability.

Even if the number of available samples and regions is too low to state whether or not there is an impact of disease on bone ultrastructure, we here show phase nano-CT as a promising tool to get insight into it. The analysis of a larger set of samples, through different locations is worth considering, and has already begun with experiments conducted through the LTP on the ID16A beamline (ESRF, Grenoble).

4.d.Further analysis of mineralization and MCF orientation

4.d.i. Quantification of mineralization gradient around lacunae and canaliculi

We briefly recall the method used for this study, which aims at determining the mineralization distribution, as a function of the distance from the lacuna and canaliculi. This method is described in the work of Hesse *et al.* (Hesse et al., 2015).

We select, out of the entire reconstructed volume, a small volume of interest (VOI) containing one lacuna and canaliculi. These particular structures were segmented by hysteresis thresholding (thresholds determined empirically). Moreover, because of local tomography, the reconstructed phase values are offset. To compensate for this offset, the volume was rescaled so that the mean grey value inside the lacuna is set to zero.

For each voxel, the shortest distance to the closest lacunar surface and to the closest canalicular surface is calculated, leading to a 3D map of distances. For a given range of distances, the equally-distanced voxels are gathered into a class. The mean and standard deviation of this class is calculated from the original volume (mass density volume or δ_n-volume). As an illustration, Figure 17 shows the obtained graphs in the study lead by Hesse *et al.*; they represent the mean mass density, as a function of the distance to the closest lacuna, for several regions. The sub-figures correspond to the different studied locations, illustrated in Figure 18.

These different locations were studied to mimic the aging of the tissues: the osteonal regions are deemed as young tissues while the interstitial regions mimic older tissues. BRONJ (Bisphosphonate-Related Osteonecrosis of the Jaw) corresponds to bone of patients treated with bisphosphonates (BPs), known as inhibitors of the osteoclasts activity (*i.e.* reduce bone resorption, as mentioned in Chapter III). As a consequence, the mineralization of the bone tissue increases, as well as the average tissue age (Roschger, Paschalis, Fratzl, & Klaushofer, 2008). Thus, the BRONJ regions mimic potentially even older tissues than healthy osteonal and interstitial tissues.

As we can see in Figure 17, the mineralization *gradient* is higher for young tissue, and the average mineralization increases with the tissue age, until saturation. It is noticeable that the maximum in mass density is not at the surface of the lacuna, most probably due to partial volume effects.

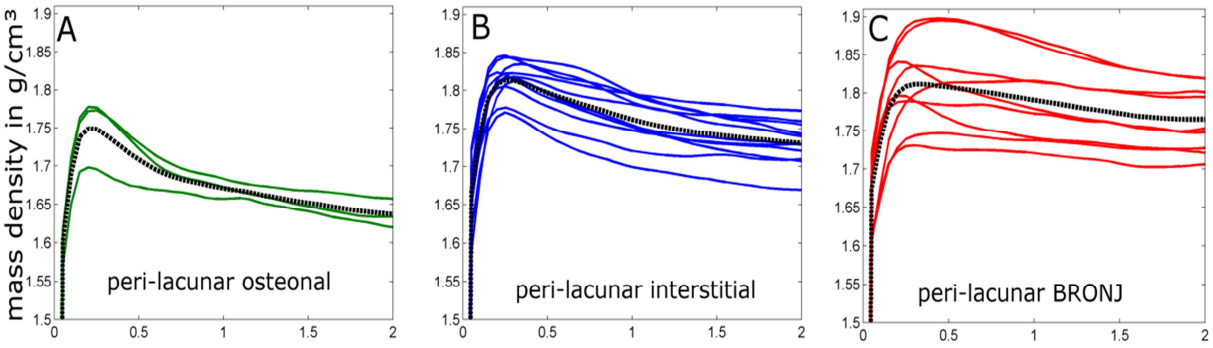

Figure 17: Average mass density of bone, as a function of the shortest distance to the lacuna, shown for (A) peri-lacunar osteonal, (B) peri-lacunar interstitial and (C) peri-lacunar BRONJ regions. The number of studied regions is (A) 3, (B) 11 and (C) 9. The average mass density in each study is represented in black dashed lines. Figure from (Hesse et al., 2015).

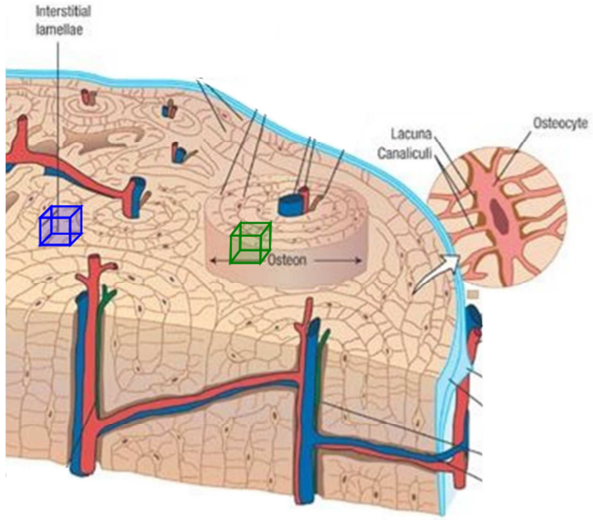

Figure 18: Illustration of the peri-lacunar osteonal region (green box) and peri-lacunar interstitial region (blue box)

Exemplary, we perform the presented analysis of mass density distribution on one VOI of an osteoporotic sample, depicted in Figure 19. This volume is of size 36µm x 18µm x 24µm, being a small part of the whole volume, for time computations reasons, but also to limit the low frequency artefact.

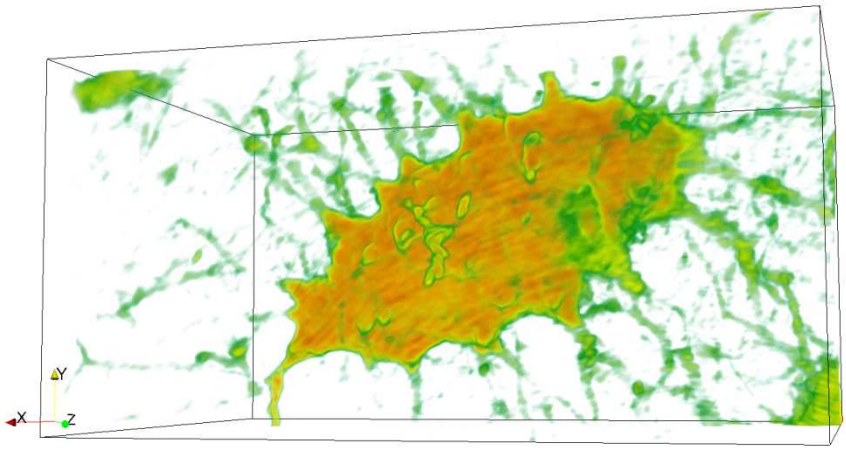

Figure 19: 3D rendering of the volume of interest (VOI) used for this mineralization study (from the osteoporotic sample). The selected VOI is of size 600x300x400, which corresponds to a physical size of 36µm x 18µm x 24µm.

In our case, as depicted in Figure 20, the mass density gradient (*i.e.* the mineralization gradient) is very low, which may indicate the presence of aged tissue, or could be related to the pathology of the sample (Roschger et al., 2008). Moreover, we could notice that the average mass density is surprisingly low with respect to the previous study (Hesse et al., 2015). A possible explanation could be the quality of the reconstruction, which present strong ring artefacts, and low-frequency artefacts. Low frequency artefacts, as shown in Figure 21, are major bottlenecks when it comes to retrieving quantitative phase values. Nevertheless, even if the studied region was kept small to limit the varying background, we cannot ensure that this kind of artefact has no influence on the reconstructed quantity.

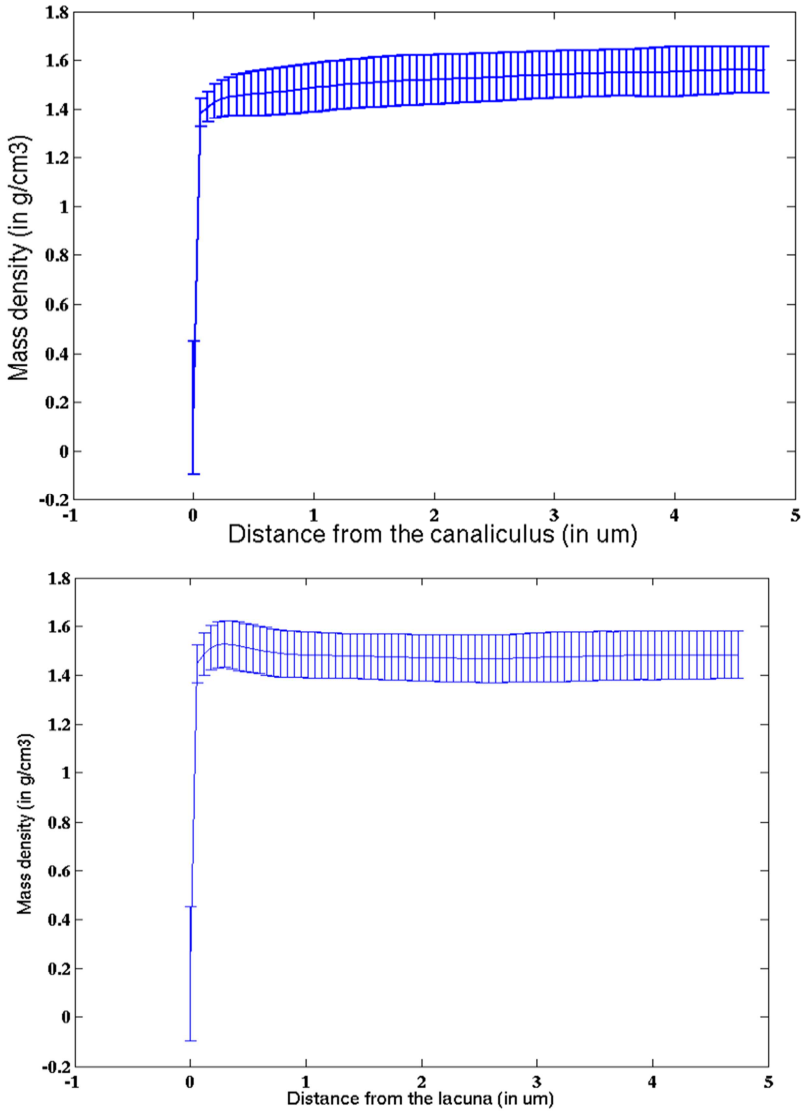

Figure 20: Mass densities of bone as a function of the distance from the canalicular surface (up) or the lacunar surface (down), in μm. The blue line represents the average value, and the error bar the standard deviation.

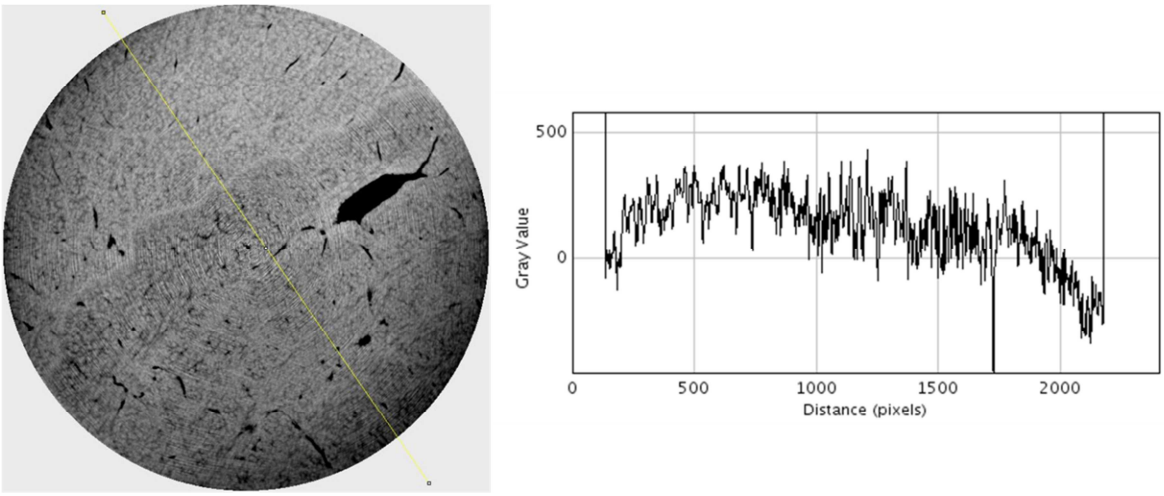

Figure 21: Reconstructed phase slice (left) and a profile (right). The profile is not flat, but has a rounded shape, indicating a non-uniform background (low-frequency noise).

4.d.ii. 3D orientation of mineralized collagen fibrils

This work was done in collaboration with P. Varga (AO Research Institute Davos, Davos, Switzerland) (Varga et al., 2013, 2014), on the healthy sample.

Previously orientation information was extracted from 2D data, and inferred to 3D (Galvis, Dunlop, Duda, Fratzl, & Masic, 2013). Here, the orientation of the mineralized collagen fibrils (MCF) is directly extracted from 3D data, by the use of a 3D-autocorrelation function (3D-ACF). It enables to determine the degree of anisotropy, and the orientation, of the collagen fibrils. The results of this study are presented in Figure 22 and Figure 23. The Figure 23 shows the orientation angle of the fibrils for different positions in the y-direction (depicted on Figure 22a).

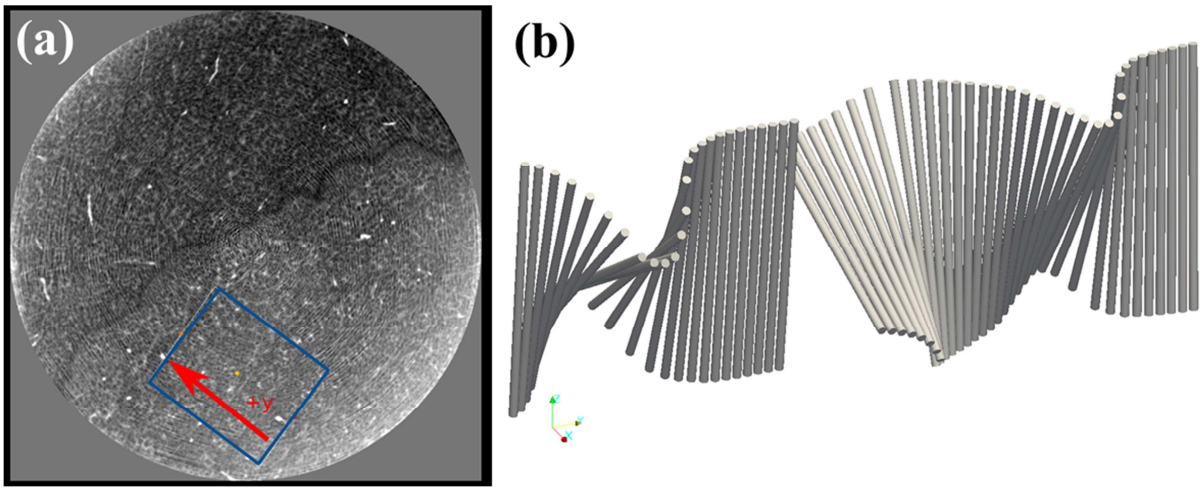

Figure 22: (a) Reconstructed phase slice of a healthy sample. The effective pixel size is 35nm. The MCF orientation was determined for the ROI (blue rectangle) from osteonal region, and is represented by cylinders in (b).

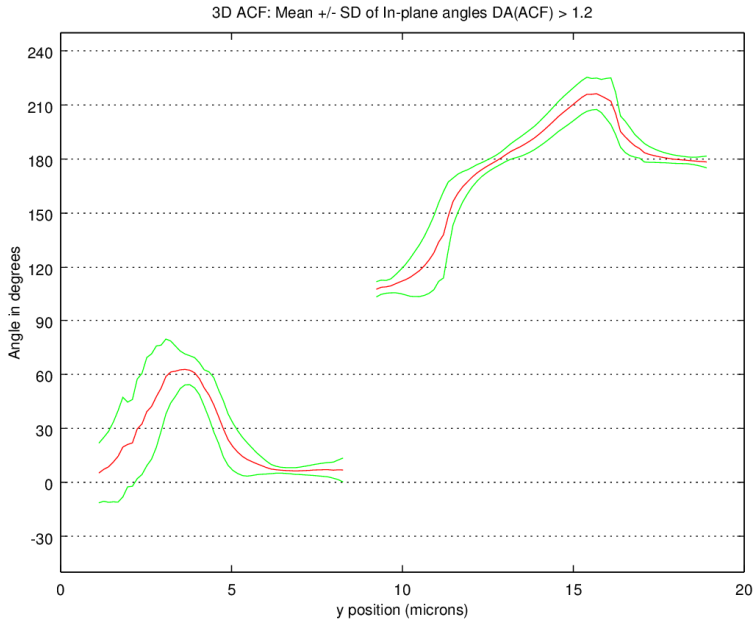

Figure 23: 3D ACF-based degree of anisotropy (DA) analysis of the collagen fibril orientation. The red line represents the mean orientation, and the green lines correspond to the standard deviation.

On Figure 22b, we observe twisted plywood (left), and oscillating plywood (right), as shown in the literature, where the authors find that these two patterns are the dominant patterns in human cortical bone (Varga et al., 2013).

5. Conclusions and perspectives

Morphological images given by phase nano-CT can help to better understand bone properties, in relation to the anatomical site and pathology. Through several projects and the long term project currently in progress on ID16A beamline, we are investigating bone cellular structures (LCN, MCF orientation, mineralization), as well as bone vascularization, on a large series of samples.

Nevertheless, the difficulties lie in the choice of the region of interest, and the large variability of bone structure depending on the location, in the same bone. To perform high quality nano-CT measurements, we actually need a very small piece of bone (~500µm in diameter), from an inherently large bone, cut manually. The analysis on a large set of samples is thus required to draw statistical relevant conclusions. Moreover, reconstructions of large number of sample are now facilitated by the new tool developed for registration of the projections, which is known as a time-consuming step.

The aim of this chapter was to present the phase nano-CT, and possible applications on bone, with tools to finely analyse its 3D structure. Since each studied element is long to compute, we only presented it on a selected volume of interest. Moreover, we showed that the presence of low frequency noise in the reconstructed volume, reflected in a slowly varying background, can be prohibitive when it comes to quantitative analysis, such as mineralization gradient study. This problem motivates the introduction of a priori knowledge in more sophisticated reconstruction algorithms, as those presented in Chapter V.

References

Ahren, J., Geveci, B., & Law, C. (2005). *ParaView: an end-user tool for large data visualization*. (C. R. Johnson & C. D. Hansen, Eds.). Burlington: Elsevier Butterworth-Heinemann.

Andrews, J. C., Almeida, E., van der Meulen, M. C. H., Alwood, J. S., Lee, C., Liu, Y., … Pianetta, P. (2010). Nanoscale X-ray microscopic imaging of mammalian mineralized tissue. *Microscopy and Microanalysis : The Official Journal of Microscopy Society of America, Microbeam Analysis Society, Microscopical Society of Canada*, *16*(3), 327–36. doi:10.1017/S1431927610000231

Canny, J. (1986). A Computational Approach to Edge Detection. *IEEE Transactions on Pattern Analysis and Machine Intelligence*, *PAMI-8*(6), 679–698. doi:10.1109/TPAMI.1986.4767851

Dai, Y. H., & Yuan, Y. (1999). A Nonlinear Conjugate Gradient Method with a Strong Global Convergence Property. *SIAM Journal on Optimization*, *10*(1), 177–182. doi:10.1137/S1052623497318992

Dong, P., Haupert, S., Hesse, B., Langer, M., Gouttenoire, P.-J., Bousson, V., & Peyrin, F. (2014). 3D osteocyte lacunar morphometric properties and distributions in human femoral cortical bone using synchrotron radiation micro-CT images. *Bone*, *60*, 172–185.

Fletcher, R. (1964). Function minimization by conjugate gradients. *The Computer Journal*, *7*(2), 149–154. doi:10.1093/comjnl/7.2.149

Galvis, L., Dunlop, J. W. C., Duda, G., Fratzl, P., & Masic, A. (2013). Polarized Raman anisotropic response of collagen in tendon: towards 3D orientation mapping of collagen in tissues. *PloS One*, *8*(5), e63518. doi:10.1371/journal.pone.0063518

Guigay, J.-P. (1977). Fourier transform analysis of Fresnel diffraction patterns and in-line holograms. *Optik*, *49*, 121–125.

Hesse, B., Varga, P., Langer, M., Pacureanu, A., Schrof, S., Männicke, N., … Raum, K. (2015). Canalicular network morphology is the major determinant of the spatial distribution of mass density in human bone tissue: evidence by means of synchrotron radiation phase-contrast nano-CT. *Journal of Bone and Mineral Research : The Official Journal of the American Society for Bone and Mineral Research*, *30*(2), 346–56. doi:10.1002/jbmr.2324

Hestenes, M. R., & Stiefel, E. (1952). Methods of conjugate gradients for solving linear systems. *Journal of Research of the National Bureau of Standards*, *49*(6), 2379.

Jaiprakash, A., Prasadam, I., Feng, J. Q., Liu, Y., Crawford, R., & Xiao, Y. (2012). Phenotypic characterization of osteoarthritic osteocytes from the sclerotic zones: a possible pathological role in subchondral bone sclerosis. *International Journal of Biological Sciences*, *8*(3), 406–17. doi:10.7150/ijbs.4221

Klein, S., Staring, M., Murphy, K., Viergever, M. A., & Pluim, J. P. W. (2010). Elastix: a toolbox for intensity-based medical image registration. *IEEE Transactions on Medical Imaging*, *29*(1), 196–205. doi:10.1109/TMI.2009.2035616

Langer, M., Pacureanu, A., Suhonen, H., Grimal, Q., Cloetens, P., & Peyrin, F. (2012). X-ray phase nanotomography resolves the 3D human bone ultrastructure. *PloS One*, *7*(8), e35691. doi:10.1371/journal.pone.0035691

McCreadie, B. R., Hollister, S. J., Schaffler, M. B., & Goldstein, S. A. (2004). Osteocyte lacuna size and shape in women with and without osteoporotic fracture. *Journal of Biomechanics*, *37*(4), 563–72. doi:10.1016/S0021-9290(03)00287-2

Moddemeijer, R. (1989). On estimation of entropy and mutual information of continuous distributions. *Signal Processing*, *16*(3), 233–248. doi:10.1016/0165-1684(89)90132-1

Paganin, D., Mayo, S. C., Gureyev, T. E., Miller, P. R., & Wilkins, S. W. (2002). Simultaneous phase and amplitude extraction from a single defocused image of a homogeneous object. *Journal of Microscopy*, *206*(1), 33–40. doi:10.1046/j.1365-2818.2002.01010.x

Polak, E., & Ribiere, G. (1969). Note sur la convergence de méthodes de directions conjuguées. *ESAIM: Mathematical Modelling and Numerical Analysis - Modélisation Mathématique et Analyse Numérique*, *3*(R1), 35–43.

Polyak, B. T. (1969). The conjugate gradient method in extremal problems. *USSR Computational Mathematics and Mathematical Physics*, *9*(4), 94–112. doi:10.1016/0041-5553(69)90035-4

Prasadam, I., Farnaghi, S., Feng, J. Q., Gu, W., Perry, S., Crawford, R., & Xiao, Y. (2013). Impact of extracellular matrix derived from osteoarthritis subchondral bone osteoblasts on osteocytes: role of integrinβ1 and focal adhesion kinase signaling cues. *Arthritis Research & Therapy*, *15*(5), R150. doi:10.1186/ar4333

Roschger, P., Paschalis, E. P., Fratzl, P., & Klaushofer, K. (2008). Bone mineralization density distribution in health and disease. *Bone*, *42*(3), 456–66. doi:10.1016/j.bone.2007.10.021

Schwiedrzik, J., Raghavan, R., Bürki, A., LeNader, V., Wolfram, U., Michler, J., & Zysset, P. (2014). In situ micropillar compression reveals superior strength and ductility but an absence of damage in lamellar bone. *Nature Materials*, *13*(7), 740–747. doi:10.1038/nmat3959

Shamonin, D. P., Bron, E. E., Lelieveldt, B. P. F., Smits, M., Klein, S., & Staring, M. (2013). Fast parallel image registration on CPU and GPU for diagnostic classification of Alzheimer's disease. *Frontiers in Neuroinformatics*, *7*, 50. doi:10.3389/fninf.2013.00050

Shewchuk, J. (1994). An introduction to the conjugate gradient method without the agonizing pain.

Taylor, D., Hazenberg, J. G., & Lee, T. C. (2007). Living with cracks: damage and repair in human bone. *Nature Materials*, *6*(4), 263–8. doi:10.1038/nmat1866

Thévenaz, P., Ruttimann, U. E., & Unser, M. (1998). A pyramid approach to subpixel registration based on intensity. *IEEE Transactions on Image Processing : A Publication of the IEEE Signal Processing Society*, *7*(1), 27–41. doi:10.1109/83.650848

van Hove, R. P., Nolte, P. A., Vatsa, A., Semeins, C. M., Salmon, P. L., Smit, T. H., & Klein-Nulend, J. (2009). Osteocyte morphology in human tibiae of different bone pathologies with different bone mineral density--is there a role for mechanosensing? *Bone*, *45*(2), 321–9. doi:10.1016/j.bone.2009.04.238

Varga, P., Hesse, B., Langer, M., Schrof, S., Männicke, N., Suhonen, H., … Raum, K. (2014). Synchrotron X-ray phase nano-tomography-based analysis of the lacunar–canalicular network morphology and its relation to the strains experienced by osteocytes in situ as predicted by case-specific finite element analysis. *Biomechanics and Modeling in Mechanobiology*. doi:10.1007/s10237-014-0601-9

Varga, P., Pacureanu, A., Langer, M., Suhonen, H., Hesse, B., Grimal, Q., … Peyrin, F. (2013). Investigation of the three-dimensional orientation of mineralized collagen fibrils in human lamellar bone using synchrotron X-ray phase nano-tomography. *Acta Biomaterialia*, *9*(9), 8118–8127.

Chapter V: Innovative algorithm to combine phase retrieval and tomographic reconstruction

In this chapter, we introduce the state of the art of methods combining phase retrieval and tomographic reconstruction, as described in Chapter II. We first present a simulation tool, developed during this thesis, aiming at creating phase contrast data in propagation based-imaging. This tool is ported to the Virtual Imaging Platform (Villeurbanne, France, www.creatis.insa-lyon.fr/vip/) in the framework of the LabEx PRIMES. Then, we propose an innovative combined algorithm, with different formulations for pure phase to attenuating objects. It aims at reconstructing the refractive index decrement of an object in a single reconstruction step, but iteratively, using the recorded intensities as input. We use the simulated intensities to test the proposed algorithms, and present here the obtained results. Finally, we discuss these algorithms and detail the perspectives.

Table of contents

1. Introduction

So far, phase tomography has mainly been considered as a two-step process, *i.e.* a 2D phase retrieval step followed by a 3D tomographic reconstruction step. The phase retrieval step usually relies on linearization of the contrast model to achieve efficient, filtering-based algorithms. The most well-known linear models include the transport of intensity equation (TIE) (Nugent, Gureyev, Cookson, Paganin, & Barnea, 1996), the contrast transfer function (CTF) (Cloetens et al., 1999), and the mixed approach (Langer, Cloetens, Guigay, Valton, & Peyrin, 2007), presented in Chapter II.

Some work has been done on improving the spatial resolution, still in 2D, by considering the full non-linear problem, as the use, in phase nano-tomography, of a non-linear conjugate gradient algorithm to refine an initial reconstruction with a linear algorithm (as presented in Chapter IV). Davidoiu *et al.* investigated the use of the Frechet derivative to define a Landweber iteration (Davidoiu, Sixou, Langer, & Peyrin, 2011), and Moosmann *et al.* used a non-linear filtering-based approach (Moosmann, Hofmann, Bronnikov, & Baumbach, 2010).

There are various ways to solve combined problems in imaging, and particularly in phase contrast imaging. As an example, Nilchian *et al.* (2016) recently proposed a combined method in grating-based radiography, which consists in denoising the absorption image while retrieving the phase information from the measured radiographs, all being constrained by TV-regularisation (Nilchian et al., 2016).

Combined methods in phase contrast tomography consist in combining the phase retrieval step, with the tomographic reconstruction of the refractive index into a single step. Such methods have gained ground during the last decade, since they enable to add constraints in the object domain, or use less data (*i.e.* reduce the number of projections, to save time and dose). Moreover, to further reduce the assumptions on the imaged object, it seems that truly 3D iterative algorithms (*i.e.* direct retrieval of the complex refractive index) have to be used. Such algorithms, extensively described in the Chapter II, Section 6, are summed up in the following.

In 2013, Kostenko *et al*. first proposed a combined method, using Paganin's method and a total variation (TV) penalty term in the object domain, by the use of Fast Iterative Shrinkage-Thresholding Algorithm (FISTA) (Beck & Teboulle, 2009). They introduced an algorithm that, albeit still requiring homogeneous objects, allows to reduce the number of views acquired in the tomographic scan (Kostenko, Batenburg, Suhonen, Offerman, & van Vliet, 2013), and outperformed classical two-step approaches. A few years later, this method was refined by Kongskov *et al.* (Kongskov, Jørgensen, Poulsen, & Hansen, 2016), by the use of a primal-dual method (Chambolle & Pock, 2010) instead of FISTA for the TV regularisation. Ruhland *et al.* used a Gerchberg-Saxton type algorithm with a consistency constraint, coupled to an algebraic tomographic reconstruction technique (ART), to reconstruct the complex refractive index (A. Ruhlandt, Krenkel, Bartels, & Salditt, 2014). Unlike previous methods, their algorithm does not imply any restrictive assumption on the object. Nevertheless, it is unclear if this algorithm is robust to phase wrapping, however, since it was only demonstrated on weak objects. Two years later, Ruhlandt and Salditt (Aike Ruhlandt & Salditt, 2016) proposed to do first the tomographic reconstruction and then perform the phase retrieval in 3D, to achieve a more efficient phase reconstruction. This algorithm was tested on simulated data, demonstrating that the method is robust to the presence of Poissonian noise, as well as on experimental freeze-dried cells (Bartels et al., 2012). In 2016, Anastasio and Chen (Chen et al., 2016) proposed to use a non-linear phase retrieval operator, based on the Frechet derivative (Davidoiu et al., 2011), coupled to TV penalty terms. Notwithstanding, this method was not robust to phase wrapping (*i.e.* when the phase shift is larger than 2π).

The aim of this work is to combine iterative tomographic reconstruction and phase retrieval to retrieve directly the 3D refractive index distribution, with the intention to reduce the assumptions on the imaged object by allowing less restrictive priors. To this aim, we present a new algorithm for 3D refractive index retrieval that combines the CTF and the simultaneous algebraic reconstruction technique (SART) (Andersen & Kak, 1984).

2. Data simulation for propagation-based imaging

Synchrotron radiation beamtime is rare and non-easily available. To alleviate this experimental limitation, and in order to test new algorithms, we first propose to simulate propagation-based imaging datasets of known objects. A few simulators have been developed for particular PCI set-up, that is analyzer-based imaging (Khromova et al., 2010), grating-based imaging (Wang, Huang, Zhang, Chen, & Kang, 2009) and more recently propagation-based imaging (Peter et al., 2014), using Monte-Carlo method (Binder & Heermann, 2002). Our idea was to develop a simple analytical tool to simulate PBI data, and to port it into the open-source Virtual Imaging Platform (VIP) of Creatis (Villeurbanne, France), so that it could be used by all the community.

In this section, we present all the simulation steps, as depicted in Figure 1. The simulated acquisition geometry is depicted in Figure 2. We first present the numerical objects that can be used in the simulations. Given the linear attenuation coefficient and the refractive index decrement volumes (step 1), attenuation and phase projections are created (step 2, Section 2.b). They are used as input to in-line phase contrast models, recalled in Section 2.c. Propagated images can additionally be corrupted by noise (Section 2.d). Finally, the interfacing on the platform, and the tunable parameters are presented, as well as some perspectives.

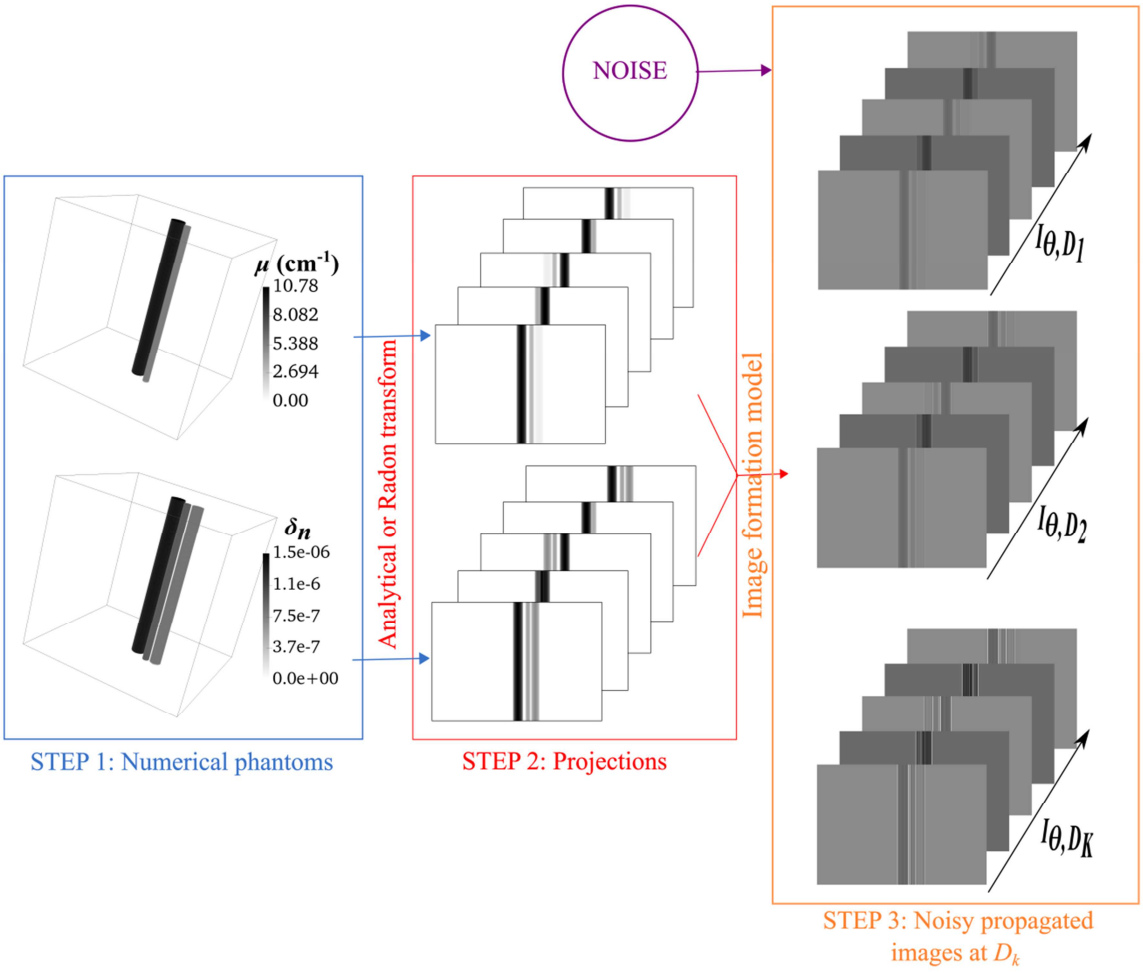

Figure 1: Scheme of the simulation workflow.

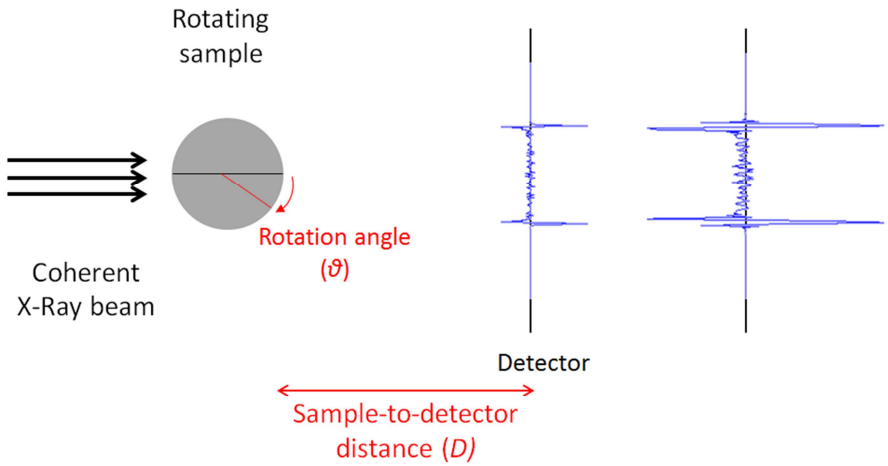

Figure 2: Schematic of the acquisition geometry in X-ray in-line phase tomography, in 2D. The object is here a polystyrene sphere, a transparent material. θ denotes the rotation angle and D the propagation distance.

2.a. Numerical phantoms

These simulations were implemented for numerical phantoms. The phantoms included so far are:

- a simple sphere, for which the user can choose the size and the composition

- a pure phase Shepp-Logan phantom, widely used for numerical assessment of algorithms

- a three-wire phantom, inspired from a real phantom, designed in the framework of an optimization study for holotomography acquisitions (Frachon et al., 2015). It is made of a wire of aluminum (Al) of diameter 250µm, a wire of magnesium (Mg) of diameter 125µm and a wire of polyethylene terephthalate (PET) of diameter 200µm, as shown in Figure 3.

- another numerical phantom was derived from the one previously described. It is composed of three wires, of fixed diameters (250, 200 and 125µm), for which the material can be defined, given its attenuation coefficient μ (in cm-1) and its refractive index decrement δ_n.

It is noticeable that, these phantoms can be used either in 2D (*i.e.* the object is 2D, and the corresponding simulated projections are in 1D), or 3D (in this case, the object is 3D and its corresponding simulated projections are 2D).

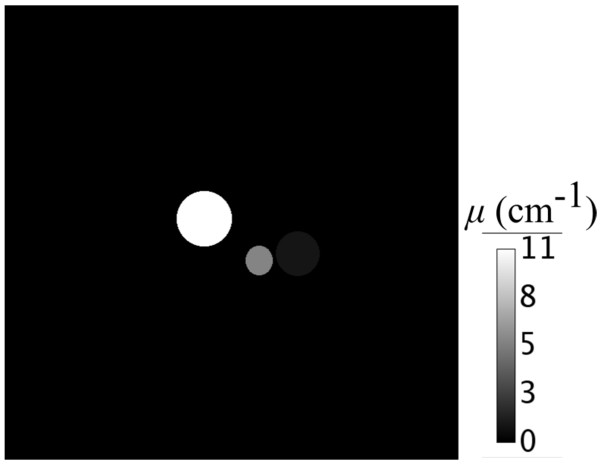

Figure 3: Example of an attenuation slice of the three-wire phantom. Wires, from left to right: Al, Mg and PET, of diameters 250µm, 125µm and 200µm respectively.

In addition, the simulation of data from any real voxelated objects was developed to enable the simulation of more complex objects. In this case, the inputs are two .mhd volumes: one being the 3D distribution of the linear attenuation coefficient μ, and the other being the 3D map of the refractive index decrement, δ_n.

2.b. Projections creation

The Radon transform is performed using the `radon()` function of Matlab/Octave. It uses the μ- or δ_n-maps, as well as the tomographic angles as inputs. The number of tomographic angles is set by the user, as well as the tomographic range (180° or 360°). The projections can also be calculated analytically, when possible. For instance, when the object is a circle of radius r_0, centered in $(x_0; y_0)$, its Radon transform at an angle θ, $\mathcal{R}_\theta g$, can be expressed as:

$$\mathcal{R}_\theta g(u) = 2\sqrt{{r_0}^2 - (u - x_0\cos(\theta) - y_0\sin(\theta))^2} \tag{5.2.1}$$

The data are oversampled by a factor of 2 before being propagated in the Fourier domain, to avoid aliasing.

2.c. Image formation models for in-line phase contrast

The image formation models in propagation-based imaging were extensively described in Chapter II. Here, we briefly recall the context and the two main models used for data simulations. The scheme axis used is the same than previously: the *z*-axis is the beam propagation axis, and the $\boldsymbol{x} = (x, y)$ plane is the projection plane.

2.c.i. CTF model

The first model is the Contrast Transfer Function (CTF). It is a linear contrast model, valid for objects that have a slowly varying phase and are weakly attenuating. CTF expresses the Fourier transform of the recorded intensity, $\tilde{I}_{D,\theta}$, as a function of the Fourier transforms of the phase shift and the absorption, respectively denoted as $\tilde{\varphi}_\theta$ and $\tilde{B}_\theta$:

$$\tilde{I}_{D,\theta}(\boldsymbol{f}) = \delta_{Dirac}(\boldsymbol{f}) - 2\cos\left(\pi\lambda D|\boldsymbol{f}|^2\right)\tilde{B}_\theta(\boldsymbol{f}) + 2sin\left(\pi\lambda D|\boldsymbol{f}|^2\right)\tilde{\varphi}_\theta(\boldsymbol{f}), \tag{5.2.2}$$

where ~ denotes the Fourier transform, and δ_{Dirac} the Dirac distribution.

2.c.ii. Fresnel model

The second model is the Fresnel model. It is less restrictive than the CTF, since it has no assumption on the phase or the absorption of the object. It is valid for spatially coherent beam illuminating an object, The intensity recorded by the detector, at an intermediate distance *D* from the sample (*Fresnel region*), is:

$$I_{D,\theta}(\boldsymbol{x}) = \left|u_{D,\theta}(\boldsymbol{x})\right|^2, \tag{5.2.3}$$

where

$$u_{D,\theta}(\boldsymbol{x}) = \mathcal{F}^{-1}\tilde{P}_D\mathcal{F}\{u_{0,\theta}\}(\boldsymbol{x}). \tag{5.2.4}$$

The operators $\mathcal{F}$ and $\mathcal{F}^{-1}$ respectively correspond to the forward and inverse Fourier transform, and P_D is the Fresnel propagator, which models the free space propagation over a distance *D* (Goodman, 2005), and is expressed as:

$$P_D(\boldsymbol{x}) = \frac{1}{i\lambda D}\exp\left(i\frac{\pi}{\lambda D}|\boldsymbol{x}|^2\right). \tag{5.2.5}$$

The Fourier transform of the Fresnel propagator is expressed as:

$$\tilde{P}_D(\boldsymbol{f}) = \exp(-i\pi\lambda D|\boldsymbol{f}|^2), \tag{5.2.6}$$

where $\boldsymbol{f} = (f, g)$ are the frequency variables corresponding to (x, y).

The two of these models can be used for data simulations. The Fresnel model is obviously very realistic and relevant, since it does not assume restrictive constraint on the object, while the CTF is only valid for low attenuation and slowly varying phase. Nevertheless, this model was included for comparison.

2.d.Noise

The simulated projected phase images can also be corrupted by noise. Since simulations deal with X-rays, a Poisson noise model is known as more relevant. Nevertheless, for high photons counting, as it is the case here, the Poisson distribution approaches a Gaussian distribution. Thus, we let the user to choose the noise distribution: Gaussian or Poisson distribution.

2.d.i. Poisson noise

The Poisson probability distribution function (pdf) of parameter λ_P is

$$P_{\lambda_P}(X) = \frac{{\lambda_P}^X e^{-\lambda_P}}{X!}, \tag{5.2.7}$$

where X is a random variable. The Poisson noise is generated from the simulated data, using the Matlab function `poissrdn()`. It generates random numbers (in our case, one single number) from the Poisson distribution of mean parameter λ_P. The parameter λ_P is set as the intensity value of the "clean" simulated image:

$$\lambda_P(\boldsymbol{x}) = I_{D_k}(\boldsymbol{x}). \tag{5.2.8}$$

Then, the intensity is replaced by the generated number, leading to:

$$I_{D_k}(\boldsymbol{x}) = P_{\lambda_P}(X), \tag{5.2.9}$$

X being an integer, chosen randomly. The noise level can be tuned by the user by specifying a scaling factor.

2.d.ii. Gaussian noise

The Gaussian noise is added to the simulated data. We generate a noise map, following a Gaussian's distribution (Equation (5.2.10)) of mean m and standard deviation σ, using the Matlab function `randn()` and add it to the original image.

$$p_{m,\sigma}(x) = \frac{e^{\frac{-(x-m)^2}{2\sigma^2}}}{\sqrt{2\pi}.\sigma} \tag{5.2.10}$$

The user can tune the amount of additive Gaussian noise by specifying the PPSNR (Peak to Peak Signal-to-Noise Ratio), expressed (in dB) as:

$$\mathrm{PPSNR} = 20.\log_{10}\left(\frac{I_{amp}}{n_{amp}}\right) \tag{5.2.11}$$

where $I_{amp}$is the maximum amplitude of the signal (*i.e.* the recorded image), and $n_{amp}$the maximum amplitude of the noise.

2.e. Interface with the Virtual Imaging Platform

The Virtual Imaging Platform (VIP), developed at Creatis (Villeurbanne, France) is a versatile platform dedicated to medical imaging simulations (Glatard et al., 2013). Currently, various modalities are available, such as magnetic Resonance Imaging (MRI), ultrasounds (US), Positron Emission Tomography (PET) and X-ray Computed Tomography (CT). A phase-contrast CT simulator was missing. This work was done in collaboration with Sorina Pop from Creatis, for the porting of the application to VIP.

We choose to develop only in-line phase contrast modality, since it is the modality we are interested in. To this aim, we developed a Python interface (see Figure 4), as an example of what our VIP application could look like.

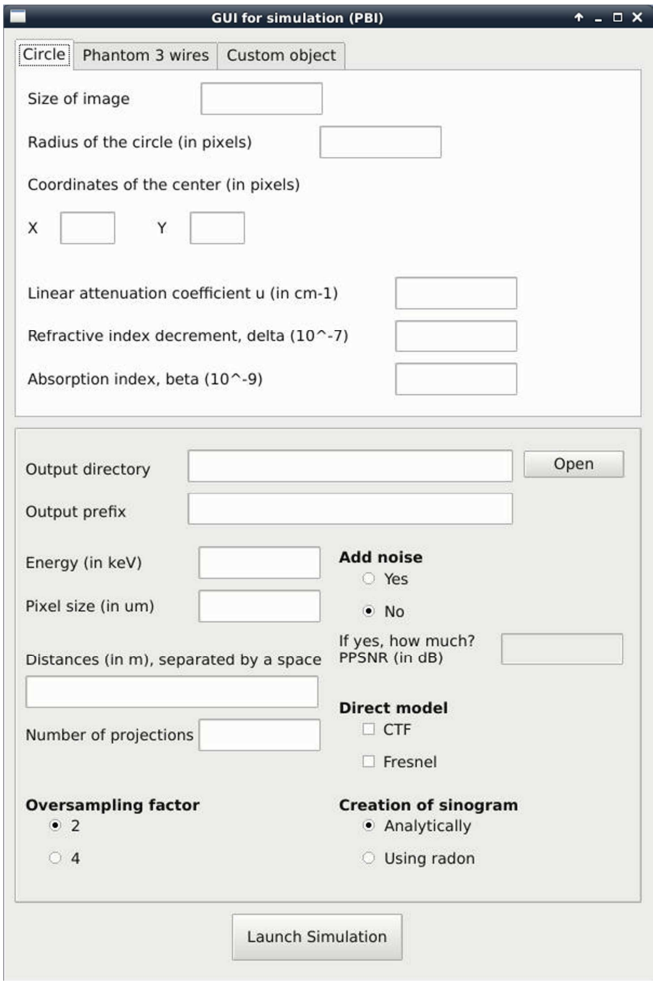

Figure 4: Python interface for data simulation, when the object is a 2D-circle. The upper part (white background) corresponds to the parameter related to the chosen object. The lower part (gray background) refers to the general settings.

The energy, the pixel size, the propagation distances, as well as the chosen direct contrast model (CTF or Fresnel) can be set by the user, as well as other practical settings (output directory, name of the output, …). Once the settings are fixed, the simulation can be launched. The simulation being finished, the propagated projections are then available and downloadable by the user.

The simulations were first proposed in 1D, *i.e.* we begin with a 2D object, calculate the Radon transform of this image, to get the 1D projections that will be propagated using the chosen phase contrast model.

For 2D simulations, i.e. starting with a 3D object, we proposed a parallelization scheme, to benefit from computational resources available on the grid. It consists in calculating the Radon transform of each slice of the volume, in parallel. Since this option usually takes long, benefiting from the resources of several machines can reduce the computation time. We obtained, for each slice, a sinogram.

We recombined each sinogram to get 2D projections, which will be propagated in parallel. Finally, we obtain a complete dataset of propagated projections, as the ones acquired at the ESRF.

To easily distribute our programs on different machines, we use the software Docker (https://www.docker.com/). We are thus able to run our programs using the same operating system (Centos) and the same version of the software Octave, and the same libraries. In a few words, we build an image of our environment (Docker image), which can be copied on every machines, so that the programs will run exactly the same, whatever the existing OS and programs installed on it. It is a very interesting solution for parallelization, were the machines used can be very different from each other. The Docker image we used is available at:

https://hub.docker.com/r/camarasu/creaphase/

2.f. Perspectives

In medical physics, Monte-Carlo simulations have been widely used to model the transport of particles (photons, electrons) in matter. The type of the interaction (Compton, Photoelectric, and Rayleigh) is stochastic, conditioning the interactions of the particle with matter. Given the model of the considered media and the source of the particle beam, we can determine the evolution of every particle (energy, direction) after each interaction using a Monte Carlo simulation. This simulation modality has been considered as a powerful and accurate tool, to calculate, for example, the energy deposit in every position of a medium (radiation therapy planning treatment) or the amount of scattered radiation (radiology, CT). Moreover, it can handle complex geometries such as the anatomy of a patient.

An interesting perspective of this work is to implement, on the VIP, a modelling that combines Monte Carlo simulation of the stochastic process for attenuation imaging with an analytical model for free-space propagation and phase shift. This is being done in collaboration with a trainee (Zhenjie Cen). Moreover, to better fit with real experimental data, it could be worth to take into account the distortions induced by the optical elements of the beamline (slits, attenuators, monochromators, mirrors, etc.) and transfer function of the detector.

The simulated data presented previously were used to test these proposed algorithms. It enables to play with the object composition (from pure phase objects to strongly attenuating objects), while varying some parameters (propagation distances, pixel size, energy, data size, etc.).

3. Theoretical formulation of the proposed algorithm

This section presents a new iterative algorithm for phase reconstruction in SR micro-CT, using multi-distance propagation-based phase contrast imaging. Up to now, phase retrieval and tomographic reconstruction were processed as two separated problems. Here, the aim is to jointly reconstruct the 3D phase map from the propagated images (Figure 5).

Our approach combines a linearized version of the contrast model (namely the CTF, extensively described in the Chapter II) with an algebraic tomographic reconstruction method (SART, described in the Chapter II). We come up with the formulation of an algorithm we named CTF-SART, formulated for different types of objects: pure phase, and mixed object with known or unknown attenuation. We also consider including TV regularisation within the reconstruction algorithm.

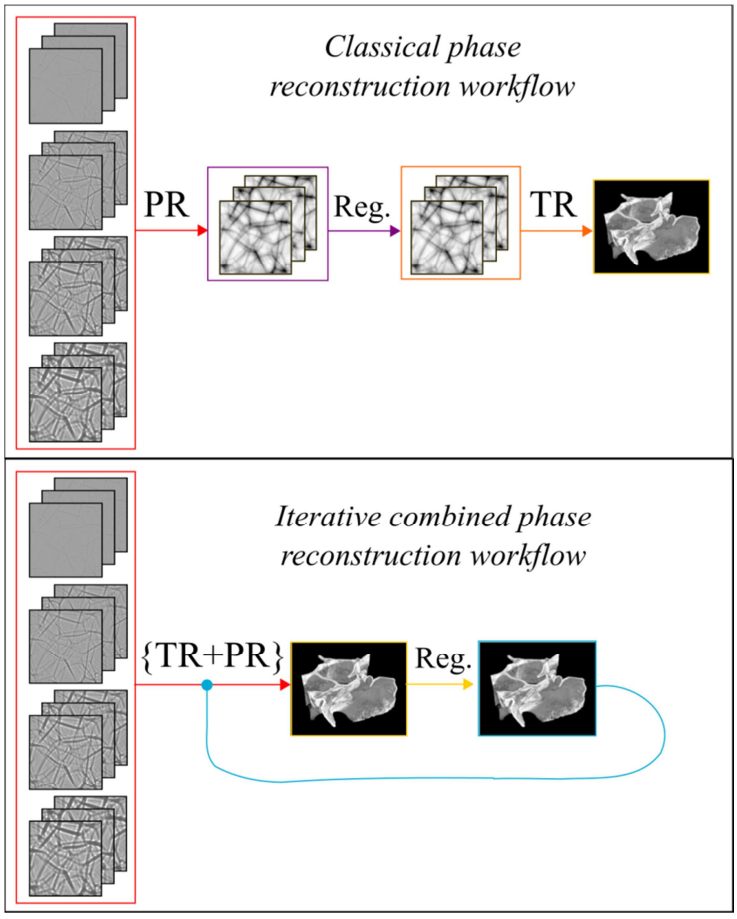

Figure 5: Schemes of the classical phase reconstruction workflow (up), presented in the previous chapters, and the iterative combined phase reconstruction workflow (bottom) proposed in this chapter. "PR" stands for phase retrieval, "TR" for tomographic reconstruction, and "Reg." for regularisation.

3.a. Phase retrieval using the linear least squares method

In this section we give the expression of phase and attenuation using the linear least-squares method, used later in the proposed combined algorithm.

The linear CTF contrast model (5.2.2) can be used to solve for phase (or attenuation) using linear least squares optimization, assuming the attenuation (or phase, respectively) is known. We here express the

estimation of the solution in three cases: known attenuation, known phase shift, and non-attenuating object (pure phase).

Assuming the attenuation at an angle θ, B_θ, is known, we can express the estimated Fourier transform of the phase shift at an angle θ, $\tilde{\varphi}_\theta$, as:

$$\widehat{\tilde{\varphi}_\theta}(\boldsymbol{f}) = \frac{\sum_{k=1}^{K} 2.\sin(\pi\lambda D_k|\boldsymbol{f}|^2)\left[\tilde{I}_{D_k,\theta}(\boldsymbol{f}) + 2\cos(\pi\lambda D_k|\boldsymbol{f}|^2)\tilde{B}_\theta(\mathbf{f}) - \delta_{Dirac}(\boldsymbol{f})\right]}{\left[\sum_{k=1}^{K} 4.\sin^2(\pi\lambda D_k|\boldsymbol{f}|^2)\right] + \alpha} \quad (5.3.1)$$

where α is an arbitrary regularisation parameter, and $\widehat{\tilde{\varphi}_\theta}$ designates the estimate of $\tilde{\varphi}_\theta$.

In the same way, if the phase shift at an angle θ, φ_θ, is known, the least square method yields an estimation of the Fourier transform of the attenuation at an angle θ, $\tilde{B}_\theta$:

$$\widehat{\tilde{B}_\theta}(\boldsymbol{f}) = \frac{-\sum_{k=1}^{K} 2.\cos(\pi\lambda D_k|\boldsymbol{f}|^2)\left[\tilde{I}_{D_k,\theta}(\boldsymbol{f}) - 2\sin(\pi\lambda D_k|\boldsymbol{f}|^2)\tilde{\varphi}_\theta(\mathbf{f}) - \delta_{Dirac}(\boldsymbol{f})\right]}{\left[\sum_{k=1}^{K} 4.\cos^2(\pi\lambda D_k|\boldsymbol{f}|^2)\right] + \alpha} \quad (5.3.2)$$

For a pure phase object, the cosine term disappears in the CTF expression. The estimate of the Fourier transform of the phase, $\widehat{\tilde{\varphi}_\theta}(\boldsymbol{f})$, then becomes:

$$\widehat{\tilde{\varphi}_\theta}(\boldsymbol{f}) = \frac{\sum_{k=1}^{K} 2.\sin(\pi\lambda D_k|\boldsymbol{f}|^2)\left[\tilde{I}_{D_k,\theta}(\boldsymbol{f}) - \delta_{Dirac}(\boldsymbol{f})\right]}{\left[\sum_{k=1}^{K} 4.\sin^2(\pi\lambda D_k|\boldsymbol{f}|^2)\right] + \alpha}. \quad (5.3.3)$$

The regularisation parameter should be set to a low value, in order not to influence the denominator. Some preliminary tests showed that setting the α parameter to 10^{-30} is a good choice, to quantitatively retrieve the phase.

3.b.Combined algorithm for pure phase object

Here, we combine CTF and SART to achieve a refractive index retrieval algorithm, for pure phase object.

3.b.i. Formulation

We start by expressing the Fourier transform of the intensity as a function of the refractive index decrement, for a pure phase object (the attenuation term vanishes):

$$\tilde{I}_{D_k,\theta}(\boldsymbol{f}) = \delta_{Dirac}(\boldsymbol{f}) + 2\sin(\pi\lambda D_k|\boldsymbol{f}|^2)\mathcal{F}\left[-\frac{2\pi}{\lambda}\mathcal{R}_\theta\delta_n\right](\boldsymbol{f}). \quad (5.3.4)$$

where $\mathcal{R}_\theta$ is the projection operator at angle θ, and $\mathcal{F}$ is the Fourier transform.

For simplicity, we rewrite this as:

$$\tilde{I}_{D_k,\theta}(\boldsymbol{f}) = \delta_{Dirac}(\boldsymbol{f}) + A_{D_k}(\boldsymbol{f})\mathcal{F}[\mathcal{R}_\theta \delta_n](\boldsymbol{f}), \tag{5.3.5}$$

where

$$A_{D_k}(\boldsymbol{f}) = -\frac{2\pi}{\lambda}.2\sin(\pi\lambda D_k|\boldsymbol{f}|^2). \tag{5.3.6}$$

The contrast can then be written in the spatial domain as:

$$I_{D_k,\theta}(\boldsymbol{x}) - 1 = \mathcal{F}^{-1}\{A_{D_k}\mathcal{F}[\mathcal{R}_\theta \delta_n]\}(\boldsymbol{x}). \tag{5.3.7}$$

Substituting the contrast operator for $\mathcal{R}$ in the SART formula yields the following iteration formula:

$$\hat{\delta}_n^{(i)}(\boldsymbol{x}) = \hat{\delta}_n^{(i-1)}(\boldsymbol{x}) + \left[\mathcal{F}^{-1}\left\{A_{D_k}\mathcal{F}\{\mathcal{R}_\theta\}\right\}\right]^{\mathrm{T}} \times \frac{I_{D_k,\theta}(\boldsymbol{x}) - 1 - \mathcal{F}^{-1}\left\{A_{D_k}\mathcal{F}\left\{\mathcal{R}_\theta\left(\hat{\delta}_n^{(i-1)}\right)\right\}\right\}(\boldsymbol{x})}{\left\|\mathcal{F}^{-1}\left\{A_{D_k}\mathcal{F}\{\mathcal{R}_\theta\}\right\}\right\|^2}. \tag{5.3.8}$$

3.b.ii. Discussion of the proposed formulation

In the following, we simplify and discuss the obtained expression at Equation (5.3.8).

On one hand, the denominator can be simplified using Parseval's theorem, yielding:

$$\left\|\mathcal{F}^{-1}\left\{A_{D_k}\mathcal{F}\{\mathcal{R}_\theta\}\right\}\right\|^2 = \left\|A_{D_k}\mathcal{F}\{\mathcal{R}_\theta\}\right\|^2. \tag{5.3.9}$$

On the other hand, the transpose term $\left[\mathcal{F}^{-1}\{A_{D_k}\mathcal{F}\mathcal{R}_\theta\}\right]^T$, if seen as a product of matrices, can be rewritten to:

$$\left[\mathcal{F}^{-1}\{A_{D_k}\mathcal{F}\mathcal{R}_\theta\}\right]^T = {\mathcal{R}_\theta}^T\mathcal{F}^T A_{D_k}^T[\mathcal{F}^{-1}]^T. \tag{5.3.10}$$

A_{D_k} can be seen as a propagator, enabling to go from $\tilde{\varphi}_\theta$ to $I_{D_k,\theta}$. Thus, $A_{D_k}^T$ can be seen as a backpropagator from the recorded intensity to the phase. This is performed using the least squares method, and denoted as A_{-D_k}.

Equation (5.3.10) is thus written:

$$\left[\mathcal{F}^{-1}\{A_{D_k}\mathcal{F}\mathcal{R}_\theta\}\right]^T = {\mathcal{R}_\theta}^T\mathcal{F}^{-1}A_{-D_k}\mathcal{F} \tag{5.3.11}$$

For the denominator, we performed some unsuccessful preliminary tests keeping the whole term that mixes the real and the Fourier domains. By excluding the propagator from the normalisation term, keeping only the Radon normalisation in the real domain, the results seem better:

$$\left\|\mathrm{A_{D_k}}\mathcal{F}\{\mathcal{R}_\theta\}\right\|^2 \approx \|\mathcal{R}_\theta\|^2. \tag{5.3.12}$$

Concerning the choice of the algebraic tomographic reconstruction algorithm, it is noticeable that using SIRT (*i.e.* calculate the correction projection by projection, but go through all the projection before updating the object) instead of SART would be equivalent to perform a least squares approach on all the projection, and then a tomographic reconstruction. This would be equivalent to a classical two-step approach, but would enable the addition of priors in the object domain. On the contrary, using SART as tomographic reconstruction enables to combine the phase retrieval and the tomographic reconstruction, by updating the reconstructed object at every projection.

Concerning the backpropagation using the least-squares method, we come up to two possibilities:

- either we iterate only on the projection angles (instead of iterating on the projection angles and the propagation distances), and perform the classical least-squares on the intensities of all the propagation distances.

- or we iterate over the projection angles and the propagation distances, and we perform a "shortened least-squares", that consists of performing a least square on one distance instead of on all the propagation distances.

3.b.iii. Final proposed formulation

Combining the proposed simplifications, we come up with the following formulation:

$$\begin{aligned}&\hat{\delta}_n{}^{(i)}(\boldsymbol{x})\\&\approx \hat{\delta}_n{}^{(i-1)}(\boldsymbol{x})\\&+\mathcal{R}_\theta{}^T\mathcal{F}^{-1}A_{-D_k}\mathcal{F}\left\{\frac{I_{D_k,\theta}(\boldsymbol{x})-1-\mathcal{F}^{-1}\left\{A_{D_k}\mathcal{F}\left\{\mathcal{R}_\theta\hat{\delta}_n{}^{(i-1)}\right\}\right\}(\boldsymbol{x})}{\|\mathcal{R}_\theta\|^2}\right\}\end{aligned} \tag{5.3.13}$$

Noticing that applying consecutively the forward and inverse Fourier transforms leads to the identity, as well as applying consecutively the operator A_D and A_{-D}. The previous expression is rewritten:

$$\begin{aligned}\hat{\delta}_n{}^{(i)}(\boldsymbol{x}) \approx \hat{\delta}_n{}^{(i-1)}(\boldsymbol{x})\\+\mathcal{R}_\theta{}^T\left\{\frac{\mathcal{F}^{-1}A_{-D_k}\mathcal{F}\{I_{D_k,\theta}(\boldsymbol{x})-1\}-\mathcal{R}_\theta\hat{\delta}_n{}^{(i-1)}(\boldsymbol{x})\}}{\|\mathcal{R}_\theta\|^2}\right\}\end{aligned} \tag{5.3.14}$$

This formulation was tested on simulated pure phase data.

One iteration of the proposed formulation (5.3.14) is performed by sweeping randomly all the projection angles and all the propagation distances.

3.c. Combined algorithm for mixed object

A mixed object designates an object that induces both attenuation and phase shifts of the incident X-ray wave. The absorption term in the CTF (Equation (5.2.2)) cannot be neglected anymore. The idea here is thus to iterate alternately on the absorption index (or the refractive index decrement), keeping

the refractive index decrement fixed (or the absorption index, respectively), therefore assuming it is known.

3.c.i. Known attenuation

We first assume that the attenuation, *i.e.* the absorption index β, is known.

At one angle θ, the CTF becomes:

$$\tilde{I}_{D_k,\theta}(\boldsymbol{f}) = k_\theta(\boldsymbol{f}) + A_{D_k}(\boldsymbol{f})\mathcal{F}\mathcal{R}_\theta\delta_n(\boldsymbol{f}) \tag{5.3.15}$$

with

$$A_{D_k}(\boldsymbol{f}) = -\frac{4\pi}{\lambda}\sin(\pi\lambda D_k|\boldsymbol{f}|^2) \tag{5.3.16}$$

and

$$k_\theta(\boldsymbol{f}) = \delta_{Dirac}(\boldsymbol{f}) - 2\cos(\pi\lambda D_k|\boldsymbol{f}|^2)\,\mathcal{F}\left\{\frac{2\pi}{\lambda}\mathcal{R}_\theta\beta\right\}(\boldsymbol{f}) \tag{5.3.17}$$

Separating the known terms from the unknown terms leads to:

$$I_{D_k,\theta}(\boldsymbol{x}) - \mathcal{F}^{-1}\{k_\theta\}(\boldsymbol{x}) = \mathcal{F}^{-1}\left\{A_{D_k}\mathcal{F}\{\mathcal{R}_\theta(\delta_n)\}\right\}(\boldsymbol{x}) \tag{5.3.18}$$

This problem can be solved using the SART by:

$$\begin{aligned}&\hat{\delta}_n{}^{(i)}(\boldsymbol{x})\\&= \hat{\delta}_n{}^{(i-1)}(\boldsymbol{x})\\&+ \left[\mathcal{F}^{-1}\left\{A_{D_k}\mathcal{F}\{\mathcal{R}_\theta\}\right\}\right]^T \frac{I_{D_k,\theta}(\boldsymbol{x}) - \mathcal{F}^{-1}\{k_\theta\}(\boldsymbol{x}) - \mathcal{F}^{-1}\left\{A_{D_k}\mathcal{F}\left\{\mathcal{R}_\theta\left(\hat{\delta}_n{}^{(i-1)}\right)\right\}(\boldsymbol{x})\right\}}{\left\|\mathcal{F}^{-1}\left\{A_{D_k}\mathcal{F}\{\mathcal{R}_\theta\}\right\}\right\|^2}\end{aligned} \tag{5.3.19}$$

From the simplifications discussed in the previous section, we obtain:

$$\hat{\delta}_n{}^{(i)}(\boldsymbol{x}) = \hat{\delta}_n{}^{(i-1)}(\boldsymbol{x}) + \mathcal{R}_\theta{}^T\left\{\frac{\mathcal{F}^{-1}\left\{A_{-D_k}\{\tilde{I}_{D_k,\theta} - k_\theta\}\right\}(\boldsymbol{x}) - \left\{\mathcal{R}_\theta\hat{\delta}_n{}^{(i-1)}\right\}(\boldsymbol{x})}{\|\mathcal{R}_\theta\|^2}\right\} \tag{5.3.20}$$

It is noticeable that the term $\mathcal{F}^{-1}\left\{A_{-D_k}\{\tilde{I}_{D_k,\theta} - k_\theta\}\right\}$ can be calculated once, before iterating on the refractive index decrement.

3.c.ii. Unknown attenuation

If the imaged object is attenuating, but the attenuation is unknown (*e.g.* in nanotomography, we do not have access to an attenuation scan for instrumentation reasons), the problem has two unknowns.

In this case, we first assume that the refractive index decrement δ_n is known. The CTF can then be rewritten as:

$$\tilde{I}_{D_k,\theta}(\boldsymbol{f}) = l_\theta(\boldsymbol{f}) + C_{D_k}(\boldsymbol{f})\mathcal{F}\{\mathcal{R}_\theta\beta\}(\boldsymbol{f}) \tag{5.3.21}$$

with

$$C_{D_k}(\boldsymbol{f}) = -\frac{4\pi}{\lambda}\cos(\pi\lambda D_k|\boldsymbol{f}|^2) \tag{5.3.22}$$

and

$$l_\theta(\boldsymbol{f}) = \delta_{Dirac}(\boldsymbol{f}) + 2\sin(\pi\lambda D_k|\boldsymbol{f}|^2)\,\mathcal{F}\left\{-\frac{2\pi}{\lambda}\mathcal{R}_\theta\delta_n\right\}(\boldsymbol{f}) \tag{5.3.23}$$

leading to

$$I_{D_k,\theta}(\boldsymbol{x}) - \mathcal{F}^{-1}\{l_\theta\}(\boldsymbol{x}) = \mathcal{F}^{-1}\left\{C_{D_k}\mathcal{F}\{\mathcal{R}_\theta\beta\}\right\}(\boldsymbol{x}) \tag{5.3.24}$$

In the same way than for known attenuation in the previous section, we obtain the following formulation:

$$\hat{\beta}^{(i)}(\boldsymbol{x}) = \hat{\beta}^{(i-1)}(\boldsymbol{x}) + {\mathcal{R}_\theta}^T\frac{\mathcal{F}^{-1}\left\{A_{-D_k}\left\{\tilde{I}_{D_k,\theta} - l_\theta\right\}\right\}(\boldsymbol{x}) - \left\{\mathcal{R}_\theta\hat{\beta}^{(i-1)}\right\}(\boldsymbol{x})}{\|\mathcal{R}_\theta\|^2} \tag{5.3.25}$$

Combining Equations (5.3.20) and (5.3.25) let us to **iterate alternatively between the absorption index and the refractive index decrement**, assuming turn by turn that the refractive index decrement and the absorption index (respectively) is known. This could lead to retrieve both indexes iteratively.

3.d. TV regularisation

TV denoising can be enforced at the end of each iteration.

To do so, we used the TVAL3 Matlab solver, developed by Li *et al.* (Li, Yin, Jiang, & Zhang, 2013), using augmented Lagrangian and alternating direction algorithms for anisotropic total variation minimization. We enforce a positivity constraint on the solution, since the retrieved values of δ_n (or β) are positive. The minimized objective function is:

$$\sum_i \left\|D_i\hat{\delta}_n\right\|_1 \text{ s.t. } \hat{\delta}_n \geq 0 \tag{5.3.26}$$

where $\|.\|_1$ is the 1-norm, $D_i\hat{\delta}_n$ is the discrete gradient vector of $\hat{\delta}_n$ at position *i*.

3.e. Implementation of the reconstruction framework

Here, we present the numerical implementation of the proposed framework. Projections and distances are randomly swept. The projection loop and the distance loop could be permuted, in an equivalent way.

```
## Loop
for it=1:iterations
     for j=1:projections
          for k=1:distances
               1/ Projection of delta_rec at the angle j
               2/ Propagation of this projection
               3/ Calculation of the difference between measured
and propagated projection
               4/ Phase retrieval on this difference using least
squares
               5/ Normalisation of the difference
               6/ Backprojection of the difference
               7/ Apply a mask on the reconstructed image
(constrained to be null outside the object)
               8/ Update delta_rec
          end of sweeping the distances
     end of sweeping the projections

     9/ (optional) Apply TV regularisation on the result
end of iterations
```

3.f. Numerical simulations and phase wrapping effect

The X-ray energy used for these simulations was 19keV and the pixel size was 3.5µm, which corresponds to common experimental conditions on the beamline ID19 of the ESRF.

3.f.i. Pure phase Sheep-Logan phantom

We simulate a pure phase object using the Shepp-Logan phantom, of dimensions 256x256. The 2D-attenuation map was null, and the 2D δ_n-map was the numerical Shepp-Logan phantom, with values rescaled between 0 and 10^{-6} or 10^{-7}; in the first case, the phase ranges between 0 and 22.35, thus largely exceeding 2π (Figure 6). In the second case, the phase ranges between 0 and 2.24, being lower than 2π. Based on the energy and pixel size, the four following propagation distances were chosen according to Zabler *et al.* (Zabler, Cloetens, Guigay, Baruchel, & Schlenker, 2005): D=[0.303; 0.636; 1.635; 1.968]m. 360 projections were simulated over a 360° angular range. Detection was simulated by possibly adding noise so that the Peak-to-Peak Signal to Noise Ratio (PPSNR) is equal to 48 dB in the simulated intensities, which is in agreement with the amount of noise observed in data acquired at the ESRF.

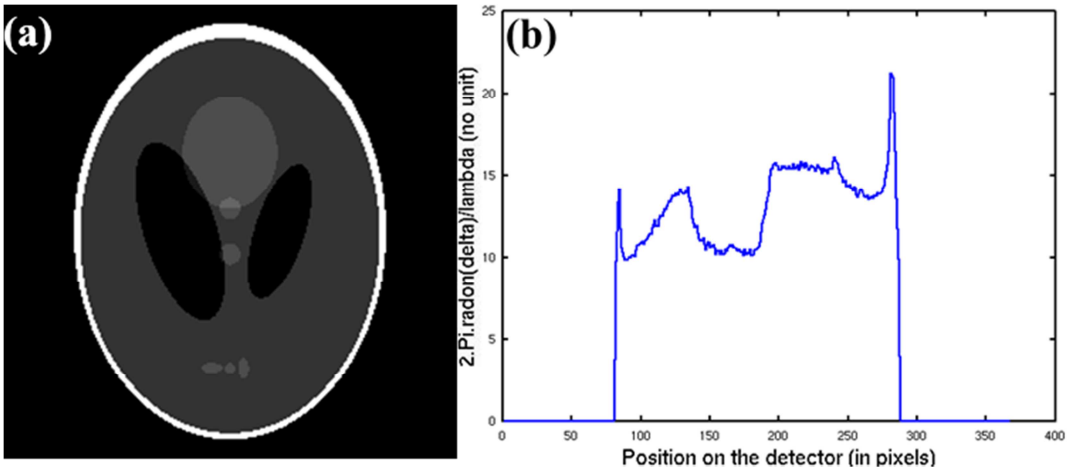

Figure 6: (a) Original object, a modified Shepp-Logan phantom, and (b) a phase projection. Note that the phase exceeds 2π.

3.f.ii. Attenuating phantom

We used an attenuating numerical phantom, inspired by the one used in the study of Frachon *et al.* (Frachon et al., 2015), to test the robustness of algorithms facing attenuating objects. The phantom is described in details in Section 2.a. The attenuation and/or the phase maps were possibly reduced by a factor of 15, the phase shift ranging, in this case, from 0 to 3.93 (lower than 2π). If no phase reduction, φ ranges from 0 to 58.03. Three propagation distances were chosen according to the study of Frachon *et al.* (2015): D = [0.100; 0.280; 1.056]m. 599 projections were simulated over a 360° angular range.

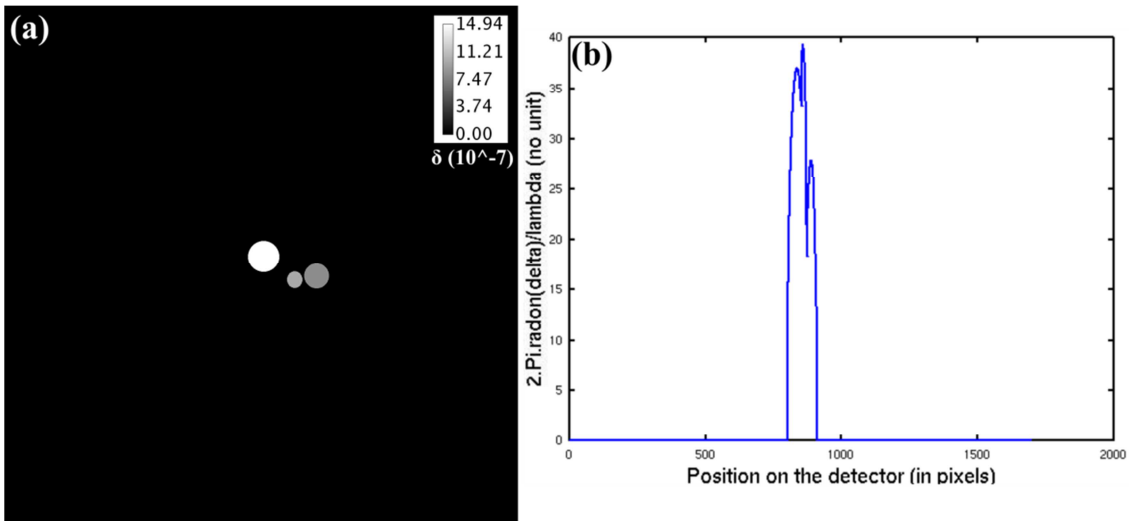

Figure 7: (a) $\boldsymbol{\delta_n}$-map of the three-wire phantom (Al, Mg, PET) used in the study of Frachon *et al.* (Frachon et al., 2015), and (b) a phase projection map.

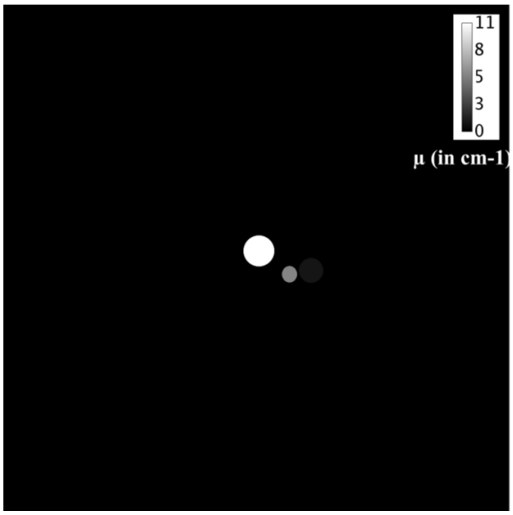

Figure 8: Attenuation map of the 3-wire phantom.

As mentioned in several publications (Chen et al., 2016; Davidoiu, Sixou, Langer, & Peyrin, 2013; Sixou, 2014), the phase retrieval can suffer from *phase wrapping effects*, when the retrieved phase exceeds 2π. Ruhland *et al.* used a Gerchberg-Saxton type algorithm with a consistency constraint to reconstruct the complex refractive index (A. Ruhlandt et al., 2014). It is unclear if this algorithm is robust to phase wrapping, however, since it was only demonstrated on weak objects.

3.g. Evaluation of the algorithms

We mainly test the algorithms on the presented data: the modified Shepp-Logan phantom for pure phase objects, and the three-wire phantom for attenuating object.

The three-wire phantom is made of PET (a weakly attenuating material), Al, and Mg, as described above. The Table 1 presents the theoretical values of the linear attenuation coefficient μ (in cm^{-1}), the absorption index β and the refractive index decrement δ_n for the cited material, at 19keV.

Material	μ (cm-1)	β (10^-9)	δ_n (10^-7)
Al	10.78	5.59	15.03
Mg	5.57	2.89	9.92
PET	0.89	0.46	8.27

Table 1: Theoretical values of the linear attenuation coefficient μ, the absorption index β, and the refractive index decrement $\boldsymbol{\delta_n}$ for the three studied materials (Aluminum, Magnesium, and Polyethylene Terephthalate), at 19keV.

Moreover, we tested the algorithm on 2D data, *i.e.* the reconstructed objects are 2D, and the corresponding projections are 1D. In the absence of satisfactory results, we did not perform further tests in 3D, but the theoretical part described above might as well be applied on 3D reconstructed object.

To quantitatively evaluate the reconstructed refractive index decrement slice, we calculated the normalized error (NE), and the relative standard deviation (RSD), for each of the three materials of the wires phantom, and for selected regions of the Shepp-Logan phantom (as depicted on Figure 9).

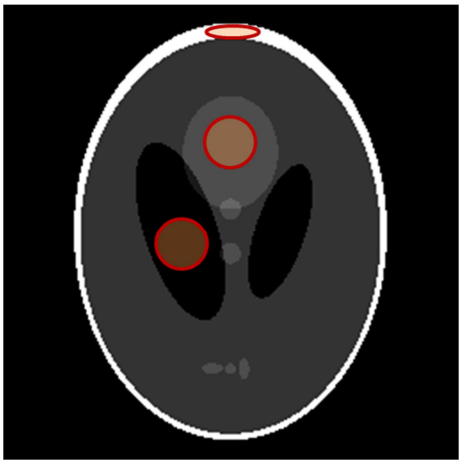

Figure 9: ROIs selected for qualitative assessment on the Shepp-Logan phantom reconstruction. The upper ROI corresponds to bone, the middle ROI to soft tissues (ST) and the bottom ROI to air.

The NE, expressed in percentage, is defined as:

$$\mathrm{NE}(\%) = 100.\frac{\delta_{n,th} - \delta_{n,meas}}{\delta_{n,th}}, \tag{5.3.27}$$

where $\delta_{n,th}$ and $\delta_{n,meas}$ stand for the theoretical the measured (mean) value of the refractive index decrement, respectively. The smaller the NE is, the more correct are the reconstructed δ_n values with respect to the expected theoretical values.

The RSD, expressed in percentage, is defined as:

$$RSD(\%) = 100.\frac{\sigma_{\delta_{n,meas}}}{\delta_{n,meas}}, \tag{5.3.28}$$

where $\sigma_{\delta_{n,meas}}$ is the standard deviation of the measured value of the refractive index decrement, and $\delta_{n,meas}$ is the mean measured value of the refractive index decrement.

4. Results

4.a. Phase retrieval and TV regularisation

The following section presents the results of the phase retrieval step only, using least squares method, adding, or not, TV regularisation, for different simulated images (pure phase object and attenuating object). TV denoising is enforced on the retrieved phase maps, before the tomographic reconstruction. The phase was retrieved in 1D on projection, and the slice is reconstructed using FBP.

4.a.i. Pure phase object (Shepp-Logan)

Using CTF as the forward phase contrast model for data simulation, the results are qualitatively satisfying whatever the range of the phase shift (*i.e.* phase wrapping or not). The normalized error ranges from 2.63% to 7.33%, using, or not, TV regularisation (Table 2).

	Forward contrast model : CTF					
	gaussian noise (48 dB)			no noise		
	No phase wrapping			Phase wrapping		
	theoretical value	No TV denoising	TV denoising	theoretical value	No TV denoising	TV denoising
NE (%) bone		2,63E+00	2,95E+00		5,26E+00	2,60E+00
RSD (%) bone	1,00E-07	2,19E+00	2,37E+00	1,00E-06	4,60E+00	9,92E-01
NE (%) ST		6,33E+00	6,33E+00		7,20E+00	7,33E+00
RSD (%) ST	3,00E-08	2,98E-01	2,76E-01	3,00E-07	2,57E-01	2,35E-01

Table 2: Normalized error (NE) and Relative Standard deviation (RSD), expressed in percentage, for bone and soft tissues (ST). The data were simulated using CTF as forward contrast model. The results are calculated for data presenting no phase wrapping, but additive Gaussian noise (48dB) and for unnoisy data but with phase wrapping.

Consequently, a linear phase contrast model enables to retrieve quantitatively the phase on a pure phase object, whatever the range of the phase shift (Figure 10).

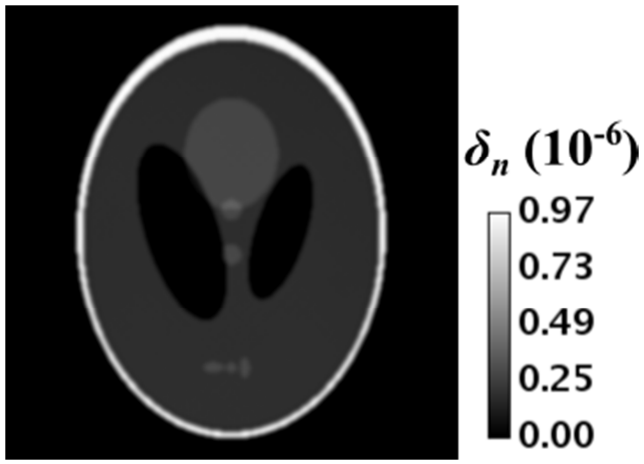

Figure 10: Example of retrieved phase for data simulated using the CTF model, with phase wrapping and additional gaussian noise (48dB). TV denoising was added after the phase retrieval.

Using Fresnel as the forward phase contrast model for data simulation, the results are qualitatively satisfying if there is no phase wrapping, as depicted in Figure 11. Quantitatively, the error ranges from 3 to 6.33%, if no phase wrapping, which looks reasonable. On the contrary, if the phase shift is higher than 2π, the error is around 16 to 19% (Table 3), and the reconstructed phase map presents artefacts. The strongly attenuating structure, mimicking the bone, could be responsible for such artefacts.

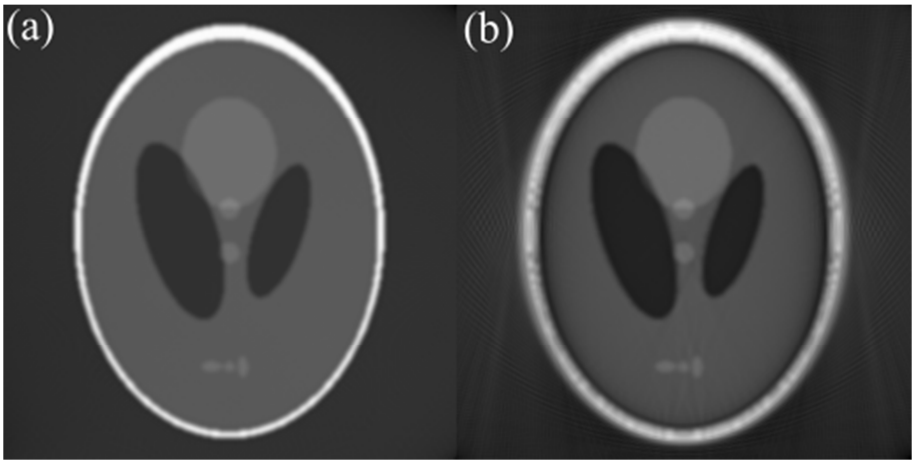

Figure 11: Reconstructed phase without (a) and with (b) phase wrapping effect.

	Forward contrast model : Fresnel					
	gaussian noise (48 dB)			no noise		
	No phase wrapping			Phase wrapping		
	theoretical value	No TV denoising	TV denoising	theoretical value	No TV denoising	TV denoising
NE (%) bone		3,30E+00	3,63E+00		1,93E+01	1,94E+01
RSD (%) bone	1,00E-07	3,07E+00	3,25E+00	1,00E-06	4,62E+00	4,53E+00
NE (%) ST		6,33E+00	6,33E+00		1,66E+01	1,66E+01
RSD (%) ST	3,00E-08	2,79E-01	3,25E+00	3,00E-07	6,28E-01	6,12E-01

Table 3: Normalized error (NE) and Relative Standard deviation (RSD), expressed in percentage, for bone and soft tissues (ST). The data were simulated using Fresnel as forward contrast model. The results are calculated for data presenting no phase wrapping, but additive Gaussian noise (48dB) and for unnoisy data but with phase wrapping.

As a conclusion, if one uses the CTF as direct contrast model, the reconstruction will always be close to the ground truth, because the direct and forward models are the same in this case. Nevertheless, the CTF poorly describes the Fresnel diffraction phenomenon, particularly in case of strong objects. On the contrary, the Fresnel model is more realistic, but also potentially induces more errors in the reconstructed phase, as the object is harder. This preliminary result can be helpful in the evaluation of the proposed combined algorithm. Moreover, we note that the regularisation of the result shows not outstanding quantitative improvement (see NE and RSD), probably because little noise was added; but it qualitatively enables to get rid of possible reconstruction artefact at the borders of the image (smoothing of the reconstructed image).

4.a.ii. Attenuating object (three-wire phantom)

For data simulated using the CTF as forward contrast model, the retrieved refractive index decrement show very good agreement with the theoretical values, with normalized error being lower than 1%, even if the data are noisy or have large phase shifts.

As an example, Table 4 presents the results of refractive index decrement of the three considered materials. They were obtained using the least square method for phase retrieval, followed by FBP, for simulated intensities at three propagation distances, without any reduction of phase or attenuation.

This can be considered as the "worst" case, since the attenuation is not weak, neither is the phase variation. The attenuation is assumedly known. The corresponding reconstructed map and a line profile are shown in Figure 12. We notice that the reconstructed slice is a bit blurred around the edges of the wires.

Material	Theoretical value $\delta_{n,th}$	Mean measured value $\delta_{n,meas}$	Standard deviation of measured value $\sigma_{\delta_{n,meas}}$	NE (%)	RSD (%)
Al	1,50E-06	1,49E-06	1,49E-06	0,67	3,90E-02
PET	9,92E-07	9,88E-07	9,88E-07	0,41	4,48E-01
Mg	8,27E-07	8,25E-07	8,25E-07	0,23	6,22E-02
Background (air)	0	-1,33E-09	4,11E-10	X	X

Table 4: Normalized error (NE) and Relative Standard deviation (RSD), expressed in percentage, for the different materials (Al, PET, Mg, air). The data were simulated using CTF as forward contrast model, without any attenuation/phase reduction (μ lies in the range [0 : 10.78]cm^{-1} and φ lies in the range [0 : 22.4]). The cross (X) indicates an undefined result (division by zero).

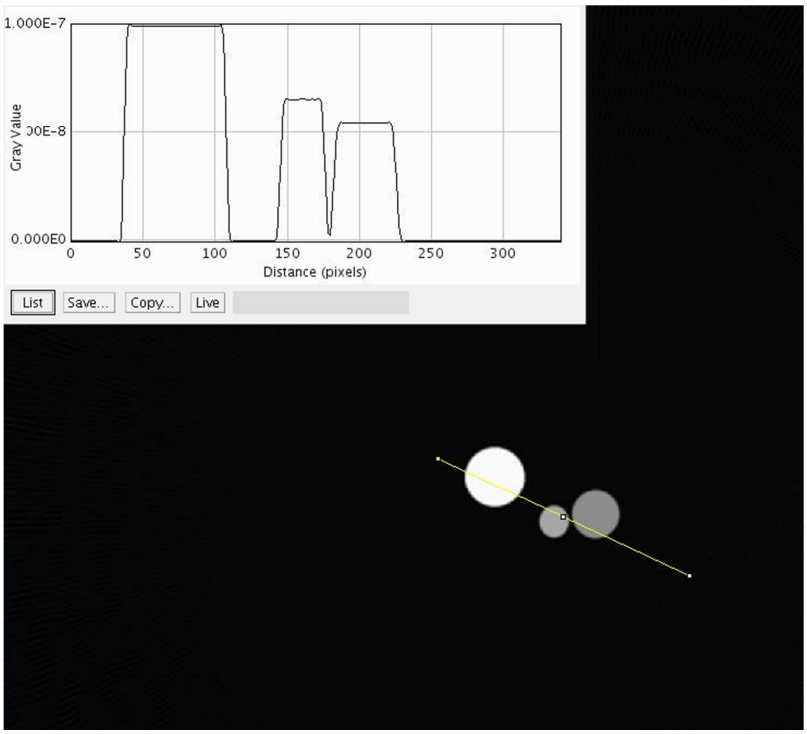

Figure 12: Reconstructed δ_n-map for conditions described above (CTF as forward model, no attenuation and phase reduction).

For data simulated using Fresnel contrast model, the results are satisfying if the attenuation is reduced. Actually, Figure 13 suggests that strong attenuation is more critical than the phase wrapping for phase retrieval using least squares.

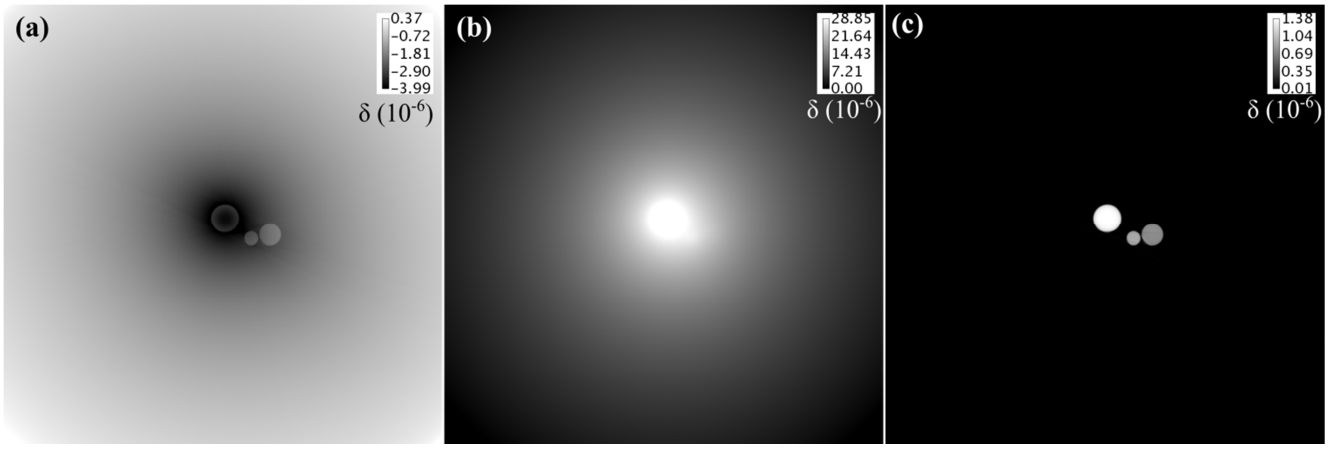

Figure 13: Retrieved refractive index decrement for: (a) the original data (no phase or attenuation reduction), (b) a phase reduction by a factor of 15, (c) attenuation reduction by a factor of 15.

Moreover, if we considered three wires all made of plastic, without any attenuation or phase reduction, we achieve satisfying results, as presented in Table 5.

	Theoretical $\delta_n$value	**Measured mean δ_n value**	**Measured standard deviation**	**NE (%)**	**RSD (%)**
PET	8,27E-07	8,53E-07	8,19E-09	-3,16E+00	9,61E-01
Background (air)	0	1,00E-08	9,26E-09	X	9,26E+01

Table 5: Retrieved $\boldsymbol{\delta_n}$-values, for a three-plastic wires phantom, with corresponding normalized error (NE, in %) and relative standard deviation (RSD, in %). The cross (X) indicates an undefined value (division by zero).

This leads to conclude that a strongly absorbing structure is more critical for quantitative phase retrieval than a structure inducing large phase shifts, which is in agreement with CTF validity conditions.

4.b.Proposed combined algorithm

In this section, we present the results obtained using the innovative proposed algorithm, on simulated data, in various conditions.

4.b.i. Pure phase objects

First, the results of the combined algorithm (with TV regularisation at each iteration), on simulated intensities of a pure phase object, without addition of noise, are presented on Figure 14 and Figure 15. The reconstruction was performed based on Equation (5.3.14). The results are presented for data simulated using the Fresnel model as direct contrast model, because it was the more critical case. The retrieved δ_n-map was initialized to zero. The number of iterations was set experimentally, so that the results converge. The regularisation parameter was set to 10^{-30}, according to the phase retrieval preliminary study (Section 4.a).

Figure 14 shows the reconstructed δ_n-map (on the left), with a corresponding profile (on the right), at different iterations (1, 20 and 40). We note that the reconstruction becomes sharper as the iteration increases. To assess the quality of the reconstruction along the iterations, we plot the normalized error

for bone- and soft tissues-like materials (Figure 15). We can see that the solution converges to a normalized error around 15%; so, the phase is not as accurately retrieved as desired. We notice an offset at the border of the image (visible on the plotted profile).

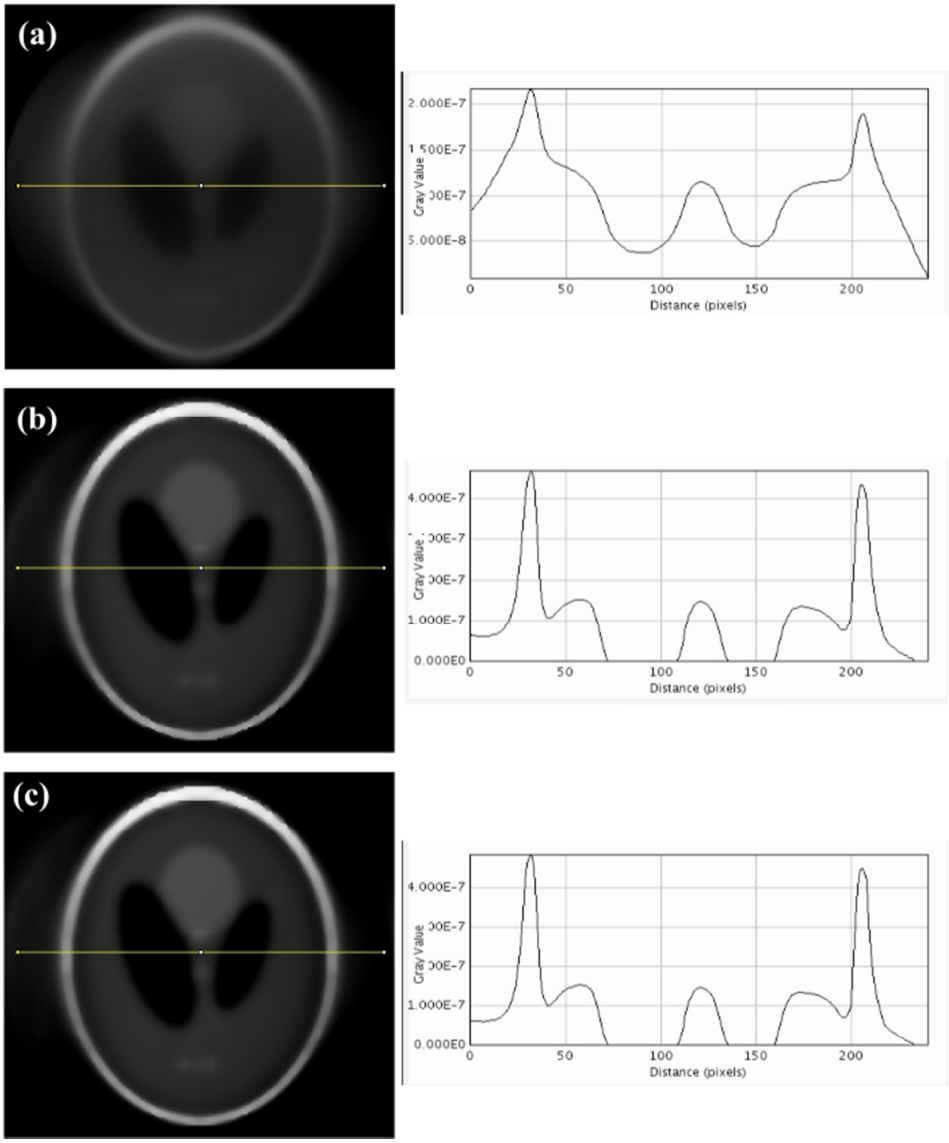

Figure 14: Retrieved $\boldsymbol{\delta_n}$-map for data simulated with Fresnel as contrast model, without noise, and phase exceeding 2π. The resulting map (on the left), and a corresponding profile (on the right) are presented at (a) the 1st iteration, (b) the 20th iteration, and (c) the 40th iteration of the proposed algorithm.

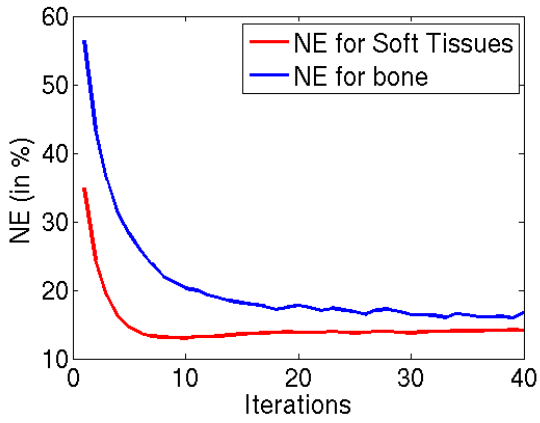

Figure 15: Normalized error (NE), in %, for Soft tissues zone and Bone zone, as a function of the iterations, for unnoisy data.

Then, we used the same data, with addition of noise up to 48dB PPSNR. The results are presented, the same way as previously, on Figure 16 and Figure 17. Figure 16 shows the reconstructed δ_n-map (on the left), with a corresponding profile (on the right), at different iterations (1, 20 and 40). We plot the normalized error for bone- and soft tissues-like materials, as a function of the iterations, on Figure 17. We can see that the solution converges, but the phase is not accurately retrieved. Surprisingly, the result of noisy data seems to be sharper than without noise. We notice an offset at the border of the image (visible on the plotted profile). If putting the borders at zero, the delta values would be closer to the theoretical values. This could show that the algorithm is robust to the presence of noise.

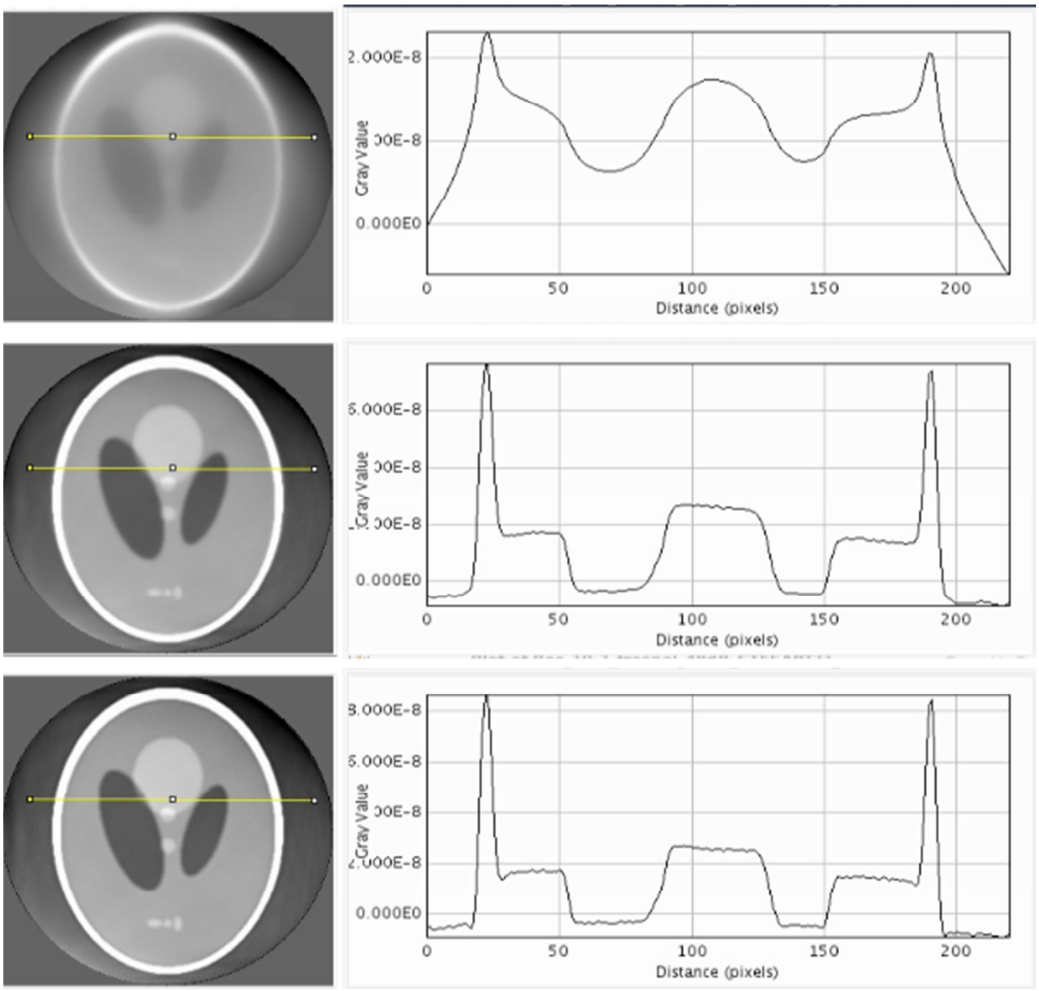

Figure 16: Retrieved $\boldsymbol{\delta_n}$-map for noisy data simulated with Fresnel as contrast model, and phase exceeding 2π. The resulting map (on the left), and a corresponding profile (on the right) are presented at (a) the 1st iteration (b) the 20th iteration, and (c) the 40th iteration of the proposed algorithm.

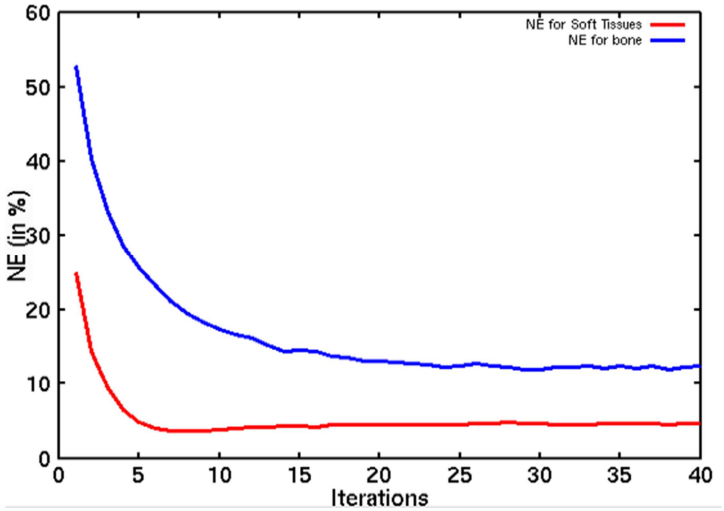

Figure 17: Normalized error (NE), in %, for Soft tissues zone and Bone zone, as a function of the iterations, for noisy data.

4.b.ii. Weakly attenuating object

In a second time, we applied our proposed algorithm (see Section 3.c.ii) on weakly attenuating object. For the sake of computation time, the reconstructed image was cut to 256 x 256 pixels. We tested the algorithm proposed in, on the three wires phantom (composed of Al, Mg and PET), but we reduced its attenuation by a factor of 15. Note that even if the attenuation was reduced, it is no-null (the linear attenuation coefficient μ, in this case, ranges in $[0.08: 1.07]$ cm^{-1}, roughly corresponding to air and soft tissues at imaging energies.

The reconstruction was performed based on Equation (5.3.20). The retrieved δ_n-map was initialized to zero. The number of iterations was set experimentally, so that the results converge. The regularisation parameter was set to 10^{-30}, according to the phase retrieval preliminary study (Section 4.a).

Data were simulated using the Fresnel model. The results are presented in Figure 18 (reconstructed δ_n-maps and profiles) and Figure 19 (normalized error). As in the previous section, results converge, despite being not fully quantitative. The errors are around 5% for weakly attenuation material, and around 10% for aluminum, a more attenuating material.

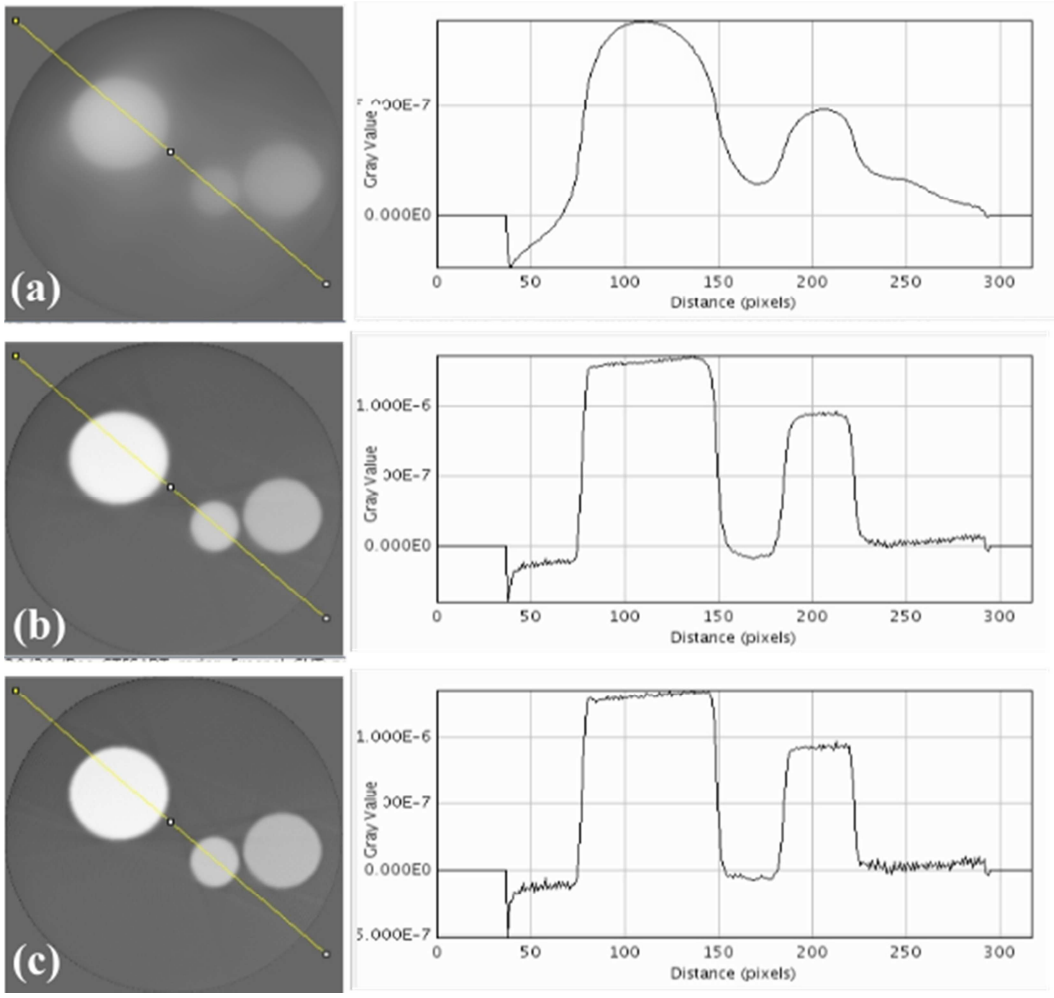

Figure 18: Retrieved $\boldsymbol{\delta_n}$-map for data simulated with Fresnel as contrast model, without noise, and phase shifts exceeding 2π. The attenuation map was reduced by a factor of 15. The resulting map (on the left), and a corresponding profile (on the right) are presented at (a) the 1st iteration, (b) the 15th iteration, and (c) the 30th iteration of the proposed algorithm.

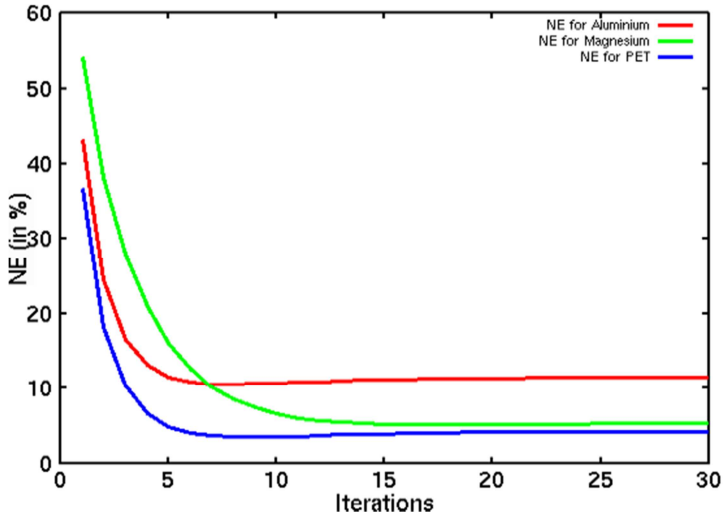

Figure 19: Normalized error (NE), in %, for Al (red), Mg, (green) and PET (blue), as a function of the iterations of the proposed algorithm. The attenuation was not reduced, and the CTF contrast model was employed. No noise was added on the simulated intensities.

As a comparison, we perform the same study on data simulated with CTF as contrast model. As Figure 20 and Figure 21 show, the results are very satisfying, whether it be qualitatively or quantitatively.

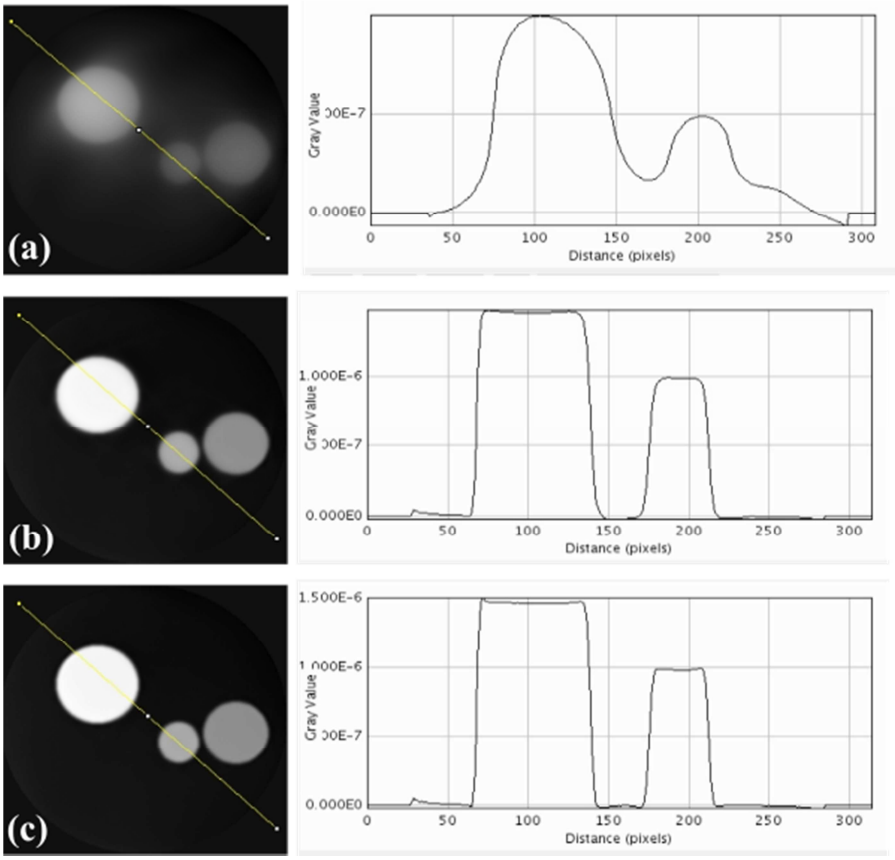

Figure 20: Retrieved $\boldsymbol{\delta_n}$-map for data simulated with CTF as contrast model, without noise, and phase shifts exceeding 2π. The attenuation map was reduced by a factor of 15. The resulting map (on the left), and a corresponding profile (on the right) are presented at (a) the 1st iteration, (b) the 15th iteration, and (c) the 30th iteration of the proposed algorithm.

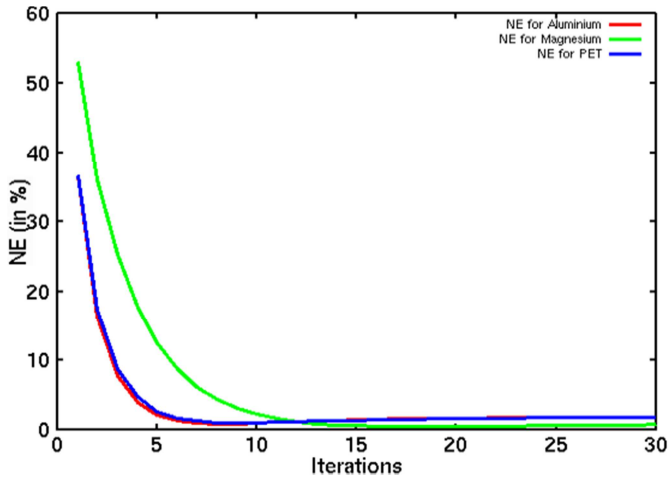

Figure 21: Normalized error (NE), in %, for Al (red), Mg, (green) and PET (blue), as a function of the iterations of the proposed algorithm. The attenuation was not reduced, and the CTF contrast model was employed. No noise was added on the simulated intensities.

4.b.iii. Strongly attenuating object

Finally, we test the combined algorithm on the three-wire phantom data, without reducing the attenuation. No noise was added on the simulated intensities, and Fresnel and CTF were used as contrast models.

The reconstruction was performed based on Equation (5.3.20). The retrieved δ_n-map was initialized to zero. The number of iterations was set experimentally, so that the results converge. The regularisation parameter was set to 10^{-30}, according to the phase retrieval preliminary study (Section 4.a). The corresponding retrieved phase maps are presented on Figure 22.

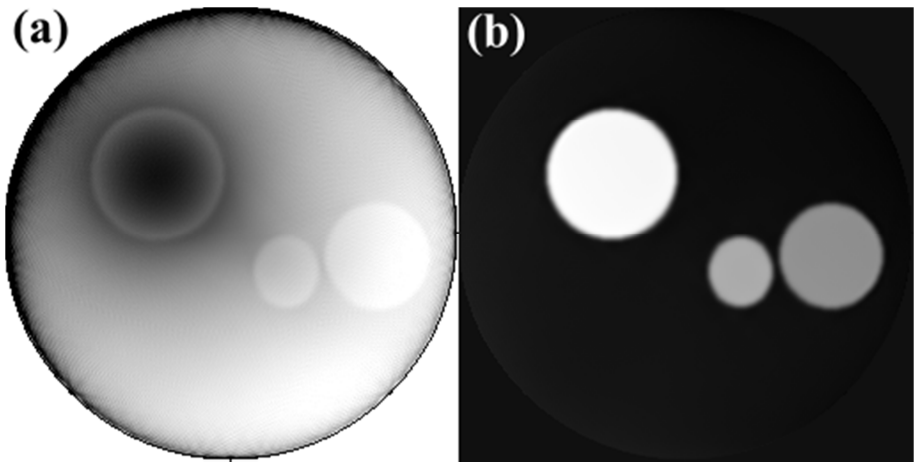

Figure 22: Retrieved $\boldsymbol{\delta_n}$-map of a strongly attenuating object, using the combined algorithm. Data are simulated using (a) the Fresnel contrast model and (b) the CTF contrast model.

The Fresnel model is more realistic, because it does not required any restrictive assumptions on the object. Therefore, our proposed algorithm does not lead to satisfying results, when applied on

attenuating object. For completeness, we assess the error of the reconstructed quantities, as a function of the iterations (Figure 23). The error exceeds several orders of magnitude for all the material, whether it be weakly or strongly attenuating.

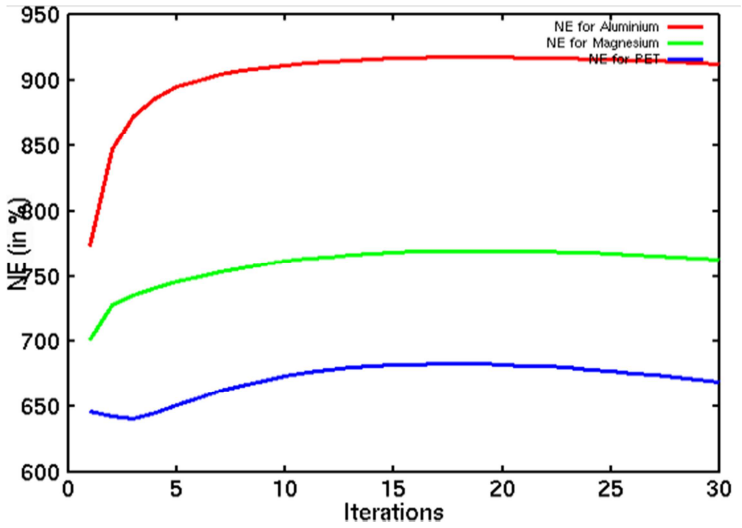

Figure 23: Normalized error, in %, for Fresnel data of attenuating object.

5. Discussion

We presented the first results obtained with the combined algorithm. One advantage of the combined approach is that it enables the introduction of regularisation in the object domain. We obtained encouraging results for pure phase and weakly attenuating objects. However, the results show that we may obtain large errors in some situations, particularly for strongly attenuating objects. It seems that the model employed for the simulation of the data plays a predominant role in the algorithm. Actually, the Fresnel model induces larger errors in the reconstruction, but is also more realistic since it does not assume restrictive constraints on the object. The theoretical formulation of our proposed algorithm is probably limited because of the linear contrast model used, which makes it restricted to a certain type of object (slowly varying phase and weakly attenuating object). To go further, the mixed approach (Guigay, Langer, Boistel, & Cloetens, 2007) could be considered as contrast model employed in the combined phase reconstruction method.

6. Conclusion

In this chapter, we presented a tool developed for phase-contrast data simulation, and ported on the Virtual Imaging Platform. Secondly, we set up the theoretical formulation of a new algorithm that combines phase retrieval with tomographic reconstruction, and includes TV regularisation. It enables the introduction of a priori in the object domain. Some preliminary results, obtained on simulated data, are then presented. Thanks to tailor-made simulated data, we investigated several objects (pure phase, weakly attenuating, strongly attenuating), and evaluated qualitatively and quantitatively the results. We showed that the results are very dependent on the contrast model used, and the algorithm is probably restricted to weakly attenuating objects.

7. Perspectives

Further investigations on running this algorithm for solving the attenuation and the phase, turn by turn, should be considered.

In a practical point of view, and for the sake of computation time, the ASTRA toolbox is worth considering, particularly when it comes to 3D (van Aarle et al., 2015). This would be true for both simulations and phase reconstruction algorithm. Unfortunately, in this work, we failed to use it, because of compatibility between Octave and the toolbox, but it seems possible since recently using a Python overcoat layer (Pelt et al., 2016). This step appears to be crucial for the implementation of this work on real and 3D data, usually much larger than the one employed here.

The reconstruction with less data is also a potential advantage of such combined and regularised method, and could be investigated. Actually, the introduction of constraints usually enables to achieve the same reconstruction quality with less data. The major benefit of this, particularly when it comes to synchrotron data, is the potentially reduced time scan and delivered dose when acquiring less projections; it could facilitate the imaging of more samples, even *in vivo* imaging, or reconstruct data from sparse acquisition, as it is the case in fluorescence tomography for example.

References

Andersen, A. H., & Kak, A. C. (1984). Simultaneous algebraic reconstruction technique (SART): a superior implementation of the art algorithm. *Ultrasonic Imaging*, *6*(1), 81–94.

Bartels, M., Priebe, M., Wilke, R. N., Krüger, S. P., Giewekemeyer, K., Kalbfleisch, S., … Salditt, T. (2012). Low-dose three-dimensional hard x-ray imaging of bacterial cells. *Optical Nanoscopy*, *1*(1), 10. doi:10.1186/2192-2853-1-10

Beck, A., & Teboulle, M. (2009). A Fast Iterative Shrinkage-Thresholding Algorithm for Linear Inverse Problems. *SIAM Journal on Imaging Sciences*, *2*(1), 183–202. doi:10.1137/080716542

Binder, K., & Heermann, D. (2002). *Monte Carlo simulation in statistical physics* (4th editio.). New York.

Chambolle, A., & Pock, T. (2010). A First-Order Primal-Dual Algorithm for Convex Problems with Applications to Imaging. *Journal of Mathematical Imaging and Vision*, *40*(1), 120–145. doi:10.1007/s10851-010-0251-1

Chen, Y., Wang, K., Gursoy, D., Hoyuelos, C. S., De Carlo, F., & Anastasio, M. A. (2016). Joint reconstruction of absorption and refractive properties in propagation-based x-ray phase-contrast tomography via a non-linear image reconstruction algorithm. In D. Kontos, T. G. Flohr, & J. Y. Lo (Eds.), *SPIE Medical Imaging* (p. 97835H). International Society for Optics and Photonics. doi:10.1117/12.2217443

Cloetens, P., Ludwig, W., Baruchel, J., Van Dyck, D., Van Landuyt, J., Guigay, J. P., & Schlenker, M. (1999). Holotomography: Quantitative phase tomography with micrometer resolution using hard synchrotron radiation x rays. *Applied Physics Letters*, *75*(19), 2912. doi:10.1063/1.125225

Davidoiu, V., Sixou, B., Langer, M., & Peyrin, F. (2011). NON-LINEAR ITERATIVE PHASE RETRIEVAL BASED ON FRECHET DERIVATIVE AND PROJECTION OPERATORS. In *Optics EXPRESS* (Vol. 19, pp. 106–109). Barcelona, Spain. doi:10.1364/OE.19.022809

Davidoiu, V., Sixou, B., Langer, M., & Peyrin, F. (2013). In-line phase tomography using nonlinear phase retrieval. *Annals of the University of Bucharest (Mathematical Series)*, *4 (LXII)*, 115–122.

Frachon, T., Weber, L., Hesse, B., Rit, S., Dong, P., Olivier, C., … Langer, M. (2015). Dose fractionation in synchrotron radiation x-ray phase micro-tomography. *Physics in Medicine and Biology*, *60*(19), 7543–7566. doi:10.1088/0031-9155/60/19/7543

Glatard, T., Lartizien, C., Gibaud, B., da Silva, R. F., Forestier, G., Cervenansky, F., … Friboulet, D. (2013). A virtual imaging platform for multi-modality medical image simulation. *IEEE Transactions on Medical Imaging*, *32*(1), 110–8. doi:10.1109/TMI.2012.2220154

Goodman, J. W. (2005). *Introduction to Fourier Optics*. New York: Roberts and Company Publishers.

Guigay, J. P., Langer, M., Boistel, R., & Cloetens, P. (2007). Mixed transfer function and transport of intensity approach for phase retrieval in the Fresnel region. *Optics Letters*, *32*(12), 1617. doi:10.1364/OL.32.001617

Khromova, A. N., Arfelli, F., Besch, H. J., Plothow-Besch, H., Menk, R. H., & Rigon, L. (2010). Monte Carlo Simulation of X-ray Multiple Refractive Scattering from Fine Structure Objects imaged with the DEI Technique. In *IEEE Symposium Conference Record Nuclear Science 2004.* (Vol. 6, pp. 4014–4018). Medical Physics; Accelerator Physics, IEEE. doi:10.1109/NSSMIC.2004.1466758

Kongskov, R. D., Jørgensen, J. S., Poulsen, H. F., & Hansen, P. C. (2016). Noise robustness of a combined phase retrieval and reconstruction method for phase-contrast tomography. *Journal of the Optical Society of America A*, *33*(4), 447. doi:10.1364/JOSAA.33.000447

Kostenko, A., Batenburg, K. J., Suhonen, H., Offerman, S. E., & van Vliet, L. J. (2013). Phase retrieval in in-line x-ray phase contrast imaging based on total variation minimization. *Optics Express*, *21*(1), 710–23. doi:10.1364/OE.21.000710

Langer, M., Cloetens, P., Guigay, J. P., Valton, S., & Peyrin, F. (2007). Quantitative evaluation of phase retrieval algorithms in propagation based phase tomography. In *IEEE International Symposium on Biomedical Imaging (ISBI)* (pp. 552–555). Arlington, USA.

Li, C., Yin, W., Jiang, H., & Zhang, Y. (2013). An efficient augmented Lagrangian method with applications to total variation minimization. *Computational Optimization and Applications*, *56*(3), 507–530. doi:10.1007/s10589-013-9576-1

Moosmann, J., Hofmann, R., Bronnikov, A., & Baumbach, T. (2010). Nonlinear phase retrieval from single-distance radiograph. *Optics Express*, *18*, 25771–25785. doi:10.1364/OE.18.025771

Nilchian, M., Bostan, E., Wang, Z., Nilchiyan, M. R., Stampanoni, M., & Unser, M. (2016). Joint absorption and phase retrieval in grating-based x-ray radiography. *Optics Express*, *24*(7), 7253. doi:10.1364/OE.24.007253

Nugent, K., Gureyev, T., Cookson, D., Paganin, D., & Barnea, Z. (1996). Quantitative Phase Imaging Using Hard X Rays. *Physical Review Letters*, *77*(14), 2961–2964. doi:10.1103/PhysRevLett.77.2961

Pelt, D. M., Gürsoy, D., Palenstijn, W. J., Sijbers, J., De Carlo, F., & Batenburg, K. J. (2016). Integration of TomoPy and the ASTRA toolbox for advanced processing and reconstruction of tomographic synchrotron data. *Journal of Synchrotron Radiation*, *23*(Pt 3), 842–9. doi:10.1107/S1600577516005658

Peter, S., Modregger, P., Fix, M. K., Volken, W., Frei, D., Manser, P., & Stampanoni, M. (2014). Combining Monte Carlo methods with coherent wave optics for the simulation of phase-sensitive X-ray imaging. *Journal of Synchrotron Radiation*, *21*(Pt 3), 613–22. doi:10.1107/S1600577514000952

Raven, C., Snigirev, A., Snigireva, I., Spanne, P., Souvorov, A., & Kohn, V. (1996). Phase-contrast microtomography with coherent high-energy synchrotron x rays. *Applied Physics Letters*, *69*(13), 1826. doi:10.1063/1.117446

Ruhlandt, A., Krenkel, M., Bartels, M., & Salditt, T. (2014). Three-dimensional phase retrieval in propagation-based phase-contrast imaging. *Physical Review A*, *89*(3), 033847. doi:10.1103/PhysRevA.89.033847

Ruhlandt, A., & Salditt, T. (2016). Three-dimensional propagation in near-field tomographic X-ray phase retrieval. *Acta Crystallographica Section A Foundations and Advances*, *72*(2). doi:10.1107/S2053273315022469

Sixou, B. (2014). Reconstruction of the complex refractive index in nonlinear phase contrast tomography. *Inverse Problems in Science and Engineering*, 1–12. doi:10.1080/17415977.2014.947480

van Aarle, W., Palenstijn, W. J., De Beenhouwer, J., Altantzis, T., Bals, S., Batenburg, K. J., & Sijbers, J. (2015). The ASTRA Toolbox: A platform for advanced algorithm development in electron tomography. *Ultramicroscopy*, *157*, 35–47. doi:10.1016/j.ultramic.2015.05.002

Wang, Z., Huang, Z., Zhang, L., Chen, Z., & Kang, K. (2009). Implement X-ray refraction effect in Geant4 for phase contrast imaging. In *2009 IEEE Nuclear Science Symposium Conference Record (NSS/MIC)* (pp. 2395–2398). IEEE. doi:10.1109/NSSMIC.2009.5402180

Zabler, S., Cloetens, P., Guigay, J.-P., Baruchel, J., & Schlenker, M. (2005). Optimization of phase contrast imaging using hard x rays. *Review of Scientific Instruments*, *76*(7), 073705. doi:10.1063/1.1960797

Conclusions et perspectives

Dans ces travaux, nous présentons des développements et des applications de la tomographie de phase. En effet, cette nouvelle technique qui offre un contraste bien supérieur à celui de l'absorption, possède de nombreuses applications potentielles pour l'investigation des tissus biologiques. Nos travaux se sont essentiellement concentrés sur des systèmes de micro-tomographie et de nano-tomographie de phase par propagation, développés sur des lignes de lumière à l'ESRF (Grenoble), pour les applications au tissu osseux.

Les deux premiers chapitres ont été consacrés au contexte des travaux.

Nous avons rappelé en détail les principes physiques des interactions entre les rayons X et la matière, ainsi que les principes physiques sous-jacents au contraste de phase. Nous avons ensuite introduit les notions de tomographie et de tomographie par contraste de phase. Un deuxième chapitre a été employé à présenter les différents modèles de contraste de phase, ainsi que les méthodes d'estimation de phase existantes. La plupart de ces algorithmes font l'hypothèse d'objets observés homogènes, comme c'est le cas pour la méthode de Paganin, largement utilisée. Cette méthode trouve ses limites dans l'estimation des informations de hautes fréquences, et conduit donc à un résultat souvent légèrement flou. Pour pallier à cela, l'acquisition multiple de scanographes est couramment utilisée. Des méthodes basées sur un modèle de contraste mixte ont alors été développées, et permettent l'imagerie quantitative d'objets supposés homogènes ou hétérogènes. Ces méthodes sont régularisées via l'introduction d'a prioris dans le domaine des projections. Néanmoins, l'acquisition multiple de données se fait au détriment de la dose délivrée et du temps de scanographie. D'autre part, l'ajout de régularisation dans le domaine des projections n'est pas forcément idéal ; par exemple, l'emploi de régularisation TV, qui favorise une image homogène par morceaux, a plus de sens dans le domaine objet que dans celui des projections. L'emploi d'algorithmes itératifs régularisés pourrait alors permettre l'utilisation de moins de données, réduisant alors la dose délivrée et le temps d'acquisition, ou l'ajout de régularisation dans le domaine objet, plutôt que dans celui des projections. Ainsi, nous avons présenté, à la fin de cette partie relative au contexte des travaux, les méthodes qui visent à combiner l'estimation de phase et la reconstruction tomographique en une seule étape.

Les trois autres chapitres ont été dédiés aux contributions apportées par ces travaux.

Dans une première étude, nous avons appliqué la micro-tomographie de phase à des biomatériaux ensemencés de cellules osseuses. Les cellules osseuses étudiées ici étaient les ostéoblastes, responsables de la formation de l'os, et les ostéoclastes qui induisent au contraire la résorption de l'os. Nous avons présenté différentes méthodes d'estimation de phase : la méthode de Paganin, qui fait l'hypothèse d'un objet homogène, et les méthodes basées sur le modèle de contraste mixte, qui ont été adaptées à des objets homogènes, ou hétérogènes, et introduisent des a prioris dans le domaine des projections. Nous avons d'une part automatisé le processus de reconstruction en micro-CT de phase, qui rend le traitement des acquisitions plus simple et rapide, laissant plus de temps pour l'analyse des données. Cette automatisation a pu être utilisée en pratique, et prochainement valorisée sur des images de dents, dont l'analyse est en cours. D'autre part, nous avons montré que, dans le cadre de l'holotomographie, l'utilisation de méthodes régularisées avancées permettait d'améliorer qualitativement et quantitativement la reconstruction par rapport aux méthodes employées jusqu'ici. Nous avons également quantifié les différentes phases composant les échantillons (à savoir les cellules, le biomatériau, l'os nouvellement formé. Pour les échantillons étudiés, nous avons montré

que la présence d'ostéoblastes augmentait la part d'os nouvellement formé, contrairement à la présence d'ostéoclastes. Malheureusement, le nombre peu élevé d'échantillons, et l'accès limité au rayonnement synchrotron, n'a pas permis d'en tirer des conclusions statistiquement significatives. Néanmoins, nous avons développé les protocoles complets d'acquisition, de reconstruction et d'analyse pour ce type d'échantillons.

Une seconde étude a été consacrée à la nano-tomographie de phase sur des échantillons d'os humains. Nous avons imagé et reconstruit les volumes 3D de plusieurs échantillons (sain, souffrant d'ostéoarthrose et souffrant d'ostéoporose), et nous avons présenté plusieurs outils d'étude visant à caractériser la structure fine de ces échantillons. Après avoir décrit les méthodes d'estimation de phase propres à la nano-CT de phase, nous avons présenté un nouvel outil automatique visant à recaler entre elles les projections acquises à différentes distance de propagation. Pour ce faire, il utilise l'information mutuelle plutôt qu'un critère de corrélation, utilisé habituellement. Nous l'avons appliqué sur des données réelles, et nous avons montré qu'il est souvent plus robuste que le critère de corrélation classique, en plus d'être complètement automatisé. L'application de cette technique d'imagerie à l'os nous a permis d'avoir une vision approfondie du réseau cellulaire osseux. Par exemple, nous avons pu déterminer le volume et la forme des lacunes, et comparer nos résultats avec ceux d'études menées par d'autres instituts de recherches. Nous avons présenté des outils dédiés à la caractérisation de la minéralisation de l'os et à l'orientation des fibres de collagène. Une telle caractérisation peut permettre de mieux comprendre les propriétés de l'os, probablement liées à sa pathologie.

La dernière étude a été dédiée au développement d'algorithmes de simulation et de reconstruction d'images de phase tridimensionnelles. Nous avons proposé un outil de simulation d'image en contraste de phase, analytique. Cet outil, nommé « CreaPhase », a été porté sur la plateforme d'imagerie virtuelle VIP (Creatis, Villeurbanne, France) afin de la rendre accessible à toute la communauté scientifique. Ceci a également permis de mieux représenter la modalité de contraste de phase sur la plateforme. Des axes d'amélioration, tel que le développement d'un code Monte Carlo pour la simulation de contraste de phase, est en cours par le biais d'un stage. D'autre part, nous avons étudié plusieurs algorithmes pour la reconstruction de phase en 3D, que nous avons ensuite pu tester sur des données simulées. Ces algorithmes sont innovants car ils combinent l'estimation de phase avec la reconstruction tomographique en une seule étape, auparavant découplées en deux étapes distinctes. Pour ce faire, nous avons utilisé un modèle de contraste linéaire, couplé à un algorithme algébrique de reconstruction tomographique. Ceci nous permet par ailleurs l'ajout de régularisation TV (Variation Totale) dans le domaine objet, alors qu'elle était auparavant introduite dans le domaine des projections. Les résultats obtenus sont prometteurs quand il s'agit d'objets dont l'atténuation est faible ou connue, mais montrent des limites pour des objets très atténuants, ce qui est néanmoins cohérents avec les hypothèses de validité du modèle de contraste employé. Ce travail ouvre le champ à de multiples perspectives d'amélioration et de recherche : emploi d'autres types de régularisation, ou d'autres modèles de contraste moins restrictifs que la CTF, comme le modèle mixte, par exemple. Les applications et le potentiel de ce type d'algorithme sont diverses : reconstruction de données acquises avec peu de projections (qui limiterait ainsi le temps d'acquisition et la dose délivrée), reconstruction de données volumineuses, etc. La possibilité d'une reconstruction quantitative d'objet hétérogènes s'avère également particulièrement intéressante pour l'imagerie de l'articulation du genou par exemple, sans ajout d'agent de contraste, car une telle région comprend des tissus mous, de l'os, du cartilage et des vaisseaux. Ainsi, nous avons développé plusieurs outils visant à automatiser la reconstruction, ainsi qu'un outil de simulation qui peut s'avérer utile pour tester de nouveaux algorithmes, avant de les tester sur des données réelles, moins facilement accessibles. À travers une

étude de données en nanotomographie de phase, nous avons pu constater que l'amélioration des outils de segmentation (ici, du réseau lacuno-canaliculaire) est un point essentiel quant à l'analyse des images. De tels outils pourraient également être appliqués à la segmentation de la vascularisation de l'os ou de tumeurs par exemple.

Annexe : étude dosimétrique

Une courte étude, visant à calculer un ordre de grandeur de la dose reçue par un échantillon, a été menée sur la ligne ID19 (ESRF, Grenoble) en avril 2014. Cette étude n'a pas vocation à faire une dosimétrie de précision, mais bel et bien avoir un ordre de grandeur des doses délivrées durant une acquisition tomographique.

1. Protocole de mesures

La chambre d'ionisation utilisée au cours de cette étude est une chambre d'ionisation semi-flexible PTW de type 31010 (PTW-Freiburg, Allemagne). Son volume de mesure est d'environ 0,125 cm^3.

La chambre d'ionisation est introduite dans un fantôme de plexiglas de type « souris » (PTW31002) (Figure 1), de manière à ce que l'échantillon puisse tourner librement (acquisition tomographique), tout en veillant à ce que la totalité de la partie active de la chambre soit dans le faisceau d'irradiation. Les dimensions du fantôme sont précisées dans les Figures 1 et 2.

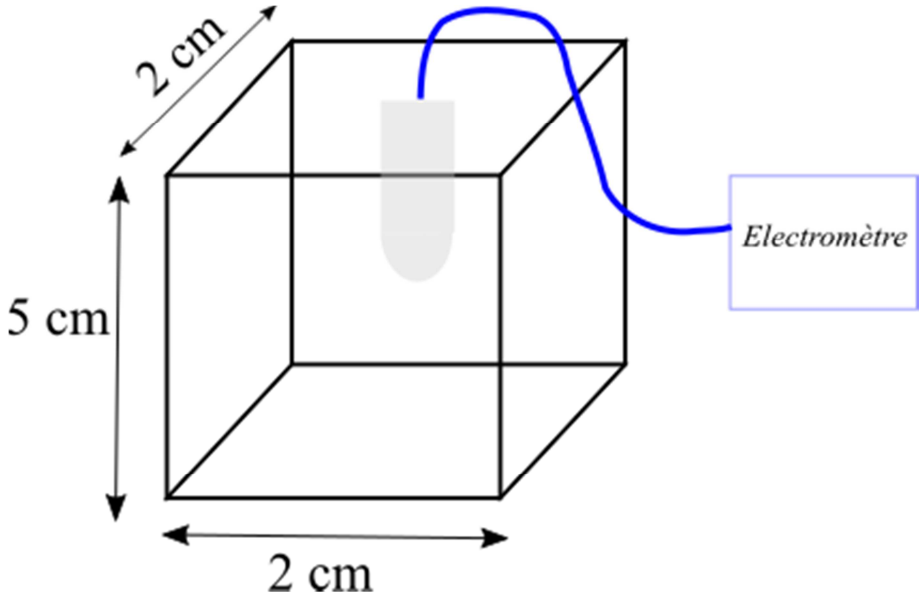

Figure 1: Schéma du montage (vue de face). La chambre d'ionisation est connectée à un électromètre.

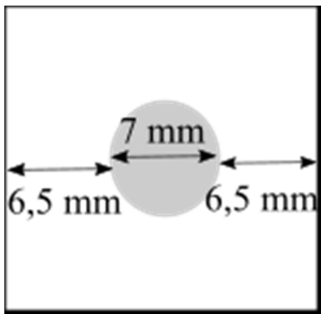

Figure 2: Vue du dessus du fantôme. Le trou destiné à l'insertion de la chambre crayon est coloré en gris.

Compte tenu de la géométrie du fantôme 'souris' (PTW-Freiburg, Allemagne) utilisé (Figure 1 et Figure 2), on a les taux d'absorption et de transmission suivants :

- Transmission totale du fantôme à 19,6 keV = $\exp(-0.849 \text{ x } 2 \text{ x } 0.65)$ = 33.16%
- Absorption totale du fantôme à 19,6 keV = $1 - \exp(-0.849 \text{ x } 2 \text{ x } 0.65)$ = 66.84%

- Transmission à mi-profondeur à 19,6 keV = $\exp(-0.849 \text{ x } 0.65)$ = 57.59 %
- Absorption à mi-profondeur à 19,6 keV = $1 - \exp(-0.849 \text{ x } 0.65)$ = 42.41%

D'autre part, on néglige l'atténuation de l'air.

2. Conditions expérimentales

La dose délivrée est égale au débit de dose multiplié par le temps d'irradiation. Dans nos conditions, le temps d'irradiation correspond approximativement au nombre de projections multiplié par le temps d'exposition. On néglige dans ce cas l'irradiation subie par l'échantillon durant son centrage, et l'irradiation pendant les images de références.

On se propose d'évaluer la dose délivrée durant un « scan type ». Le dispositif expérimental est celui utilisé durant l'expérience LS2292 (collab. Marlène Wiart, CREATIS, Villeurbanne) destiné à l'imagerie en propagation libre de cerveaux de souris ischémiques.

Le dispositif utilise l'onduleur U17.6, dont le gap est réglé entre 28 et 34 mm. Aucune filtration additionnelle n'a été ajouté dans le faisceau. L'énergie du faisceau vaut environ 19,6 keV.

Concernant les conditions d'imagerie, une seule distance de propagation a été utilisée. Le temps d'exposition pour chaque projection est de 0,1 s. 1995 projections ont été acquises. Ainsi, le temps d'exposition est évalué à environ 200s.

3. Estimation du débit de dose

3.a. Calcul à partir d'une estimation de la fluence

Le TERMA (*Total Energy Released per Mass unit*) désigne l'énergie totale délivrée par unité de masse ; la totalité de cette énergie n'est pas transférée aux électrons et positrons du milieu. On note KERMA (*Kinetic Energy Released per Mass unit*) la portion d'énergie effectivement transférée. Le KERMA présente lui-même deux composantes : le K_{coll} (énergie transférée au milieu par collisions) et le K_{rad} (énergie transférée au milieu par collisions).

K_{coll} représente l'énergie déposée dans le milieu par collisions (élastiques ou inélastiques). C'est ce qui représente la dose, sous condition d'équilibre électronique. Le K_{rad} représente l'énergie perdue par radiation (brehmsstrahlung, annihilation électron/positron). Cette énergie est typiquement de l'ordre de 1 à 5%, et peut être négligée dans notre cas (photons de basses énergies).

Le KERMA collisionnel est défini par :

$$K_{coll} = \psi \frac{\mu_{en}}{\rho} \tag{7.3.1}$$

où $\frac{\mu_{en}}{\rho}$ représente le coefficient massique d'absorption d'énergie (*mass–energy absorption coefficient*), exprimée en cm^2/g, et ψ est la fluence en énergie, exprimée en J/cm^2.

La dose reçue à l'entrée de l'échantillon s'exprime comme :

$$D_E = \psi_0 . E . \frac{\mu_{en}}{\rho} \tag{7.3.2}$$

où ψ_0 est la fluence en entrée, μ_{en}/ρ le coefficient d'absorption massique et E l'énergie des photons.

Pour un point P se trouvant à une profondeur z d'un matériau de coefficient d'atténuation μ, on a :

$$D_P = \psi_0 \exp(-\mu z) . E . \frac{\mu_{en}}{\rho}$$

La valeur de $\frac{\mu_{en}}{\rho}$ pour l'eau à 19,6 keV, notée $\frac{\mu_{en}}{\rho}\Big)_{\text{eau,19.6keV}}$ a été déterminée par régression linéaire entre les valeurs tabulées à 15 et 20keV (NIST, http ://www.nist.gov/). On trouve :

$$\frac{\mu_{en}}{\rho}\Big)_{\text{eau,19.6keV}} = 0{,}616 \text{ cm}^2\text{g}^{-1}$$

De la même manière, le coefficient d'atténuation pour l'eau à 19,6 keV vaut :

$$\mu_{\text{eau,19.6keV}} = 0{,}849 \text{ cm}^{-1}$$

La fluence nous est donnée par une modélisation qui prend en compte les différents facteurs et éléments propres à la ligne (ID19, ESRF), tels que le courant du faisceau, le « gap » des onduleurs, les filtres, le wiggler, … (P. Tafforeau). Pour nos conditions expérimentales (wiggler U17.6, pas de filtre), on obtient une énergie moyenne de 19,6keV, et un flux à l'entrée de l'échantillon estimé à :

$$\psi_0(gap = 28\,mm) = 2{,}43 . 10^{11} \text{ph/mm}^2\text{/s}$$

$$\psi_0(gap = 34\,mm) = 2{,}86 . 10^{10} \text{ph/mm}^2\text{/s}$$

Cette fluence nous permet d'estimer le débit de dose à la surface d'entrée de l'échantillon, noté $\dot{D}_E$, en utilisant la formule (7.3.2) :

$$\dot{D}_E(gap = 28\,mm) = 47{,}00\,Gy/s = 2820\,Gy/min$$

$$\dot{D}_E(gap = 34\,mm) = 5{,}53\,Gy/s = 331{,}8\,Gy/min$$

On peut ainsi calculer le débit de dose à mi-profondeur, qui correspond aussi au débit de dose au point de mesure de la chambre d'ionisation :

$$\dot{D}_P(gap = 28\,mm) = 23{,}69\,Gy/s = 1421\,Gy/min$$

$$\dot{D}_P(gap = 34\,mm) = 3{,}18\,Gy/s = 190{,}8\,Gy/min$$

Pour une irradiation de 200s, comme c'est le cas durant un scan, la dose d'entrée s'élève donc à :

$$D_E(gap = 28\,mm) = 9400\,Gy$$

$$D_E(gap = 34\,mm) = 1106\,Gy$$

3.b. Estimation du débit de dose à partir de mesures

3.d.i. Corrections des mesures données par la chambre d'ionisation

Les mesures données par la chambre d'ionisation (CI) peuvent être influencées par différents facteurs ambiants, tels que la température, l'humidité, la pression atmosphérique, la polarité de la tension appliquée. Ainsi, ces mesures doivent être multipliées par les cinq facteurs correctifs suivants :

- k_{TP}, facteur de correction de la pression et température. Il est défini par :

$$k_{TP} = \frac{P_0.(273{,}2 + T)}{(273{,}2 + T_0).P} \tag{7.3.3}$$

où T et P sont la température et la pression ambiantes au moment de la mesure, respectivement. T est exprimée en °C et P en hPa. P_0et T_0 sont les pression et température de référence, indiquées dans la notice de la chambre d'ionisation. Dans notre cas, les valeurs de références sont :

$$\begin{cases} P_0 = 1013{,}25\ \text{hPa} \\ T_0 = 20°C \end{cases} \tag{7.3.4}$$

Le jour des mesures, les valeurs ambiantes étaient de :

$$\begin{cases} P = 999{,}30\ \text{hPa} \\ T = 19{,}6°C \end{cases}$$

Ceci nous donne un facteur correctif de :

$$k_{TP} = 1{,}013$$

- k_H, facteur de correction de l'humidité

Il vaut 1 si l'hygrométrie est comprise entre 20% et 80%. Dans notre cas, l'hygrométrie ambiante au moment des mesures était de 30%. On considère donc :

$$k_H = 1 \tag{7.3.5}$$

- k_{pol}, facteur de correction de la polarisation

À conditions de mesure identiques, une polarité différente de la tension appliquée à la CI peut entrainer une variation de la valeur affichée. Le facteur correctif correspondant s'exprime comme :

$$k_{pol} = \frac{|M^+| + |M^-|}{2M^{+/-}} \tag{7.3.6}$$

où $|M^+|$ et $|M^-|$ sont les valeurs absolues des mesures sous une polarité positive et négative respectivement, toute conditions étant identique par ailleurs. $M^{+/-}$ est le signal obtenu à la polarité utilisée habituellement. Dans notre cas, nous avons considéré :

$$k_{pol} = 1$$

Néanmoins, la littérature stipule que cette approximation n'est peut-être pas tout à fait adapté pour des faisceau de photons basse énergie (Podgorsak, 2005).

- k_{sat}, facteur de correction de la saturation

Ce facteur tient compte de l'effet de la recombinaison, qui dépend de la tension appliquée à la chambre. Il s'exprime comme :

$$k_{sat} = a_0 + a_1 \frac{M_1}{M_2} + a_2 \left(\frac{M_1}{M_2}\right)^2 \quad (7.3.7)$$

où M_1 et M_2 sont les mesures réalisées sous les tensions de polarisation $V_{pol,1}$et $V_{pol,2}$ respectivement, et a_0, a_1 et a_2 sont des constantes tabulées (IAEA TRS398).

- k_{QQ_0}, facteur de correction de l'énergie

k_{QQ_0} reflète la dépendance en énergie de la chambre d'ionisation. Le facteur de correction n'a pas été établi pour les basses énergies (comme celles que nous utilisons). Nous la considérons égale à 1, tout en gardant à l'esprit que cette approximation peut être invalide.

3.d.ii. Mesures

Notre CI est calibrée selon le protocole TRS 398 (Dose dans l'eau). Le facteur de calibration de la chambre est $N_{D,w}$:

$$N_{D,w} = 3{,}045.\,10^8 Gy/C$$

$$D = N_{D,w}.k_{T,P}.M \quad (7.3.8)$$

Les mesures *m* ont été faites en plaçant la chambre dans un fantôme PTW 31002, pour différentes valeurs de gap de l'onduleur. Les autres conditions expérimentales sont données à la Section 2.

$$m\,(gap = 28\,mm) = 44.95\,nC/s$$

$$m\,(gap = 34\,mm) = 5.49\,nC/s$$

Ce qui nous donne le débit de dose suivant (dose dans le fantôme), en appliquant la formule (7.3.3) :

$$\dot{D}_p(gap = 28\,mm) = 13.82\,Gy/s$$

$$\dot{D}_p(gap = 34\,mm) = 1.69\,Gy/s$$

Si on se rapporte à la surface d'entrée du fantôme, on obtient :

$$\dot{D}_E(gap = 28\,mm) = 24.00\ Gy/s$$

$$\dot{D}_E(gap = 34\,mm) = 2.93\ Gy/s$$

Pour une irradiation de 200s, comme c'est le cas durant un scan, la dose d'entrée s'élève donc à :

$$D_E(gap = 28\,mm) = 5600\ Gy$$

$$D_E(gap = 34\,mm) = 586\ Gy$$

4. Discussion

Tout d'abord, on observe que les doses estimées à partir de mesure à la chambre sont environ deux fois moins importantes que celles estimées à partir de la modélisation du flux.

Les différences entre les deux méthodes peuvent s'expliquer d'une part par les différents facteurs correctifs que nous avons négligés, faute de les avoir déterminés. L'ouvrage de Podgorsak (Podgorsak, 2005) nous indique que cette approximation n'est pas adaptés pour le facteur de polarisation k_{pol} pour des faisceau de photons basse énergie. D'autre part, Il est à noter que le débit de dose maximum mesurable par la CI semble dépassé pour les flux les plus intenses (gap faible).

Ensuite, notons que les doses exceptionnellement élevées dans ces conditions expérimentales particulières n'autorisent pas l'imagerie *in vivo*. Pour ce faire, il conviendrait de diminuer le flux de photons (par l'ajout de filtres), ou diminuer drastiquement le temps d'exposition (réduction du nombre de projections, diminution du temps d'exposition).

Références

Podgorsak, E. B. (2005). Radiation Oncology Physics: A Handbook for Teachers And Students.

Liste des travaux

Communications dans des conférences internationales

Weber L., Langer M., Cloetens P. and Peyrin F. Combining SART and CTF for 3D phase retrieval in X-ray in-line phase tomography, *IEEE International Symposium on Biomedical Imaging* (April 2015), New York, USA.

Weber L., Langer M. and Peyrin F. Regularized phase retrieval algorithms for X-ray phase tomography of 3D bone cell culture analysis, *IEEE International Symposium on Biomedical Imaging* (April 2015), New York, USA.

Weber L., Langer M., Cloetens P., Pacureanu A., Varga P., Hesse B. and Peyrin F., In-line phase nano-tomography of human femoral bone in osteoporosis and osteoarthritis, *Material Science and Engineering* (September 2014), Darmstadt, Germany.

Weber L., Langer M., Cloetens P. and Peyrin F., Regularized phase retrieval algorithms for X-ray phase tomography of 3D bone cell culture analysis, *Medical Applications of Synchrotron Radiation* (October 2015), Villard-de-Lans, France.

Communications dans des conférences nationales

Weber L., Langer M. and Peyrin F. Refractive index retrieval by combining the contrast transfer function and SART in X-ray in-line phase tomography, *GRETSI* (September 2015), Lyon, France.

Weber L., Langer M., Cloetens P. and Peyrin F. Comparison of regularized phase retrieval algorithms for X-ray phase contrast tomography – application on experimental data, *9ème Journées d'imageries optiques non conventionnelles* (March 2014), Paris, France.

Article dans des revues internationales à comité de lecture

Weber, Loriane, Max Langer, Sara Tavella, Alessandra Ruggiu, and Françoise Peyrin. 2016. "Quantitative Evaluation of Regularized Phase Retrieval Algorithms on Bone Scaffolds Seeded with Bone Cells." *Physics in medicine and biology* 61(9):N215–31.

Frachon, T., Weber, L., Hesse, B., Rit, S., Dong, P., Olivier, C., … Langer, M. (2015). Dose fractionation in synchrotron radiation x-ray phase micro-tomography. *Physics in Medicine and Biology*, *60*(19), 7543–7566. doi:10.1088/0031-9155/60/19/7543

Applications

"CreaPhase" sur la plateforme VIP (*http://vip.creatis.insa-lyon.fr/*), outil de simulation d'images en contraste de phase en propagation libre.

FOLIO ADMINISTRATIF

THESE DE L'UNIVERSITE DE LYON OPEREE AU SEIN DE L'INSA LYON

NOM : WEBER

DATE de SOUTENANCE : 30/09/2016

Prénoms : Loriane (Julie)

TITRE : Iterative tomographic X-Ray phase reconstruction

NATURE : Doctorat

Numéro d'ordre : 2016LYSEI085

Ecole doctorale : E.E.A. (Électronique, Électrotechnique, Automatique)

Spécialité : Traitement du Signal et de l'Image

RESUME :
Phase contrast imaging has been of growing interest in the biomedical field, since it provides an enhanced contrast compared to attenuation-based imaging. Actually, the phase shift of the incoming X-ray beam induced by an object can be up to three orders of magnitude higher than its attenuation, particularly for soft tissues in the imaging energy range. Phase contrast can be, among others existing techniques, achieved by letting a coherent X-ray beam freely propagate after the sample. In this case, the obtained and recorded signals can be modeled as Fresnel diffraction patterns. The challenge of quantitative phase imaging is to retrieve, from these diffraction patterns, both the attenuation and the phase information of the imaged object, quantities that are non-linearly entangled in the recorded signal.

In this work we consider developments and applications of X-ray phase micro and nano-CT.

First, we investigated the reconstruction of seeded bone scaffolds using sed multiple distance phase acquisitions. Phase retrieval is here performed using the mixed approach, based on a linearization of the contrast model, and followed by filtered-back projection. We implemented an automatic version of the phase reconstruction process, to allow for the reconstruction of large sets of samples. The method was applied to bone scaffold data in order to study the influence of different bone cells cultures on bone formation. Then, human bone samples were imaged using phase nano-CT, and the potential of phase nano-imaging to analyze the morphology of the lacuno-canalicular network is shown. We applied existing tools to further characterize the mineralization and the collagen orientation of these samples.

Phase retrieval, however, is an ill-posed inverse problem. A general reconstruction method does not exist. Existing methods are either sensitive to low frequency noise, or put stringent requirements on the imaged object. Therefore, we considered the joint inverse problem of combining both phase retrieval and tomographic reconstruction. We proposed an innovative algorithm for this problem, which combines phase retrieval and tomographic reconstruction into a single iterative regularized loop, where a linear phase contrast model is coupled with an algebraic tomographic reconstruction algorithm. This algorithm is applied to numerical simulated data.

MOTS-CLÉS : X-ray imaging, phase contrast, tomography, computed tomography, holotomography, phase micro-CT, phase nano-CT, bone, tissue engineering, phase retrieval, tomographic reconstruction, data simulation, combined algorithm, regularisation.

Laboratoire (s) de recherche : Centre de Recherche en Acquisition et Traitement de l'Image pour la Santé (CREATIS), CNRS UMR 5220, INSERM U1206.

Directeur de thèse: Dr Françoise PEYRIN (DR INSERM)

Président de jury :

Composition du jury : Dr Pierre BLEUET (Rapporteur) ; Pr Jean-Yves BUFFIERE (Examinateur) ; Dr Peter CLOETENS (Invité) ; Dr Max LANGER (Co-directeur) ; Dr Rajmund MOKSO (Rapporteur) ; Dr Françoise PEYRIN (Directrice) ; Pr Francis VERDUN (Président)